Characterisation of oxidation techniques on wide bandgap semiconductor surfaces.

Simon Astley

Department of Physics

Aberystwyth University

This thesis is submitted for the degree of

Doctor of Philosophy

January 2020

Declaration and Statements.

Word Count of thesis: DECLARATION	32,821
This work has not previously been accepted in substance for any degree and is not concurrently submitted in candidature for any degree.	
Candidate name	Simon Astley
Signature:	
Date	31/1/2020

STATEMENT 1

This thesis is the result of my own investigations, except where otherwise stated. Where *__correction services__ have been used, the extent and nature of the correction is clearly marked in a footnote(s).
Other sources are acknowledged by footnotes giving explicit references. A bibliography is appended.

Signature:	
Date	31/1/2020

[*this refers to the extent to which the text has been corrected by others]

STATEMENT 2

I hereby give consent for my thesis, if accepted, to be available for photocopying and for inter-library loan, and for the title and summary to be made available to outside organisations.

Signature:	
Date	31/1/2020

NB: *Candidates on whose behalf a bar on access (hard copy) has been approved by the University should use the following version of Statement 2:*

I hereby give consent for my thesis, if accepted, to be available for photocopying and for inter-library loans after expiry of a bar on access approved by Aberystwyth University.

Signature:	
Date	31/1/2020

Contents

Abstract

This work discusses the relevance of the oxidation procedure on wide-band gap semiconductors and the effect that has on the surface chemistry. It has been shown that acid treatment procedures produce an incomplete termination resulting in a reduction in thermal stability. Pure oxygen anneals have been conducted on diamond surfaces and measured using Photoelectron Spectroscopy(PES) techniques in-situ at near ambient pressures and have shown that 400°C is an optimum temperature for the removal of sp^2 carbon and achieving a complete oxygen coverage of the surface. The effect of surface termination of Detonation Nanodiamonds (DNDs) and single crystal diamonds have been studied experimentally and theoretically using PES and Density Functional Theory to determine the most stabilised terminations for device applications and drug adsorption. These have then been measured experimentally and molecule coverage has been characterised using optical scattering and absorption techniques.

Watch your back, but more importantly when you get out the shower, dry your back. It’s a cold world out there.

DJ Khaled.

I would like to dedicate this thesis to my loving parents, who when presented with a 3 year old son who still couldn't walk and talk, decided to force him to: Take dance lessons, play numerous sports, try gymnastics, do swimming lessons, do physiotherapy, do speech therapy, biomechanics appointments, spend an hour every night practicing writing and stretch him out for 2 hours every night even when he screamed that he hated them and wanted to run away as his twin and all the other kids his age didn't suffer this much and he couldn't understand why. No matter how much he was bullied initially in the early years of school because he couldn't write or walk into school somedays so had to be carried in a pram at the age of 6, you consistently told me that it would all be worth it and I'd appreciate this all when I'm older and successful.

All my success in academia, sports and life is entirely due to the financial and emotional stress you underwent at the time to ensure my disability limits me as little as possible, and I'll be eternally thankful that I was lucky enough to have parents who wanted their son to achieve great things no matter what. I hope I've made you both proud of me and yourselves as everything I achieve is a result of your own hard work of which I can never truly repay.

This may be much longer than a traditional page for dedications, but even this is not truly enough to thank them for what they have done for me. That and my admittedly still poor English writing skills probably is not doing them justice either. Thankfully a PhD thesis is all computerised, otherwise I'd also be apologizing to them in this thesis for my writing as that has remained dreadful throughout all these years.

Acknowledgements.

Firstly, I would like to thank my supervisor Prof Andrew Evans, for his continued support throughout the entirety of my PhD. Whether it was for work related or even concern for my surgery/injuries occurred from playing rugby he was supportive. His guidance and knowledge on all my work has been invaluable and I hope the quality and novelty of the research demonstrated in this thesis is something that reflects well on him. Secondly, I'd like to thank my 2nd supervisor Dr Rachel Cross for her support throughout my PhD with learning specific experimental techniques, bouncing ideas off and being there to rant towards. I would also like to thank her for picking me to work with Andy on a project in my masters year, without which I imagine I wouldn't have found a topic of research and a PhD I would have enjoyed so much. The two of you together have made an ideal supervisory team which I doubt many people in the world would be lucky to have.

I would also like to acknowledge the entirety of the materials research group at Aberystwyth including fellow PhD students, lecturers and technicians whom have been extremely helpful to be working alongside. From fixing/maintenance of equipment, the friendships made and conversation during coffee to brighten grey days which made the PhD a lot more enjoyable and Aberystwyth such a unique and wonderful place to be in. A few deserving of mention are Carys Huntly, who helped me make several posters look a lot more presentable and kept me motivated throughout the PhD and helped me with shopping and work when I was unable to walk for several weeks. Anita Brady-Boyd who I have shared an office with for the past year who has become a good friend and helped with proof-reading my thesis. John Tomes who has helped with AFM, TEM and Confocal measurements and maintaining the labs where his help has been invaluable. Kerry Whittlesea whom I have worked together on diamond/nanodiamond research for close to 2 years now, we have worked together at several beamlines and experimental times and her knowledge in the area has helped immensely.

I'd like to thank my family where my parents are recognised in the page above. Finally, and most deservingly, I'd like to thank my partner. Who has consistently made sure I have looked after myself and pushed me to do the best work I can do. The completion of this thesis has probably been more stressful on herself then me, so I'm glad I can submit this just so she can finally breathe a sigh of relief.

Chapter 1 - Introduction and thesis layout.

Wide-band gap semiconductors have relevance in multiple scientific fields such as; Quantum, power electronics, optoelectronics, optics, and biological sensing. However, the surface states of a semi-conductor can vastly affect the band-bending of a material, which make some semiconductors versatile as the bandgap can be controlled. The materials studied in this thesis are single crystal diamonds, gallium oxide (Ga_2O_3) and nanodiamonds.[1-4]

Diamond is attracting more attention as it becomes more mature as a semiconductor material. Due to it's amazing properties which outshine other materials such as silicon or gallium nitride (GaN), it is highly appealing for device fabrication such as power electronics. Growth of high quality diamond on a large scale was difficult to fabricate in bulk, however with consistent advances in the growth field looking promising, with epitaxial growth of CVD diamond on iridium substrates believed to be one of many potential methods of solving this issue for mass manafacturing of device quality diamond.[5-6] Diamond has a downward band-bending however this can be altered through the surface termination of the crystal, altering the electron affinity of the diamond surface.[7] This can also be altered in the growth stage by careful doping of the crystal with n- or p- type dopants (such as nitrogen or boron). [8-9] Nanodiamonds have the same bulk properties as single crystal diamond but on a nanoscale.[10] Due to their large surface to bulk ratios and the more modifiable surface there is increasing interest for their uses in drug delivery and quantum optics where nitrogen vacancies are of particular interest[11]. Gallium oxide, specifically β-Ga_2O_3 is showing promise as an emerging wide-bandgap semiconductor. Initial devices fabricated using β-Ga_2O_3 show remarkable results considering its maturity in the field and is progressing faster than other materials such as Si and GaN with similar levels of research. [12-13]

This body of work looks at the effect the method of oxidation has on these wide-band semiconductors and analysis on the chemical and physical properties they produce[14,15]. Samples are primarily analysed using Photo-Electron Spectroscopy techniques (PES) where the surface chemistry, band-bending and workfunctions can be monitored in-situ dependant on temperature and various adsorbates on the surface. Complimentary techniques such as Density Functional Theory (DFT), Raman spectroscopy, Atomic Force Microscopy (AFM),

Transmission Electron Microscopy (TEM), Dynamic Light Scattering(DLS) and Photoluminescence (PL) have also been used to study these materials.

This thesis covers the importance of the method of oxidation used on wide-band gap semiconductors when obtaining an oxygen terminated surface. Various methods of oxidation involving acids, alkalis, gases and water have been investigated and the resulting chemical species along with their thermal stability have been discussed[16,17]. Single crystal (001) and (111) moderately boron-doped diamonds, nano diamonds and single crystal $(\bar{2}01)$ gallium oxide have been analysed under various conditions using; X-ray photoelectron Spectroscopy, Near-Ambient Pressure X-ray photoelectron Spectroscopy, Near Edge X-ray Absorption Fine Structure, Ultraviolet Photoelectron Spectroscopy, Raman Spectroscopy, Photoluminescence, Confocal Microscopy, Dynamic Light Scattering, Atomic Force Microscopy and Transmission Electron Microscopy to determine the chemical species that have formed on the surface, along with the resulting change in band-gap, crystal quality etc.

Experiments have been conducted here at Aberystwyth University using our PES system, known as the Real-time Electron Emission Spectroscopy (REES) system, as well as at Diamond Light Source using the Near-Ambient Pressure(NAP) branchline (B07) as well as the NAP-PES system at Manchester University. These have allowed for modification and quantification of surface species on diamond substrates at NAP for studies into the oxidation process to be observed in real-time. More on these will be discussed in Chapter 4.

Chapter 2 is an introduction into the materials that were used during these experiments of single crystal diamond and gallium oxide, and DNDs. The relevance of these materials and the importance on the oxidation of the surface will be described.

Chapter 3 introduces the techniques used throughout this thesis with a heavy focus on photo-electron spectroscopy techniques and mentions the processes behind the other supplementary techniques.

Chapter 4 discusses the instrumentation used throughout this thesis and focuses on the PES equipment, which is unique to Aberystwyth, as well as mentioning the NAP facilities at Manchester and B07, and descriptions of equipment used for the supplementary techniques is also given.

Chapter 5 shows the results from single crystal (001) and (111) diamonds which were oxidised using various methods, and the chemical species that formed and the amount of remaining sp^2 carbon remaining on the surface were analysed, with the focus of the investigation to determine the ideal method for oxygen termination, we found that depending on the technique used the ratios of ether, hydroxyl and ketone bonding was vastly different and in some cases peroxide also formed. Measurements of core levels of carbon and oxygen in real-time under near ambient pressures to see the change in chemical species based on the gas/liquid exposed to the surface as well as temperature dependence, and have found that acid etches produce the most weakly bonded surface whilst also having a much lower band bending, and increasing the surface roughness of the diamonds. The results from this work potentially may suggest a best operating procedure for the terminations of diamonds for device applications.

Chapter 6 discusses the results from various oxidation methods performed on high quality nanodiamonds. We found that the oxidation procedure not only removes over 90% of the initial starting sp^2 carbon, but the oxidation states are very similar to single crystal. DFT calculations have been conducted for both single crystal and nanodiamonds and the process at which the diamond oxidises and key stoichiometry changes on the surface have been identified.

Chapter 7 discusses how the knowledge gained from diamond and nanodiamond surfaces being oxidised has been used to apply chemotherapy drugs called Fluorouracil (5FU) onto nanodiamonds for drug delivery applications, it has been shown that in comparison to how the drug is typically delivered, we can reduce the particle size deposited into patients by 50 times. This might allow increased chance of cell absorption, meaning a reduction in the overall amount of chemotherapy drug being used, whilst also with the potential of taking advantage of many of nanodiamonds various applications in the drug-delivery field such as targeting specific organs and bio-sensing.

Chapter 8 discusses the results from experiments conducted on gallium oxide which has undergone various surface preparation treatments and the change in thermal stability and downward band-bending using real-time measurements have been conducted, which may also suggest a preferred treatment method for device fabrication such as Gallium Oxide FET's.

Chapter 9 gives a summary of all the work conducted in this thesis along with further work which is needed to complete/compliment this body of research, along with a few closing remarks summarising the importance of oxidation from knowledge gained from all three materials.

References:

[1] - Gabriele Grosso ; Benjamin Lienhard ; Hyowon Moon ; Diego Scarabell ; Tim Schroeder et al. Quantun Emission From Atomic Defects In Wide-Bandgap Semiconductors. 2017 IEEE Photonics Society Summer Topical Meeting Series.

[2] -E .Woerner C. Wild W.Mueller – Serbert, P. Koidl. CVD-Diamond Optical Lenses. Diamond And Related Materials Volume 10, P557-560.July 2001..

[3] -Windfriend Monch.Occuptation Of Surface States and Surface Band-Bending In Thermal Equilibrium. Semiconductor Surfaces and Interfaces. Springer. Vol 26. P51-57. 1995.

[4] - I. Lundstrom, Anita Spetz And F. Winquist. Semiconductor Biosensors. Royal Society of Chemsitry. Series B Biological Sciences. Vol 316. P47-59. Augyst 1987.

[5] – Medelung, O. Data in Science And Technology. Semiconductors Group IV Elements and III-V Compounds. Springer. 1991. ISBN 3-540-53150-5.

[6] – Diamond Wafer Technologies For Semiconductor Device Applications. Power Electronics Device Applications of Diamond SemiConductors. P 1-97. 2018. Woodhead Publishing. https://doi.org/10.1016/B978-0-08-102183-5.00001-7

[7] – R. Gtaupner. M. Hollering. A. Ziegler. J. Risten. L. Ley And A. Stampel. Disperions Of Surface States on Diamond (001) And (111). Physical Review B. Vol 55. P.10841. 1997.

[8] – Dan Wu. Y. C. Ma, Z. L. Wang, Q. Luo, C. Z. Gu, N. L. Wang, C. Y. Li, X. Y> Lu, And Z. S, Jin. Optical Properties Of Boron-Doped Diamond Phys. Rev. B. Volume 73. 012501. January 2006.

[9] Majchrowicz D, Kosowska M, Sankaran. KJ, ET AL. Nitrogen-Droped Diamond Film For Optical Investigation Of Hemoglobin Concentration. Materials (Basel). January 2018.

[10] - Mochalin. V. N, Shenderova. O, Ho. D, Gogotsi. Y. The Properties And Applications Of Nanodiamonds. Nature Nanotechnology. Vol7. P11–23. 2012. https://doi.org/10.1038/nnano.2011.209

[11] - Nagl. A, Hemelaar. S. R, Schirhagl. R. Improving Surface and Defect Center Chemistry of Fluorescent Nanodiamonds For Imaging Purposes- A review. Analytical and Bioanalytical Chemsitry. Vol 407. P7521-7536. Springer Verlag. https://doi.org/10.1007/s00216-015-8849-1.

[12] – C. Janowitz ET AL. Experimental Electronic Structure of In2O3 And Ga2O3. New Journal Of Physics. Volume 13. August 2011.

[13] – A. Kuramata, K. Koshi, S. Watanabe, Y. Yamaoka, T. Masui, S. Yamakoshi. High-Quality B- Ga2O3 Single Crystals Grown By Edge-Defined Film-Fed Growth. Japanese Journal OF Applied Physics. 2016.

[14] – Oktyabrsky, Serge, Ye, Peide. Fundamentals of III-V Semiconductor MOSFETS. Springer. P74-76. 2010.

[15] – Sun. C, Hao. T, Li. J, Ye. H, Gu. C. The Design And Performance of Hydrogen-Terminated Diamond Metal-Oxide-Semiconductor Field-Effect Transistors With High K Oxide HFO2. Micro and Nano Engineering. Vol 6. 2020. https://doi.org/10.1016/J.MNE.2020.100046.

[16] – M. P. Kiskinova. Poisoning And Promotion In Catalysis Based On Surface Science Concepts And Experiments. Volume 701ST Edition. P40-42. Elsevieir Science. November 1991.

[17] – P. M. Martin. Handbook Of Deposition Technologies For Films And Coatings (Third Editions) . Chapter 3. Surface Preparation for Film And Coating Deposition Processes. Elsevier. P 93-134. 2010.

Chapter 2 - Materials

2.1 Diamond

2.1.1 Introduction to Diamond.

Diamond is a naturally occurring wide-bandgap semiconductor with a cubic crystal structure with tetrahedral bonding consisting entirely of carbon atoms in a sp^3 state. sp^3 is the electron hybridization arising from the L-shell ($2s^2 2p^2$). Electrons from an s-orbital overlaps the p-orbitals forming 4 hybridised sp^3 orbitals, all of which are at 109.5° to each other.[1] This is the reasoning behind diamonds structure. Although graphite (honeycomb sp^2 lattice is a preferred state of carbon (standard enthalpy difference of 2.9kJ mol^{-1}) the conversion between sp^2 and sp^3 can occur in high temperature high pressure (HPHT) scenarios. The high activation energy required for the reverse process means diamond is a stable material. Natural diamonds are formed from carbon in the upper mantle of the earth being exposed to these conditions.[2,3]

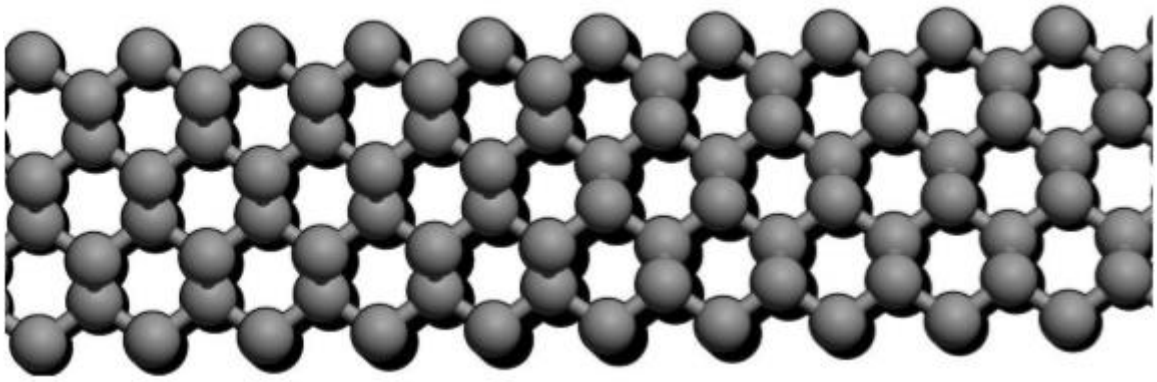

Figure 2.1.1 – A diamond slab showing the tetrahedral structure. Made from a diamond unit cell in Avogadro.

However, these diamonds are subject to many defects or inclusions which alter the optical and electronic properties of diamond. While these defects or inclusions may produce unique specialties depending on the nature of them, for scientific applications these deformities mean taking advantages of the many mechanical and electrical properties diamond excels at.[4] Many of diamond's unique properties come from its bulk properties, and carbon atoms being replaced or defect/strain occurring in the lattice can make the diamond drastically different, turning it from being transparent to obtaining colour and altering its bandgap. [5-7]

Due to continuing improvements in diamond growth techniques, single crystal diamonds with controllable doping levels with low defects and dislocations are increasingly available at the dimensions required for device fabrication. New variations of diamond growth such as the

introduction of an indium growth substrate for the hetero-epitaxial growth of diamond are showing signs of being extremely promising for the production of device quality diamonds on much larger scales[8-9]. Moissan was one of the first to attempt diamond growth in 1893, mimicking the HPHT conditions that they naturally formed in. In an electric arc furnace with carbon electrodes 2cm apart, he passed 450A of current through them generating 3500°C, he used the molten iron already present in the furnace and the contraction of the metal upon being exposed to water to create the required pressure. [10] He believed tiny crystals he had found were synthesized diamonds, but he later confirmed he had instead formed silicon carbides (SiC). It wasn't until 1956 when General Electric created the first commercial diamond[11]. By producing 10Gpa and 2000°C environment with transition metals present to act as catalysts for the formation of synthesized diamond. However due to the limited sizes they were able to create at the time (<0.15mm), their only uses were in industrial applications such as polishing and drilling taking advantage of diamonds hardness[12]. Although HPHT synthesis has increased drastically since then, the lack of control of dopants (specifically nitrogen) and lattice defects has meant that this growth method is unviable for fabricating diamonds used in optical and electronic applications.

The 1950's was the start of Chemical Vapour Deposition (CVD) work on diamond. In 1952 Eversole created a CVD procedure for diamond growth with significantly reduced pressure constraints (100Kpa) and reduced temperature conditions (1000°C), (although it wasn't until 1962 he improved the growth technique to remove graphitic deposits in the diamond. Slow growth rates meant this wasn't practical of mass production)[13]. It has since then evolved through the work of the soviets in the 1970's and National institute for Research in Inorganic Materials (NIRIM) in the 1970's-1980's until it had been perfected and improved to the standard operating procedure that is used now. [14]

CVD is a method of diamond growth where the dopant levels can be controlled. It involves using a seeding layer (nanodiamonds) and the use of usually methane as a carbon-source[15]. The methane is activated (either by a hot filament, or more typically microwave/R.F method to create plasmas) and flowing in hydrogen gas to help with the breaking apart of the methane molecules. This activation produces the following products:

$$H_2 + \text{heat } (e^-) = 2H$$

$$CH_4 + H = CH_3 + H_2$$

These CH_3 particles give rise to diamond nucleation sites, and the continuous growth creates a layer-by-layer epitaxial growth method for diamond. The atomic hydrogen also etches away any graphitic carbon and also etch away at the diamond growth too, however the growth rate of diamond is allowing for a net growth of diamond whilst reducing graphitic carbon.[16] By flowing in various other gases such as N_2, ammonia, borane and trimethyl boron, nitrogen or boron can be incorporated into the growth allowing for diamonds with specific dopant concentrations.[17] However, gas ratios must be carefully controlled otherwise lattice defects and graphitic regions will become more prevalent. This allows for fine controlling of the electronic and optical properties of diamond, where boron doped diamond is useful in electrochemistry and electronics and nitrogen doped diamond has interest in quantum applications due to nitrogen vacancies. Nitrogen vacancies are caused due to a point defect in the diamond lattice, caused by a bonded nitrogen being unable to pair to 4 carbon atoms, this means there is a unpaired electron which can exist in two different electron spin states. The electron although having a net Spin of S=1, can exist on a sublevel as (-1,0,1). The coherence times of these spin states can be extended from micro to milliseconds dependent, and the electrons can be easily flipped, making it suitable for future quantum devices. [18-21]

Although growth rates can be slow (0.1-10µm/hour) CVD has the benefit of creating a diamond film of extremely high quality and where the dopants can be carefully controlled. Due to the improvement of CVD growth the quality, variability and availability of the diamonds produced has increased the capability of using diamonds for a large variety of applications. Diamond is gaining interest in for use in: Quantum devices, power electronics, wave-guide structures, electrodes, optical lenses, biomedical applications and much more. [18-27] Table 2.1.1 summarizes various properties diamond exhibits at room temperature which make diamond a highly versatile material and therefore desirable in a range of scientific fields when compared to other semiconducting materials such as Si and GaN[28]. Along with those properties it also very resistant to chemical erosion, broad optical transparency, bio-inert and high sound propagation capabilities. [29-30]

Properties/Material	**Diamond**	**Si**	**GaN**	**β-Ga_2O_3**
Bandgap (eV)	*5.47*	*1.12*	*3.5*	*4.85*
Electron Mobility (Cm^2/Vs)	*1900-2300*	*1400*	*1250*	*200-250*
Hole Mobility (Cm^2/Vs)	*1500-2300*	*600*	*200*	*12*
Dielectric constant	*5.7*	*11.9*	*9.5*	*16.3*
Thermal Conductivity (W/cm.K)	*25*	*1.48*	*1.3*	*0.13*
Electron Saturation velocity (10^7cm/s)	*2.7*	*1*	*2.7*	*2.0*
Breakdown Field (10^5 V/cm)	*100*	*3*	*30*	*80*
Debye temperature (K)	*1860*	*645*	*608*	*738*
Hardness (kg/mm^2)	*10000*	*1000*	*1224*	*989*
Johnsons FoM	*81,000*	*1*	*215*	*2844*

Table 2.1.1 – Properties of diamond, GaN, Si and β-Ga_2O_3 demonstrating why diamond is such an extraordinary material.

There are four main categories which diamonds fall into due to the variations of inclusion formation in natural diamonds, and the variations of dopants which can be controlled for lab made diamonds, these are shown in Table 2.1.2.[31]

- Type Ia – Nitrogen content around 3000ppm (0.3%)
- Type Ib – Nitrogen content up to 500ppm (0.05%)
- Type IIa – Nitrogen content which is immeasurable
- Type IIb – Nitrogen content which is immeasurable, Boron content of at least 1ppm, P-type semiconductor.

Table 2.1.2: Classification of diamonds dependant on the dopants inside the crystal.

Most natural diamonds fall into type Ia due to the high nitrogen presence in the mantle, and in increasing rarity from Ib to IIb which is extremely rare. The increase in growth capabilities and diamond availability has made diamond a viable option for real world applications.

2.1.2 Diamond Surfaces

There has been an increasing interest in diamond for electronic device applications due to its large number of desirable properties and it becoming easier to grow large crystals.[32] An estimation of density of free electrons in the conduction band can be calculated from:

$$Eq\ 2.1.1 \quad n = N_c \exp\left[\frac{-E_c - E_f}{k_B T}\right]$$

which produces an effectively zero carrier density result. Where N_c is the effective density of states in the conduction band, $k_B T$is the Boltzmann constant, E_c and E_f are the energies of the conduction band and fermi level respectively. Due to this phenomenon the band-gap states are heavily dependent on the dopant, defect and extrinsic contaminants. Another factor which influences diamond's electronic properties which can be controlled post-growth of the diamond's is the surface of the crystal, i.e. whether it's terminated with a specific element or any surface reconstructions that occur. These specifically are labelled as surface states due to the localization of the wavefunctions where electrons or holes from bulk can be accommodated. The diamond surface is important as the termination can affect the bandgap by up to 0.5eV changing its electronic and optical properties, can alter the electronegativity by up to 3eV from positive to negative and vice-versa and the surface stability of some functional groups will vary dependent on the crystal orientation of the diamond and the number of free electrons at the surface.[33]

There is also a difference in these surface states dependent on the crystal orientation of the diamond, where depending on where the crystal lattice is cut from will leave a different top-arrangement (crystal plane) which will affect the surface of the crystal. These can be denoted using Miller Indices, which are used to describe the plane and direction of atoms in reciprocal space of a crystal lattice. These are used to describe the orientation of a unit cell of a crystal of which the research is conducted. The (111) orientation only has one free electron on the surface, and the (001) plane has two. This also causes variations in type of chemical species that can be formed on the surface, where (001) can share two pairs of electrons with an atom whilst the (111) is stuck to a singular. There is also the (011) plane but that orientation is not considered in this body of work.[34-35]

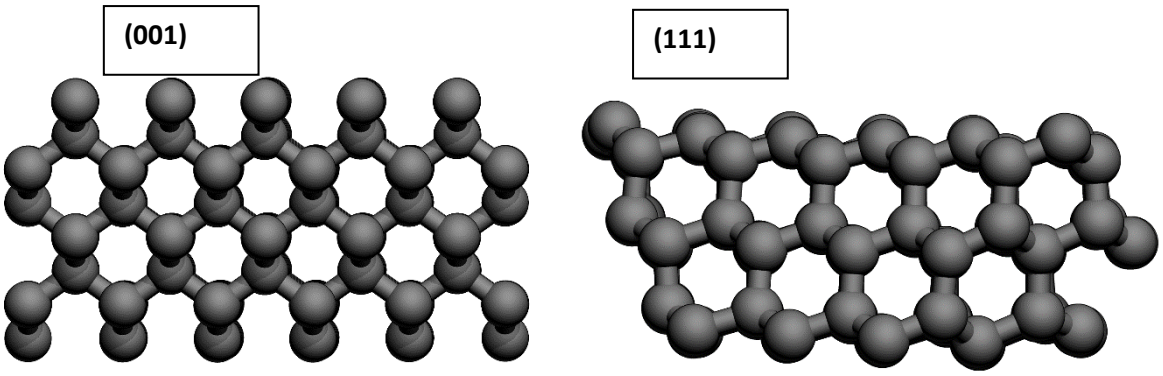

Figure 2.1.2: Unit cell of the (001) and (111) crystal orientations of diamond. Due to the structure in each plane the available electrons and therefore surface species available to the differing planes can vary drastically.

The perfectly clean surface is unstable and highly reactive, specifically for the (001) orientation. Surface reconstructions refer to two-dimensional change in the surface, where surface atoms can change positions. For (001) diamonds surface atoms reconstruct to form a (2x1) sections such that across the crystal face the top layer of atoms actually bond together in pairs, rather then what its normally denoted as (1x1) where they are singular. This means that for the(2x1) (001) substrate there is only one free electron instead of the usual two.

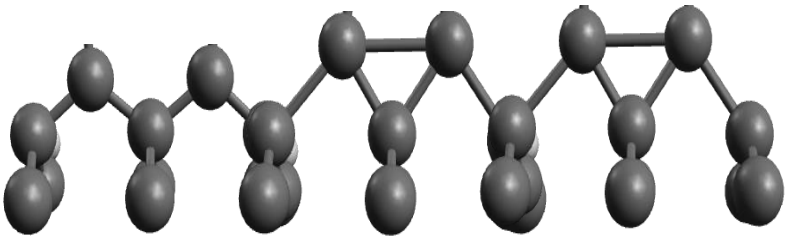

Figure 2.1.3: the difference between the typical (001) diamond surface on the reconstructed.

2.1.3 Diamond surface terminations: Oxygen and Hydrogen

Oxygen and hydrogen terminations on diamond are the easiest terminations to achieve yet due to their vastly different properties are the most researched and trialed for use in device fabrication. The surface chemistry is dependent on crystal orientation, roughness, reconstruction and the method of terminating the crystal[36-37]. Even the difference between functional groups on the surface such as ketone and a hydroxyl group produce differences in work-function, conductivity and electron affinity. Differences in electron affinity from -1.3eV for H and +1.7eV for O have been observed for (001) surfaces, where the oxidation state has also affected the measurements for O termination, reducing the positive affinity by over

1ev.[33] For the (111) orientation this effect is less drastic due to the reduced amount of surface atom coverage. This change in workfunction and electronegativity is due to oxygen possessing a greater electronegativity then carbon, causing a negatively polarized surface, which in turn creates a potential step which shifts the vacuum level above the conduction band; for hydrogen terminations the reverse of this true.

A lot of work from various groups have tried to determine the ideal surface oxidation state of the (001) diamond, although multiple groups have differing opinions and DFT calculations providing varied results.[35,38-40]The relationship between the various types of typically reported surface species including ketone (C=O), hydroxyl (C-OH) and ether (C-O-C) are the biggest talking points, with many groups insisting the ether should be predominant oxygen bonding mechanism and ketones and hydroxyl groups attach to carbon atoms which are missing from chains. Some calculations even show that the C-O-C shouldn't form under any circumstances. Other theoretical work states that unless the (001) diamond is perfectly terminated, reconstructions occur to enforce the optimal termination, resulting in a (2x1) reconstruction.[41,42] Work by De Leon's group show's that the method of preparation of the surface is important, and that using plasma's and specialized annealments, the specific type of oxygen group on the surface can be controlled to some degree and also has an effect of the stability of near-surface nitrogen vacancies (NV^-'s) for quantum applications. [43] This work is also validated by work done by Di Hu from Aberystwyth materials research group who also reported similar findings in his thesis.[44] However, the issue with techniques such as XPS measurements of surface groups is that upon terminating your diamond and then transferring it into a UHV system, surface contaminants will adsorb on your surface, and if the surface is particularly unstable it will be altered by these adsorbates. This means a perfect understanding of processes behind oxidation of both (111) and (001) diamond might be lacking. To overcome these disagreements the measurement of the surface chemistry during oxidation is essential.

2.2 Nanodiamonds

2.2.1 Properties and Formation of Nanodiamonds.

Nanodiamonds (ND's) are crystalline diamonds in the size ranges of 5nm to 100's of nm in diameter. Whilst maintaining many of the bulk properties of diamond it also has a much larger surface to bulk ratio making surface termination important. [45-47]

The method of production of nanodiamonds vastly alters properties such as the radius, sp^2 to sp^3, dopant levels and crystallinity. Research on the formation of nanodiamonds was first started by Ryabinin in 1956 using dynamic synthesis, although his experiments proved unsuccessful.[48] Research into shock-compression started in 1960 however it wasn't until 1963 where the production of nanodiamonds started producing quantifiable results.[49] However, yield rates were very small (20%) and graphitic carbon and diamond like carbon (DLC) was also produced. Research into ND's increased again in 1983, which was still heavily focused in the USSR despite the scale of production far outweighing any practical applications for the product at the time. Due to the inability to make use of these materials research slowed down and several sites at which ND's were produced from shut down by the late 90's.

Interest in nanodiamonds for applications such as drug delivery, tribology, and CVD diamond growth has exponentially increased over the past 20 years. There were less than 10 publications per year before 1997, finally increasing past 50 per year in 2004. In 2016 there was 550 publications related to nanodiamonds, where roughly 150 of those were related to biological applications. The number of publications in the first month of 2020 related to nanodiamonds is already above 70.

Table 2.2.1 lists some of the properties of nanodiamonds, many of which are similar to bulk diamond, which have contributed to the increase in research to nanodiamond applications.

- High modifiable surfaces for a range of applications (O, H, NH_2, COOH, OH etc.) These modifications change the chemical reactivity, optical and electronic properties of the nanodiamonds.
- Bio-inert for drug delivery and tribology applications
- Distinct NV^- emission for bio-sensing
- Similar properties of bulk diamond (Good thermal conduction, hardness etc.)

Table 2.2.1: Properties of the nanodiamond which are making them widely researched for applications in various fields.

The synthesis of nanodiamonds can be split into three main categories: static synthesis, dynamic synthesis and laser ablation.

Static synthesis is a replication of the HPHT growth of single crystal diamond and uses the waste products of HPHT diamond growth for the formation of nanodiamonds. Micron sized diamonds whose properties are undesirable (too small, high N concentration, disfigured shape) from HPHT methods are milled together until the particle size is heavily reduced. This process in comparison to the others produced mono-crystalline ND's whose production cost is an order of magnitude cheaper than dynamic or laser synthesis, however the limitation of this method is that particle size is limited to >20nm. These ND's are primarily used in photo-luminescence applications due to the high density of N incorporation and low cost. [52-54]

Dynamic synthesis is used to produce typically what we define as detonation nanodiamonds (DND's) which can be sub-categorized into three types: Shock-compression of metals and graphite, ND's produced from a carbon precursor (graphite, coal etc.) and explosives, and DND's which are created from the elemental carbon within the explosives themselves. The explosives used for these methods is normally a 3:2 ratio of TNT (2-methyl-1,3,5-trinitrobenzene) to RDX (1,3,5-trinitroperhydro-1,3,5-triazine) in either inert gas or ice.[50]

For DND's, formation of diamond crystal structure is believed to follow this process:

1. At the initial point from the explosive charge (TNT), the initial shockwave compresses the explosive material, which in turn induces heat and chemical decomposition of the explosive. this releases extremely large amounts of energy, much greater than the initial explosions, on a nanosecond scale, after which the following reaction forms atomic carbon and byproducts.

Eq 2.1.2 $CNOH \rightarrow N_2 + H_2O + CO + CO_2 + C$

2. Due to the immense heat and pressure during this process, liquid carbon can form on the nanoscale near the location of the shockwave. However, as the carbon propagates and attaches itself to other nanoscale liquid carbon, the temperature drastically decreases to a point of where the liquid form is unstable. [35, 51]
3. As the size of these droplets increase and temperature decreases, crystallization occurs in the liquid carbon under a specific set of conditions whilst the pressure is still above the diamond-graphite boundary, after which nanocarbon particles form. [45]

Due to the precise temperature and pressure ranges for the formation of nanodiamonds from liquid carbon, the time frame in which the crystallization occurs is very small. The chemical decomposition of the explosive takes 1ns, the formation of these carbon droplets occurs with 10ns, with formation of nanocrystalline diamond occurring in the 100-1000ns's timeframe. These DND's then follow the gaseous products in the shockwave, colliding with each other and forming tight agglomerations with each other until they hit the chamber walls, after which they are recovered. These DND's are tightly agglomerated to each other via the dangling surface bonds binding to each other and the process of breaking down the agglomeration to form a perfect suspension of DND's is difficult. Due to the nature of the agglomeration the method of breaking it down differs from typical naturally occurring agglomerations such as electrostatically or Van der Waals which are weak attractions between particles.[55,56]

Current research for improving the detonation process is achieving higher purity DND's by introducing oxidizing reagents to break down any sp^2 formation. This also allows for a reduction in average particle sizes whilst trying to control aggregation due to reduction in sp^2 dangling bonds. There is the potential of doping during the synthesis itself, where natural nitrogen doping occurs from the N released from the breakdown of TNT becoming trapped in the liquid carbon droplets. There is a strong desire for a fabrication method to produce DND's which require no secondary treatments after manufacturing and to have a purer starting material for future functionalisation purposes. [57]

2.2.1 Nanodiamond surface

Typically, nanodiamonds will be coated in graphitic sp^2 carbon on their surfaces[58]; this is due to a combination of an unstable surface which reconstructs or graphitizes upon formation of the DND, or a collection of graphitic rings which surround the DND's.[47,59] There is also the potential for impurities such as metal oxides (typically SiO_2) to become embedded into the surfaces. When purchasing the product of detonation process, known as detonation soot, the percentage of DND's with respect to the soot can range from anywhere between 30% and 80% depending on the conditions of the process. This is due the small-time frame and conditions required during the detonation process for which crystallization for diamond occur, as all other products are sp^2 contamination.

Due to the much larger surface to bulk ratio for DNDs with respect to single crystal diamonds, the surface termination more drastically affects the properties of DNDs; including altering its optical properties such as shifting the absorption of light 100s of nm; change in stabilization of NV^- centers near the surface; what chemicals it will readily react with, to its zeta potential. Zeta potential (also referred to as electrokinetic potential) is the measurement of a surface charge in relation to the medium it is suspended in, typically in mV. Measurements of around 50-60mV mean there is a good stability of particles in solution, meaning the suspension of particles is good, whereas values between 0-10 suggest the particles to be colloidal in nature. A stable, colloidal suspension of nanodiamonds is important for applications in drug delivery where drugs will be attached to the surface, therefore maximum surface coverage is essential. The graphitic layers have their uses in certain applications for controlled terminating specific areas of the diamond. The removal of sp^2 carbon and the functionalisation of nanodiamonds during various stages of the oxidation process must be better understood for nanodiamonds to be more desirable in various applications where they show promise. [58, 60-62]

Fig 2.2.1 shows a diamond of an DND, labelled with the various crystallographic planes also seen in bulk diamond.

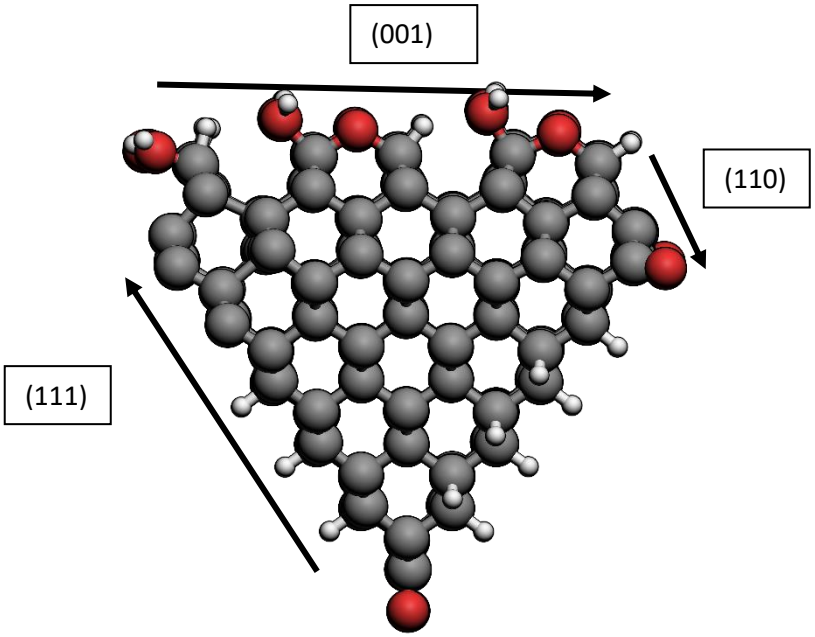

Figure 2.2.1: Optimised structure of an DND with a variety of bonding on different labelled planes.

If you assume you have a pure, sp^3 DND then we can describe the DND surface as being a combination of the various different crystal faces of a bulk diamond. As previously discussed in 2.1.2, each orientation has preferential bonding or specific oxygen groups it is limited to, such as the (111) being capable of only hydroxyl. This will mean that the method of purifying and oxidation of these DNDs is a lot more important in the initial stages when compared to that of the single crystal. Single crystal diamond in UHV will start to desorb oxygen species at 400°C and obtain a bare crystal surface at 900°C, but graphitization of the surface occurs at over 1000°C unless a metal catalyst is present.[63,64] This is useful if you are required to return to an original surface which might be preferred when preparing the diamond from an already terminated diamond where the surface species may inhibit the desired termination. However, all NDs will start forming sp^2 carbon at 500°C, which indicates that before a full desorption of surface species can be obtained, the nanodiamonds will be damaged. Therefore, the initial treatment must be as efficient as possible to avoid damaging the DNDs or getting to a point of no return where the termination is irremovable.[65,66] For the removal of sp^2 and generation of an oxygenated surface, there are two main methods which have differing results.

The first method of oxygenation is the use of acid treatments, generally a 3:1 ratio of H_2SO_4 and HNO_3 at low temperatures (80-120°C) is used, where the sulphuric acid breaks down any non-diamond carbon on the surface, and the nitric acid acts as an oxidizing agent[53]. The

alternative method is annealing the sample up to 400/450°C in either a pure O_2 atmosphere or in air (21% oxygen) and letting the oxygen burn away any sp^2 and leave an oxidized surface. The differences between these methods will be discussed later on in this thesis in chapter 6.

2.2.2 H and O Terminated DND's.

Much like with bulk diamond, O and H surface terminations provide various different applications for the nanodiamonds. The surface terminations alter the zeta potential, electron affinity and chemical reactivity of the nanodiamonds.[69,70] Research has been conducted for biomedical applications which suggest that due to the intrinsic nature of each termination, when used for drug delivery the DND's will have preferred sites or organs where they will trend towards[45,62]. The methods of achieving these terminations will now be discussed.

DNDs are naturally hydrogen terminated after being processed from the detonation soot to remove due to abundance of hydrogen available. however due to the process in which sp^2 carbon which occurs from the detonation process they must first be oxidized and then treated either chemically, annealing at temperature with a gas or through gentle plasma treatments to achieve hydrogenation[70,71]. The Barton-McCombie method can be used for the de-oxygenation of hydroxyl groups, through the use of methyl radicals from trimethylborane and water, although the reagents used can be detrimental when suspension is attempted and hard to remove as they stay adsorbed onto the surfaces[72]. Hydrogen gas anneal provides a good alternative, achieving an almost complete hydrogenated surface however OH groups often remained prevalent.[73] This process can be improved by using hydrogenation catalysts (usually platinum or nickel) to break down H_2 to produce H atoms. This results in a more complete hydrogen termination. Plasmas provide some of the best results due to H* ions reactivity and the temperature at which plasmas occur, and even help in the reduction of sp^2 by etching away sp^2 like in the CVD growth process. However, when using plasma's there is evidence that the C=O group remains stable and difficult to remove[74].

The oxygen species which occur on the DND during the oxidation is thought to be well understood and is dependent on the oxidation method used. Whilst air annealing may provide a wider-range of oxygen containing species, specific acids and chemical treatments mean the oxidized nanodiamonds can have a surface predominantly of one termination. The

main oxygen containing groups are; C=O, C-OH, and COOH however due to the three crystal faces of DND's as shown in fig 2.2.1, a complete termination of a single functional group is impossible due to the aforementioned preferred surface species.[75-78]

Carboxylic groups are achieved by treating DND's in carboxylic acid during the acid etch procedure and generally occur more commonly than other groups through the generic acid etch. These groups however have a large chance of being bonded to any residual sp^2 on the surface due to the requirement of having C=O and C-OH bonded to a single carbon. Hydroxyl functionalisation was initially achieved by processing H-terminated DND's and treating them with either borane or lithium aluminum hydride, however nowadays Fenton reagents are more commonly used. Fenton reagents make use of OH radicals to treat already hydrogenated or bare surfaces, they form a comparatively lower amount of C=O groups compared to others but can also not remove them. C=O groups are found to be preferentially bound to the surface through ozone treating hydrogenated DND's under UV irradiation, and the air anneal produces a predominantly ether and hydroxyl functionalised surface, with ketones.[77,79-80]

The formation of specific groups during air annealments will be discussed later on in Chapter 6 of this thesis.

The oxygen species the surface is funtionalised with is incredibly important because each one provides different properties, unlike in diamond where the acid etch and air anneals both produce a positive electron affinity at the surface, carboxyl and OH terminated DNDs produce an electronegative surface when compared to C-O-C. The ketone terminated DNDs even show an acidic nature and have been found to have unusual interactions with organic molecules. All these functional groups will react differently when attempting to attach specific linker groups or molecules onto DNDs for applications in drug delivery, with some groups being easier to break down than others. The hydrophobicity of H-DNDs and the hydrophilicity of O-DNDs can be described by the electronegativity also. Due to the positive electron affinity, H-DNDs disperse in water well as they are repelling themselves away from the H_2O ions, however for O-terminations the water traps itself between individual DNDs, this can cause coagulation of the particles and as such stable suspensions of O-DNDs are difficult [71,81].

2.2.3 Applications of Nitrogen Vacancy Centres in DND's

Vacancies occur when nitrogen is either doped into the bulk crystal growth via a precursor gas, or during the detonation process when nitrogen gets trapped in the liquid carbon droplets. In the detonation process as previously mentioned the nitrogen is obtained through the breakdown of trinitrotoluene (TNT). Due to nitrogen having only 3 free electrons in its outer shell, when its inside the crystal lattice as shown in Figure 2.2.2, there is a carbon atom which has an unpaired electron which interacts with the remaining lone-pair of electrons from the nitrogen[20,21,56]. There isn't always a vacancy where a nitrogen atom is, as during the detonation process the N impurities are interstitial and may be surrounded entirely by carbon. However, during anneal the vacancies will move around the crystal until it 'finds' a nitrogen. There are several types of nitrogen vacancies (NV^0, NV^-, N-V-N etc) however only NV^0 and NV^- will be discussed.

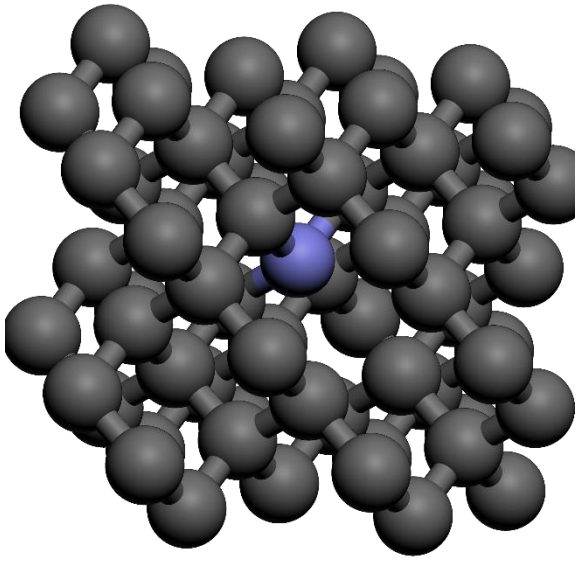

Figure 2.2.2: A diagram demonstrating the N atom shown as an blue sphere incorporation into a diamond , showing there the vacancy underneath the nitrogen atom.

The unpaired electron from the nitrogen can exist in two different charge states, known as NV^0 and NV^-, which both have differing properties such as absorbance, photoluminescence and magnetic resonance. NV^0 is the result of the unpaired carbon electron floating and remaining in a stable state, whereas the NV^- an electron from the nitrogen lone pair bonds with the carbon electron, forming a spin s=1 pair.

NV^- is a promising defect in nanodiamonds due its high efficiency in the absorbance of 400nm-600nm radiation and conversion into a definable peak at 632nm, thus making it an ideal material for use as a biomarker as it can utilize this strong optical emission whilst taking advantage of many of the properties of nanodiamonds which make them desirable in bio-applications[82-85].

2.3 Gallium (III) Oxide

2.3.1 History and Applications

Gallium (III) oxide is a wide-band gap transparent semiconducting oxide (TSO) which can exist in five different structural variations, with the most common being β-Ga_2O_3. It was first discovered in 1875 when Boisbaudran found gallium in sphalerite ore in the Pyrenees[86]. Initial studies focused on microwave and optical maser experiments for applications in electroluminescent devices, phosphors, catalysis, and conductive coatings where due to it's wide-band gap, which is close to diamond, makes it highly desirable for electronic devices[87-89]. However due to limitations in crystal purity and crystal size available at the time meant it could not be widely used. This initiated an increase in research and further development into types of growth methods. Multiple methods have been incorporated into the growth of β-Ga_2O_3 including chemical synthesis, thermal sublimation, CVD, molecular beam epitaxy (MBE) and flux growth. However, all the methods have individual flaws for gallium-oxide growth, which makes them inappropriate for device fabrication quality crystals.

Currently, Edge-defined Film-Fed Growth (EFG) techniques are mostly used in gallium oxide fabrication due to its advantages in larger scale growth. It was founded by Labelle and Miavsky in the late 1960's for sapphire growth. Crucibles containing the liquid oxide at high temperature and desirable dopants are fed through a capillary onto the center of a seeding crystal, and at this interface a single crystal is formed. The seeder is then moved away from the capillary and crystal growth then expands to the exposed area between the seeder and liquid. This is continued until the surface area of the seeder is coated in Ga_2O_3. The crystallographic orientation produced is controlled by the growth angle, and the meniscus of the liquid on the seeder controls the thickness of crystal produced[91].

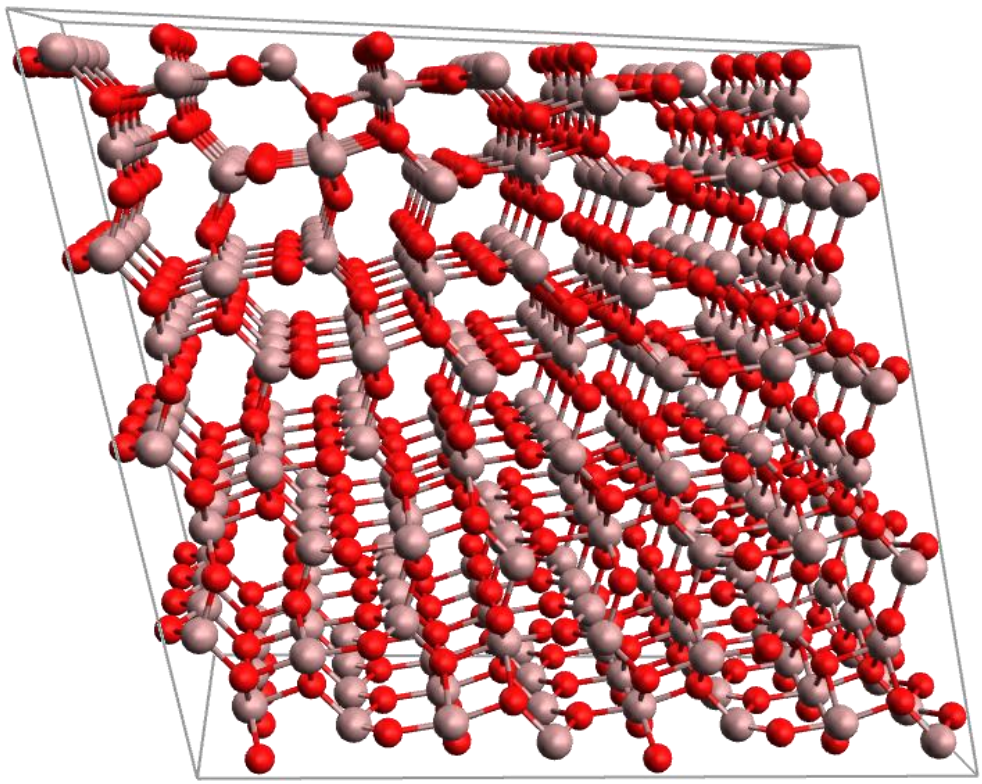

Figure 2.3.1: β-Ga_2O_3 (001) Crystal structure.

β-Ga_2O_3 exists as a monoclinic crystal structure, with various unique properties summarized in Table 2.3.1 for the (201) orientation[91-94].

- High band-gap (4.85ev)
- Large refractive index (1.93)
- Large Baliga's Figure of Merit (FoM) value
- Excellent chemical stability
- Breakdown voltage of 80 (10^5 V/cm)
- High melting point (1795°C)
- Low thermal conductivity (13W/mK)
- High density (5.88/cm^3)

Table 2.3.1: Some properties of Ga_2O_3 which make it an promising wide-band semiconductor for use in device fabrication.

Where some of the other properties are listed in Table 2.1.1. Baliga's FoM is a value which describes a materials resistive loss and therefore can be used as a comparative value to other materials where Silicon is the baseline with a value of 1. Baliga's FoM is derived from a materials bandgap and electron mobility.

Since growth yield of gallium oxide has been improved, interest has increased proportionally, with Ga_2O_3 being researched for UV photodetectors and high-voltage and power electronics due to its high breakdown fields (8MV/cm) and the materials uniqueness among TSO's has showed increased interest as the surface shows a different electronic behavior. Where materials such as ZnO show a surface metallicity and surface accumulation layer, β-Ga_2O_3's surface exhibits a naturally depleted surface. Work previously done by Aberystwyth materials research group has showed that the downward band bending in materials such as ZnO is affected by the OH bonding on the surface, where the method of oxidation can flip the properties from accumulation to depletion[95]. The surface stability of β-Ga_2O_3 therefore needs to be studied and the effects of various chemical states investigated.

Ga_2O_3 has also been investigated for its use as a substrate for III-nitride epitaxy, specifically for the MOCVD growth of GaN on (100) β-Ga_2O_3 and potential applications for creation of blue-LEDs[89].

The only downside in comparison to other typical semiconductors is the very poor thermal conductivity, which is due to the crystalline anisotropy of the material. The different crystal orientations of β-Ga_2O_3 also exhibit different conductivities. The [010] direction shows over a 100% increase in thermal conductivity in comparison to [001] or [201]. It's been shown this low conductivity is limited by both the free electron and phonon scattering[93].

Despite this, β-Ga_2O_3 FET's have shown a lot of promise, with the use of AlN or diamond substrate hosting an Ga_2O_3 membrane, and whilst it is still behind SiC and GaN devices of today, when compared to the initial first GaN devices of the early 1990's it achieves much better performance. It is thought to be the 2nd most promising wide-band gap semiconductor based purely of potential capabilities after diamond.

2.4 Fluorouracil

Fluorouracil (5FU) is a highly unstable, insoluble, polar molecule, which is used in chemotherapy for various cancers such as bowel and skin cancer and is shown in Figure 2.4.1. [96]

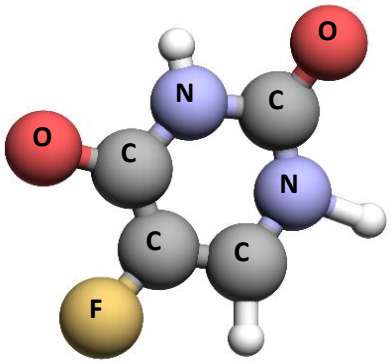

Figure 2.4.1: Image of a 5FU molecule which a highly unsymmetrical, polar molecule.

Research has shown that 5FU is unstable on silver and various other metals, this can mean that due to the nature of delivery of the drug either via a catheter or cannula which contain silver coatings for its anti-bacterial properties, that the efficiency of the drug might be drastically reduced[97]. Di Hu has shown that not only is 5FU inert on single crystal diamonds, that the surface electronegativity can alter the amount of 5FU that is physically adsorbed onto the surface[44]. This could allow of the design of coatings for various types of drugs which may suffer catalytic degradation on metals, whilst still maintaining anti-bacterial properties through the use of boron doping and surface patterning to inhibit growth.

As previously discussed, nanodiamonds are being increasingly researched for applications in drug delivery, in Chapter 5 the effect of surface termination of DNDs with the adsorption of 5FU will be analyzed for applications in drug delivery. Current methods of delivering 5FU involve either the use of solvents such as dimethyl sulfoxide or anti-critical super solvents to disperse the molecule.[98] However, particle sizes of this molecular remain in the 100's of nm as a best case, and typically sit in the µm range due to 5FU's polarity causing agglomeration, due to DNDs being around 3-5nm the belief is that the particle size of the 5FU in-situ can be reduced, and then the many advantages of DNDs in bio-medical applications such as targeted delivery and bio-imaging can be used also[99-100] .

References:

[1] - C.Y.Fong and B.M.Klein, "Electronic and Vibrational Properties of Bulk Diamond", Diamond: Electronic Properties and Applications, L. S. Pan and D. R. Kania, Eds., ed Boston, MA: Springer US, 1995, pp. 1-29

[2] – G.P Bulanova. Diamond Exploration: Into The 21ST Century, Journal of Geochemical Exploration. W. L. Griffin. Volume 53, Issues 1–3, March 1995, Pages 1-23

[3] - Bundy, F. P. (1989). Pressure-temperature phase diagram of elemental carbon. Physica A: Statistical Mechanics and Its Applications, 156(1), 169–178. https://doi.org/10.1016/0378-4371(89)90115-5

[4] - Collins, A. T. (2000). Spectroscopy of defects and transition metals in diamond. Diamond and Related Materials, 9, 417–423.

[5] – Nesládek, M., Meykens, K., Haenen, K., Stals, L. ., Teraji, T., & Koizumi, S. (1999). Photocurrent and optical absorption spectroscopic study of n-type phosphorus-doped CVD diamond. Diamond and Related Materials, 8(2–5), 882–885. https://doi.org/10.1016/S0925-9635(98)00291-X

[6] - Dan Wu, Y. C. Ma, Z. L. Wang, Q. Luo, C. Z. Gu, N. L. Wang, C. Y. Li, X. Y. Lu, and Z. S. Jin. Optical properties of boron-doped diamond Phys. Rev. B 73, 012501 – Published 6 January 2006.

[7] Majchrowicz D, Kosowska M, Sankaran KJ, et al. Nitrogen-Doped Diamond Film for Optical Investigation of Hemoglobin Concentration. Materials (Basel). 2018;11(1):109. Published 2018 Jan 11. doi:10.3390/ma11010109

[8] - Kazuki Ohtsuka, Kazuhiro Suzuki1, Atsuhito Sawabe and Tadao Inuzuka. Japanese Journal of Applied Physics logo. Volume 35. Part B. 1996.

[9] – S. Koizumi Power Electronics Device Applications of Diamond Semiconductors Woodhead Publishing Series in Electronic and Optical Materials2018, Pages 99-189

[10] - Moissan, Henri (1893). The diamond: lecture to the Society of Friends of Science May 17, 1893. Europeana. Archived from the original on 2013-02-13. Retrieved 2012-06-27.

[11] Gems and Gemology. Gemological institute of america. Summer 1997.

[12] - Wang, Z. Y., Dong, L. H., Wang, D. S., & Dong, Y. H. (2012). Study of HPHT single crystal diamond as precision cutting tool material. Precision Engineering, 36(1), P162-167.Https://doi.org/10.1016/J.PRECISIONENG.2011.07.009

[13] - Eversole, W. G. (April 17, 1962) "Synthesis of diamond" U.S. Patent 3,030,188

[14] - Balmer, R. & Brandon, J. Chemical vapour deposition synthetic diamond: materials, technology and applications. J. Phys Volume 21. 1–51 (2009).

[15] - Ralchenko V. et al. (2005) Nanodiamond Seeding for Nucleation and Growth of CVD Diamond Films. In: Gruen D.M., Shenderova O.A., Vul' A.Y. (eds) Synthesis, Properties and Applications of Ultrananocrystalline Diamond. NATO Science Series (Series II: Mathematics, Physics and Chemistry), vol 192. Springer, Dordrecht.

[16] - J E Butler, Y A Mankelevich, A Cheesman, Jie Ma and M N R Ashfold. Understanding the chemical vapor deposition of diamond: recent progress. Journal of Physics: Condensed Matter, Volume 21, Number 36 August 2009.

[17] - Xie, Z. ., Edgar, J. ., McCormick, T. ., & Sidorov, M. . (1998). The effects of the simultaneous addition of diborane and ammonia on the hot-filament-assisted chemical vapor deposition of diamond II. Characterization of diamond and BCN film. Diamond and Related Materials, 7(9), 1357–1363. https://doi.org/10.1016/S0925-9635(98)00207-6

[18] - Luong, J., Male, K., & Glennon, J. Boron-doped diamond electrode: synthesis, characterization, functionalization and analytical applications. Volume 10. P1965-1979. August 2009. Analyst. http://pubs.rsc.org/en/content/articlehtml/2009/an/b910206j

[19] - Melnikov, A. A., Denisenko, A. V., Zaitsev, A. M., Shulenkov, A., Varichenko, V. S., Filipp, A. R., Dravin, V. A., Kanda, H., & Fahrner, W. R. (1998). Electrical and optical properties of light-emitting p–i–n diodes on diamond. Journal of Applied Physics Vol 84. P6127-6134. https://doi.org/10.1063/1.368880

[20] - Donggyu Kim, Mohamed I. Ibrahim, Christopher Foy, Matthew E. Trusheim, Ruonan Han, Dirk R. Englund. CMOS-Integrated Diamond Nitrogen-Vacancy Quantum Sensor. Nature Electronics, Vol 2, P284-289 (2019).
[21] - Boretti, A.; Rosa, L.; Blackledge, J.; Castelletto, S. Beilstein J. Nanotechnol. Nitrogen-vacancy centers in diamond for nanoscale magnetic resonance imaging applications. 2019, Vol10, P2128–2151. oi:10.3762/bjnano.10.207
[22] - Strother, T., Knickerbocker, T., Russell, J. N., Butler, J. E., Smith, L. M., & Hamers, R. J. (1995). Photochemical Functionalization of Diamond Films. J. Electrochem. Soc, 117(3), 968–971. https://doi.org/10.1021/la0112561
[23] - Maida, O., Tada, S., & Ito, T. (2014). High growth rate deposition of phosphorus-doped homoepitaxial (001) diamond films for deep-ultraviolet light emitting device. Thin Solid Films, 557, P227–230. https://doi.org/10.1016/j.tsf.2013.08.114
[24] - Satoshi Koizumi, Hitoshi Umezaw. Power Electronics Device Applications of Diamond Semiconductors. Woodhead Publishing Series. Electronic and Optical Materials.2018.
[25] - Choi, H. W., Gu,) E, Liu, C., Griffin, C., Girkin, J. M., Watson, I. M., & Dawson, M. D. (n.d.). Fabrication of natural diamond microlenses by plasma etching. Journal of Vacuum Science and Technology. Vol 23. P130-132. 2005.https://doi.org/10.1116/1.1843826
[26] - Julian Haas, Ernesto Vargas Catalán, Pierre Piron, Fredrik Nikolajeff, Lars Österlund, Mikael Karlsson, and Boris Mizaikoff. Polycrystalline Diamond Thin-Film Waveguides for Mid-Infrared Evanescent Field Sensors. ACS Omega 2018 Vol3 (6), P6190-6198 DOI: 10.1021/acsomega.8b00623
[27] - Chanier, T., Pryor, C. E., & Flatté, M. E. (n.d.). Substitutional nickel impurities in diamond: decoherence-free subspaces for quantum information processing. EPL. Vol 99. October 2012.
[28] – Medelung, O. Data in science and technology. Semiconductors group iV elements and III-V compounds; springer, isbn 3-540-53150-5. 1991.
[29] - Shenderova, O. A., & Gruen, D. M. . Ultrananocrystalline diamond : synthesis, properties, and applications. William Andrew Pub. 2006.
https://www.sciencedirect.com/science/book/9780815515241
[30] - Alexander M. Zaitsev. Optical Properties of Diamond. Springer. Feb 2010. 978-3-662-04548-0.
[31] - Breeding, C. M. & Shigley, J. E. The 'Type' Classification System of Diamonds and Its Importance in Gemology. Gems Gemol. 45, 96–111 (2009).
[32] – Nebel, c, e. Electronic properties of cvd diamond. semicond. sci. technol. 18, s1-s11. inst of physics publishing. 2003
[33] – R. graupner, M. hollering. A. ziegler. j. risten, l. ley and a. stampfl. dispersions of surface states on diamond (001) and (111). physical review b. vol. 55, p.10841. 1997.
[34] - Kian Ping Loh,*, X. N. Xie,S. W. Yang, and, and J. C. Zheng. Oxygen Adsorption on (111)-Oriented Diamond: A Study with Ultraviolet Photoelectron Spectroscopy, Temperature-Programmed Desorption, and Periodic Density Functional Theory. The Journal of Physical Chemistry B 2002 106 (20), 5230-5240 DOI: 10.1021/jp0139437
[35] - Karin Larsson. Simulation of Diamond Surface Chemistry: Reactivity and Properties. Intechopen. June 27th 2019. DOI: 10.5772/intechopen.86865
[36] - Baumann, P. ., & Nemanich, R. .. Surface cleaning, electronic states and electron affinity of diamond (100), (111) and (110) surfaces. Surface Science, Vol409(2), P320–335. (1998) https://doi.org/10.1016/S0039-6028(98)00259-3
[37] - Derry, T. E., Madiba, C. C. P., & Sellschop, J. P. F. Oxygen and hydrogen on the surface of diamond. Nuclear Instruments and Methods in Physics Research, Vol218(1), P559–562. 1983. https://doi.org/10.1016/0167-5087(83)91042-6
[38] - Petrini, D., & Larsson, K. Origin of the Reactivity on the Nonterminated (100), (110), and (111) Diamond Surfaces: An Electronic Structure DFT Study. The Journal of Physical Chemistry C, 112(37), P14367–14376. . 2008. https://doi.org/10.1021/jp711190r
[39] - S. J. Sque, R. Jones, and P. R. Briddon. Structure, electronics, and interaction of hydrogen and oxygen on diamond surfaces. Phys. Rev. B Vol 73 P8-15 –February 2006.

[40] - Navas, Javier; et al. Oxygen termination of homoepitaxial diamond surface by ozone and chemical methods: An experimental and theoretical perspective. Applied Surface Science, Volume 433, p. 408-418. March 2018.
[41] - Krüger, Pete, Pollmann, Johannes. Dimer Reconstruction of Diamond, Si, and Ge (001) Surfaces. Physical Review Letters 74(7):1155-1158 · March 1995.
[42] - A. V. Petukhov A. Fasolino D. Passerone F. Ercolessi. Reconstruction of Diamond (001) Surface: A Monte Carlo Study with the Tersoff Potential. physica status solidi. Volume174, Issue1 July 1999.
[43] - Sorawis Sangtawesin et al. Origins of Diamond Surface Noise Probed by Correlating Single-Spin Measurements with Surface Spectroscopy. Physical Review X.Vol 9. Issue 3. September 2019.
[44] – Di Hu. Surface Modification and Electronic Structure Characterisation of Carbon-based and Iron-based Materials. PhD Thesis. Awarded 2017. http://hdl.handle.net/2160/04016083-f5c2-4542-a75a-74ee93b36100.
[45] - Mochalin, V. N., Shenderova, O., Ho, D., & Gogotsi, Y. The properties and applications of nanodiamonds. Nature Nanotechnology, Vol7(1), P11–23. 2012.
https://doi.org/10.1038/nnano.2011.209
[46] - Shenderova, O. A., Zhirnov, V. V., & Brenner, D. W. Carbon nanostructures. Critical Reviews in Solid State and Materials Sciences, Vol27(3–4), P227–356. 2002.
https://doi.org/10.1080/10408430208500497
[47] – Dolmatov, V. Y. Detonation nanodiamonds: synthesis, structure, properties and applications. Russ. Chem. Rev. Volume 67. Issue 4. 2007.
[48] - V. V. Danilenko .On the History of the Discovery of Nanodiamond Synthesis Physics of the Solid State, Vol. 46, No. 4, P595-599. 2004.
[49] - V. V. Danilenko. Advances in the synthesis of nanodiamond particles. in sarin, v. ed., comprehensive hard materials; elsevier, 2014.
[50] - V. V. Danilenko. Synthesis and sintering of diamond by explosion. explosion physics, technique, technolohu; 2010.
[51] - V. V. Danilenko. features of carbon condensation in a detonation wave and the conditions for optical synthesis of nanodiamonds. j. superhard. mater. 2006.
[52]- shenderova, o., eds. ultrananocrystaline diamond; 2nd edition, elsevier, 2012.
[53]-vul. a, shenderova. o, eds, detonation nanodiamonds – science and applications. 1st edition.; pan stanford publishing, 2014.
[54] – Davydov v. et al. on the nature of the simultaneous formation of nano- and micronsize diamond fractions under pressure-temperature induced transformation of binary mixtures of hydrocarbons and flourocarbon compounds. carbon. Vol 90. P231-233. August 2015.
[55] -Kuznewsov v. l, chuvlin, a. l, butenko. y. v, malkov. i. y, titov, v. m. onion-like carbon from ultra-disperse diamond . chem phys lett. Vol 222. P343-348. 1994.
[56] – shendrova. o. a, et al. nitrogen control in nanodiamond produced by detonation show-wave assisted synthesis. j. phys chem. Vol 115. P14014-14024. 2011.
[57] – Mitev D. Dimitrova, r. spassova. m, michev. c, starev. s, surface peculiarities of detonation nanodiamonds in dependence of fabrication and purification methods. diam. relat. mater. Vol 16. P776-780, July 2007.
[58] – Osswald S, Yushin G, Mochalin V, Kucheyev SO, Gogotsi Y. Control of sp2/sp3 carbon ratio and surface chemistry of nanodiamond powders by selective oxidation in air. J Am Chem Soc. Vol 128. P11634-11642. September 2006.
[59] – dolmatov, v. y. in detonation nanodiamonds; st petersburg. 2011. p 530.
[60] - Salava, J., Trojánek, F., Stehlík, Š., Varga, M., Rezek, B., & Malý, P. Influence of air annealing on the luminescence dynamics of HPHT nanodiamonds. Diamond and Related Materials, 68, P62–65. 2016. https://doi.org/10.1016/j.diamond.2016.06.001
[61] - Mona, J., Tu, J.-S., Kang, T.-Y., Tsai, C.-Y., Perevedentseva, E., & Cheng, C.-L. Surface modification of nanodiamond: Photoluminescence and Raman Studies. Diamond and Related Materials, Vol24, P134–138. 2012. https://doi.org/10.1016/J.DIAMOND.2011.12.027

[62] - Hsiao, W. W.-W., Hui, Y. Y., Tsai, P.-C., & Chang, H.-C. Fluorescent Nanodiamond: A Versatile Tool for Long-Term Cell Tracking, Super-Resolution Imaging, and Nanoscale Temperature Sensing. Accounts of Chemical Research, Vol49(3), P400–407. 2016. https://doi.org/10.1021/acs.accounts.5b00484
[63] - Bai Q, Wang Z, Guo Y, Chen J, Shang Y. Graphitization Behavior of Single Crystal Diamond for the Application in Nano-Metric Cutting. Curr Nanosci. Vol14(5). Vol377–383. 2018. doi:10.2174/1573413714666180517080721
[64] - Cooil, S. P., Wells, J. W., Hu, D., Niu, Y. R., Zakharov, A. A., Bianchi, M., & Evans, D. A. Controlling the growth of epitaxial graphene on metalized diamond (111) surface. Applied Physics Letters, Vol107(18), 181603. 2015. https://doi.org/10.1063/1.4935073
[65] - Sun, Y., Wu, Q., Xu, Y., Bai, H., Li, C., & Shi, G. Highly conductive and flexible mesoporous graphitic films prepared by graphitizing the composites of graphene oxide and nanodiamond. Journal of Materials Chemistry, Vol21(20), 7154. 2011. https://doi.org/10.1039/c0jm04434b
[66] – Michel Mermoux, Alexandre Crisci, Tristan Petit, Hugues A. Girard, and Jean-Charles Arnault. Surface Modifications of Detonation Nanodiamonds Probed by Multiwavelength Raman Spectroscopy. The Journal of Physical Chemistry C Vol118 (40), P23415-23425. 2014. DOI: 10.1021/jp507377z
[67]- Stehlik, S., Miliaieva, D., Varga, M., Kromka, A., & Rezek, B. Size decrease of detonation nanodiamonds by air annealing investigated by AFM. MRS Advances, Vol1(16), P1067-1073. 2016. doi:10.1557/adv.2016.36
[68]- Shenderova, O., Petrov, I., Walsh, J., Grichko, V., Grishko, V., Tyler, T., and Cunningham, G., Modification of detonation nanodiamond by heat treatment in air. Diam. Relat. Mater. Vol15. P1799–1803. 2006.
[69] - Lee, Y.-C., Pradhan, D., Lin, S.-J., Chia, C.-T., Cheng, H.-F., & Lin, I.-N. Effect of surface treatment on the electron field emission property of nano-diamond films. Diamond and Related Materials, Vol 14(11–12), P2055–2058. 2005. https://doi.org/10.1016/J.DIAMOND.2005.08.059
[70] - Krüger, A., Liang, Y., Jarre, G., & Stegk, J. Surface functionalisation of detonation diamond suitable for biological applications. Journal of Materials Chemistry, Vol16(24), P2322–2328. 2006. https://doi.org/10.1039/b601325b
[71] - Krueger, A. Current issues and challenges in surface chemistry of nanodiamonds. Nanodiamonds, P183–242.2017. https://doi.org/10.1016/B978-0-32-343029-6.00008-8
[72] – Chenneburg, L.; Goddard,J,P; fensterbank, L. reduction of saturated alchohols and amines and alkanes. Comprehensive organic synthesis. vol 8. elsevier. 2014.
[73] - Oliver A. Williams, Jakob Hees, Christel Dieker, Wolfgang Jäger, Lutz Kirste, and Christoph E. Nebel. Size-Dependent Reactivity of Diamond Nanoparticles ACS Nano Vol4 (8), P4824-4830. 2010. DOI: 10.1021/nn100748k
[74] – H. A. Girard, a T. Petit,a S. Perruchas,b T. Gacoin,b C. Gesset,a J. C. Arnaulta and P. Bergonzoa . Surface properties of hydrogenated nanodiamonds: a chemical investigation. Phys. Chem. Chem. Phys., Vol13. P11517-11523. 2011.
[75] - Smith, B. R., Gruber, D., & Plakhotnik, T. The effects of surface oxidation on luminescence of nano diamonds. Diamond and Related Materials, Vol19(4), P314–318. 2010. https://doi.org/10.1016/J.DIAMOND.2009.12.009
[76] - Dean Ho . Nanodiamonds: Applications in Biology and Nanoscale Medicine. Springer publications. 2009.
[77] - Schmidlin L, Pichot V, Comet M, Josset S, Rabu P and Spitzer D Identification, quantification and modification of detonation nanodiamond functional groups Diam. Relat. Mater. Vol22. P113-117. 2012.
[78] - Y Astuti, F D Saputr,, S Wuning, Arnelli and G Bhaduri. Enrichment of Nanodiamond Surfaces with Carboxyl Groups for Doxorubicin Loading and Release. IOP Conference Series: Materials Science and Engineering, Volume 172. 2017.

[79] - Kinga Adach, Mateusz Fijalkowski & Janusz Skolimowski. Antioxidant Effect of Hydroxylated Diamond Nanoparticles Measured in Soybean Oil, Fullerenes, Nanotubes and Carbon Nanostructures, Vol23:12. P1024-1032. 2015. DOI: 10.1080/1536383X.2015.1057701
[80] - Popov M, Churkin V, Kirichenko A, et al. Raman Spectra and Bulk Modulus of Nanodiamond in a Size Interval of 2-5 nm. Nanoscale Res Lett. Vol;12(1):561. Oct 2017.. doi:10.1186/s11671-017-2333-0
[81] - Ostrovskaya, L., Perevertailo, V., Ralchenko, V., Dementjev, A., & Loginova, O. Wettability and surface energy of oxidized and hydrogen plasma-treated diamond films. Diamond and Related Materials, Vol 11(3–6), P845–850. 2002. https://doi.org/10.1016/S0925-9635(01)00636-7
[82] - Fu, C.-C., Lee, H.-Y., Chen, K., Lim, T.-S., Wu, H.-Y., Lin, P.-K., Wei, P.-K., Tsao, P.-H., Chang, H.-C., & Fann, W. Characterization and application of single fluorescent nanodiamonds as cellular biomarkers. Proceedings of the National Academy of Sciences of the United States of America, Vol104(3). P727–732. 2007. https://doi.org/10.1073/pnas.0605409104
[83] - Chipaux, M., van der Laan, K. J., Hemelaar, S. R., Hasani, M., Zheng, T., & Schirhagl, R. Nanodiamonds and Their Applications in Cells. Small, Vol14(24), 1704263. 2018. https://doi.org/10.1002/smll.201704263
[84] - Nagl, A., Hemelaar, S. R., & Schirhagl, R. Improving surface and defect center chemistry of fluorescent nanodiamonds for imaging purposes-a review. In Analytical and Bioanalytical Chemistry (Vol.407, Issue 25, P7521–7536). Springer Verlag. 2015. https://doi.org/10.1007/s00216-015-8849-1
[85] – Hui,. Y et al. recent developments and applications of nanodiamonds as versatile bioimaging agents. Chinese Chemical Society. Vol 61. P67-76. 2013. https://doi.org/10.1002/jccs.201300346
[86] - Lecoq de Boisbaudran, [Paul-Émile] (1877). Sur un nouveau metal, le gallium. Paris: s.n.
[87] - Sasaki, Kohei; Higashiwaki, Masataka; Kuramata, Akito; Masui, Takekazu; Yamakoshi, Shigenobu. MBE grown Ga2O3 and its power device applications Journal of Crystal Growth, Volume 378, p. 591-595. September 2013
[88] - S.-L. Wang, J.-W. Yu, P.-C. Yeh, H.-W. Kuo, L.-H. Peng, a), A. A. Fedyanin, E. D. Mishina, and A. S. Sigov. High mobility thin film transistors with indium oxide/gallium oxide bi-layer structures View Affiliations Applied Physics Letters Vol100:6. 2012.
[89] - Kiyoshi Shimamura, Encarnación G. Víllora, Kay Domen, Keiichi Yui1, Kazuo Aoki and Noboru Ichinose. Epitaxial Growth of GaN on (1 0 0) b-Ga2O3 Substrates by Metalorganic Vapor Phase Epitaxy. Japanese Journal of Applied Physics. Vol 44. December 2004.
[90] - Akito Kuramata, Kimiyoshi Koshi, Shinya Watanabe, Yu Yamaoka, Takekazu Masui and Shigenobu Yamakoshi. High-quality b-Ga2O3 single crystals grown by edge-defined film-fed growth. Japanese Journal of Applied Physics.Vol 55. November 2016.
[91] - G. Víllora, , Kiyoshi Shimamura, Yukio Yoshikawa, Takekazu Ujiie, and Kazuo Aoki. Electrical conductivity and carrier concentration control in b-Ga2O3 by Si doping Encarnación View Affiliations Applied Physics Letters 92:20. Vol 92. 2008.
[92] - Cristoph Janowitz et al. Experimental electronic structure of In2O3 and Ga2O3. New Journal of Physics, Volume 13, August 2011.
[93] - Zhi Guo, Amit Verma, Xufei Wu, Fangyuan Sun, Austin Hickman, Takekazu Masui, Akito Kuramata, Masataka Higashiwaki, Debdeep Jena, and Tengfei Luo. Anisotropic thermal conductivity in single crystal b-gallium oxide. Applied Physics Letters Vol 106:11. Feb 2015. https://doi.org/10.1063/1.4916078.
[94] - Galazka, Zbigniew; Irmscher, Klaus; Uecker, Reinhard; Bertram, Rainer; Pietsch, Mike; Kwasniewski, Albert; Naumann, Martin; Schulz, Tobias; Schewski, Robert; Klimm, Detlef; Bickermann, Matthias. On the bulk b-Ga2O3 single crystals grown by the Czochralski method. Journal of Crystal Growth, Volume 404, p. 184-191. Oct 2014.
[95] - Heinhold, R., Williams, G. T., Cooil, S. P., Evans, A. & Allen, M. W., Influence of polarity and hydroxyl termination on the band bending at ZnO surfaces. Physical Review B. Vol 88. P23-31. Dec 2013.

[96] - POLK A, VISTISEN K, VAAGE-NILSEN M, NIELSEN DL. A SYSTEMATIC REVIEW OF THE PATHOPHYSIOLOGY OF 5-FLUOROURACIL-INDUCED CARDIOTOXICITY. BMC PHARMACOL TOXICOL. SEPT 2014. DOI:10.1186/2050-6511-15-47
[97] - MAZZOLA, F., TRINH, T., COOIL, S., ØSTLI, E. R., TORBJØRN, E., SKJØNSFJELL, B., KJELSTRUP, S., PREOBRAJENSKI, A., CAFOLLA, A. A., EVANS, D. A., BREIBY, D. W., & WELLS, J. W. SILVER CATALYZED FLUOROURACIL DEGRADATION; A PROMISING NEW ROLE FOR GRAPHENE. NOVEMBER, 2014.
[98] - KALANTARIAN P, NAJAFABADI AR, HARIRIAN I, ET AL. PREPARATION OF 5-FLUOROURACIL NANOPARTICLES BY SUPERCRITICAL ANTISOLVENTS FOR PULMONARY DELIVERY. INT J NANOMEDICINE. VOL5. P763–770. OCTOBER 2010. DOI:10.2147/IJN.S12415
[99] - STURSA, J., HAVLIK, J., PETRAKOVA, V., GULKA, M., RALIS, J., ZACH, V., PULEC, Z., STEPAN, V., ZARGALEH, S. A., LEDVINA, M., NESLADEK, M., TREUSSART, F., & CIGLER, P. MASS PRODUCTION OF FLUORESCENT NANODIAMONDS WITH A NARROW EMISSION INTENSITY DISTRIBUTION. CARBON, VOL96, P812–818. 2016. https://doi.org/10.1016/J.CARBON.2015.09.111
[100] - SCHRAND, A. M., DAI, L., SCHLAGER, J. J., HUSSAIN, S. M., & OSAWA, E. DIFFERENTIAL BIOCOMPATIBILITY OF CARBON NANOTUBES AND NANODIAMONDS. DIAMOND AND RELATED MATERIALS, VOL16(12). P2118–2123. 2007. HTTPS://DOI.ORG/10.1016/J.DIAMOND.2007.07.020.

Chapter 3 – Techniques

This chapter will discuss the techniques used in this thesis and the scientific theories behind them. This work primarily employs PES based techniques such as XPS and NEXAFS as well optical techniques and DFT as supplementary data. PES based techniques are inherently surface sensitive whilst optical techniques are more bulk sensitive. Using this range of techniques is essential to build a complete understanding of a material. To ensure the cleanliness of a sample, it is placed inside a UHV chamber. The sample can then be treated in-situ, by annealing or administering gas into the chamber. The samples can then be analysed for any changes by using PES. However recent advancements in technology have allowed for these techniques which previously were limited to UHV to be conducted at near-ambient pressures (NAP). This allows for the investigation of changes to a surface whilst undergoing a reaction. This thesis has a strong focus on these near-ambient pressure techniques, and the advantages of measuring a sample whilst at its most pristine state during the surface preparation and oxidation procedure.

Other techniques such as Raman, Atomic Force Microscopy (AFM), Dynamic Light Scattering (DLS) and Photoluminescence (PL) will also be discussed.

3.1 Electromagnetic Spectrum

Electromagnetic (EM) radiation consists of waves, which have differing photon energies and wavenumbers such that:

$$Eq\ 3.0 \qquad E_p = \mathrm{hv}$$

Where E_p is the energy of the photon, h is planks constant, and v is the frequency of the wave. As the wavelength decreases, the photon energy increases. The majority of experimental techniques in this thesis use various forms of EM wave. Table 3.1 below summarise the radiation used[1,2].

EM radiation	**Wavelength (nm)**	**Photon energy (eV)**
Visible light	*400-700*	*1.8-3.1*
Ultraviolet light	*400-10*	*3.1-300*
X-ray light	*10-0.01*	*300-200000*

Table 3.1: List of the types of radiation used through this thesis for experimental purposes.

Any technique which is named with spectroscopy is the use of radiation (waves, atoms, ions and molecules) to produce a spectrum through various methods, of which many are discussed throughout this thesis.

3.2 Photoelectron techniques

3.2.1 Brief introduction into PES

Photoelectron spectroscopy (PES) is defined as the measurement of kinetic energy emitted from the surface of a material, with the same principle as the photoelectric effect theorized by H. Hertz which is where electrons are emitted from a metal when irradiated by light. Figure 2.1.1 shows the brief outline of PES. Starting in 1957, Siegbahn developed X-ray photoelectron spectroscopy, to measure the energy levels of atomic core electrons. Core level electrons have different binding energies which is dependent on the chemical environment of the electron. For example, an electron from an oxygen atom in a C-O bond is more strongly bound then an oxygen atom in a C=O state, and therefore the emitted electrons will have a different kinetic energy[3,4,5].

A similar technique can be conducted using ultraviolet photons, known as ultraviolet photoelectron spectroscopy (UPS), this technique was developed by Vilesov in 1961. In UPS there isn't enough energy supplied from the incident ultraviolet photons to excite electrons from the core level. The ultraviolet photons supply enough energy to excite electrons from the valence band which allows for probing of the molecular orbitals. This provides useful information such as vibrational levels of individual materials as well as their workfunction [6,7,8].

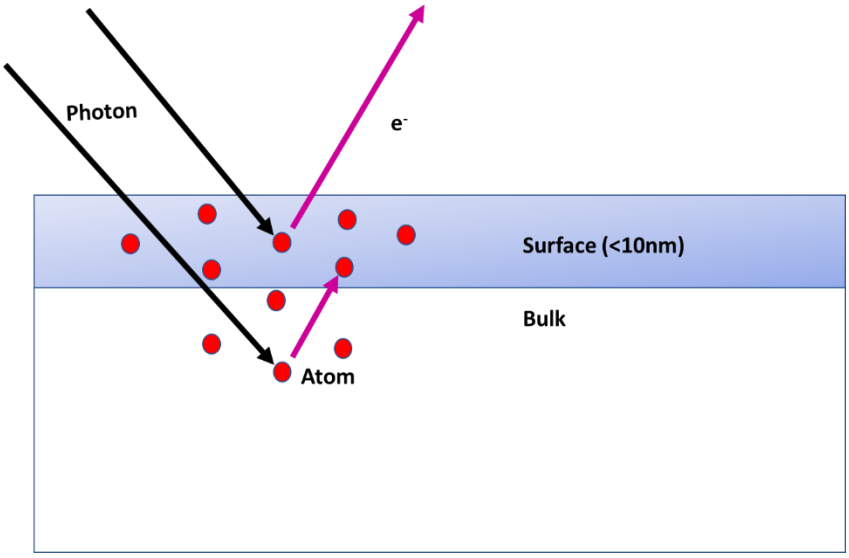

Figure 3.2.1: Diagram showing the basic principle behind PES. A electron is excited from an incoming photon, and if enough energy is transferred the elctron can escape it's parent atom and leave the surface.

Photons incident on the surface are absorbed by an electron inside the material. If the photon transfers a sufficient energy to the electron it can be ejected from the atom and subsequently the surface of the material providing there are no collisions. Although incident X-rays can penetrate >100nm into a material the electrons escape depth is much smaller. This is due to the chance of interactions between excited electrons and atoms and other electrons increases based on the depth. Through these inelastic collisions the electrons lose their kinetic energy and whilst having just enough energy to escape will not contribute to any peaks in a spectrum but contribute to a rising background as the measured kinetic energy decreases. The probability of interactions occurring is estimated by a statistical prediction on the inelastic mean free path (IMFP) of a material. IMFP Is defined as the mean distance an electron with a specific kinetic energy will travel before a collision occurs and energy is lost via collisions, attenuation, recombination, scattering and excitation of the material. Is the main parameter used to describe inelastic scattering of electrons in XPS and through the work of Seah and Dench an expression for the IMFP of a given material can be calculated by Eq 3.1[9]

$$Eq\ 3.1 \qquad \lambda_{IMFP} = \frac{528}{E^2} + 0.41a^{\frac{3}{2}}E^{\frac{1}{2}}$$

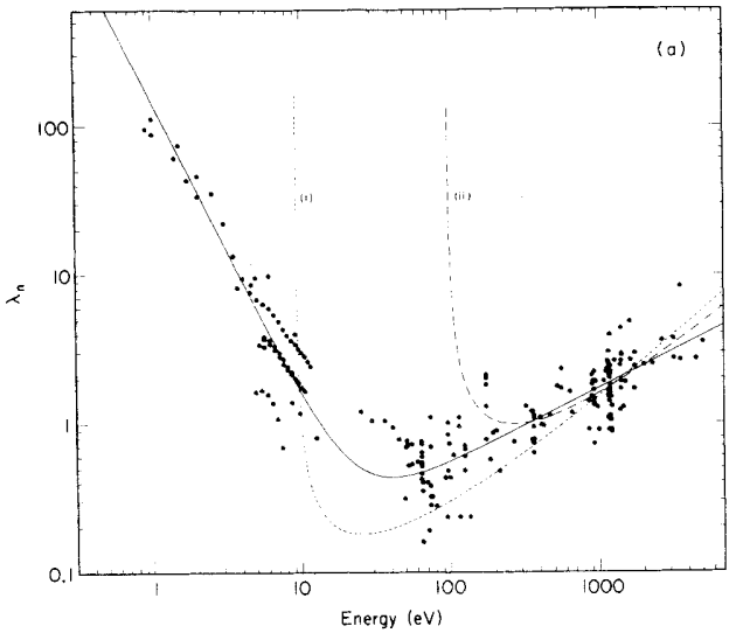

Figure 3.2.2: the IMFP Curve from the original study conducted my M. Seah on the escape depth of electrons, in nm, dependant on the element of the material and the kinetic energy of the electron. The curve shows that electrons with energies >50eV are surface localised[9].

Where *a* is the mean atomic distance, and *E* is the kinetic energy of electrons. For larger kinetic energies (>100eV) the first term can essentially be ignored. Meaning there is proportionality between $E^{\frac{1}{2}}$ and the IMFP. This also shows that statistically, the probability of detecting low kinetic energy electrons only occurs from those close to the surface. The atomic distance also plays a factor into the chance of collisions, where larger distances (smaller atoms) means there is more free space for the electrons to travel through the material.

Once the electron has escaped from the surface it can then "detected" by collecting it and storing information based on its kinetic energy. Due to the IMFP typically only electrons emitted from the top 10nm of the surface can be measured depending on the angle between the sample and the analyser, the sampled used and the photon energy used for excitation. Typically, PES experiments are conducted in UHV conditions such that the maximum number of ejected electrons reach the detector[10].

Since PES techniques are based on the photoelectric effect, they obey Einstein's equation:

$$Eq\ 3.2 \qquad E_p - E_k = E_b$$

Where E_p is the energy of the photon, E_k is the measured kinetic energy of an emitted electron, and E_b is binding energy.

However, since the photon must interact with an electron in a material to transfer enough energy for the electron to escape the surface, the equation becomes:

$$Eq\ 3.3 \qquad E_b = E_p - E_k - \Phi_{sample}$$

Where Φ_{sample} is the workfunction of a material defined as the energy difference the vacuum and fermi levels. However, there is also the workfunction of the spectrometer to be taken into account. If both the spectrometer and sample are grounded, then the fermi levels are equal such that the measured kinetic energy of an electron is:

$$Eq\ 3.4 \qquad E_k = E_{k-initial} + (\Phi_{sample} - \Phi_{spectrometer})$$

Which when substituted into Equation 3.3 produces the following equation:

$$Eq\ 3.5 \qquad E_b = E_p - E_k - \Phi_{spectrometer}$$

Showing that measured binding energy is dependent on the workfunction of the spectrometer and independent of the workfunction of the sample. This requires spectrometers to be calibrated which is usually conducted on a reference sample such as gold or silver and measuring the Fermi edge as reference[11].

As a result of the photoemission process, the electrons are emitted at discrete kinetic energies which produces a spectrum. Since the kinetic energies of the peaks are known it allows the user to identify the elements present at the surface region as each element has a unique set of core level energies. From the record spectra we can identify properties such as chemical composition, bonding structure, valence band structure and conduction band structure. This is done by using techniques like X-ray photoelectron spectroscopy (XPS), Ultraviolet Photoelectron Spectroscopy (UPS) and Near-edge X-ray Absorption Fine Structure (NEXAFS) respectively.

3.2.2 X-ray Photoelectron Spectroscopy (XPS)

XPS is a technique which uses an X-ray source to excite core electrons from the top 8nm of a solid material. Eq 3.2 shows that if the kinetic energy is known then the binding energy can be found. The binding energy is then used to analyze the chemical environment the electron has escaped from. This information can be defined from the atomic orbital it's originated from (1s,2s,2p,3s,3d etc.) along with the bonding state it's from with differences dependent on type of bonding (C-OH, C=O, C-O-C, C-O-O-C all emit electrons with different binding energies.) where there are standardized values for each[12,13,14].

Figure 3.2.3 shows the process of the emission of a Ga 2p electron in the photoemission process. It shows the electron excitation and the process it goes through, and also shows a survey of an XPS scan, with several peaks labelled and the diagram showing where the Ga 2p peak resides which is a result of detecting those electrons. Note that the gallium 3p has a higher kinetic energy, as $E_{binding}$ is much lower for the 3p orbital then it is for the 2p. It also shows the different core levels of Gallium which has an electron configuration of $[1s^2,2s^2,2p^6,3s^2,3p^6,4s^2,3d^{10},4p^1]$.

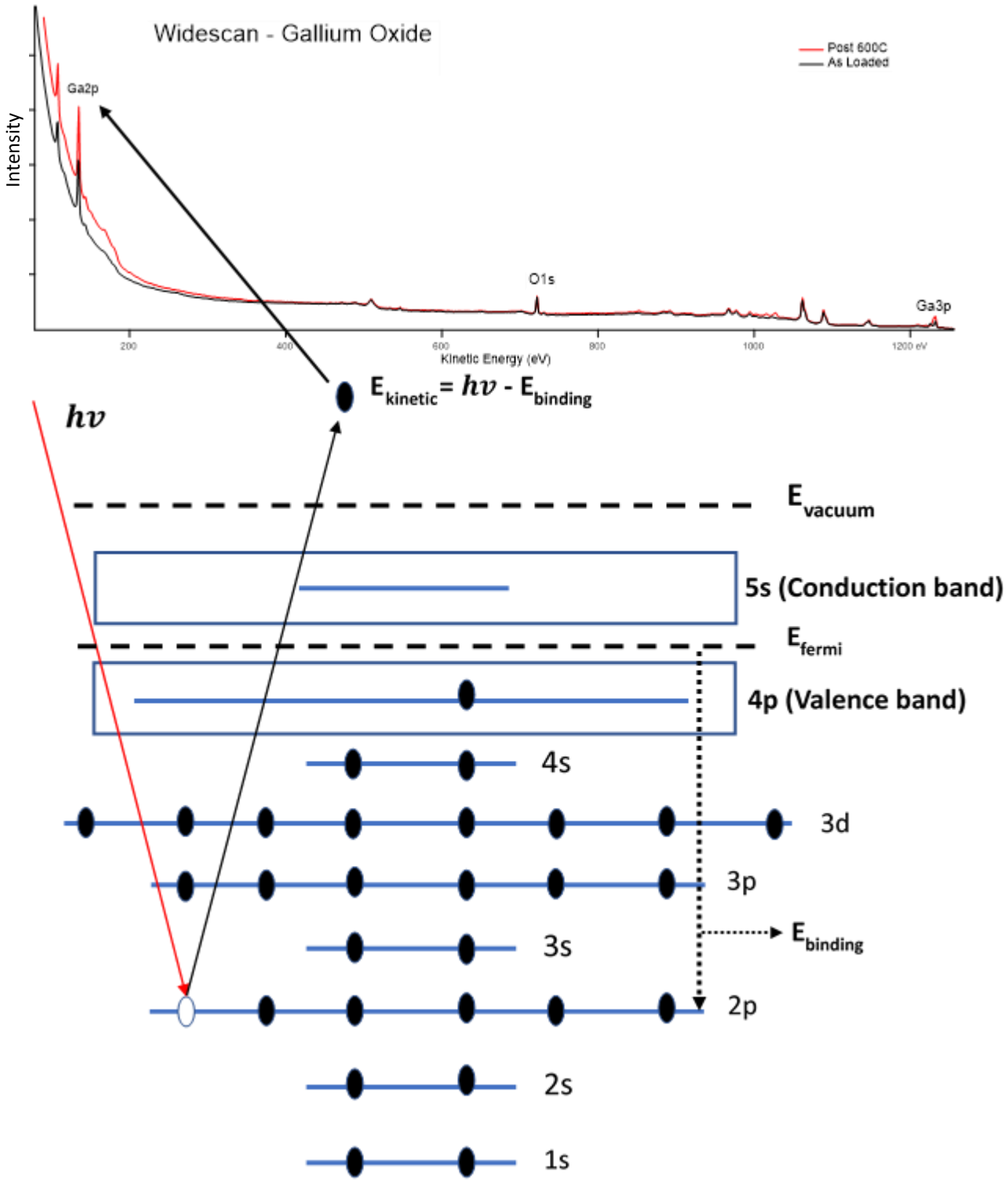

Figure 3.2.3: Diagram which demonstrates the photoemission process for a gallium electron.

Generically an X-ray photon used for XPS can vary in energy from 600-2000eV. Utilizing the Beer-Lambert law we can estimate the depth within the material that the electrons can escape from. This is given by:

$$Eq\ 3.6 \qquad I_d = I_0 E^{-\frac{d}{\lambda}}$$

where I_d is the intensity of electrons from a probing depth d. I_0 is the intensity of the surface electrons and λ is the (IMFP). Using a gaussian distribution, the probing of one sigma (σ) can be stated as giving 68% of all electrons, from a depth of λ, the majority of electrons (3σ) can be estimated to come from 3λ. This insinuates that for 2p electrons the probing depth is much smaller than for an 3p electron dependant on the kinetic energy of the electron from the specific orbital. This also means that the measurement of lower kinetic energy electrons is more surface sensitive (1-2nm) then it would be for electrons of a higher energy.

However, after the initial emission process the parent atom is left in an unstable state due to the electron leaving the core shell. To solve this issue electrons in a higher molecular orbital may decide to either (i) fluoresce, (ii) de-excite and drop to a lower molecular orbital to stabilize the atom whilst emitting an X-ray, or (iii) the process of Auger emission can occur. In this process an electron drops from a high-molecular level down to the vacant core levels. A secondary electron from the same shell or higher is emitted to compensate for the gain in energy. These secondary electrons are defined as Auger electrons and their kinetic energy is given by:[15,16]

$$Eq\ 3.7 \qquad E_{kin} = E_k - E_{l,1} - E_{l+1}$$

Where K is the shell containing the hole was created, $E_{l,1}$ is the electron which undergoes de-excitation, and E_{l+1} is an electron which undergoes Auger emission.

It is clear from Eq 3.7 that the energy of the emitted Auger electrons is dependent on the energy difference between the core levels and not the incident photon energy. Hence Auger electrons are always emitted at a certain K.E for a given element and transition. Care must be taken when performing XPS such that photoemission peaks and Auger peaks do not overlap.

Figure 3.2.3 shows the same core diagram as 3.2.2 but with reference to the Auger effect for Gallium.

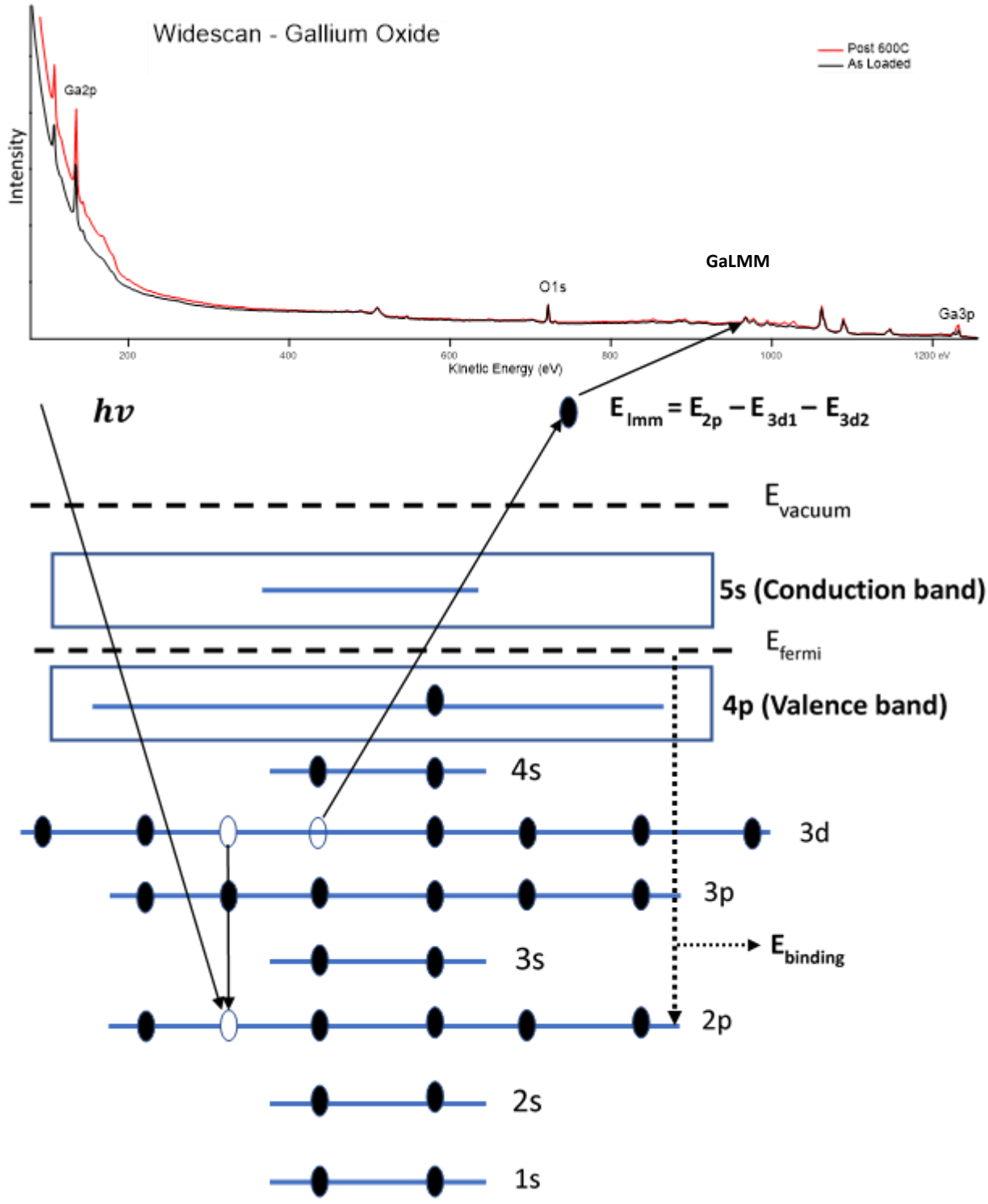

Figure 3.2.4: Auger electron emission process diagram indicating how the auger peak (GaLMM) differs from the photoemission peak in the widescan survery.

There are even more features that occur in XPS such as plasmon features, spin orbit coupling and satellite peaks each from differing processes[17,18].

In reality, electron shells are not as simple as shown in Figures 3.2.3 and 3.2.4, each electron sub-shell has its own quantum number, n. However electrons have a quantum angular momentum, l.

$$Eq\ 3.8 \qquad J = l + s$$

where s is +/-0.5. All orbitals exhibit what we call spin orbit coupling, except the S orbital which has no angular momentum. Table 3.2.1 shows the respective J and area ratios of respective electron shells[19].

Subshell	J number	Area ratio
S	0.5	-
P	0.5, 1.5	1:2
D	1.5, 2.5	2:3
F	2.5, 3.5	3:4

Table 3.2.1: Table showing the respective J number and area ratios for each electron orbital.

Where the ratio between the different J numbers for the respective orbital is given via $(2_{j-}+1):(2_{j+}+1)$, this is demonstrated in figure 3.2.5 below for the Au $4f_{7/2}$ core level of gold nanoparticles

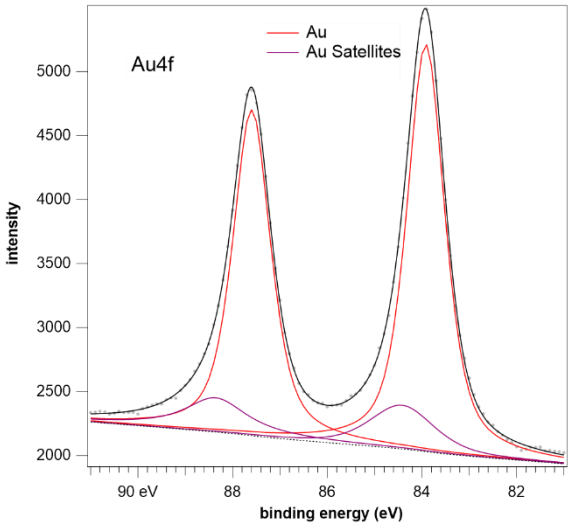

Figure 3.2.5: Au $4f_{7/2}$ core level showing a 4:3 ratio between the Au $4f^{7/2}$ and Au $4f^{5/2}$ and some satellite features.

As displayed in figure 3.2.5, there are satellite features in XPS spectra which arise due to a variety of processes. A non-monochromated X-ray source produces low intensity X-rays such as $K\alpha_{3,4}$ as well as the characteristic $K\alpha_{1,2}$. These $K\alpha_{3,4}$ X-rays produce satellite peaks at lower binding energy from the mean peak and at a much lower intensity[20].

Another formation of satellites called shake up features occurs in transition metal oxides where relaxation effects cause small satellites dependent on the oxidation state and surface of the metal. These satellites have defined positions such that the difference between Fe(II) and Fe(III) for Fe_2O_3 and Fe_3O_4 can be identified making these satellites effective as an fingerprint reference[18]. Unbonded Surface atoms will also produce satellites due to the difference in electron surface plasmon effects[21].

The shape and intensity of XPS spectra can be heavily dependent on various factors. The line shape of a core level peak is a combination of electrons from a variety of chemical species. A clean diamond surface would only exhibit one component peak in the C 1s, while an oxidized diamond surface will also have component peaks from C-O, C=O, C-OH environments. In other words, a photoemission peak can consist of several component peaks which denote a different chemical state. The component peaks are distinguishable as they have their own distinct binding energy. The peak width and shape are normally fit as a Voigt function, where each component is a combination of a Gaussian and Lorentzian peaks. During the photo-emission process Gaussian broadening occurs due to the instrumentational resolution, local-bonding differences, and sample processing such as heating. Peaks are often assigned a Gaussian/Lorentzian (G/L) ratio when fitting using a Voigt profile, where the total width of a peak is defined as a ratio between a Gaussian and Lorentzian component. This is important as for example the method of excitation is a large determining factor of the G/L ratio, synchrotron vs Lab-based x-ray sources due to lab sources being non-monochromatic have vastly different ratios. Spectra obtained from lab sources are mostly gaussian due to non-monochromaticity, whilst at a synchrotron the peaks are mostly Lorentzian. The peak position, width, and intensity is calculated for each component peak until the total fit matches the peak envelope. In a widescan spectrum each individual bond for a certain peak,(C-O, C-C, C-Fe etc) should share the same G/L ratio. However, the peak width between an Fe electron in the Fe 2p core level will be larger than the C 1s core electron for the same environment

[21,22]. This is due to the line width depending on the core hole lifetime, and the instrumentational resolution. The core-hole lifetime is a Lorentzian function and provides the inherent line shape of photoemission. The natural line width due to the core-hole lifetime, ΔE_L, can be estimated be the Heisenberg uncertainty principle by:

$$Eq\ 3.9: \qquad \Delta E_L = \frac{h}{e\tau}$$

Where *h* is Planck's constant, *e* is the electron charge and τ is the core-hole lifetime in seconds. This demonstrates that for elements with a higher electron number, the Lorentzian component will be broader.

Each core level will have its own individual photoionization cross-section, *σ*, which is the probability of electron excitation, which can be defined as[23]:

$$Eq\ 3.10 \qquad \sigma_{n,l}(E) = \frac{4}{3}\pi^2 a_0^2 \alpha [N_{n,l}[E - E_{n,l}] \left(\frac{1}{2l+1}\right) [IR^2{}_{E,l-1} + (l+1)IR^2{}_{E,l+1}$$

Where *n,l* are the quantum numbers for the orbitals, a_0 is the bohr radius, $N_{n,l}$ is the number of electrons in each orbital, $E_{n,l}$ is the energy of the electrons in each orbital, and E is kinetic energy of the emitted electrons α is the fine structure constant and R refers to the radial dipole matrices. The energy at which the cross-section reaches its lowest probability , known as the Cooper minimum, is atom dependent. From this the photoemission intensity for each molecular orbital can be calculated from Eq 3.10.

$$Eq\ 3.11 \qquad I_i = N_i \sigma_i \lambda_i K$$

Where I_i is the intensity for element *i*, of an atomic concentration *N*, with the inelastic mean free path of a photoelectron, λ_i, the cross section for the element, σ_i and *K* which is assumed consistent through the experiment such as detector settings.

From these parameters the equation can be re-arranged such that the atomic concentration ratio between two different elements can be determined such that[9]:

$$Eq\ 3.12 \qquad \frac{N_1}{N_2} = \frac{I_2 \sigma_1 \lambda_1}{I_1 \sigma_2 \lambda_2}$$

3.2.3 Ultra-violet Spectroscopy (UPS).

UPS is the similar to XPS except ultra-violet radiation is used instead of X-rays. The photon energy of UPS is much lower than an X-ray, so only valence electrons are excited from the atom. The photons for lab-based sources are generated by the splitting of helium atoms to create a UV photon With energies of 21.2 and 40.8eV from He(I) and He(II)[6,7]. UPS is a low kinetic energy technique which uses valence electrons to establish the density of states (DoS) of a material. Other useful information such as the workfunction of the material and the hybridization of the molecular orbitals can also be obtained. Materials can then be identified from their unique electronic structure fingerprint displayed in the UPS spectra.[24,25]

Valence band electrons sit at the edge of the Fermi level unless the bands are shifted. Band-bending occurs when the valence and conduction bands shift, either due to surface functionalisation changing the electron affinity or the addition of an interface. Dopants and can also alter the band profile of a material. The workfunction of a material can be determined which is an important physical property in electronic device fabrication. It's calculated by measuring the Fermi edge and the Low-E_k cut off tail and using the following equation[26]:

$$Eq\ 3.13 = E_{Photon} - E_{Fermi} - E_{cut-off}$$

Where θ is the workfunction of the material, and E_{Photon} is the excitation energy. The shape of the spectra can also give interesting information such as electron affinity, where negative electron affinities will produce a much large cut-off tail then a positive will.

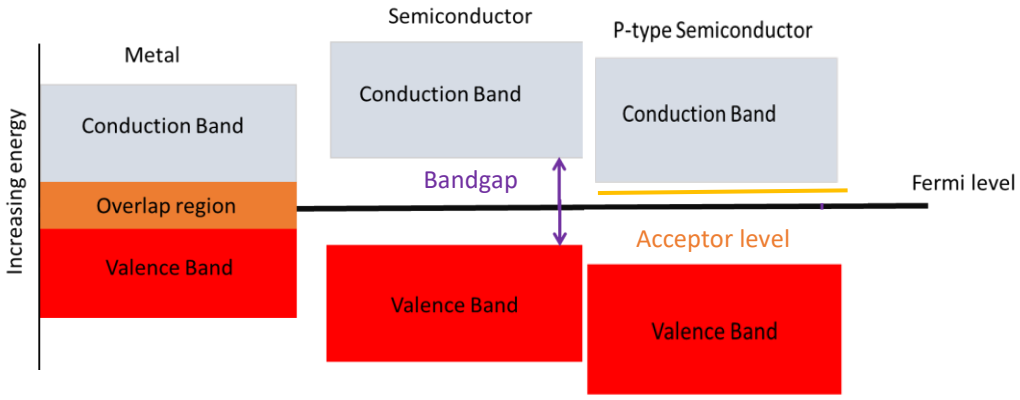

Figure 3.2.6: Simplified band diagrams showing the differences been Metals, intrinsic(pure) semiconductors and extrinsic(doped) semiconductors. P type doping shifts the Acceptor level above the Fermi level

Where materials will have different band profiles dependent on their doping levels, another method of altering the profile is through surface band-bending of the material. This can be done by either creating depletion or accumulation layers of electrons. For diamond this is achieved by terminating with either hydrogen or oxygen. Oxygen terminations will cause a depletion by pulling electrons away from the surface, whereas hydrogen is the opposite as shown in Figure 3.2.7.

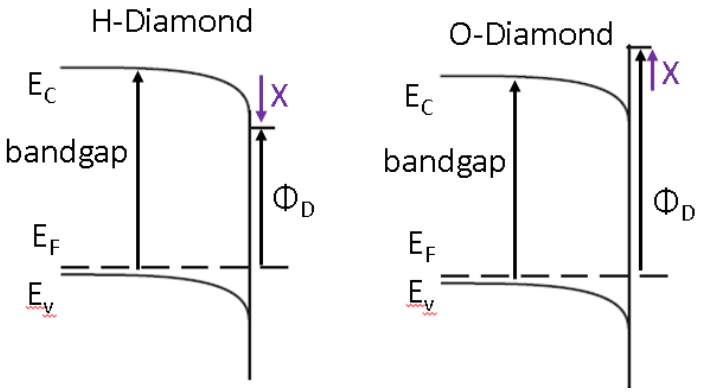

Figure 3.2.7: Simplified band diagrams showing the different of the band profiles in diamonds due to the surface functionalisation, where oxygen has a positive electron affinity, and hydrogen a negative. Where X is the electron affinity, E_c and E_v are the conduction and valence band, and Φ_D is the workfunction of diamond.

There is also band-bending at a metal-semiconductor interface. The wavefunction of electrons at the surface of the semiconductor must match that of the metal, therefore a charge transfer and band-bending will occur to match the fermi levels at the interface.

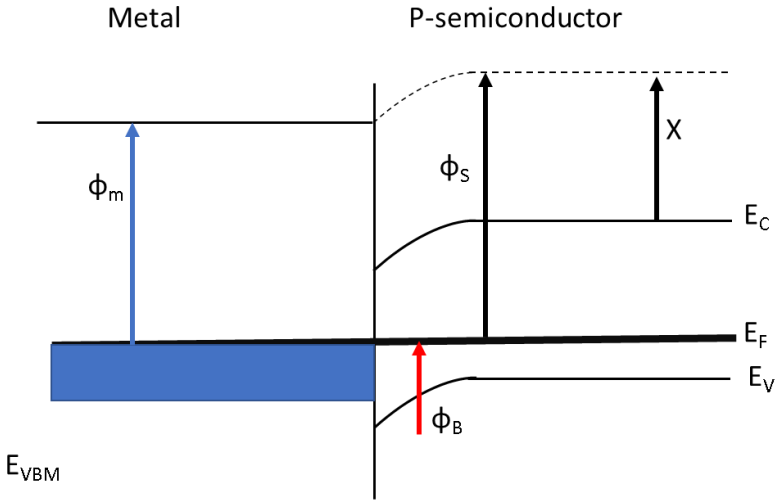

Figure 3.2.8: Simplified band diagrams showing the band-bending that occurs to a P-type semiconductor when a metal is deposited on its surface.

Where X is the electron affinity, Φ_m is the workfunction of the metal, Φ_S is the workfunction of the semiconductor, and Φ_B is the measurement of the band-bending (Schottky Barrier height).

This has the potential advantage as when a voltage is applied across the interface of the junction, an electrical potential barrier is encountered for moving a hole from the semiconductor into the metal. Metal-Semiconductor interfaces can form either Schottky barriers or ohmic contracts if the barrier height is too low.

3.2.4 Near-Edge X-ray Absorption Fine Structure (NEXAFS)

NEXAFS is a measurement of the absorption fine structure close to an absorption edge such as a K-edge. A K-edge is the increase of x-ray absorption due to the photon energy being just above the binding energy of the 1s core electrons. Measurements are usually taken just before and after the edge such as to include and pre-edge and post-edge features[27]. These regions provide information on the electronic structure of unoccupied molecular orbitals, with pre-edge features being able to determine the surface states of a material also[28].

Unlike in XPS where the photon energy is constant through a measurement, in NEXAFS the photon energy is varied throughout. There are three methods for NEXAFS known as Total Electron Yield (TEY), Partial Electron yield, (PEY) and Auger Electron yield (Auger) (AEY). This thesis a focus will be set on AEY. In TEY the photoelectrons that are created by the absorbed X-rays are measured however it can be dominated by other processes. These emitted core electrons create holes which are then filled by Auger decay which then release Auger electrons. The measurement of these primary Auger electrons can also be used to determine the x-ray absorption process, which is known as AEY but is much slower than the other methods due to reduction of total electrons measured. PEY is where you differentiate between core and Auger electrons and reject other electrons, at the expense of intensity.

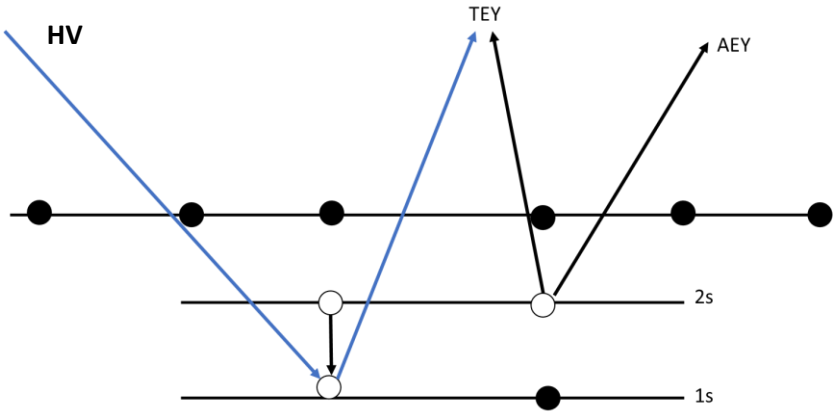

Figure 3.2.9: Diagram to demonstrate how TEY and AEY NEXAFS are measured, where PEY then different between the Core and Auger electrons received in TEY to reject other electrons.

AEY is much more surface sensitive then TEY, as due to Auger electrons having a low kinetic energy, they can only escape typically from the first nanometer of the surface. NEXAFS is also extremely sensitive to the chemical environment of each electron. Correct interpretation of the fine structure in the Spectra can be used to determine differences between the σ* and π* bonding. This allows for characterisation of the differences in hybridization of bonds such as sp^2 and sp^3 bonding and the orientation of the chemical species with respect to the detector due to the techniques polarization dependence and features related to the density of states such as the 2^{nd} Bandgap features of diamond. This allows for NEXAFS to be the perfect complimentary technique to XPS as they provide different information whilst maintaining some form of comparisons.

The absorption structure is a result from the allowed bound-state absorptions, K-edges are resultant from the excitations 1s, L edges from the 2s/p, etc. The pre-edge features sensitivity to the chemical environment is dependent on the elements themselves, where lighter elements show much more sensitivity. Due to synchrotron radiation being linearly polarised, bound-state transitions which have symmetries for the probed element can be used to determine specific orbitals of that element and the orientation of molecules on the surface of a substrate can also be determined.

The emitted electrons will affect the occupied and unoccupied molecular orbitals of the material. Rydberg transitions are caused by excited electrons interacting with the positively charge nucleus, π*and σ* transitions will also appear before and post edge respectively.

The nature of whether it is π*or σ* is dependent on the symmetry and energy of the unoccupied orbitals, there also transitions into unbound orbitals which usually are typical of σ*. The width of these peaks is dependent on the lifetime of both the excited electron and core hole state.

π* occur for unsaturated molecules such as benzene rings and graphitic carbon where graphite consists of two single (sigma) bonds and one pi bond (one sigma and one pi bond). They are typically the lowest energy feature observable in NEXAFS. σ* transitions can occur in both saturated and unsaturated molecules, the peak is usually observable post-edge however in instances of weak bonds such as C-H is sometimes observable pre-edge.

Figure 3.2.9 shows a diagram of this effect.

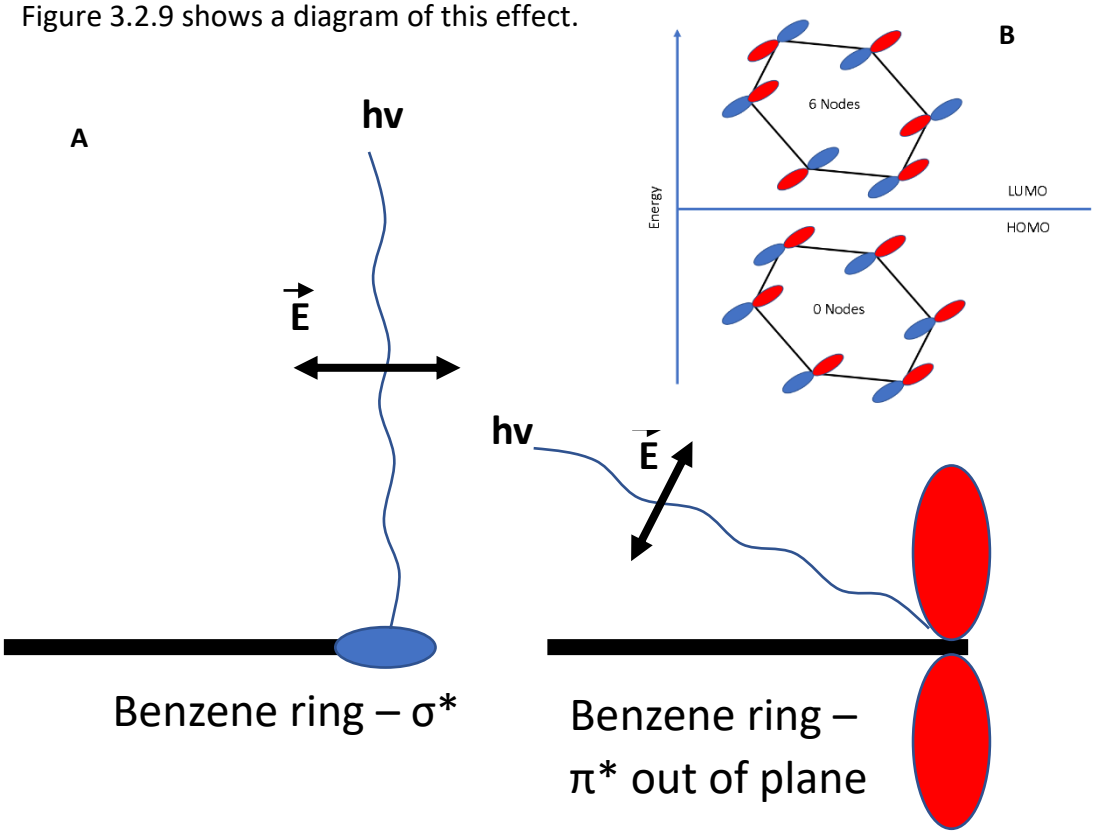

Figure 3.2.9: A: Diagram showing how the rotation of the sample with respect to the beam will change the polarisation, such that different molecular orbitals can be measured for orientation information. B: Molecular orbital energy level plot for benzene ring, where the middle ling represents a p ortibal. Benzene is made up of 6 sp_2 hybridised bonds. π bonding occurs in the LUMO which can also be described as the antibonding.*

Where dependent on whether there is an observable π* feature, the molecule can be determined whether it is flat laying on the surface or not.

3.3 Optical Scattering

3.3.1 Raman Spectroscopy

Raman spectroscopy was initially developed in 1928 by C. V. Raman after an initial study into the molecular diffraction of light back in 1922[29]. For his work on Raman spectroscopy he received the Nobel prize in 1930. Photon scattering is defined as when an incident photon interacts with a material and changes its direction. The energies of these photons are either increased or decreased by quantized increments, corresponding to differences in the vibrational and rotational energy states of a material.

Raman scattering occurs when an optical phonon is absorbed exciting a molecule into an imaginary state and the re-emitted phonon is of a higher or lower frequency. This is defined as in-elastic scattering. Rayleigh scattering is an elastic scattering where the phonon energy is conserved. The inelastic scattering from phonons can be described as two different types of emission; Stokes and Anti-stokes scattering. Stokes scattering refers to the absorption of a phonon and re-emission of a lower energy phonon leaving the molecule in a higher energy. Anti-stokes is the opposite where the molecule ends up in a lower vibrational state. Figure 3.3.1 shows a diagram indicating the differences between the different scattering methods.

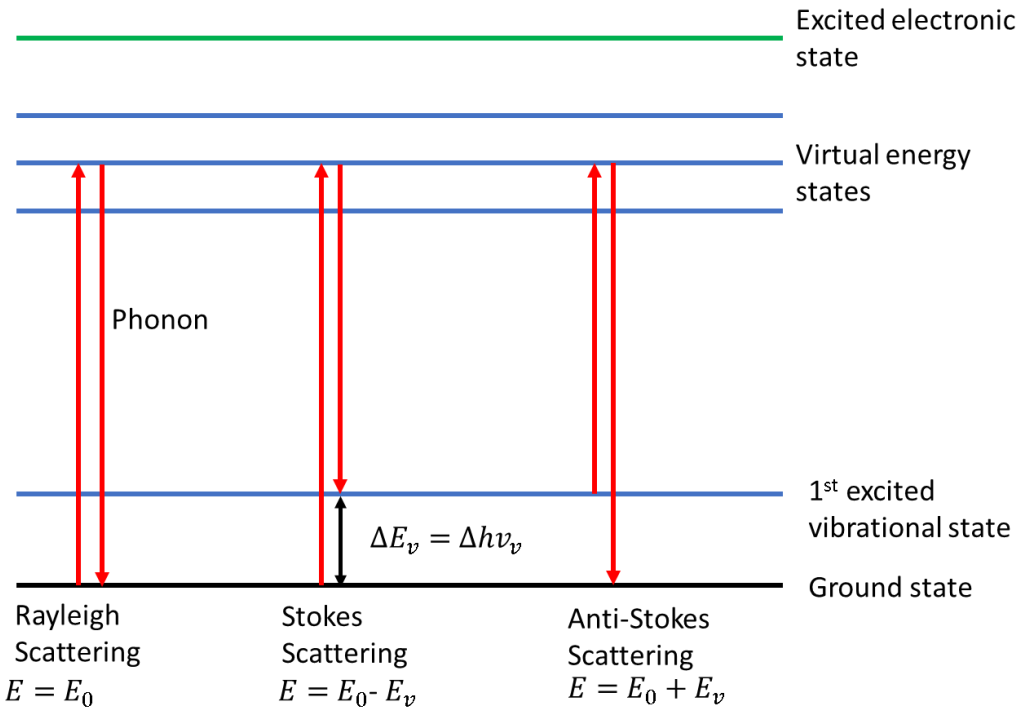

Figure 3.3.1: Diagram displaying the 3 main types of phonon scattering; Rayleigh, Stokes and Anti-Stokes and the differences between them.

Raman spectroscopy is the measurement of the inelastic scattering of a monochromatic light source, where energy is transferred between the incident photon (hv_0) and the substrate. The inelastically scattered photons (hv_v) are compared such that the shift of the photon is given by:

$$Eq\ 3.3.1\ \Delta\hat{v} = \left(\left(\frac{1}{hv_0}\right) - \left(\frac{1}{hv_v}\right)\right)$$

Where $\Delta\hat{v}$ is denoted as the shift in wavenumbers. This shift measures the specific energy difference between different vibrational states and the ground state. This allows for characterization of a material via the specific vibrational states in crystallographic and molecular structures. As diamond is a single crystal consisting of one element, the shifted photons can only exist in a limited range. Graphite, which is also carbon, due to its different crystal structure produces photon shifts different then diamond. This makes Raman beneficial for measuring differences between sp^2 and sp^3 bonding and characterizing diamond[30].

As Raman is a bulk technique, for bulk materials with high symmetry of similar vibrational mode the intensity emitted is large. However, for small molecules or materials which are highly asymmetrical the signal to noise can be low, which due to the nature of these samples such as organic molecules being relatively unstable with temperature, makes increasing the intensity of the photons for more excitation is not possible.

Surface-Enhanced Raman Spectroscopy (SERS) allows for measurement of these small molecules or materials with vastly increased intensities. The process by which SERS occurs is currently under debate. According to literature the two most highly regarded theories describe the processes as either the interaction of localized surface plasmons, or from charge transfer between the sample and SERS substrates. Recent research is currently in favor of the plasmon theory[31,32].

Silver and Gold are commonly used as SERS substrates as their plasmon resonance frequencies are close to the visible and near-infrared radiation required for the excitations of the vibrational modes required for Raman spectroscopy. There is also a lot of research already conducted in the processing of silver and gold on the nanoscale to increase the surface area of particles/substrates and therefore increase the total SERS.

3.3.2 Dynamic Light Scattering (DLS)

DLS is a method of measuring the size of molecules and particles in solution and having the capabilities of deducing the distribution of these sizes, with resolution ranging from 0.3nm to 10µm[33].

A laser is aimed at a known solution at nanoparticles where the scattered light is measured at a 175-degree angle from the laser source and the intensity of the light is collected. A speckle pattern is created on the detector of which from the intensity sizes of particles can be deduced.[34]

For a solution of known viscosity at a given temperature, the Brownian motion of nanoparticle will be dependent on the size of particles, where larger particles are slower moving in comparison to smaller ones. This change in relative speed can be defined using the Stokes-Einstein equation. The light intensity on the detector due to light scattering will fluctuate dependent on the scattering of photons by the particles in the solution. Due to Brownian motions, these fluctuations in intensity are measured with respect to time where measurements of fluctuations are taken in nanoseconds. A correlation function is deduced at each time step, from which the size distribution of particles can be calculated. From the size distribution calculations, the volume of each particle in the solution via size can be deduced. A diagram showing the basic process is shown in Figure 3.3.2.

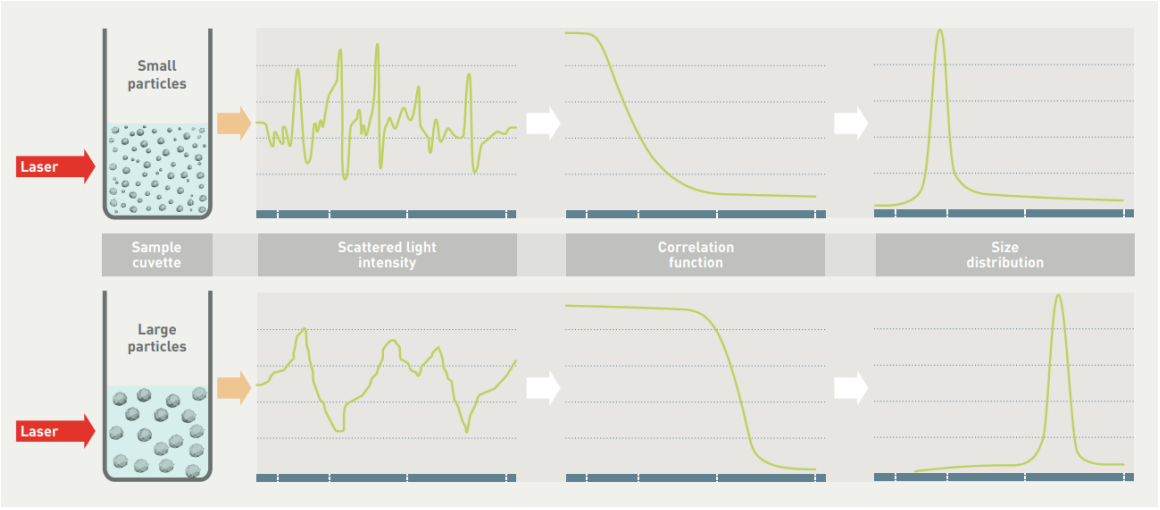

Figure 3.3.2: Diagram demonstrating the process of DLS showing the process of how size distribution is calculated. Image obtained from Malvern Panalytical.[35]

3.4 Microscopy.

3.4.1 Photoluminescence

Photoluminescence studies began as early as 1845 with Herschel's observations of blue fluorescence observed from quinine. Photoluminescence defines any process which involves the absorption and re-emission of photons from a material[36].

The re-emission of a photon can occur in two different variations known as fluorescence and phosphorescence. The differences of these can be explained using a Jablonski energy diagram which is shown in Figure 3.4.1.

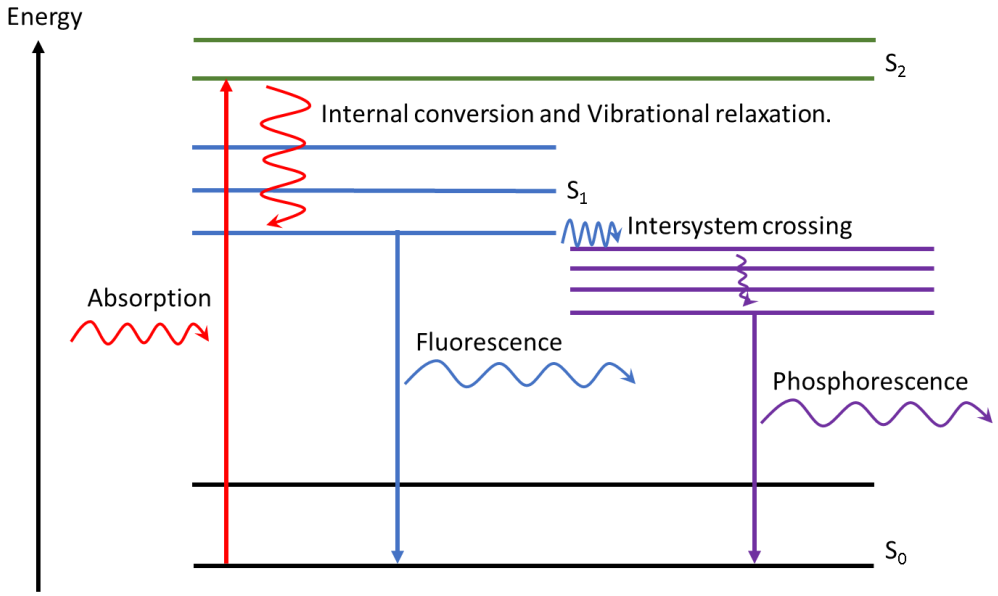

Figure 3.4.1: Diagram explaining the process of Photoluminescence and the two types of photons that can be emitted.

Due to the process of the intersystem crossing, fluorescence is a faster process compared to phosphorescence, and is the emission when an electron drops from an S_1 to an S_0 state.

Phosphorescence is a slow process, which allows for the measurement of emitted photons even after the excitation source has been isolated. It arises from forbidden spin transitions from a T_1 state down to S_0. The ground state of a molecule is a singlet (S_0) state, due to conservation of angular moment the photo-excited state must also be a singlet. Intersystem crossing usually occurs in samples which have a large amount of spin-orbit coupling. Coupled orbital and spin angular momentum allows for these forbidden transitions (T_1 to S_0) to occur, albeit at a much slower timeframe.

Photons emitted from the sample can be measured using a detector and photoluminescence can be used to obtain information about defects of wide-bandgap semiconductors, and has applications in biosensing where fluorescent bio-markers are attached to a molecule during drug delivery to track the location of the drug and analyze any biological changes at the location[37].

Confocal microscopy was first theorized in 1957 by Minsky, with the purpose of achieving better resolution than fluorescence microscopes[38]. It measures the fluorescence of a material by using a laser to excite a material and cause fluorescent photons to be emitted from the sample. The laser is focused onto the sample via a dichroic mirror and scanning mirrors and being passed through a microscope and then radiating onto the sample. Emitted photons follow the same process back up and pass through the dichroic mirror and through a pinhole into the detector. This pinhole rejects non-focused fluorescent photons allowing for a small depth of field image from the sample to be obtained. If this is done by scanning through thin sections of a sample via focusing in different Z directions, a 3D image can be produced. Figure 3.4.2 shows a simplified diagram visualizing this[39].

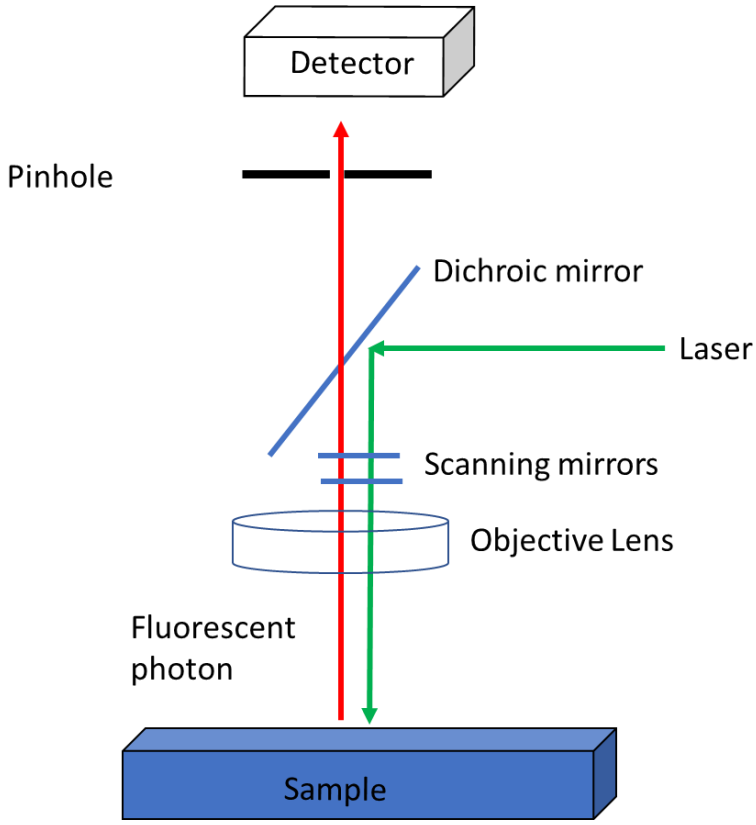

Figure 3.4.2 – Diagram of a Confocal Microscope.

3.4.3 Transmission Electron Microscopy (TEM)

TEM works by passing a focused electron beam through a set of condenser lenses at very high speeds through the use of very high voltages. The electrons pass through the material at a rate which is dependent on the transparency of the material to electrons and its crystallographic structure. An objective lens focuses the electrons transmitted through the material onto a phosphorescent screen which saves an image. As the electrons don't pass through a material well colliding with atoms, the crystallographic structure and morphology can be seen at very high resolutions of around 0.2nm, such that individual atoms may be seen [40,41].

3.4.4 Atomic Force Microscopy (AFM)

AFM works by using a cantilever of around 100μm with a tip sharpness of a few atoms wide which scans across the surface of a sample. As the tip gets near the surface, the attractive force between the cantilever bends it towards the surface and as it gets too close the Van-der Waals forces cause deflections and the cantilever deflects away from the sample. The deflections or bends of the cantilever are then measured as the tip is mapped across the sample. These deflections allow for a 3D image to be produced, where X and Y represent the surface mapped, and Z is the measurement of the cantilever's movement for obtaining topography information from the surface. This allows for measurements of the surface roughness to be obtained, where the resolution is in the sub nanometer range[42].

3.5 Density Functional Theory (DFT)

3.5.1 Born-Oppenheimer approximation and Hartree-Fock method.

All computer simulations of molecules to achieve accurate data must calculate the ground-state energy of a system, this is achieved through considering Schrödinger's equation, which is shown in Eq3.5.1:

$$Eq\ 3.5.1:\ \ \widehat{H}\Psi = E\Psi$$

Where E refers to the electronic energy of the system, Ψ can be described as a set of wave-functions, such as:

$$Eq\ 3.5.2: \Psi = (x_{1,}x_2x_{3\ldots\ldots}x_n)$$

The Hamiltonian, $\widehat{H}$, itself can be explained as three separate components, representing the Kinetic energy associated with the atoms of the molecule, an attraction component representing the nucleus-electron interaction, and a final component representing the electron-electron interaction which is shown in equation 3.5.3:

$$Eq\ 3.5.3: \widehat{H} = -\sum_{i=1}^{N}\frac{\hbar^2}{2m_e}\nabla_i^2 + \frac{1}{2}\sum_{i<j}^{N}\frac{1}{4\pi\varepsilon_0}\frac{e^2}{|r_i - r_j|} - \sum_{k=1}^{M}\sum_{i=1}^{N}\frac{1}{4\pi\varepsilon_0}\frac{Z_k e^2}{|R_k - r_i|}$$

Where the first term models the Kinetic energy of electrons, in terms of the modified Planck's constant, $\hbar(1.05 * 10^{-34}\ m^2kg/s)$ mass $m_e(9.11 * 10^{-31}kg)$, the second term is in relation to electron-electron interactions, where electron *I* has a charge $e(-1.6 * 10^{-19}C)$ is measured against all other electrons, such that if *I=1* then *j=(2,3..N)* for their respective positions r_i and r_j and final term is to model the nucleus-electron interaction such that it measures the potential of *N* electrons, against *M* nuclei, where Z_k is the charge of the nuclei, at position R_k.

This equation can be reduced as measurements of distance are in terms of the Bohr radius ($a_0 = 0.5292 * 10^{-10} = 0.05292nm$) and energy measurements are now in Hartree's, ($E_h = 27.21eV$) we can there refer to $\hbar$, $4\pi\varepsilon_0$, m_e and e all being equal to 1, such that it can be simplified into equation 3.5.4:

$$Eq\ 3.5.4:\ \widehat{H} = -\frac{1}{2}\sum_{I}^{N}\nabla_i^2 + \left(-\sum_{k=1}^{M}\sum_{i=1}^{N}\frac{Z_k}{|R_k - r_i|}\right) + \sum_{i<j}^{N}\frac{1}{|r_i - r_j|}$$

Equation 3.5.4 is better known as the Born-Oppenheimer approximation, which is the starting block of Hartree-Fock method. The aim of all simulations as previously mentioned is to obtain the ground state energy, in terms of a wave-function this is described as:

$$Eq\quad 3.5.5:\qquad E_0 \geq E\langle\Psi_0\rangle$$

Such that the ground-state wave-function, Ψ_0, is a property of the ground-state energy, E_0. This can be solved using the variation principle:

$$Eq\ \ 3.5.6:\quad E[\Psi] = \frac{\langle\Psi|\widehat{H}|\Psi\rangle}{\langle\Psi|\Psi\rangle}$$

Where:

$$Eq\ 3.5.7:\quad \langle\Psi|\widehat{H}|\Psi\rangle = \int \Psi^*\,\widehat{H}\Psi\,dx$$

The average of the trial wave-function, Ψ in respect to the Hamiltonian produces a guess to the lowest ground state energy, the answer is then resubmitted, $E\langle\Psi\rangle$ back into the equation to keep obtaining a more accurate representation, although this method has its limitations. For an *N* electron system, the ground state energy could be defined as:

$$Eq\ 3.5.8:\qquad E_0 = E[N, Vext]$$

Where $Vext$ is defined as the second component of Equation 3.5.5. Using this knowledge, a determinant can be written which describes a wave-function which can be used as an initial trial. This is known as the Slater determinant, named after John Slater and is as follows:

$$Eq\ 3.5.9:\qquad \Psi_{HF} = \frac{1}{\sqrt{N}}\begin{pmatrix}\Psi_1 x_1 & \cdots & \Psi_n x_1\\ \vdots & \ddots & \vdots\\ \Psi_1 x_n & \cdots & \Psi_n x_n\end{pmatrix}$$

Such that a product by taking $\Psi_I x_j$, *X* can be individual molecular orbitals, such that if $\Psi_1 = \Psi_2$ then $\Psi X = 0$. These products much obey the Pauli-Exclusion principle by allowing only specific spin configurations of the electrons. The Slater determinant can then be calculated.

$$Eq\ 3.5.10:\ E_0 = \sum_{K<J}^{M} \frac{Z_K Z_J}{|r_K - r_J|} + \int \left((\Psi_{HF} - \nabla_i^2 \Psi_{HF}^*) + (\Psi_{HF} \sum_{i=1}^{N} \frac{Z_k}{|R_k - r_i|} \Psi_{HF}^*) \right) + \sum_{i<j}^{N} (J_{ij} - I_{ji})$$

Where the first term is also taking into consideration a nuclear-nuclear interaction, this is what is known as the Hartree-Fock (HF) method, where the central component of equation 3.5.10 refers to one electron configurations. This method is known as being a Self-Consistent Field theory (SCF), where every-time a new E_0 is created, a new Ψ_{HF} is guessed, and this process continues until $E_{new} - E_{old} = 0$. This allows for recalculations of the lowest energy at each step until the ground state is achieved.

The disadvantages of using the HF method are quite severe; the electron-electron interaction is taken as an average value due to other electrons, rather than considering the correlation between them all. Calculation time also increases exponentially with electron number (N^4) making it computationally expensive. [43-46]

3.5.2 Density Functional Theory (DFT)

As we know from the previous sub-section, computer simulations try to solve the Schrödinger equation (Eq3.5.1) to obtain information from vibrational frequencies, molecular orbitals and optimised geometries. DFT Is the most successful method of computer simulations, ranging from the ability to accurately measure these properties of a molecule but also analyse more complex systems such as a quantum fluid.

DFT is reliant on calculating the electron density of a system. If we define electrons as having spin functional, $\vec{s}$, in a system of spatial orbitals, $\vec{r}$, we can define these in terms of spin orbitals, $\vec{x}$, as equation 3.5.11

$$Eq\ 3.5.11: \quad \vec{x} \equiv (\vec{s}, \vec{r})$$

Such that we can define probability function of the system of *N* electrons as:

$$Eq\ 3.5.12: \quad \rho(\vec{r}) = \int |\Psi(x_1, x_2 \ldots . x_n|^2\, d\vec{s} d\vec{x}_2 \ldots . d\vec{x}_n$$

$$Where\ \rho(\vec{r} \to \infty) = 0\ and \int \rho(\vec{r})\, d\vec{r} = N$$

Where $\rho(\vec{r})$ can be used to gather theoretical results on nuclear charge and ionisation energy. Based on the condition $\int \rho(\vec{r})\, d\vec{r} = N$, The variational principle can be defined in Equation 3.5.6 to obtain more correct estimations of $\rho(\vec{r})$.

The Thomas-Fermi model was the first to try and use DFT methods, it was assumed that electrons act like a uniform gas, such that the kinetic energy can be modelled

The Hohenberg-Kohn theorem fixes this problem by having two key principles:

- There is a one to one correspondence between the electron density and the ground state wave-function
- The functional will only produce ground state energies if the wave-function is with respect to the ground state density.

The first theorem implies that any observable feature can be uniquely determined by the electron density, such that:

$$Eq\ 3.5.13:\quad E = \langle \Psi | \hat{H} | \Psi \rangle, such\ that\ as\ \Psi \to min, \qquad then\ \ \Psi \to \rho_0, E \to E_0$$

We can derive a Hohenburg-Kohn functional (HK) defining the ground state energy with respect to the density wave-function as Equation 5.3.6

$$Eq\ 3.5.14:\quad E_{HK}[\rho] = E_k + E_{ee}$$

Where E_k is the kinetic energy referred to in Equation 5.2.3, and E_{ee} is defined as the electron exchange correlations, of which it has a singular classical component, which we derived earlier and is defined as E_c:

$$Eq\ 3.5.15:\quad E_c = \left(\frac{1}{2}\right) \int \int \frac{\rho(\vec{r}_1)\rho(\vec{r}_2)}{r_{12}}\, d\vec{r}_1\, d\vec{r}_2$$

However, a large part of E_{ee} is unknown, and what is unknown will be defined as E_{xc}.

Kohn-Sham investigated a more appropriate way of analysing the kinetic energy of a system, such that equation 3.5.16 defines a new term for a modelled kinetic energy, E_{ke}:

$$Eq\ 3.5.16:\quad E_{ke} = -\frac{1}{2} \sum_{I}^{N} \langle \Psi_i | \nabla_i^2 | \Psi_i \rangle$$

This now leaves us with the following functional denoted in equation 3.5.17, where the Kohn-Sham energy (E_{KS}) can now be calculated using the correlation energy.

$$Eq\ 3.5.17: \quad E_{KS}[\rho] = E_{ke} + E_c + E_{xc}$$

Where the Kohn-Sham equation is defined as:

$$Eq\ 3.5.18: \quad V_{ks}(\vec{r}_1) = \int \frac{\rho(\vec{r}_2)}{r_{12}} d\vec{r}_2 + V_{xc}(\vec{r}_1) - \sum_{k}^{M} \frac{Z_k}{|r_{1k}|}$$

[47-49] where V_{xc} is the exchange correlation potential[47-49].

3.5.3 Periodic Boundary Conditions (PBC)

Molecular dynamic and relaxation simulations aim to calculate the optimal structural and dynamic properties of a system ranging from tens to thousands of particles. However, as computation time is a function of the square of the electron number, on small scale systems the surface effect is negligible, however in reality for 2D materials of infinite length the surface effects are real. Graphene sheets bend and dip when modelled for large sizes, but small simulations will never capture that effect. Modelling an infinite film is impossible, however a more computational friendly method id to model a theoretically infinite film.

Periodic Boundary Conditions (PBC) is the method of building a unit cell around the material. This is usually in the format of a primitive unit cell such as a FCC and is designed to incorporate the unit cell of the material being modelled.

This unit cell is then repeated in N dimensions and surround the original in all dimensions with images of itself.

A particle will interact with all other particles in its own unit cell, however it also has a finite distance where it will interact with particles within another unit cell, where there is a cutoff which at a specific distance there is no longer any more interactions modelled. This allows for fine tuning of calculations to reduce the calculation time but reduces the benefits of using PBC.

3.5.4 Bloch's theorem and Pseudopotentials

As shown in equation 3.5.2 the solution of DFT is the sum of potentially infinite electrons with total freedom. This would require an infinite number of wave functions to be calculated.

Introducing a periodic potential, $V(r)$ we can express the potential with primitive lattice vectors, T, such that:

$$Eq\ 3.5.19: \quad V(r) = V(r+T)$$

Defining the system as having PBC, we can describe the translational symmetry properties with Born-von Karman periodic boundary conditions to describe the motion of the electrons through a periodic potential. If a regular plane wave is defined as:

$$Eq\ 3.5.20: \quad \phi(\mathrm{r}) = e^{i(k.r-wt)}$$

And then applying PBC, the crystal can be simulated in terms of many primitive unit cells, such that:

$$Eq\ 3.5.21: \quad \phi(\mathrm{r}) = \phi\left(\mathrm{r} + N_j A_j\right) where;\ e^{iN_j k.a_j} = 1$$

Where J is either 1,2, or 3, N is the primitive number of unit cells, N_j is the number of number of unit cells in the j[th] direction and A_j is a non-coplanar vector. Solving this for $G.T = 2\pi m$ gives a solution for allowed wave vectors:

$$Eq\ 3.5.22: \quad k = \sum_{j=1}^{3} \frac{m_j}{N_j} A_j$$

Where G is the reciprocal lattice vectors. This equation shows the Brillouin zone always has the same of primitive cells. Solving the Schrödinger equation for a periodic potential, the wave-function can be re-written as a set of plane waves

$$Eq\ 3.5.23: \quad H\psi = -\left\{\sum_{i=1}^{N} \frac{\hbar^2}{2m_e} + V(r)\right\}\psi = E\psi$$

$$Eq\ 3.5.24: \quad \psi(r) = \sum_{k} C_k e^{ik.r}$$

Taking into account the plane wave of a Bravais lattice, you can solve various potentials with their Fourier components, and that Hamiltonian matrix has a cut-off point of:

$$Eq\ 3.5.25: \quad \frac{\hbar^2}{2m_e}|k+G|^2$$

However, the number of electronic wave functions needed to accurately estimate core level electrons is overly large, however most physical properties are a by-product of number of valence electrons which are also a larger fraction of the total binding energy so a purely plane wave method is computationally inefficient and only really useful for hydrogen.

To solve this issue pseudopotentials are used, they are approximations which remove core electrons and the strong nuclear potential and replaces it with a weaker pseudopotential which follows a set of pseudo wave functions.

Pseudopotentials start with an all-electron calculation for a reference atom, to determine all electron eigenvalues, which are put into a Schrödinger equation with a pseudo-wavefunction, then the inverting of the Kohn-Sham equations with the that wavefunction (ψ_{psuedo}).

Norm Conserving Pseudopotentials operate such that when generated they have the following description:

$$Eq\ 3.5.26: \quad \int_0^{Ec} \psi_e^*(r)\psi_e(r)dr = \int_0^{Ec} \psi_{pseudo}^*(r)\psi_{psuedo}(r)dr$$

So that everything electron up until the core level generate exact charge densities, so that the E_{xc} is calculated correctly, pseudopotentials following this method have correct scattering properties over a small interval at energy of the atomic sphere's, ε.[51,52]

3.5.5 Perdew-Burke-Ernzerhof(PBE) Exchange-correlation function and the HGH method

Exchange-correlation functions work as a method to calculate the exchange-correlation energy, E_{xc}, required to solve the Kohn-Sham equations. All these methods calculate approximations, E_{xc}, however each functional has it uses in certain types of calculations and will fail in others.

Non-empirical functions such as PBE are the most used type of exchange correlation functional used, with PBE being completely parameter free it means it's able to be used for a wide range of systems giving accurate results. It uses the generalised gradient approximation (GGA), which has many advantages of the standard Local-Density approximation method (LDA). Although due to the inability to calculate Van der Waals forces extra corrections must be used.

LDA methods calculate the exchange energy using a simple density functional, shown in Equation 3.5.27

$$Eq\ 3.5.27: \quad E_{XC}^{LDA}[\rho(r)] = \int \rho(r)\varepsilon_{xc}^{GGA}[\rho(r)]dr$$

Where the GGA calculates the next derivative in the expansion, which reduces the bond dissociation error massively. The PBE functional was developed K. Burke, J.P Pewdew and M. Ernzerhof as an GGA approximation which was an adaptation of the PW91 functional. PBE has since been modified to use the Hartwigsen-Goedecker-Hutter method to form the commonly used PBE-HGH pseudopotential, which adds in a set of relativistic dual-space Gaussian pseudopotentials for the LDA using a specific set of parameters which improves the accuracy immensely[53].

3.5.6 Molecular dynamics – Car-Parrinello

Classical dynamics is a method most often used to model weak forces which are thermodynamic processes such as polypeptide folding and partitioning of solvents. The Car-Parrinello uses density functional theory initially to calculate the ground state energy much like in all the methods above. From this the forces on the nuclei can be computed and using various algorithms such as steepest descent or verlet and a velocity is calculated. Electrons in these calculations are given a mass usually 10^6 times larger than usual, this allows for the system to always stay close to the ground state energy, using Lagrangian dynamics described in the equation below:

$$Eq\ 3.5.33: \quad l = \sum_i \frac{1}{2}\mu\langle\psi_i|\psi_i\rangle - E\{(\psi_i)\ (r_i)(z_i)$$

Where μ is the fictitious mass of the electron, E is the Kohn-Sham energy functional for a system. Atomic positions, r_i, are defined by a set of periodic boundary conditions, z_i. From this the Lagrangian equations of motion can be computed. After initial velocities are calculated, temperatures are also calculated using ideal gas laws and the Boltzmann distribution. After this the new positions are calculated and based of the dynamics of the system and the time-step denoted in the settings. Based on the kinetic energy and

temperature the simulation starts again by re-calculating the forces on the atoms. There are methods such as thermostats which stop the system gaining too much energy by controlling the temperature of a system within certain ranges[53].

3.5.7 Molecular dynamics – Quantum

Unlike Car-Parrinello (CP) , Quantum Molecular Dynamics (QMD) can model the chemical reactions between two different substances, along with electron transfer and various other properties. The same principle applies to QMD as to CP, except instead of calculating the forces in a classical approach, the electrons have their regular mass and after each time-step the groundstate energy is calculated again, it is much like a standard DFT calculation except each atom will have an E_{ke} associated it along with more freedom for the evolution of the system itself.

References:

[1] - Born, M. and Wolf, E., Basic properties of the electromagnetic field in Principles of Optics, 7th edition, Cambridge University Press, Cambridge, United Kingdom, pages 1-74. 1999.

[2] -Purcell and Morin, Harvard University. Electricity and Magnetism. (3rd ed.). Cambridge University Press, New York. P430. 2013. ISBN 978-1-107-01402-2.

[3] - H. Hertz,"UebereinenEinflussdesultraviolettenLichtes auf die electrische Entladung," Annalen der Physik, vol. 267, pp. 983-1000, 1887

[4] - Vickerman, J. Surface Analysis - The Principal Techniques, 2nd ed.; John Wiley & Sons: Chichester, UK, 2009, pp 47-113.

[5] -Moulder, J. Handbook of X Ray Photoelectron Spectroscopy: A Reference Book of Standard Spectra for Identification and Interpretation of XPS Data, 2nd ed.; Chastin, J., Ed.; Perkin-Elmer Corporation: P9-29. 1992.

[6] - Vilesov, F. I.; Kurbatov, B. L.; Terenin, A. N. "Electron Distribution Over Energies In Photoionization Of Aromatic Amines in Gaseous Phase". Soviet Physics Doklady. 6: 490. Bibcode:1961SPhD....6..490V. 1961.

[7] Price, W. C. "Photoelectron Spectroscopy". Advances in Atomic and Molecular Physics. Vol10: 131. 1974. doi:10.1016/S0065-2199(08)60348-6.

[8] Baker, Arthur D.; Betteridge, David Photoelectron Spectroscopy. Chemical and Analytical Aspects (First ed.). Oxford: Pergamon Press. 1972. ISBN 0-08-016910-4. OCLC 539873.

[9] - Seah, M. P.; Dench, W. A. Quantitative Electron Spectroscopy of Surfaces: A Standard Data Base for Electron Inelastic Mean Free Paths in Solids. Surf.Interface Anal. Vol1 (1). P2–11. 1979.

[10] Chusuei, C. C. .; Goodman D Wayne. “X-Ray Photoelectron Spectroscopy.” Encycl. Phys. Sci. Technol. Vol921 (938). 2002.

[11] Alford, T.; Feldman, L.; Mayer, J. Fundamentals of Nanoscale Film Analysis; Springer: New York USA, 2007.

[12] - National Institute of Standards and Technology. NIST Database https://srdata.nist.gov/xps/main_search_menu.aspx

[13] -HÜFNER, S. SCHMIDT, AND F. REINERT, "PHOTOELECTRON SPECTROSCOPY—AN OVERVIEW," NUCLEAR INSTRUMENTS AND METHODS IN PHYSICS RESEARCH SECTION A: ACCELERATORS, SPECTROMETERS, DETECTORS AND ASSOCIATED EQUIPMENT, VOL. 547, PP. 8-23,2005.
[14] - S. HÜFNER, PHOTOELECTRON SPECTROSCOPY: PRINCIPLES AND APPLICATIONS: SPRINGER SCIENCE & BUSINESS MEDIA, 2013.
[15] - HOFMANN, S. AUGER- AND X-RAY PHOTOELECTRON SPECTROSCOPY IN MATERIALS SCIENCE, 1ST ED.; SPRINGER SERIES IN SURFACE SCIENCES; SPRINGER BERLIN HEIDELBERG: BERLIN, HEIDELBERG. VOL. 49, PP 1-204. 2013.
[16] - D. COSTERAND R.D. L. KRONIG, "NEW TYPE OF AUGER EFFECT AND ITS INFLUENCE ON THE X-RAY SPECTRUM," PHYSICA, VOL. 2, PP. 13-24. 1935
[17] - R. A. POLLAK, L. LEY, F. R. MCFEELY, S. P. KOWALCZYK, AND D. A. SHIRLEY, "CHARACTERISTIC ENERGY LOSS STRUCTURE OF SOLIDS FROM X-RAY PHOTOEMISSION SPECTRA," JOURNAL OF ELECTRON SPECTROSCOPY AND RELATED PHENOMENA, VOL. 3, PP.381-398. 1974.
[18] P. STEINER, H. HÖCHST, AND S. HÜFNER, "ANALYSIS OF THE PLASMON STRUCTURE IN XPS EXPERIMENTS OF SIMPLE METALS," PHYSICS LETTERS A, VOL 61, P410-412, 1977.
[19] - D. BRIGGS, XPS: BASIC PRINCIPLES, SPECTRAL FEATURES AND QUALITATIVE ANALYSIS, IN: D. BRIGGS, J.T. GRANT (EDS.), SURFACE ANALYSIS BY AUGER AND X-RAY PHOTOELECTRON SPECTROSCOPY, IM PUBLICATIONS, CHICHESTER, P31-56. 2003.
[20] – NSRDS, X-RAY WAVELENGTHS AND X-RAY ATOMIC ENERGY LEVELS. P7-9. 1967.
[21] - HÜFNER S. CONTINUOUS SATELLITES AND PLASMON SATELLITES: XPS PHOTOEMISSION IN NEARLY FREE ELECTRON SYSTEMS. IN: PHOTOELECTRON SPECTROSCOPY. ADVANCED TEXTS IN PHYSICS. SPRINGER. 2003.
[21] - J. F. WATTS AND J. WOLSTENHOLME, "AN INTRODUCTION TO SURFACE ANALYSIS BY XPS AND AES," AN INTRODUCTION TO SURFACE ANALYSIS BY XPS AND AES, BY JOHN F. WATTS, JOHN WOLSTENHOLME, P224. 2003.
[22] - R. Hesse, P.Streubel, and R.Szargan,"Product or sum: comparative tests of Voigt, and product or sum of Gaussian and Lorentzian functions in the fitting of synthetic Voigt-based X-ray photoelectron spectra," Surface and Interface Analysis, vol39. p381-391. 2007.
[23] - JOURNAL OF ELECTRON SPECTROSCOPY AND RELATED PHENOMENA 8 (1976) PAGES 129-137), WHICH IS STILL AN IMPORTANT RESOURCE FOR XPS ANALYSIS. CHECK OUT THE CORRECTIONS BY REILMAN AND COWORKERS (DOI:10.1016/0368-2048(76)80025-4, JOURNAL OF ELECTRON SPECTROSCOPY AND RELATED PHENOMENA 8 P389-394. 1976.
[24] - RABALAIS J.W. PRINCIPLES OF ULTRAVIOLET PHOTOELECTRON SPECTROSCOPY. WILEY. 1977. ISBN 0-471-70285-4
[25] BAKER, ARTHUR D.; BETTERIDGE, DAVID (1972). PHOTOELECTRON SPECTROSCOPY. CHEMICAL AND ANALYTICAL ASPECTS OXFORD: PERGAMON PRESS. ISBN 0-08-016910-4. OCLC 539873
[26] -PARK, Y.; CHOONG, V.; GAO, Y.; HSIEH, B. R.; TANG, C. W. WORK FUNCTION OF INDIUM TIN OXIDE TRANSPARENT CONDUCTOR MEASURED BY PHOTOELECTRON SPECTROSCOPY. APPLIED PHYSICS LETTERS. 68 (19): P2699–2701. 1996. DOI:10.1063/1.116313. ISSN 0003-6951.
[27] - D. C. KONINGSBERGER, R. PRINS; A. BIANCONI, P.J. DURHAM "X-RAY ABSORPTION: PRINCIPLES, APPLICATIONS, TECHNIQUES OF EXAFS, SEXAFS, AND XANES. CHAPTERS, CHEMICAL ANALYSIS 92, JOHN WILEY & SONS. 1988.
[28] - NEXAFS SPECTROSCOPY BY J. STÖHR, SPRINGER 1992, ISBN 3-540-54422-4.
[29] - RAMAN, C. V. (1928). "A NEW RADIATION". INDIAN JOURNAL OF PHYSICS. 2: 387–398
[30] - PRAWER, S. & NEMANICH, R. J. RAMAN SPECTROSCOPY OF DIAMOND AND DOPED DIAMOND. PHILOS. TRANS. A. MATH. PHYS. ENG. SCI. VOL362, P2537–65. 2004

[31] - Blackie, Evan J.; Le Ru, Eric C.; Meyer, Matthias; Etchegoin, Pablo G. Surface Enhanced Raman Scattering Enhancement Factors: A Comprehensive Study. J. Phys. Chem. C. Vol 111. P13794-13803. 2007.
[32] - Le Ru, Eric C.; Meyer, Matthias; Etchegoin, Pablo G. Proof of Single-Molecule Sensitivity in Surface Enhanced Raman Scattering (SERS) by Means of a Two-Analyte Technique. Vol110. P1944-1948. 2006.
[33] - Berne, B.J.; Pecora, R. Dynamic Light Scattering. Courier Dover Publications (2000) ISBN 0-486-41155-9
[34] - Goodman, J (1976). "Some fundamental properties of speckle". J. Opt. Soc. Am. 66 (11): 1145–1150. Bibcode:1976JOSA...66.1145G. doi:10.1364/josa.66.001145.
[35] Malvern Panalytical. https://www.malvernpanalytical.com/en/products/technology/light-scattering/dynamic-light-scattering.
[36] - Aoki, T. Photoluminescence Spectroscopy. In Characterization of Materials, E.N. Kaufmann (Ed.).2012. doi:10.1002/0471266965.com058.pub2
[37] - De Acha et al. Luminescence-Based Optical Sensors Fabricated by Means of the Layer-by-Layer Nano-Assembly Technique. Sensors (Basel). 2017
[38] – Confocal Microscopy Patent. Filed in 1957 and granted 1961. US 3013467
[39] Colin JR Sheppard. Confocal Microscopy. The Development of a Modern Microscopy. Imaging & Microscopy. GIT Imaging and Microscopy. 2008.
[40] - Ernst Ruska; translation by T Mulvey. The Early Development of Electron Lenses and Electron Microscopy. Applied Optics. Vol 25. p. 820. 1980. ISBN 978-3-7776-0364-3.
[41] - Meyer, Jannik C.; Girit, C. O.; Crommie, M. F.; Zettl, A. (2008). "Imaging and dynamics of light atoms and molecules on graphene" (PDF). Nature. 45. doi:10.1038/nature07094. PMID 18633414. June2012.
[42] - Ohnesorge, Frank. True atomic resolution by atomic force microscopy through repulsive and attractive forces. Science. Vol260 (5113): 1451. 1993. doi:10.1126/science.260.5113.1451
[43] - Max Born; J. Robert Oppenheimer (1927). "Zur Quantentheorie der Molekeln" [On the Quantum Theory of Molecules]. Annalen der Physik (in German). 389 (20): 457–484. Bibcode:1927AnP...389..457B. doi:10.1002/andp.19273892002
[44] - Cramer, Christopher J. (2002). Essentials of Computational Chemistry. Chichester: John Wiley & Sons, Ltd. pp. 153–189. ISBN 0-471-48552-7.
[45] - Szabo, A.; Ostlund, N. S. (1996). Modern Quantum Chemistry. Mineola, New York: Dover Publishing. ISBN 0-486-69186-1.
[46] - Pauli, W. . Über den Zusammenhang des Abschlusses der Elektronengruppen im Atom mit der Komplexstruktur der Spektren. Zeitschrift für Physik. Vol31: P765–783. 1925. doi:10.1007/BF02980631.
[47] -Kohn, Walter; Sham, Lu Jeu. Self-Consistent Equations Including Exchange and Correlation Effects. Physical Review. 140 (4A). P1133–1138. 1965.
[48] - Tkatchenko, Alexandre; Scheffler, Matthias (2009). "Accurate Molecular Van Der Waals Interactions from Ground-State Electron Density and Free-Atom Reference Data". Physical Review Letters. 102 (7): 073005.
[49] - Band, Y. B., Avishai, Y., Band, Y. B., & Avishai, Y. Density Functional Theory. Quantum Mechanics with Applications to Nanotechnology and Information Science, P871–889. 2013. https://doi.org/10.1016/B978-0-444-53786-7.00015-0
[50] L. Truflandier, M. Paris,C. Payen, and, and F. Boucher. First-Principles Calculations within Periodic Boundary Conditions of the NMR Shielding Tensor for a Transition Metal Nucleus in a

Solid State System: The Example of 51V in AlVO4 The Journal of Physical Chemistry B 2006 110 (43), 21403-21407DOI: 10.1021/jp0648137
[51] - Felix Bloch. Über die Quantenmechanik der Elektronen in Kristallgittern. Z. Phys. Vol52 (7–8): P555–600. 1928
[52] - Hellmann, Hans "A New Approximation Method in the Problem of Many Electrons", Journal of Chemical Physics, Karpow-Institute for Physical Chemistry, P61. 1935.
[53] - John P. Perdew, Kieron Burke, and Matthias Ernzerho. Generalized Gradient Approximation Made Simple. Phys. Rev. Lett. 77, 3865 –; Erratum Phys. Rev. Lett. 78, 1396. 1997.
[54] - Car, R.; Parrinello, M . Unified Approach for Molecular Dynamics and Density-Functional Theory. Physical Review Letters. Vol55 (22). P2471–2474. 1985.

Chapter 4 – Instrumentation.

This chapter will discuss all the instrumentation used for the data gathered during this thesis, with a focus on the requirements for the measurement and in-situ treatments for XPS, NEXAFS and the additional requirements for the conduction of near-ambient pressure XPS at specific circumstances. The equipment that is also used for other complimentary techniques such as microscopy and scattering will be discussed also. Discussion will go into the hardware used for DFT calculations and software used to produce the images; as well as the software required for the analysis of the data used in all the above techniques.

4.1 Ultra-high Vacuum

As previously stated, for increasing the count-rate of electrons reaching the detector, ultra-high vacuum is maintained such that the chance of electron collided with anything is reduced. This also has additional benefits such that due to the nature of surface sensitivity in PES experiments, ultra-high vacuum provides an clean environment for sample preparation and measurement. Using the Hertz-Knudsen equation which is defined as[1]:

$$Eq\ 4.1 \quad \varphi = \frac{\alpha p N_a}{\sqrt{2\pi MRT}}$$

Where φ is the flux of molecules, α is the chance of a molecule sticking to the surface, p is the pressure of the system, N_a is Avogadro's constant, M is the molar mass of the molecules, R is the gas constant, and T is the temperature of the system. From the flux we can calculate the rate at which a monolayer of surface contaminants would adsorb onto our surface from Eq 4.2

$$Eq\ 4.2 \quad \varphi = \frac{10^{19}}{t_{ml}}$$

Where t_{ml} represents the time taken for a monolayer of adsorbates to form.

Table 4.1.1 shows the ranges of vacuum levels, there pressures and formation times for a monolayer of contaminants to occur.

Vacuum range	**Pressure (mbar)**	**Formation time of a monolayer (seconds)**
Atmospheric	*1000*	*10^{-9}*
Low	*1*	*10^{-6}*
Medium	*10^{-3}*	*10^{-3}*
High	*10^{-6}*	*10*
Ultra-high	*10^{-9}*	*10000*

Table 4.1: Table showing the ranges of vacuum level, the relative baseline pressure for that range, and the rate at which a monolayer of contaminants forms on the surface in these conditions.

The time difference in monolayer formation between high and ultra-high vacuum is a factor of 1000, this is imperative for surface science analysis where samples can require hours of

preparation for surface treatments and cleaning and measurements can also take several hours.

For achieving such low pressures, a series of pumps are used which pull gases and molecules out from the vacuum chambers. The initial step is the use of either scroll or roughing pumps, which get the pressures down to pressures as low as approximately 10^{-3} mbar. Roughing pumps are called as such due to themselves doing most of the initial pumping of gases/molecules from atmospheric pressure down to low vacuum levels operating in rough conditions (>99.9% of all atoms/molecules at atmospheric pressures are pumped out in this stage). At these low vacuum pressures' turbo-molecular pumps can be operated, which consist of several rotating blades and stationary blades in A-B-A stack which are angled in a pattern to best accelerate particles to the exhaust. The rotary blades spin at incredibly high frequencies which pump energy into the gas molecules and given them a velocity in specific directions away from the vacuum chamber[2,3].

4.2 Photo-Electron Spectroscopy

4.2.1 Aberystwyth “REES” system

Figure 4.2.1 shows an image of the entirety of the REES system, which consists of 4 stainless steel chambers. There is a load lock, plasma chamber, preparation chamber and an analysis chamber. The orientation is set up such that each individual chamber can be isolated from each other via a gate valve in situations such as plasma treatments, depositions, load/unloading samples and temperature treatments.

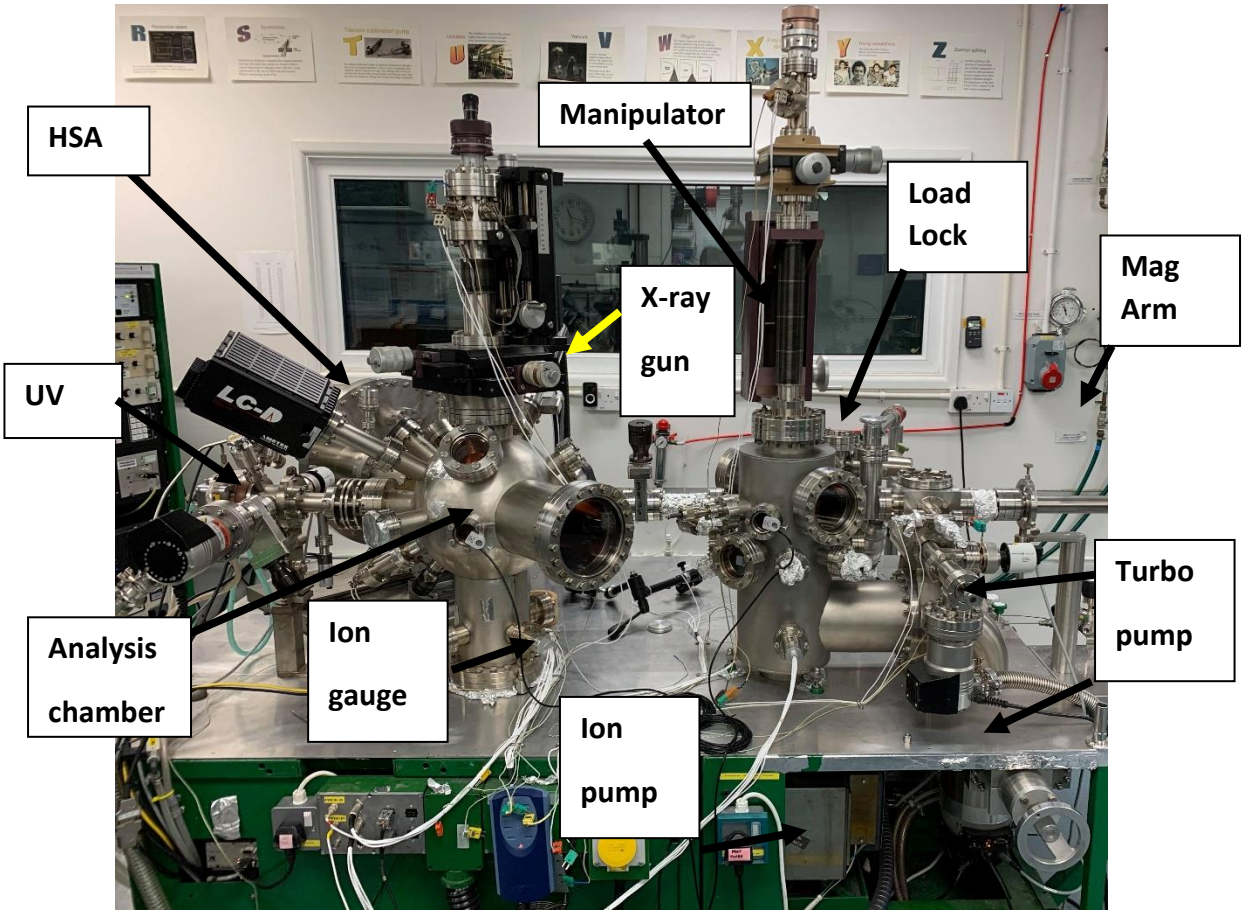

Figure 4.2.1: Diagram of the REES system with specific components labelled which have relevance throughout the rest of this chapter.

Samples if applicable are sonicated in acetone and methanol for 10 minutes and dried using N_2 gas to remove as much leftover solution as possible. They are then attached onto a tantalum faceplate either via spot-welding the metal itself if a foil is used as a substrate or using a tantalum strips or envelope if the sample cannot be spotwelded to the backplate. Figure 4.2.2 shows an example of this faceplate in-situ demonstrating the mounting of samples along with the wings of the sample plate which are required for transferring between chambers. Tantalum is used as it is thermally stable in UHV to high temperature and is unreactive at these temperatures for a lot of standard metals looked at in PES.[4]

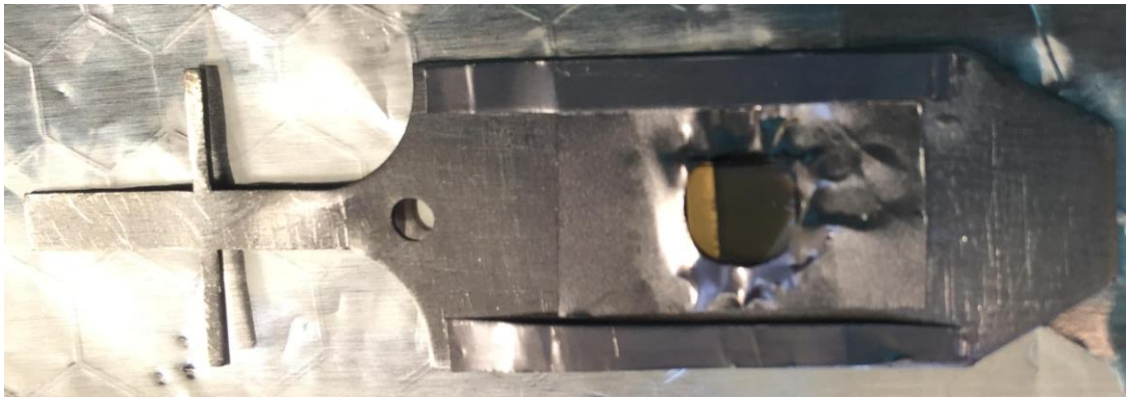

Figure 4.2.2 – Gallium oxide sample mounted onto the tantalum sample plate. The sample is kept in place by a piece of tantalum foil, which is punched and then spot-welded onto the plate, keeping the sample secure whilst maintaining a good open area for X-rays to excite electrons from the surface.

The load-lock is a small volume such that pumping down from atmospheric pressure to $5x10^{-7}$ mbar is made to be as quick as possible. The sample is then transferred from the load-lock into the preparation chamber. The load lock is also set up such that the valve between the rotary pumps and chamber can be controlled along with a leak-valve such that $5x10^{-1}$mbar can be maintained for the controlled evaporation of nano-particle solutions for creating uniform thin films, as shown in Figure 4.2.3.

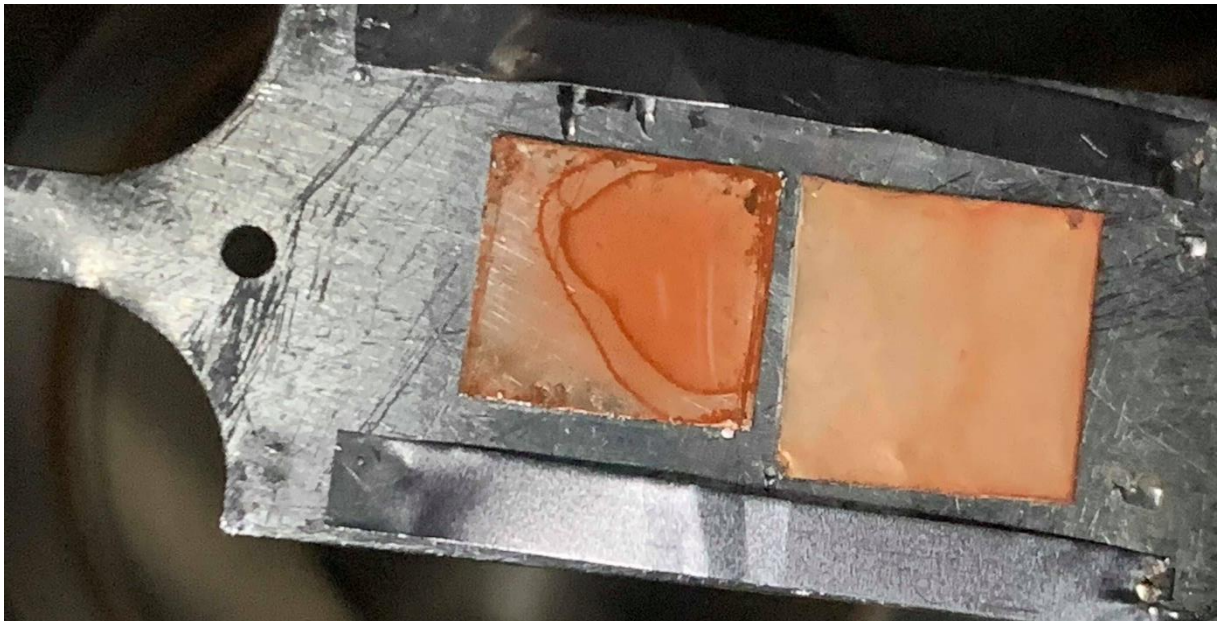

Figure 4.2.3: Image showing two hematite nanoparticle films which were created via drop-casting 3µl and 1µL respectively onto platinum films and then slowly pumping down the load lock to $5x10^{-1}$mbar and maintaining the pressure until all water has evaporated. The larger droplet formed coffee rings due to the 3µL droplet having a larger meniscus, and therefore parts of the droplet evaporating at different rates.

The sample-plate is mounted into magnetic arm via the two wings forming the cross-piece of the faceplate, which clip into the magnetic arm holding it in place. The sample is then transferred into the preparation chamber where it is placed into the heating-stage of the manipulator. Both this chamber and the analysis chamber sit in the $5x10^{-10}$ mbar pressure range to reduce surface contamination which is obtained through "baking" the system at 120°C for several days. This low pressure is maintained by baking the chambers to desorb contaminants sat on the steel walls and use the of titanium sublimination and ion pumps. The sample is then grabbed by the magnetic arm connected to the plasma chamber, from which it can either be transferred into the plasma chamber or the analysis where it will also be placed into a heating stage from which measurements can also be taken.

Samples in the analysis and preparation chambers are heated via a boralectric heater. This heater consists of three layers in total where the outer layers of Pyrolytic Boron Nitride (PBN) ceramic coat a pyrolytic graphite (PG) which current is based through and heats up the sample. PBN is highly un-reactive, has high electrical resistance and thermal conductivity, which allows for it to transfer heat between the PG and sample. Figure 4.2.4 shows the heater and sample holder for the analysis chamber whilst heating a sample, with labelling for the various components.

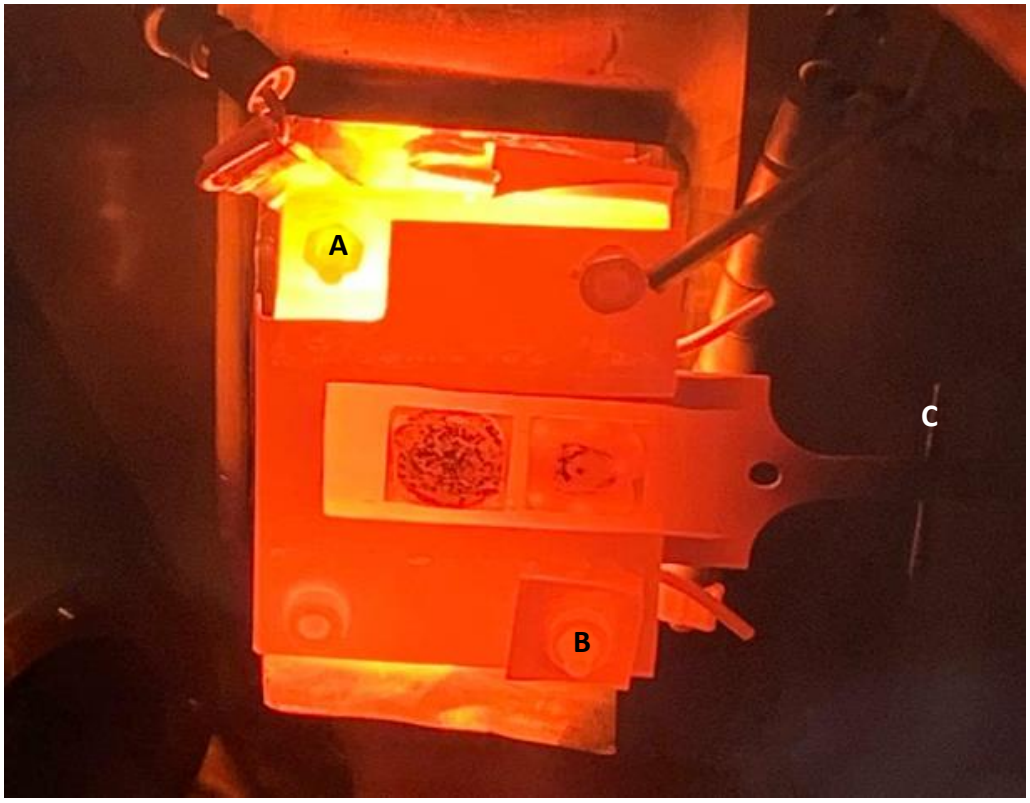

Figure 4.2.4: Boralectric heater annealing a sample at high temperature in the analysis chamber, with the cone of the analyser in the left corner. Current is passed through bolt A to B, where the bolts go through the heater and make contact with the PG centre. C labels the wings which lock the sample plate into the magnetic arm for transferring samples between chambers.

The power-supply for the heaters is a Kenwood PDS60-12 which can either be controlled manually or via a LabVIEW program where custom heating profiles can be created. Precise temperature control via a feedback procedure from the thermocouple of the heater allows for heating cycles which are less than a degree accurate to the programmed temperatures.

For both XPS and UPS measurements, Aberystwyth has a SPECS Phiobos100 hemisphere electron analyser (HSA) which has a design as shown in figure 4.2.5

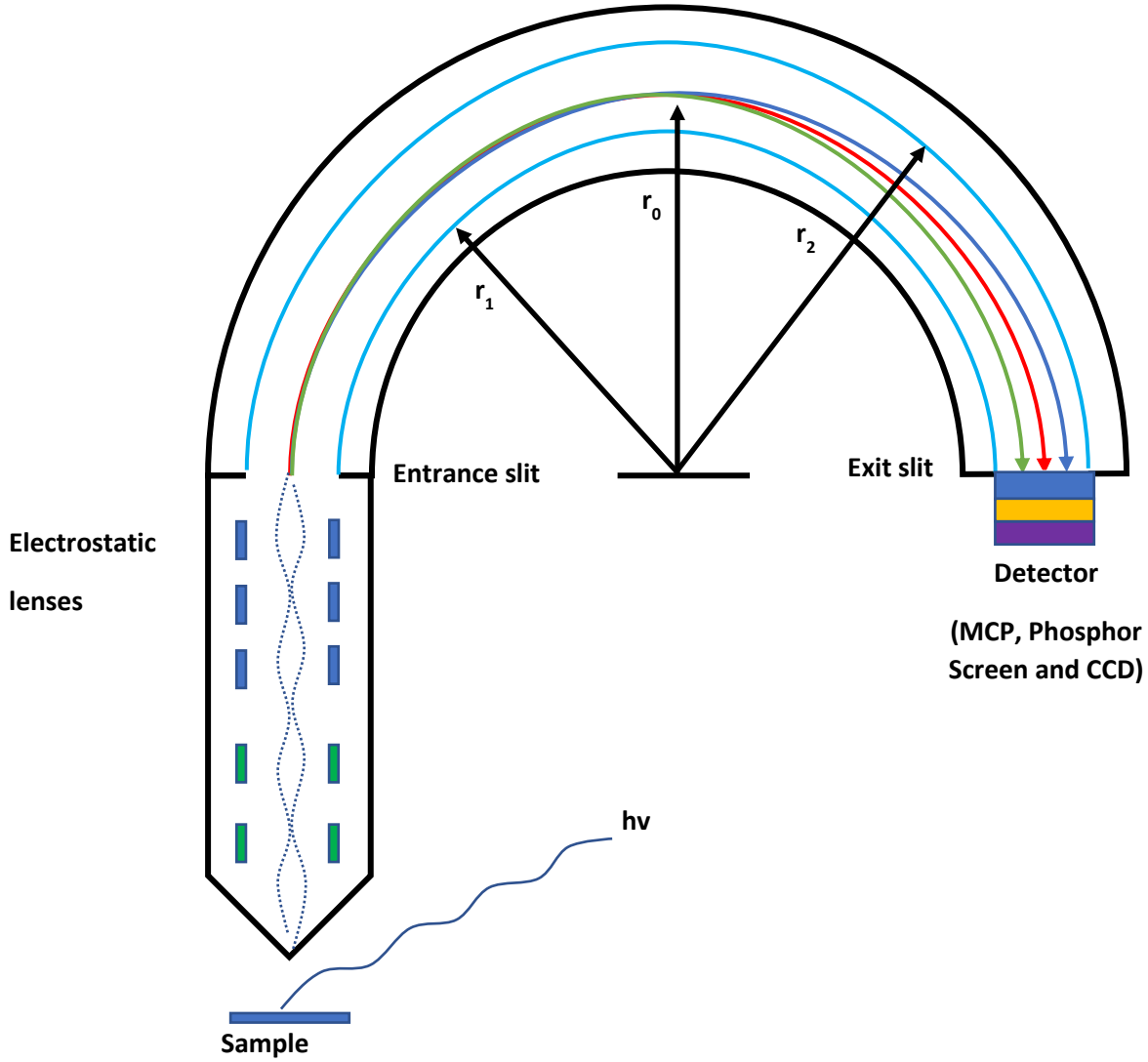

Figure 4.2.5: Diagram of the Phoibos100 analyser used at Aberystwyth university along with the entire detector stack. Labelled the processes and several stages electron travel to from the sample to the detector, and the parameters which define energy resolution.

The 180° circular travel path from the entrance slit to the exit allows for minimal to no distortion of the travel of the electrons. The entrance slits can be opened or closed to enable changes in spatial acceptance of electrons from the sample, closing the slit enables measurements of smaller areas on large samples if patterning for example has been undertaken, however the total number of electrons and therefore signal to noise is reduced. The resolution of the spectra can also be increased by decreasing the voltage between the outer and inner hemispheres, which is defined as altering the pass energy. This focusing of

the electrons to this allows for finer measurement in different path lengths of electrons which allows for better kinetic resolution, but at the cost of rejecting more electrons entering the hemisphere and therefore the intensity. The energy resolution of the spectra can be determined by equation 4.2.1[5]

$$Eq\ 4.2.1 \qquad \Delta E = E_p \left(\frac{r_1 r_2}{2r_0 + \alpha^2} \right)$$

Where r1 and r2 are labelled in figure 4.2.5, r_0 is the mean between the two, α is a constant related to the electrostatic lens system and E_p is the pass energy of the detector which can be altered by the user.

Analysers which operate in this method of collecting XPS spectra are designated as being in fixed analyser transmission (FAT) mode. This is a mode which allows the collection of electrons across large energy ranges by scanning the voltage applied to electrostatic lenses. An alternative method of acquiring data is the use of the snapshot mode, in this setting the lens mode and pass energy are assigned such that an image of the detector is taken which corresponds to the detector channels. The spectrum is given by the intensity of each pixel at the CCD and is therefore limited by the number of channels.

Aberystwyth uses a custom-made multi-channel detector[6,7] for the purpose of increasing the spectral resolution in this snap-shot mode and electrons are detected via several methods when they reach the exit slit of the analyser. Typically, channeltron's were and still are used used for their advantageous lifetime and dynamic range capabilities by altering the voltage across the analyser allowing for energy distributions to be measured. This method however has very low efficiencies as the number of electrons which do not make it past the electron slit, which had to be compensated by either increasing measurement times or reducing resolution.

Current offerings from SPECS with the Phoibos 100 offer MCD-5/9 detectors. These detectors have channel electron multipliers as collectors. Electrons are moved across each collector channel step by step, and each individual electron is counted at every collector, allowing for 5/9 spectra to be recorded simultaneously. The data from each collector is then summed together to obtain a total intensity of electrons for each kinetic energy.

Position sensitive detectors (PSD's) allow for spatially resolved electron counting at the exit slit of the analyser. Although there are four types; discrete channel, coincidence array, charge division and optical image detectors, only the latter has been used and therefore will be discussed.

Optical image detectors are an indirect measurement technique which converts electrons into an image onto a Charge Couple Device (CCD) using a phosphorescent screen. The screen undergoes luminescence when bombarded with electrons creating the image onto the CCD. This configuration has advantages over other methods due to measuring the electrons in two dimensions, such that kinetic energy and angular distribution can be determined. Due to the pixel density being a limiting factor, the pass energy defines the energy resolution and is given by Equation 4.2.2:

$$Eq\ 4.2.2 \qquad \Delta E_k = D\left(\Delta_{pixel}\right)$$

Where D refers to the dispersion in eV/pixel.

The uniqueness of the REES system at Aberystwyth it its ability to conduct these Real-time Electron Spectroscopy (REES) which allows for the measurement in real time via a MCD with 768 calibrated channels connected to a 477-pixel CCD across the energy range which takes an image of the core levels in snapshot mode connected to a Phoibos 100 HSA.[6-8] Each snapshot is saved into the SPECS prodigy software, where the real-time information such as the temperature across the boralectric heater and the pressure readings from the chamber. This means that the final spectra created can be interpreted as an 2D image, where the intensity of the core level at each ΔE_k can be assigned for each scan across the X axis, and the Y axis representing each individual scan from the first till the last. As temperature/pressure readings are also saved for each scan, the Y axis can be defined as the temperature of the snapshot at each variable, and image plots can represent the changes in a core level through changes in temperature.

UV generation for the REES system is from a SPECS UVS300 for the breakdown of helium to produce He(I) photons[9]. X-ray generation for the REES system is a twin-anode which is a pre-vac 40B1 x-ray source which is a non-monochromatic flood gun which works via the heating

of two filaments for thermionic emission of electrons which are accelerated onto the anode at a high voltage (20kV).[10,11] The impact between the electron and the anode then causes X-ray emission, which passes through an Al window and reaches the sample. The x-ray source at Aberystwyth has two anodes, an Mg and Al which produce 1253.6 and 1486.6 eV photons respectively although for this body of work only the Mg anode has been used. The X-ray source is on an linear-drive such that the flux of photons hitting the sample can be maximised, however during REES due to sample's being hot and outgassing the source is taken back slightly from typical measurements due to the risk of coating the window with contaminants. Figure 4.2.6 shows a diagram for a twin-anode X-ray source.

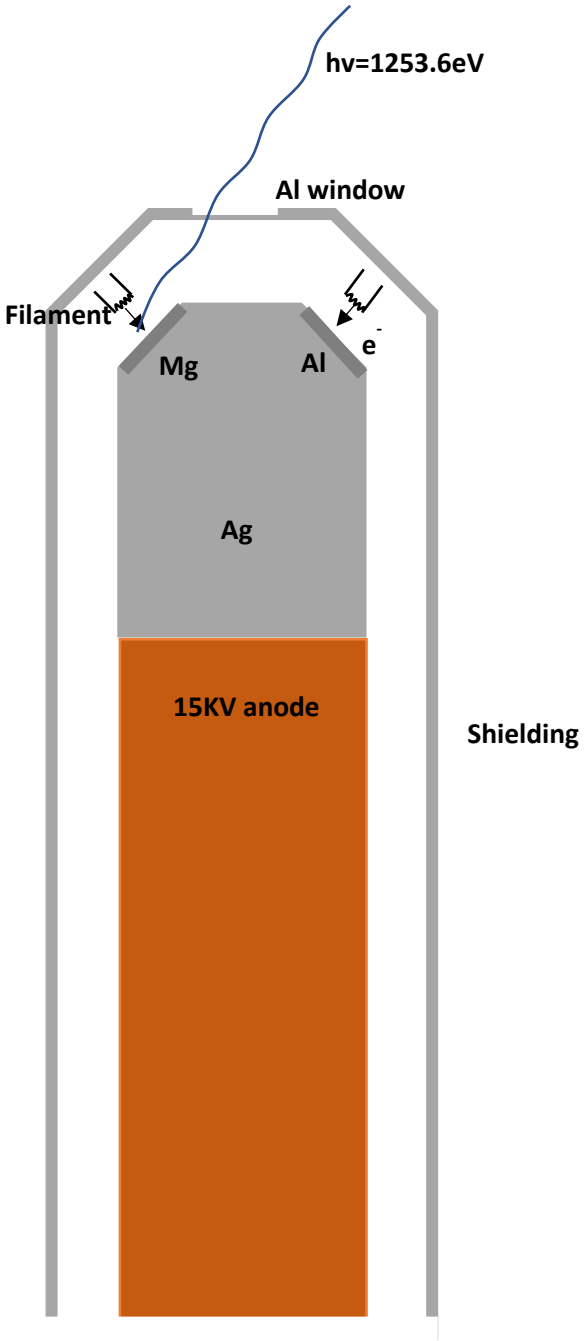

Figure 4.2.6: Diagram of a twin-anode source showing the process of generation of Mg and Al photons via thermionic emission of electrons from a filament to create photons in the respective element films.

4.2.2 Manchester NAP-XPS system and B07 at Diamond Light Source.

Although as previously mentioned that XPS typically takes place at UHV, the advancements in technology have allowed photo-emission measurements of substrates to be taken whilst at Near-Ambient Pressures (NAP) through the use of differential pumping between the sample and the HSA and control measures such that minimum contamination to the rest of the UHV system is controlled. [12]

Manchester University uses a specialised NAP reactor cell by SPECS, which is a locking manipulator which forms a vacuum seal around the Phoibos 150 NAP analyser which is driven onto the HSA by a motorised manipulator. The sample then must be loaded specifically into the NAP chamber, which is then completely isolated for the analysis chamber via this locking mechanism and viton seals. A picture of the entire system with labels is shown in 4.2.7.

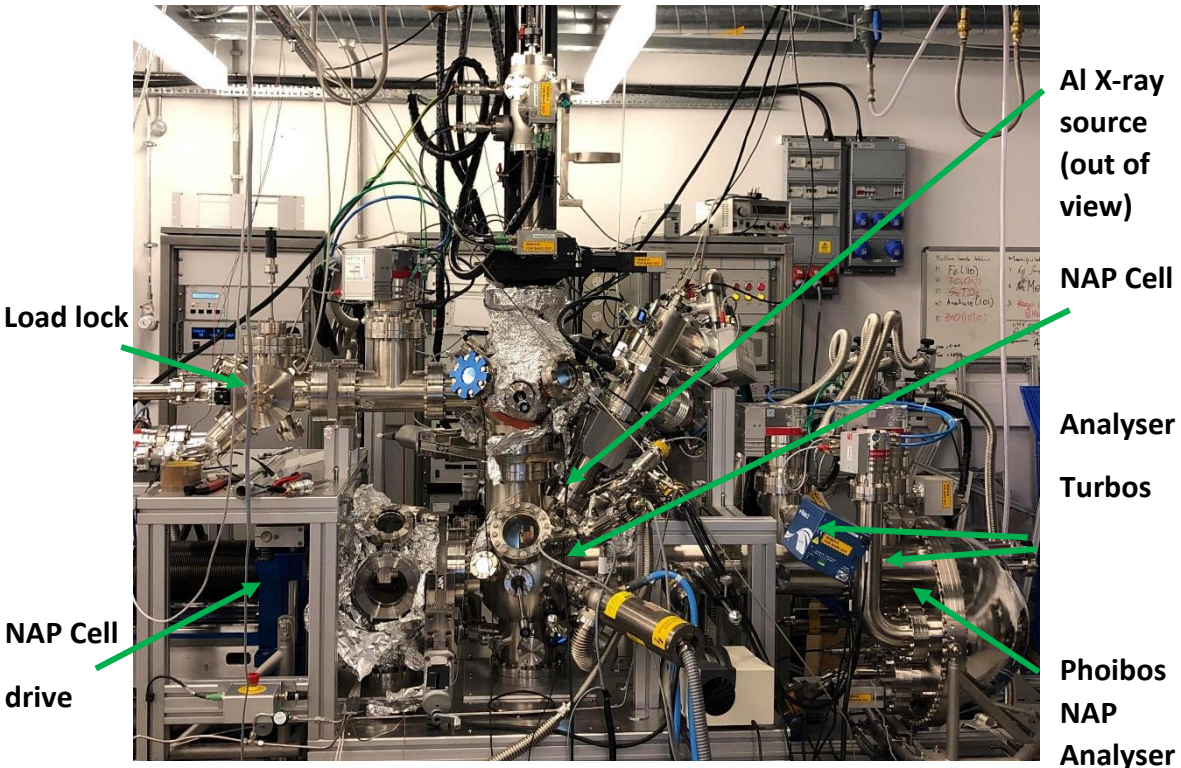

The

Figure 4.2.7: Entire NAP-XPS system at Manchester university, the bottom chamber is a typical Steel chamber where an additional NAP-chamber is driven in by the horizontal manipulator, mounting on the analyser to create a NAP-environmental cell. For more detail see SPEC's specifications.

analyser has a cone of 1µm with an 100µm aperture which is placed just above the sample. As gas is flowed into the sample, the pressure at the sample can be varied and the pressure

ranges are dependent on the flowrate of gases as there is still roughing pumping in the chamber such that over-pressurisation does not occur. At the sample substrate, there may be an effective pressure of 1-2mbar, but near the entrance slit of the analyser the pressure is still in UHV conditions. This differential pumping between the sample and entrance slit is done by sectioning the cone of the analyser into 3 section, each of which has its own dedicated turbo pump. This allows for low vacuum in the first stage, medium vacuum in the 2nd and UHV in the final which is displayed in Figure 4.2.8

Figure 4.2.8: NAP analyser showing the setup in comparison to a regular HSA. The NAP chamber physically attachs itself to the cone of the analyser creating a tight seal such that when gas is flowed in the UHV chamber maintains It's pressure. Differential pumping in different stages is done such that the analyser is kept at UHV such the high voltages required for operation is kept, and allowing for a reduction of inelastic collisions between the surface emitted electrons and the gas phase, such that the distance electrons have to travel through these NAP is minimised.

The heater at Manchester was an e-beam heater which works by applying a current across a filament to produce thermionic electrons. A high voltage bias is then placed between the

sample and filament to accelerate the electrons to the sample plate to create heat via electron bombardment. These near-ambient pressures were controlled through the controlling of a gas flow using a mass flow controller, where a flow rate, in mL/minute could be selected. The pressure in the chamber is a function of the flow rate of gas and a rate of pumping, in the NAP-cell. A flow rate of 0.3mL/min produced an internal pressure of 0.5mbar. Due to the ideal gas law, as temperature of the system increased so did the pressure. For experiments where the internal pressure was to maintain constant the flow rate of the gas had to be controlled via the mass flow controller. Fortunately, at the maximum measurable temperature of 420°C the minimum pressure was around 1mbar. The temperature the NAP chamber can reach whilst dosing is heavily dependent on the gas and pressures used. At high temperature the gas molecules become more energetic, allowing themselves to escape from the viton sealings and escape into the UHV chamber, this was more prominent with H_2 gas as the smaller molecules were able to escape easier. The gas also acts as a coolant for the sample. Whilst this is beneficial for quickly cooling samples via increasing the pressure, which is common issue in normal XPS, this can also inhibit the maximum reachable temperature.

At B07 the same analyser is used, however instead of having an independent NAP-Cell which clamps onto the analyser, the entire chamber is filled with the gas/vapour and is held in the chamber until the experiment is over. Although Manchester uses an monochromated Al-x ray source which is protected by a silicon nitride window, B07 has the advantage of being at a synchrotron and therefore the flux and changing of photon energy can be controlled for more surface sensitive XPS measurements and NEXAFS. Samples are mounted onto a heater stage which is loaded into the chamber which is capable of resistive heating up to above 700°C. Dependent on the setup there is a removable transfer station which has the capabilities for Low Energy Electron Diffraction (LEED) measurements alongside ion sputter guns. The gases available are typically oxygen and hydrogen, with water dosing also available upon request. They use the same Phoibos NAP 150 HSA however controls of the analyser and the photon energy is all conducted using Diamond Light Sources custom software.

Figure 4.2.9 shows the diagram of the B07 branchline at Diamond Light Source. Where Figure 4.2.10 shows the analysis chamber set-up, both images were obtained from diamond light source.

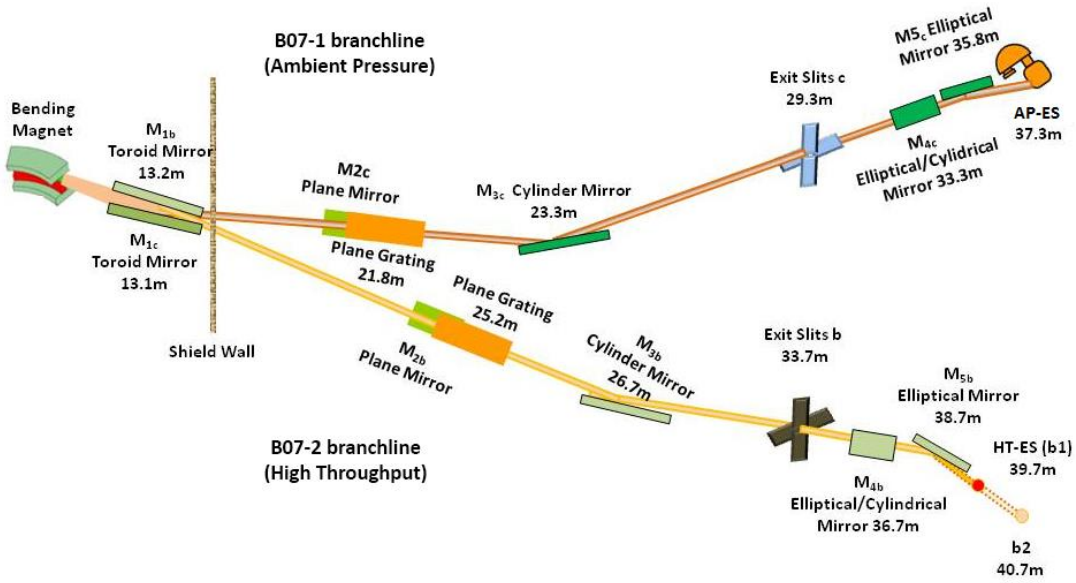

Figure 4.2.9: B07 branchline at diamond light source, where the B07-1 branch is the Ambient pressure system used in this thesis. Image acquired from Diamond Light Source website.[14]

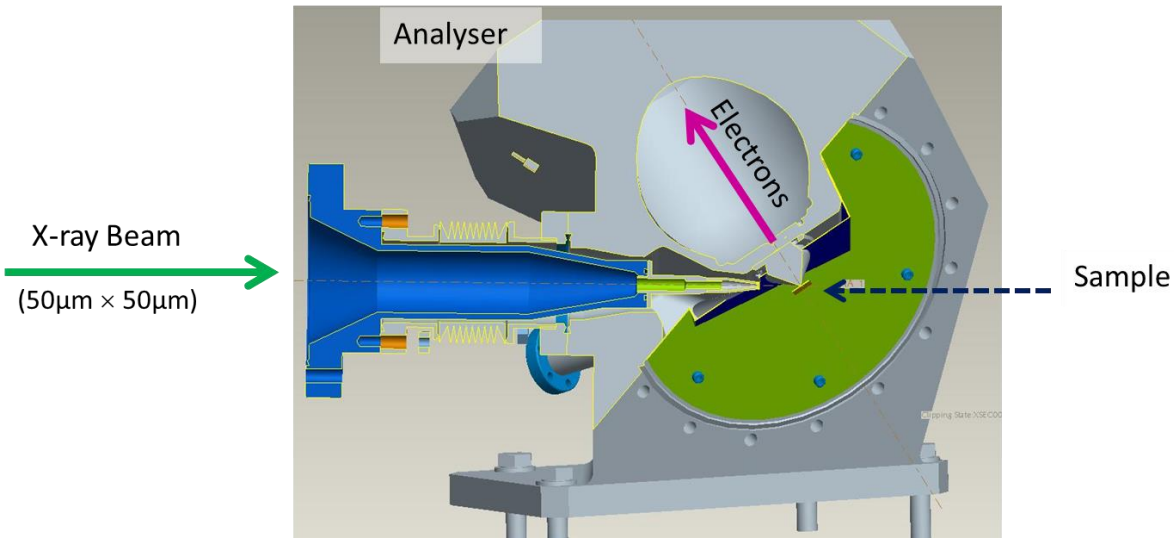

Figure 4.2.10: design set-up of the analyser and chamber at B07. Image acquired from Diamond Light Source website[14]

X-rays for a synchrotron are produced much differently from a standard lab source. Diamond Light Source is a third-generation synchrotron facility where electrons are generated via an electron gun at 90 KeV[15]. These electrons are then accelerated by a linear accelerator up to 3 GeV, where they are introduced into a storage ring with a circumference over 560 m. At these energies the electrons are travelling at close to the speed of light and have a defined travel path controlled by bending magnets. Due to deflections from the bending magnets electrons consistently lose energy, so all 3rd generation synchrotrons have booster-rings for

continuous top ups such that the total flux remains consistent. All energy lost from the bending and changes of electron velocity create photons via an energy loss process. These can be forced using wigglers and undulators. Wigglers are similar to bending magnets in that they deflect or bend electrons and photons in a much broader range then undulators, however the process results in a lot less flux then undulators, which can be beneficial if looking at unstable organic molecules which would suffer from degradation otherwise.

Figure 4.2.11 shows the design of the a typical 3rd generation storage ring like at Diamond Light Source:

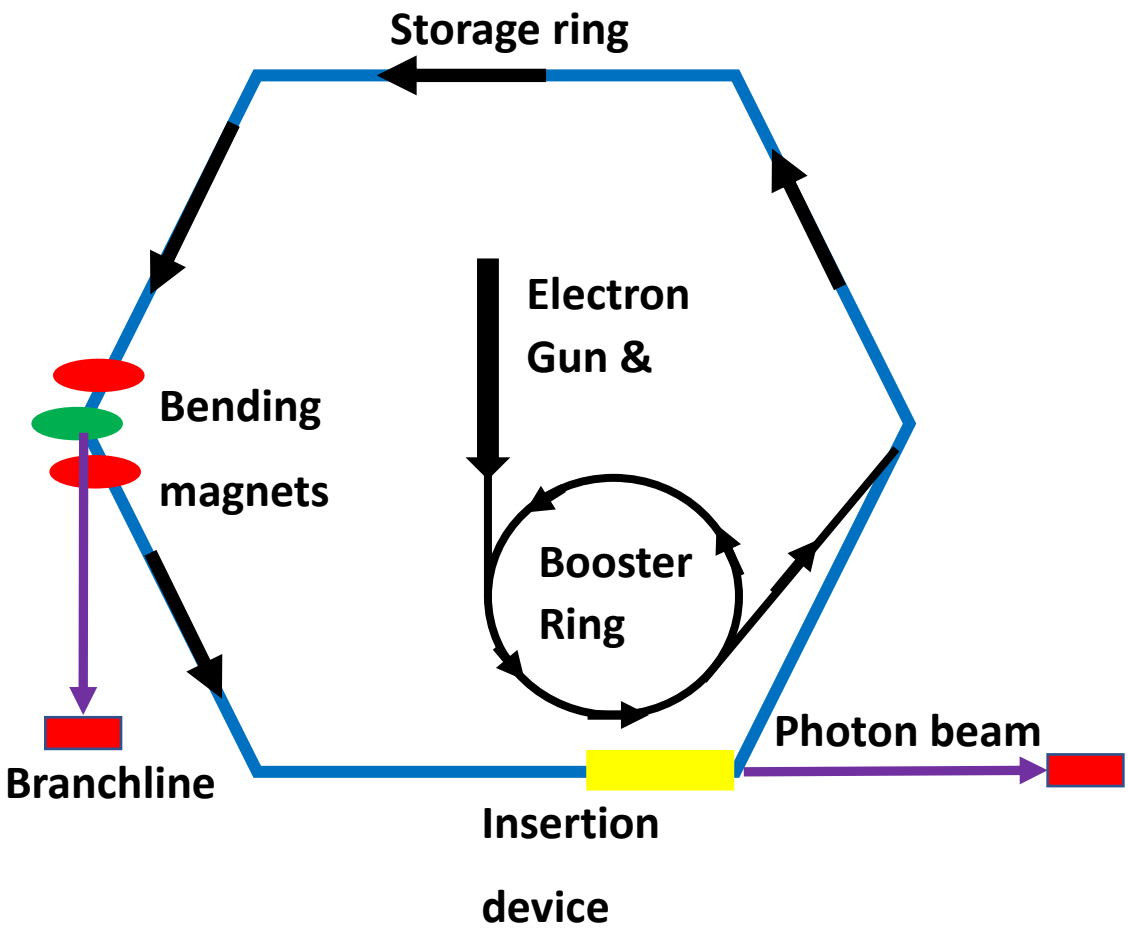

Figure 4.2.11 Shows the design set-up for the storage ring at diamond light source. The flow of electrons is designated by black arrows, and photons with purple.

B07 has the initial B at the beginning because it is a branch line which gathers photons from changes in electron velocity near a bending magnet. For the photons to reach the branchline from the storage ring a selection of precisely tuned mirrors and lenses which are hit at grazing

incidence as x-rays have a small reflection angle. The mirrors are generally configured via a Kirkpatrick-Baez configuration for calibration in vertical and horizontal directions[16].

X-rays generated via this method however are not monochromatic, which for XPS and NEXAFS experiments knowledge of the exact photon energy is essential. So upon reaching the start of the branchline grating and crystal monochromators work together to produce a monochromatic source. The grating monochromator acts much like the reflection gratings in crystals of visible light, where they are tuned to let a much narrower range of photons through. The crystal monochromator then uses Braggs diffraction to select photons of a specific energy. Even at a bending magnet branch line, the flux of photons is orders of magnitude more intense than a generic lab x-ray source, this allows for the use of lower pass energies and measurement of core electrons at lower kinetic energies. This results in spectra of a much higher surface sensitivity and better energy resolution. B07 has the capabilities of using energy ranges from 250-2800eV.

The flow rate of gases into the chamber was controlled via a needle valve and measured using a capacitance monometer, this was less precise then in Manchester in terms of a consistent pressure. when increasing temperature on the sample, it meant manually trying to fine tune the needle valve to maintain a consistent pressure.

Samples were mounted onto a SURFACE substrate manipulator which allowed for motorised control of the sample in XYZ position in-situ. This allowed for fine control of the position such that 1µm steps could be taken. Samples were heated via a resistive heater with a molybdenum surface maintaining contact with the substrates.

All PES data was analysed in IGOR using the XPST using a Psuedo-Voigt profile[17]. The individual fitting parameters will be discussed at the start of each chapter, as the G/L ratio's, peak widths will vary depending on the X-ray source used. For real-time core level snapshots each individual snapshot is fit with a certain criteria of being allowed a small width/G/L ratio range as both parameters will change whilst the sample is hot. The individual peaks, envelope and raw data will be shown in each spectrum.

4.3 Supplementary techniques

4.3.1 Density functional Theory Calculations

DFT calculations were done as a complimentary technique for comparisons to XPS and NEXAFS measurements to better understand the processes behind the modification of chemical species after treating them.

Calculations were conducted in two different ways. Small atom systems (<200atoms) and test calculations of larger atomic systems (200-600 atoms) were conducted on a custom-built PC, which had an intel-5960X 8-core processor and 32gb of RAM. Calculations were limited to these small atom size systems on this system due to bandwidth limitations in the RAM and time constraints. 300 atom systems can easily use upward of 32gb of RAM depending on how much information from the SCF and WFC, and although highly clocked the 8 core-16 thread processor will struggle to complete a 300 atomic system in less than a week unless certain parameters (such as energy-cutoff, mixing parameters, diagonalization, zeroing internal energy, etc) allow for trade-off reducing calculation time and reducing calculation accuracy. For calculations of large sizes HPC Wales was used and 2 nodes were requested allowing for the use of 40 cores and 192gb of RAM.

Quantum-espresso software was used for all relaxation and molecular-dynamics calculations, using PBE pseudo-potentials, and Gaussian09 was used for calculating vibrational modes of molecules using a B3LYP pseudo-potential with a 6.31g basis set[18-21].

4.3.2 Raman Spectroscopy

A Horiba LABRAM HR Raman spectrometer was used for the analysis of all samples using Raman with a 532nm 100mw laser. The laser was generally restricted to 1% power for nanodiamonds and 5FU samples as the samples will burn from the heat. Lower gratings were used for increased intensity at the cost of some resolution. All Raman spectra are taken as maps across 50x50µm squares, where the sample has been focused in on using an 100x/0.9 NA Mplan microscope objective. The maps are gathered by the programming of the software to move the sample in X and Y directions using a motorised sample stage, where samples start

at 0x0, go across to 0x50 and then proceed onto 50x50, where the total number of scans is depending on the step size chosen. 10x10µm squares were chosen such that a total of 25 Raman spectra are gathered which can be summed together or analysed individually. All Raman spectra was gathered at ambient temperatures as there is little resolution gains from cooling.

All data is then processed in Origin, where only backgrounds are set to linear such that the comparisons of several spectra at the same time can be conducted. The 532nm laser was used for two main reasons. Firstly, it the most powerful laser we have in the lab by a considerable margin (50x stronger then pre-installed 632nm laser). Secondly, for nanodiamonds other lasers such as 785nm will not detect the D band with good resolution. Literature also is predominantly heavily focused on the use of 532nm for organic molecules and carbon-based materials, making comparisons to literature easier. We unfortunately did not have access to lower wavelengths for use for the nanodiamonds which would have been complimentary alongside 532nm[22-24].

4.3.3 Dynamic Light scattering

DLS measurements were taken using a Malvern Zetasizer Nano ZSP. Refractive index for both nanodiamonds and 5FU was taken from literature, and measurements were taken at 25°C using a 10mW 633nm laser. Measurements were taken 3 times and averages of all spectra are displayed, however due to the nature of DLS measurements the difference between the individual 3 scans for each solution was nearly identical. There is potential for the measurement of Zeta potential which is important for nanodiamonds however due to time constraints this data was not obtained for any samples.

4.3.4 Photoluminescence and Confocal Microscopy

Photoluminescence data for the DNDs was collected using the HeLiOS[25] chamber at Aberystwyth, where measurements were taken at both 14 and 273K. However, there was no discernible differences in features in the spectra. All samples were illuminated using a 325nm UV flood source. Samples were mounted into a UHV chamber where the sample was then sitting perpendicular to a 50x optical objective which was connected via a fibre optic to a Horiba Labram HR spectrometer. Data was then plotted in Origin with the original raw data to give a genuine representation of the collected data. Hyperspectral Imaging was taken at a

series of colour ranges to analyse the difference between the 5FU/DND PL emission for the mixed solutions.

Confocal Microscopy was conducted using a Leica TCS SP8 HyVolution 2 super-resolution Laser Confocal Scanning Microscope. Although there is a large range of laser sources for photoluminescence, a 593nm laser was used as it was close to the absorption peak of NV^- centres whilst not causing PL for the bulk ND's. The images produced were correlated from 4 images taken in different spectral ranges and the final image is a focus on the regions which only exhibited a signal in the 600-660nm range, such that it focused on the NV^- peak in comparison to the rest of the PL spectra. Multiple regions were taken and for reference images were also collected for a variety of different excitation energies but provide no extra information when compared to the presented data so have been omitted.

References:

[1] - H. Hertz, Ueber einen Einfluss des ultravioletten Lichtes auf die electrische Entladung. Annalen der Physik, vol. 267, pp. 983-1000. 1887.

[2] - D. M. S. Hoffman, Bawa; Thomas, John H., Handbook of vacuum science and technology. Elsevier Science. 1998.

[3] - W.Steckelmacher, Modern techniques of surface science, 2nd edition," Vacuum, vol. 47, p. 95. 1996

[4] - Surface and Interface Science, Volumes 1 and 2. Klaus Wandelt John Wiley & Sons. April 2012

[5] - Hadjarab, F.; J.L. Erskine. Image properties of the hemispherical analyzer applied to multichannel energy detection. Journal of Electron Spectroscopy and Related Phenomena. Vol36 (3): 227. 1985. doi:10.1016/0368-2048(85)80021-9.

[6] - LANGSTAFF, D. P. & CHASE, T. A multichannel detector array with 768 pixels developed for electron spectroscopy. Nucl. Instrum. Methods Phys. Res. A, Accel. Spectrom. Detect. Assoc. Vol 573 (1–2), P169–171. 2007.

[7] - DP Langstaff, OR Roberts, GT Williams, DA Evans. A system for real-time in situ photoelectron spectroscopy. Diamond Light Source Proceedings. Cambridge University Press. October 2010.

[8] – Phoibos HSA: https://www.specs-group.com/nc/specs/productseries/detail/phoibos-100/

[9] – UV source https://www.specs-group.com/nc/specs/products/detail/uvs-300/

[10] – Twin-anode x-ray source https://www.henniker-scientific.com/products/instruments/light-sources/x-ray-source

[11] - Halmshaw R. (1995) X-ray sources. In: Industrial Radiology. Non-Destructive Evaluation Series, vol 1. Springer, Dordrecht

[12] - Salmeron, M.; Schlögl, R. Ambient pressure photoelectron spectros-copy: A new tool for surface science and nanotechnology. Surf. Sci. Rep. Vol63. P169-199. 2008.

[13] - MIN LIU, LEYING Xu, XUZHI LIN. Heating Effect of Electron Beam Bombardment. SCANNING Vol. 16, P1-5. 1994.

[14] – B07 branchline at Diamond Light Source: https://www.diamond.ac.uk/Instruments/Structures-and-Surfaces/B07.html

[15] - Donald H Bilderback, Pascal Elleaume and Edgar Weckert. Review of third and next generation synchrotron light sources. Journal of Physics B: Atomic, Molecular and Optical Physics. Vol 38. April 2005.

[16] - YOSHIO SUZUKI AND FUMIHIKO UCHIDA. X-RAY FOCUSING WITH ELLIPTICAL KIRKPATRICK-BAEZ MIRROR SYSTEM. THE JAPAN SOCIETY OF APPLIED PHYSICS. 1991.
[17] – XPS TOOLS - HTTPS://WWW.WAVEMETRICS.COM/PROJECT/XPSTOOLS
[18] - P. GIANNOZZI ET AL. QUANTUM ESPRESSO- AN AB-INITIO MODELLING PACKAGE.J.PHYS.:CONDENS.MATTER 21, 395502 (2009) HTTP://DX.DOI.ORG/10.1088/0953-8984/21/39/395502
[19]- P GIANNOZZI, ET AL. , ADVANCED CAPABILITIES FOR MATERIALS MODELLING WITH QUANTUM ESPRESSO J.PHYS.:CONDENS.MATTER 29, 465901. 2017
[20] - GAUSSIAN 09, REVISION A.02, ET AL. GAUSSIAN, INC., WALLINGFORD CT, 2016.
[21] - NARBE MARDIROSSIAN & MARTIN HEAD-GORDON (2017) THIRTY YEARS OF DENSITY FUNCTIONAL THEORY IN COMPUTATIONAL CHEMISTRY: AN OVERVIEW AND EXTENSIVE ASSESSMENT OF 200 DENSITY FUNCTIONALS, MOLECULAR PHYSICS, 115:19, 2315-2372, DOI: 10.1080/00268976.2017.1333644.
[22] – PASCAL PUECH, MARIEM KANDARA ET AL. ANALYZING THE RAMAN SPECTRA OF GRAPHENIC CARBON MATERIALS FROM KEROGENS TO NANOTUBES: WHAT TYPE OF INFORMATION CAN BE EXTRACTED FROM DEFECT BANDS. JOURNAL OF CARBON RESEARCH. NOVEMBER 2019.
[23] – VITALY I. KOREPANOV ET AL. CARBON STRUCTURE IN NANODIAMONDS ELUCIDATED FROM RAMAN SPECTROSCOPY. CARBON VOL 121. JUNE 2017. PG 322-329.
[24] – ROLAND HAUBNER. MORITZ RUDIGIER. RAMAN CHARACTERISATION OF DIAMOND COATINGS USING DIFFERENT LASER WAVELENGTHS. PHYSICS PROCEDIA 46. P71-78. 2013.
[25] – RACHEL CROSS. OPTICAL SPECTROSCOPY INSTRUMENTATION FOR THE CHARACTERISATION OF WIDE BAND GAP MATERIALS. PHD THESES. JUNE 2015. HTTP://HDL.HANDLE.NET/2160/29790.

Chapter 5 – Oxidation of (001) and (111) diamond surfaces.

The ideal method of oxidation for diamond surfaces is highly debated by various groups across the world. Several groups insist that acid treatments provide the cleanest surface as a starting point before any functionalisation should occur. Some groups believe that the acid treatment of the diamond causes some functionalisation of the surface that will inhibit later surface treatments. With NAP-XPS becoming more readily available, the ability to measure the oxidation and hydrogenation of diamond surface using high temperature anneals in gas and water dosing is a possibility. This chapter will show through various methods that the oxidation state of diamond surfaces is heavily dependent on the preparation technique.

Quantum molecular dynamic calculations on a purely ketone terminated diamond surface were conducted for analysis on the surface stability without ether bridge sites. The chemical species on diamond surfaces were analysed when (001)/(111):H diamonds are oxidised using three different methods: An acid etch using boiling sulphuric acid and potassium nitrate; oxidation in 1mbar of pure oxygen; and introduction of H_2O to a bare surface. The effects of these oxidation methods are studied with comparison to residual surface sp^2, and whether one can alter the initial oxidation state. This was tested by annealing an acid etched diamond in pure oxygen. XPS and NEXAFS spectra deduce stoichiometry differences between the method of oxidation which can produce altering purity and oxygen species, which for device fabrication can have detrimental effects on the desired bandgap.

These experiments were conducted on the NAP-XPS systems at Manchester and the B07 beamline at Diamond Light Source. A monochromated Al X-ray source was used at Manchester, and at B07 unless otherwise stated a consistent photon energy of 840eV was used for optimal surface sensitivity whilst maintaining high signal. The available range of photons at B07 was 250-2800eV.

For data from B07 all core levels were fit with a pseudo-Voigt profile with a 0.35 G/L ratio, with the peak width of the C 1s set to 0.9 and the O 1s peak set to 1.7.

5.1 Results

5.1.1 DFT calculations of Diamond (001):O surface termination.

Figure 5.1.1 shows the initial slab of (001) diamond, which has a purely ketone (C=O) termination which was set to run at 300K (RT) with large amounts of oxygen for a system of 364 atoms. Only the surface oxygen and top 4 layers of carbon were left with freedom, and the bottom 4 layers were constrained to their positions to simulate a bulk material. The marked region shows the central area of the slab where Figure 5.1.2 shows out-takes from the slab calculation where defects/processes occurred, which happened centrally in the slab circled in the blue region. The entire unit cell underwent considerable changes however due to specific parameters in the calculation the most strain in the crystal ended up being localised, whereas for a pure infinite slab these strain-sites would be more random in nature.

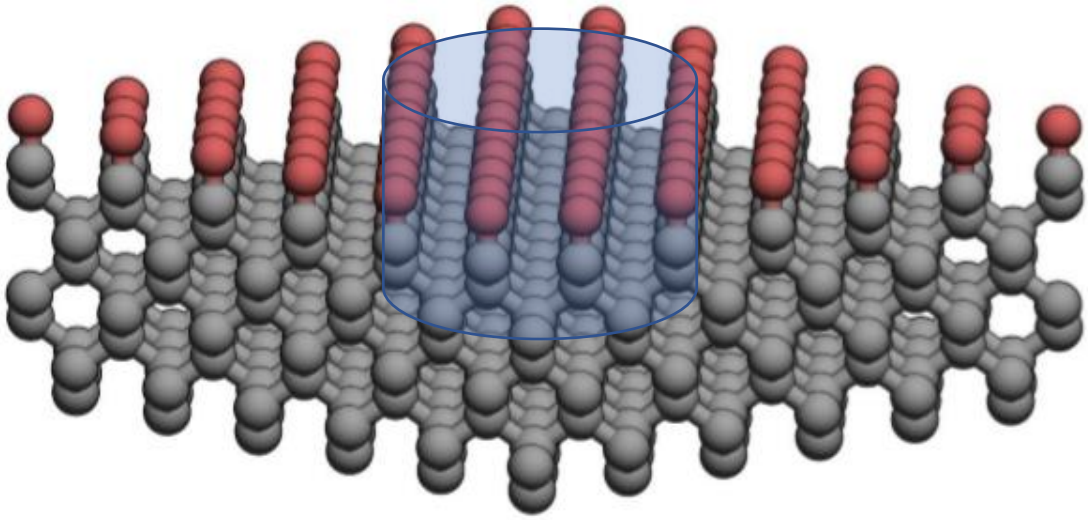

Figure 5.1.1 A single-crystal diamond of (001) diamond consisting of a purely ketonic surface. This is the calculation at a point where t=0. The region in the cylindrical area is the point which will be discussed further for small unit cells. This cell was then built upon to reach the figure above, where the MD produced a stable structure

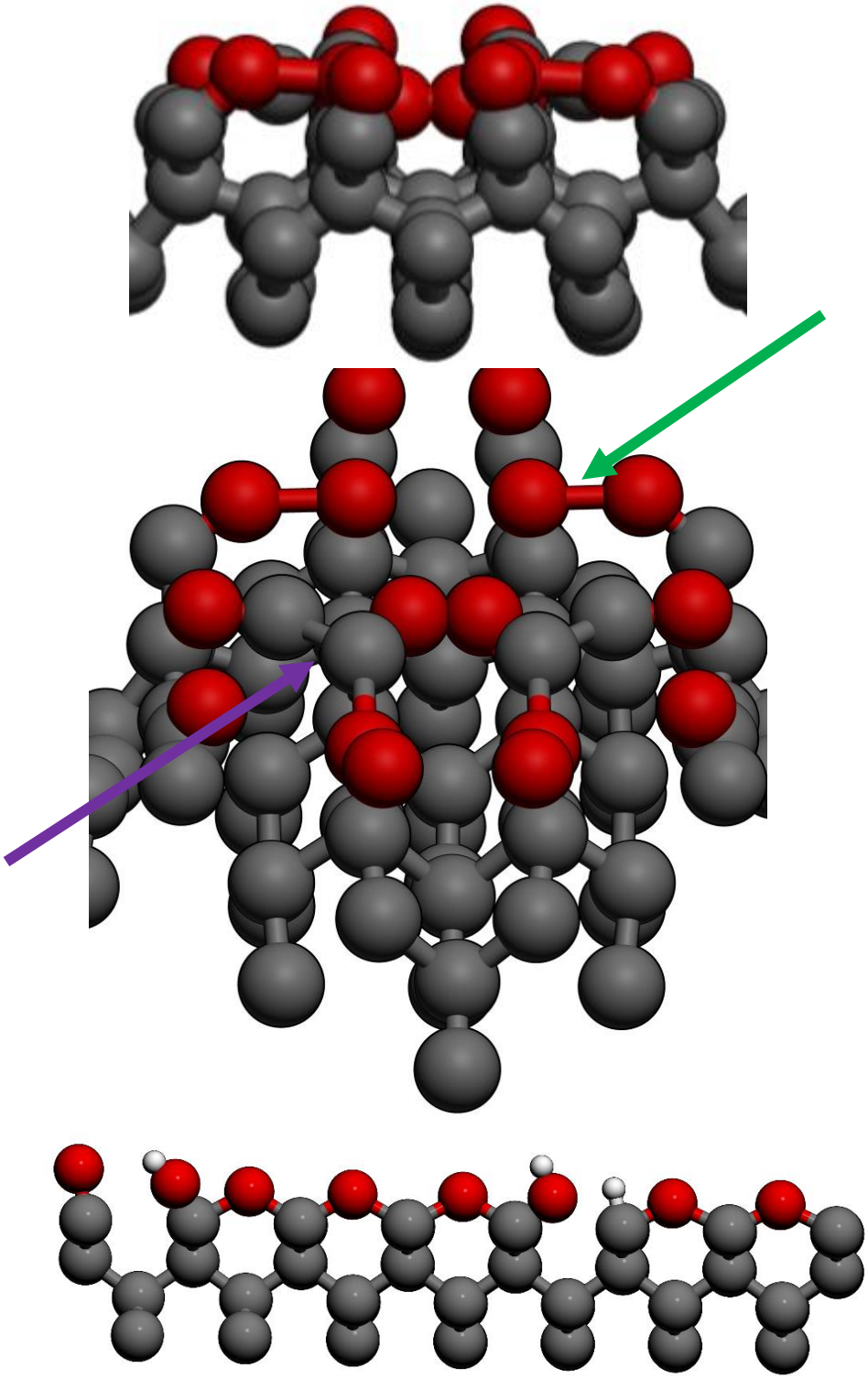

Figure 5.1.2: The centre of the slab at a t=30ps, some of the upper surface carbon atoms have started to form (2x1) reconstructions, labelled with the purple arrow. The Green arrow demonstrates the ketones bonding together to form a C-O-O-C bond. The bottom model is taken from the full slab calculation. Modelled in Quantum Espresso.

5.1.2 – oxidation and modification of (001) diamond using acid and pure oxygen

Hydrogen terminated diamonds were produced using a hydrogen plasma to hydrogenate the surfaces. The diamonds were then treated either using an acid treatment of sulfuric acid with potassium nitrate or annealed in pure hydrogen to remove surface contaminants and obtain the two comparative starting surface terminations. Both samples were annealed in 1 mbar of oxygen between 100-400°C with measurements taken at each step. Core level C 1s and O 1s scans were taken before and after each treatment such that comparisons could be made. Figure 5.1.3 shows the effect annealing in a hydrogen atmosphere for the removal of surface oxygen.

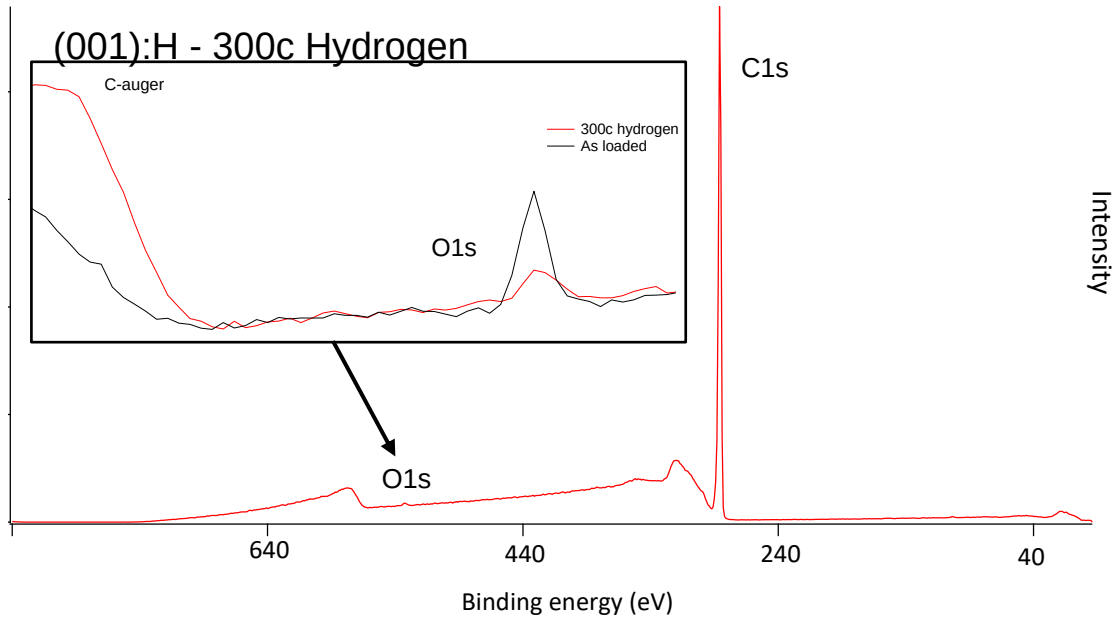

Figure 5.1.3: The effects of annealing an H:terminated (001) diamond in hydrogen at 300°C, the original signal related to having the equivalent of 0.2ML of oxygen on the surface, after the hydrogen anneal a surface coverage of <0.05ML was achieved.

Figure 5.1.4 shows the AFM of a polished diamond surface which underwent several acid etches, showing that the acid etch forms preferential pits in the surface where polishing marks were left, causing severe jagged areas in specific locations causing pits 10nm deep across several microns.

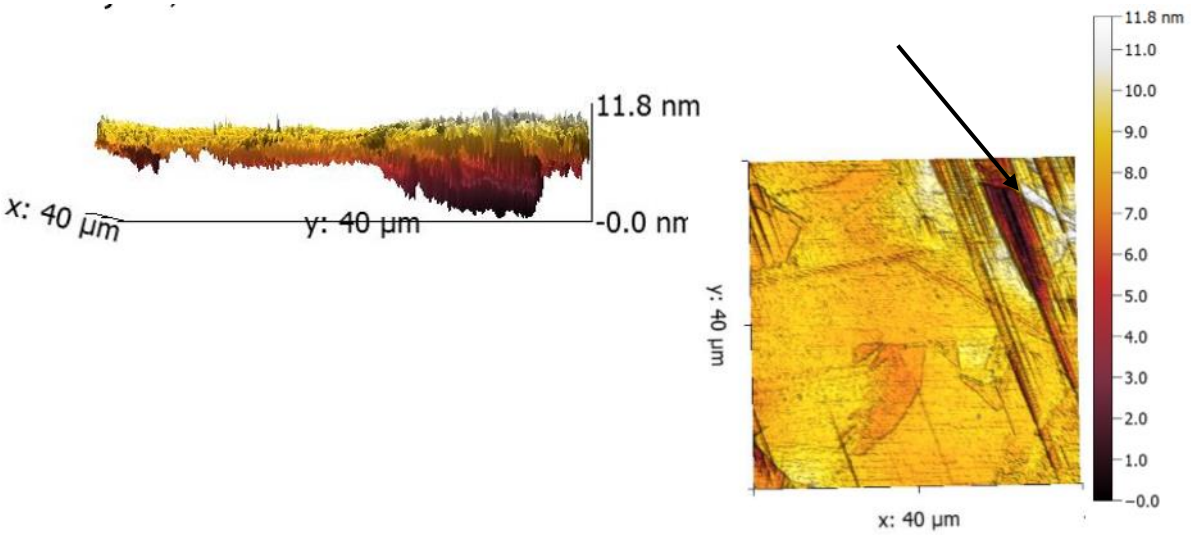

Figure 5.1.4: AFM of a diamond which has undergone several acid etches, due to the nature of the boiling sulphuric acid removing the surface carbon atoms, where there is there pre-existing defects (such as polishing lines) this causes these pits to increase in depth, as evidenced by the 10+nm pit in the top right corner, denoted by the black arrow.

Figure 5.1.5 show the O 1s for the (001) diamond for two treatments; an acid etched diamond after a 350°C anneal in UHV, and a hydrogen terminated diamond where it has undergone oxidation under O_2 for 10 minutes at 100°C.

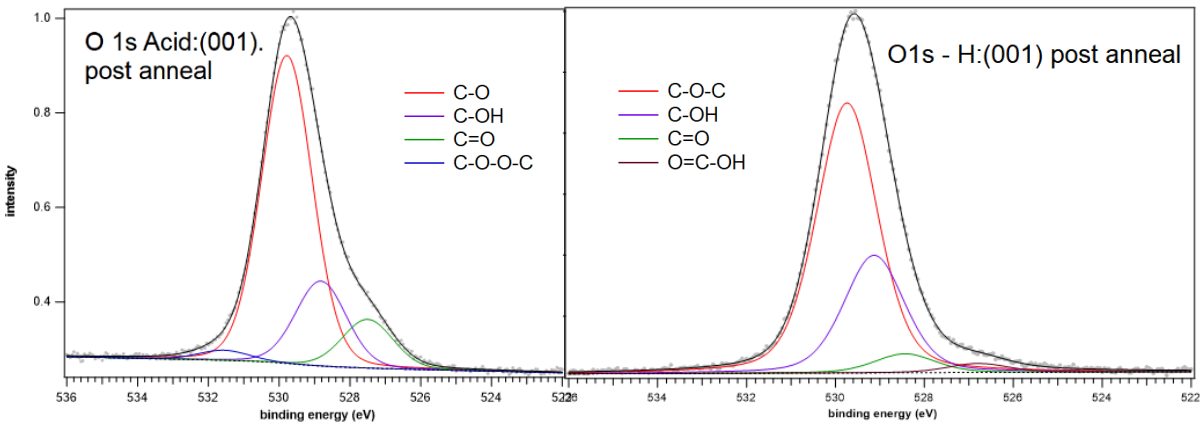

Figure 5.1.5: The difference between the acid etched diamond which has undergone a 350°C anneal to desorb surface contaminants, the hydrogen terminated diamond shows a carboxylic acid group at the lower binding energy side, this would suggest there is still residual sp^2on the surface that annealing in hydrogen at 300°C and oxygen at low temperatures is incapable of removing. Despite this, predominantly the oxygen formation at these low temperature's favours C-O-C.

Figures 5.1.6 shows the O 1s spectra for acid-etched diamond annealed in 1mbar of O_2 at 400 °C for 200 minutes, and a hydrogen terminated diamond after it has been annealed in 1 mbar of O_2 at 400 °C for 200 minutes.

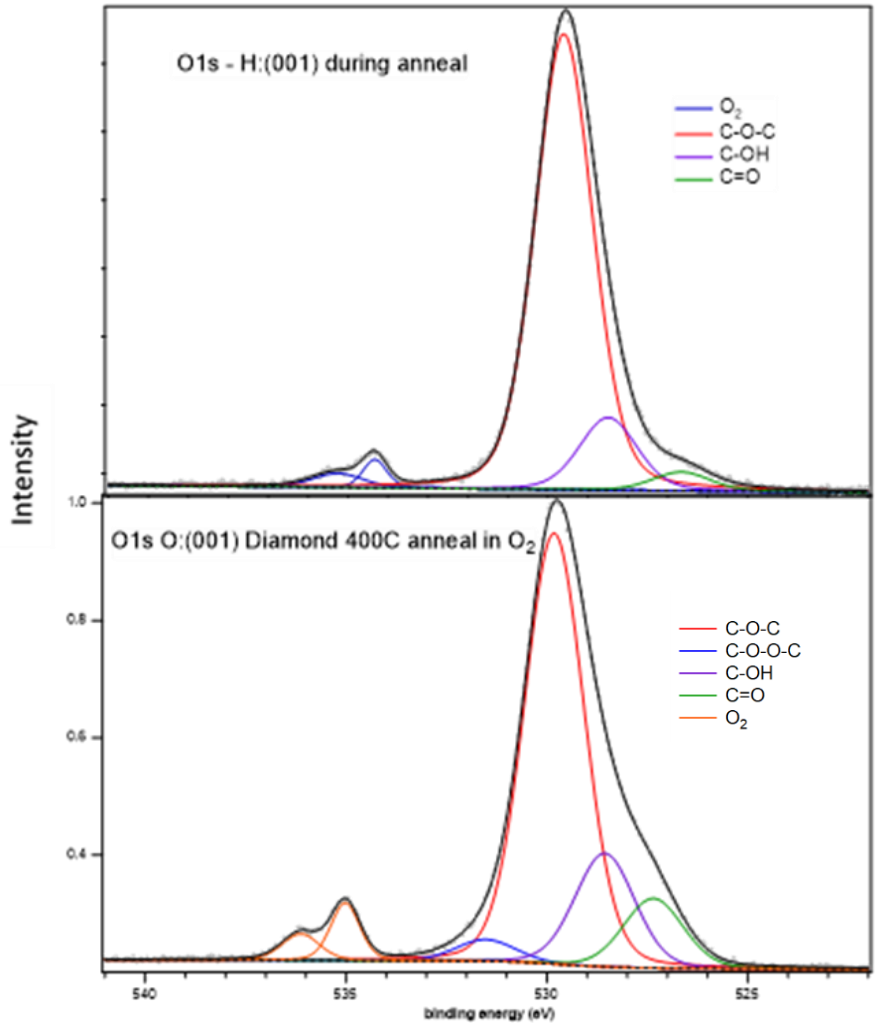

Figure 5.1.6: The O 1s comparison between an H-terminated diamond which is annealed in pure O_2 at 400°C, and an acid etched diamond which is then annealed in O_2 at 400°C, the acid etched diamond has a much lower ether to ketone ratio and show's peroxide formation whereas the pure oxygen treatment does not.

Figure 5.1.7 shows the results of various DFT calculations which proceeds to find the minimum energy state for an (001) surface purely consisting of a ketone surface, this indicates that the peroxide formation is a precursor to a reconstruction into a (2x1) surface consisting of C-O* functional groups which would likely form OH groups if H was present.

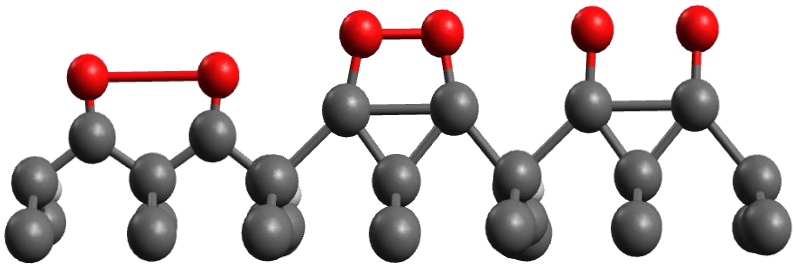

Figure 5.1.7: From left to right, the optimisation path for the diamond (001) surface to obtain the minimum energy state, initially ketone groups will bind together forming peroxide surface groups, due to the peroxide group bond length being too short for a (1x1) surface, adjacent carbon atoms then reconstruct. The peroxide bond is then a less stable surface termination due to the close proximity of the oxygen atoms to each other than a C-O, therefore the O-O bond breaks.*

Figure 5.1.8 shows the changes in the C 1s of the acid etched O-terminated (001) diamond as it's being annealed at various temperatures from 100°C to 400°C in various stages during oxidation.

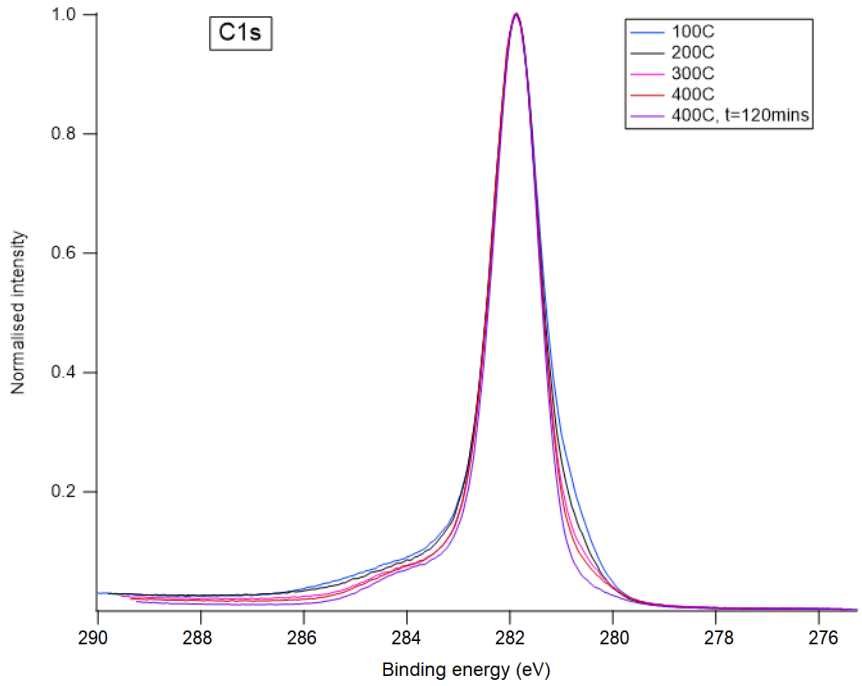

Figure 5.1.8: C 1s of the O:terminated (001) diamond whilst it is undergoing an annealing cycle in 1 mbar of O_2 at various temperatures. In the O 1s we can see very little difference, however the low binding energy side of the C 1s suggests that it takes a considerable time under hot-oxygen conditions for the complete removal of any sp^2 carbon.

5.1.3 Modification of (111) O:Diamond using pure oxygen

Figure 5.1.9 shows the O 1s for a (111) oxygen terminated diamond after it has been annealed in 1mbar of O_2 for 1 hour at 300°C, due to the surface only having one free electron, there must be surface sp^2. A diagram how this can occur is shown in Figure 5.1.10 other than (2x1) reconstructions of the (111) surface.

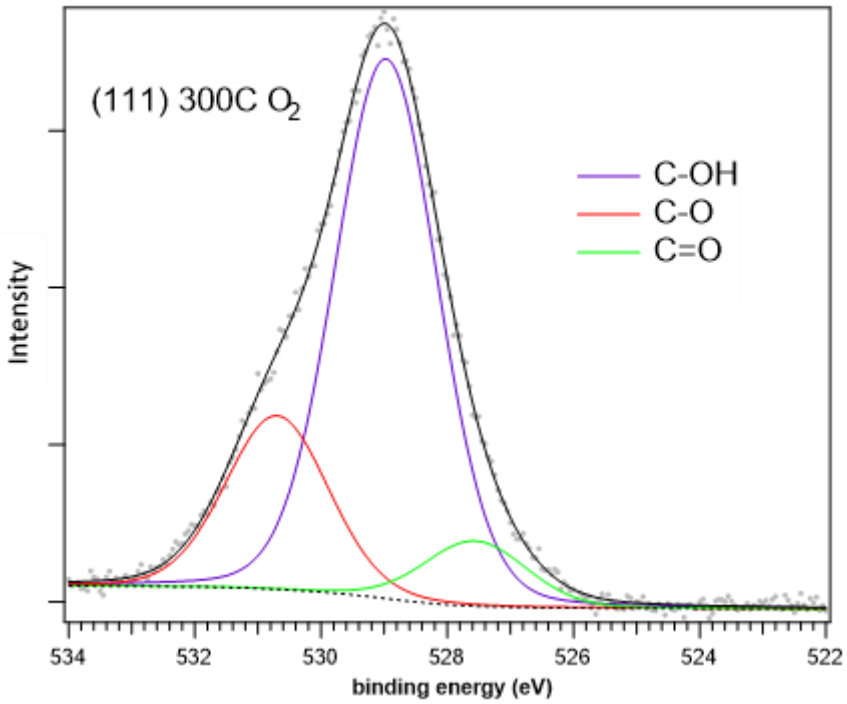

Figure 5.1.9: O 1s spectrum of an (111) oxygen terminated diamond which is being annealed at 300°C, due to the nature of the (111) surface C=O is impossible which shows that at this temperature region surface contaminants or reconstructions are still stable on the surface

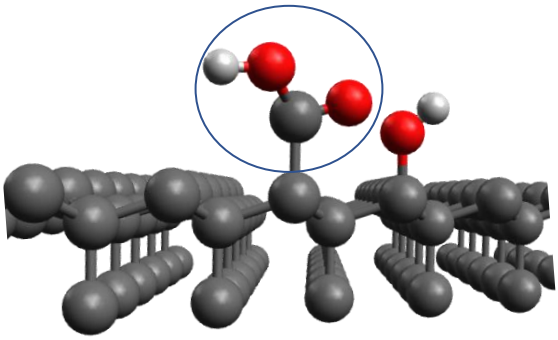

Figure 5.1.10: a diagram showing the (111) diamond surface with a sp^2 carbon bonded onto the surface circled in blue, which is only explanation for surface C=O other than carbon contaminants containing that group. Reconstructed (111) surfaces can have C=O however no LEED measurements were possible to observe any reconstructions.

Figures 5.1.11 shows the O 1s and C 1s core levels for the (111) diamond after it has been heated up to 400°C in 1 mbar of O_2 in-situ.

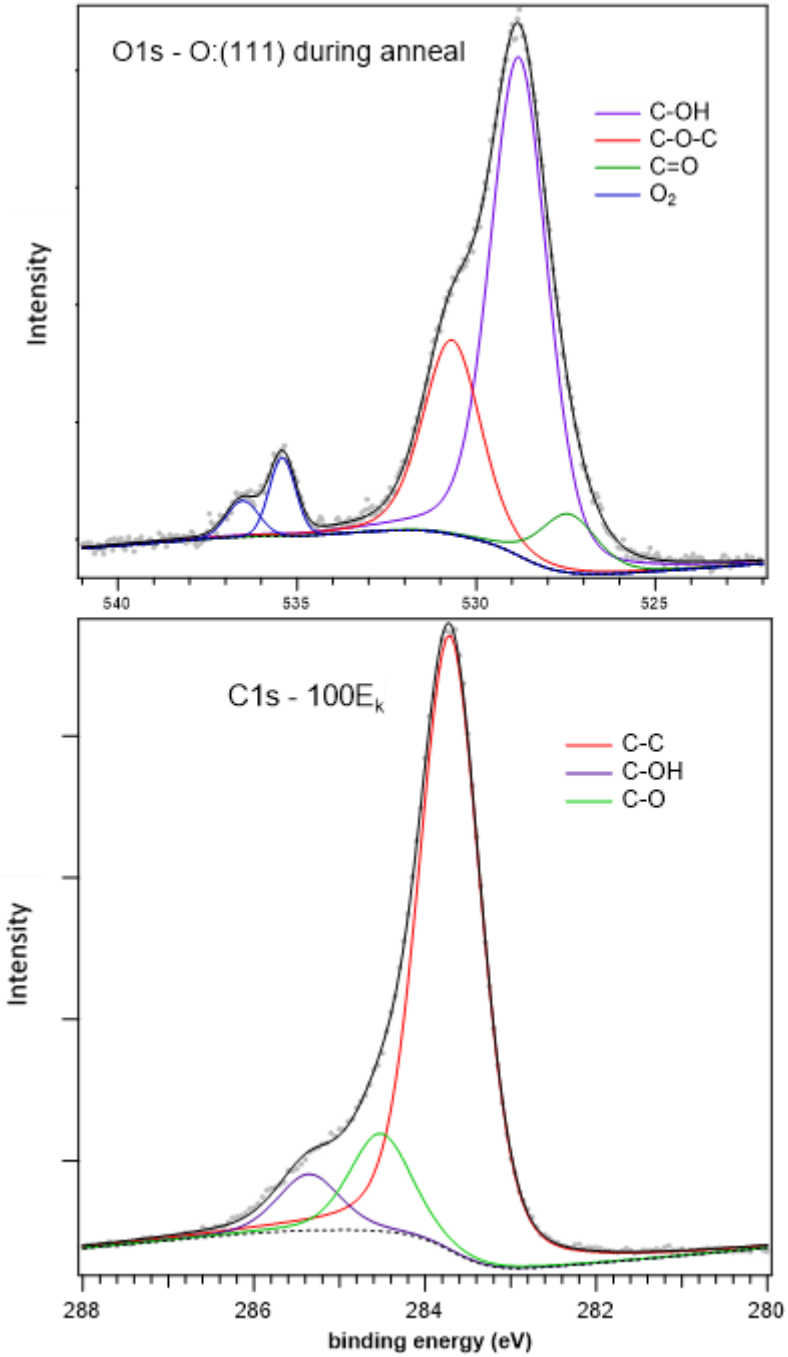

Figure 5.1.11: O 1s and C 1s spectra after reaching 400°C, In comparison to figure 5.1.9 the amount of C=O has significantly decreased, and the amount of C-O has increased. Surface sensitive C 1s measurements using a 380eV photon energy show that there is no observable sp^2 left on the surface according to the C 1s, this is thought to be due to high temperature oxygen burning it off.

Figure 5.1.12 shows the high-resolution C-K edge auger-NEXAFS spectra for the H/O:(001) and O:(111) diamond surfaces.

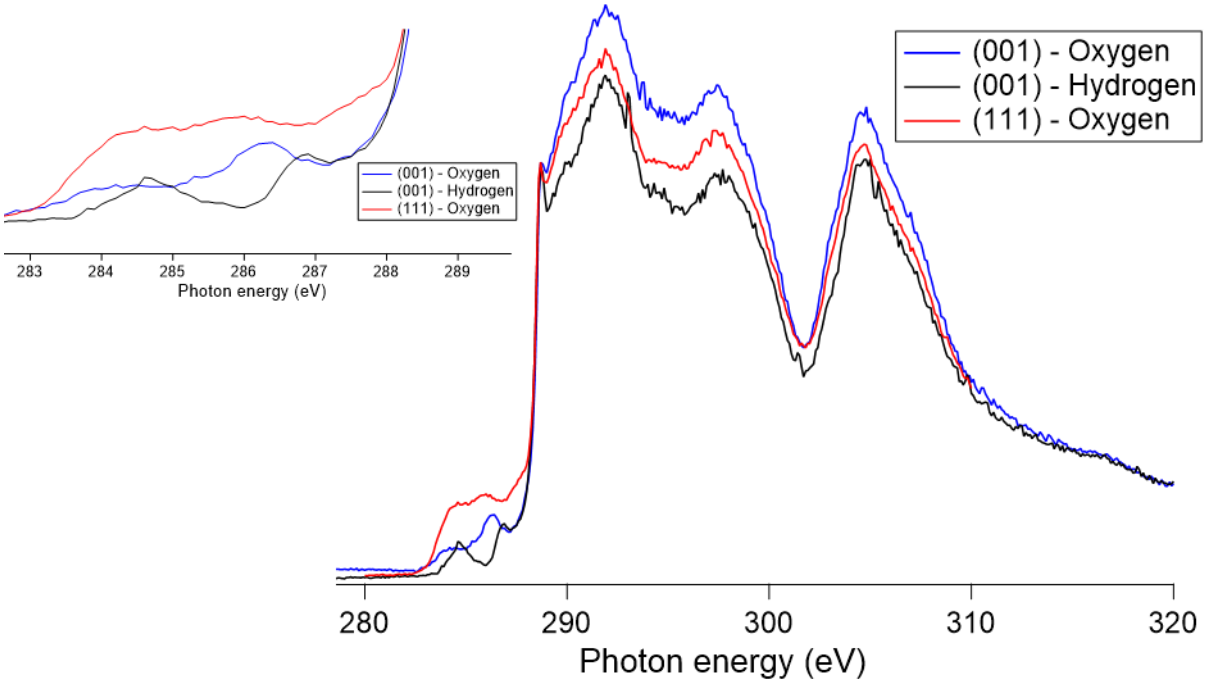

Figure 5.1.12: Auger NEXAFS spectra of the C-K edge for the various terminations. The pre-edge features hold vital information about the occupied surface states. From the various O 1s comparisons between C=O, C-OH and C-O-C ratios can be analysed with the NEXAFS providing a different method of determining these. The peak just before 290 is the diamond exciton peak where the sharp feature indicates an high quality diamond. The diamond 2nd bandgap is the dip just after 300eV. The pre-edge features are of particular interest as they can be related to the different surface groups. The rise closest to the pre-edge between at 287 to 287.5eV is C-OH, where 286.3eV to 286.9eV is C-O-C. C=O should be around 285. The slight increase around 285 for the hydrogen will be the π for sp2 carbon which was evident in the XPS.*

5.1.4 Oxidation of (001) diamond through water vapour.

(001)H:diamond was annealed up to 700°C to desorb any surface contaminants and some of the surface termination, and was then exposed to 1, 5 and 10mbar of water. Figure 5.4.13 shows the C 1s at the various pressures.

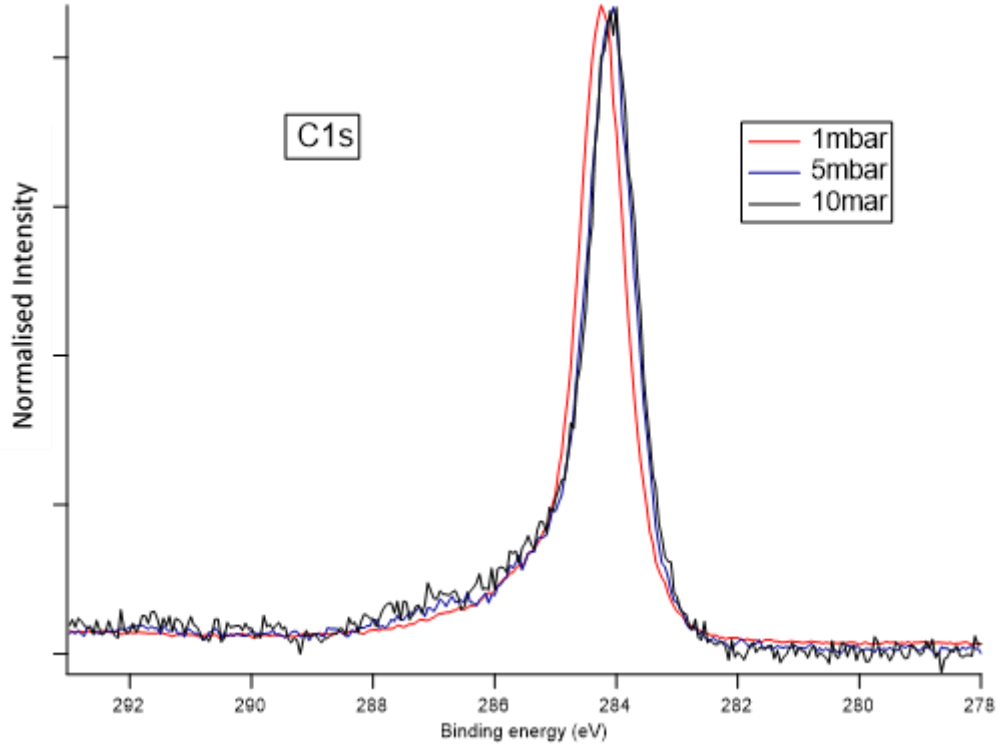

Figure 5.1.13: C 1s of the (001) diamond after being exposed to 1,5 and 10mbar of water, there are subtle differences in the higher binding-energy side of the peak, however the most notable change is the shift in the peak position.

Figure 5.1.14 shows the O 1s of the (001) diamond after being exposed to 10mbar of water post 700°C anneal showing a hydroxylation of the diamond surface.

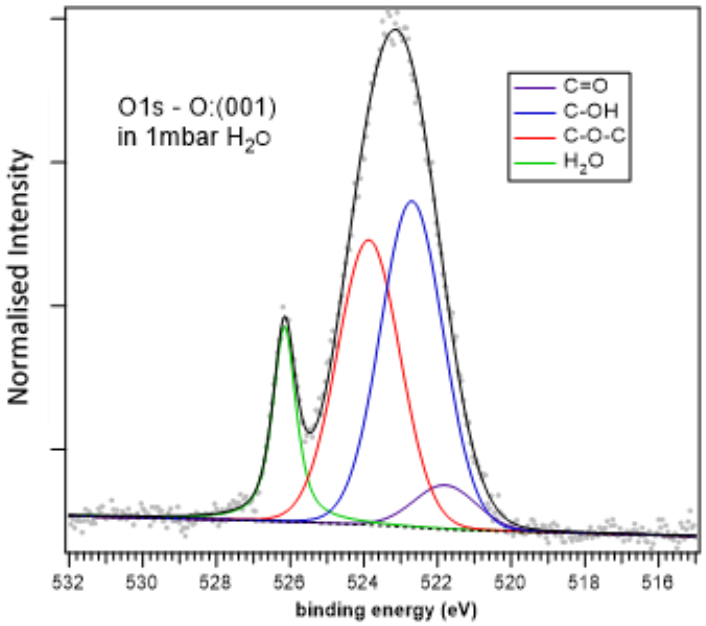

Figure 5.1.14: O 1s after exposing the diamond to 1mbar of water, there is a large increase in C-OH which suggests a hydroxylation of the diamond surface.

Figure 5.1.15 shows the Auger O-K edge for the (001) diamond whilst under 10mbar of water.

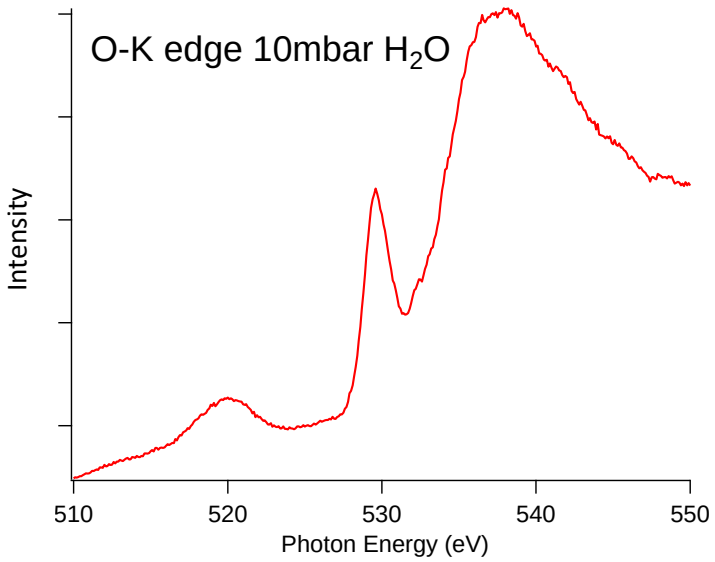

Figure 5.1.15: O-K edge of the O:(001) diamond in-situ whilst being dosed with 10mbar of water, there is a distinct shark peak centred around 530eV which is attributed to the water. 520eV is ketone on the surface.

5.1.5 –dosing of O_2 on the (001) diamond surfaces

Figure 5.1.16 shows the gas phase peak and the O 1s for the (001) terminated diamond during an oxygen pressure series where the pressure was increased from 3mbar to 10mbar.

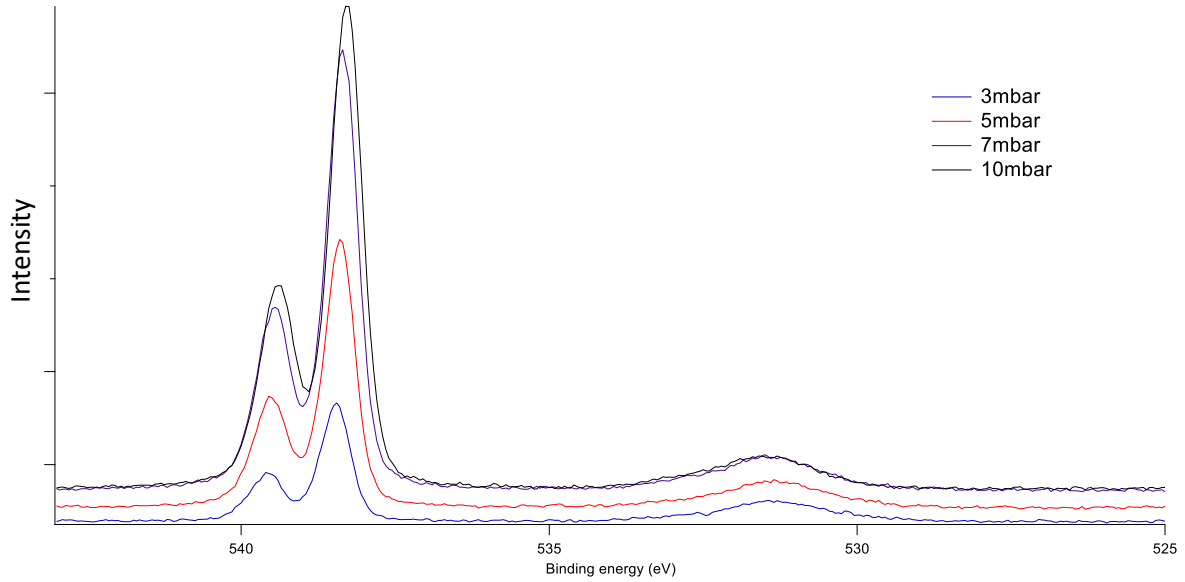

Figure 5.1.16: Oxygen pressure series showing an increase in signal of the O_2 peak, the gas phase shows increasing intensity as pressure increases, the O 1s for the single crystal is already attenuated immensely by the gas.

Figure 5.1.17 shows a zoomed in spectra of the Figure 5.1.16 focusing in on the diamond O 1s demonstrating a shift in the O 1s spectra which could indicate charge transfer.

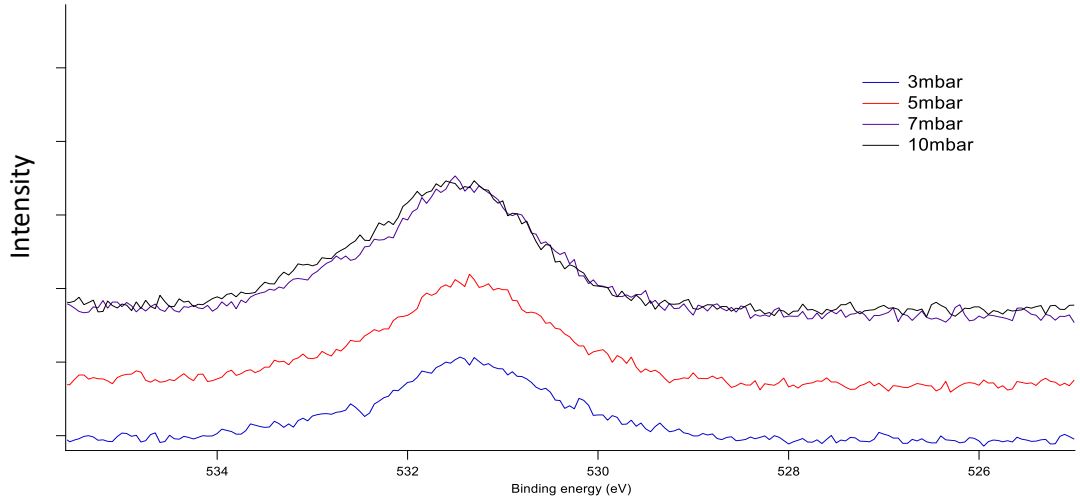

Figure 5.1.17: O 1s spectra of the diamond surface which exhibits a shift due to electron transfer between the O_2 gas and the diamond.

5.2 Discussion

5.2.1 Oxidation states of (001) diamond

There is good correlation between the DFT and the NAP-XPS data for what occurs in instances where there is an excess of ketone on the surface of the diamond. Due to the instability of C=O carbon atoms, surface and sub-surface defects occur to try and stabilise the surface[1-2]. The DFT calculations (Figures 5.1.1/2) show that this occurs via a reconstructing process, driven by the formation of peroxide (C-O-O-C) bonding which then pulls the carbon atoms close enough to each other for a (2x1) reconstruction to occur. The MD calculation also shows that in cases where it can, ether bridges are the preferred termination, and the ketone only occurs to ease lattice strain or at defect sites where C-O-C is impossible. This also matches K. Larson's work which suggests ether bonding is stable only for long ether chains (6+)[1,6]. This could be proved by repeating all these experiments in a NAP-chamber where LEED is available however the availability of both techniques being used in-situ was not available at the times of the experiments at B07 when the measurements and thoughts of a reconstruction first became apparent.

Comparing differences in the O 1s between the acid-etch and the O_2 anneals for both the hydrogen and acid etched starting surfaces, it's evident that the method of oxidation has a drastic role in the surface species that are formed on the diamond surface. The AFM shows that surface roughening is a by-product of acid treatments which is validated in literature, this could cause step-edges in the crystal lattice or these pit features where ether bridges are impossible and therefore C-OH/C=O bonding is the only choice[3,4]. Annealing a diamond in oxygen after an acid-etch did little to change the surface composition of the diamond; this is interesting as this indicates that once the surface has reached a finalised state that the changing of chemical species from one oxidation state to another is difficult or near impossible to go from one to another. This has important implications for device fabrication or surface treatments of diamond in general where annealing in acid is generally used as an initial first step due to its ability to remove contaminant adsorbates from the diamond[5,7]. Best practice for surface diamond treatments in the future may be to avoid acid-etches altogether from a surface roughness and workfunction viewpoint. As discussed in Chapter 2

De Leon's group found that the acid etched diamond produced a less-desirable surface with a lower than expected workfunction which was attributed to the smaller ether to ketone ratio when compared to other methods.[6] As shown in Figure 5.1.8 surface contaminants remained even on O:diamond when annealed to 300°C in oxygen has sp^2 carbon, whereas the 400°C anneal in oxygen for both crystal orientations provided a complete termination whilst also burning any sp^2 carbon, leaving an extremely high-purity surface and arguably the most clean diamond surface measured using PES techniques to date. Work conducted by D. Hu[8] showed that oxygen is desorbed from the diamond at 800°C, this could be a method of re-obtaining a clean diamond surface such that an complete oxidation could be achieved via annealing to high temperature and then flowing in a mixture of choice for the desired species, where from the work in Section 5.1.4 suggesting water vapour can be used to achieve an more uniform hydroxylated surface then anything previously reported in literature and by our group previously[6,8].

The annealing in hydrogen also shows that the removal of oxygen is possible via a more delicate way however this was mostly surface adsorbates rather than a reduction process. The H-terminated diamond after annealing in O_2 at 400°C also demonstrated the largest percentage of C-O-C:O 1s of anything previously reported[8], this may be due to the ability of measuring the O 1s in situ and therefore having a perfectly clean substrate to analyse. As this is the most thermally and geometrically stable surface it is perfect for device fabrication.

A method of measuring the difference in work-function is by using a method first discovered by S. Axnanda, whereby taking into account the position of the gas phase, using the following equation[9]:

$$\Phi = \frac{B}{C} - \left(\frac{E_B}{C}\right) \qquad \text{Eq 5.1}$$

Where *B* and *C* are constants related to the gas in question. Whilst Axnanda also calculated these values for oxygen, measurements were taken on Au and Pt substrates to determine these values of which we obtained approximately equal values to Axnanda. Where C was calculated to be 0.76 which is dependent on the gas used, and b is 537.8 which is a correction factor. as $\frac{B}{C}$ is constant the change in the workfunction is equivalent to -1.316E_B. Tables 5.1 and 5.2 show the position, areas and ratios of all the oxygen species for all O 1s scans shown in the results section.

	Binding energy position (eV)					
Chemical Species	(001):Acid	(001):Acid Post O_2 anneal	(001):H Post O_2 anneal	(111): O_2 at 300°C	(111): O_2 at 400°C	(001): in H_2O*
C-O	529.8	529.8	529.8	530.6	530.6	529.9
C-OH	528.8	528.7	528.7	528.8	528.8	528.8
C-O-O-C	531.3	531.3	531.3	N/A	N/A	N/A
C=O	527.6	527.5	527.5	527.5	527.5	527.5
O_2	N/A	536.1	535.1	535.3	535.5	N/A

Table 5.1: O 1s spectra data for the different chemical species and their positions, where the change of the oxygen gas position relates to changes in the workfunction. Note for the Water series the binding energies have been shifted for correction as the analyser was un-calibrated during the first experimental time at B07 for the water experiments. The (111) surface will have a different position for C-O as it will be C-O, as discussed in the next section.*

	Normalised area intensity					
Chemical Species	(001):Acid	(001):Acid Post anneal	(001):H Post O_2 anneal	(111): O_2 at 300°C	(111): O_2 at 400°C	(001): in H_2O
C-O	1.24	1.46	1.57	0.23	0.38	1.1
C-OH	0.34	0.46	0.29	0.74	0.97	1.3
C-O-O-C	0.04	0.07	N/A	N/A	N/A	N/A
C=O	0.19	0.23	0.09	0.09	0.1	0.16

Table 5.2: O 1s spectra data for the different chemical species and their area intensity, such that conclusions about the rations between the different components can be discussed.

The shift in workfunction was calculated to be approximately 1.27eV, which is similar to what has been reported in literature[6,8]. It is also worth discussing that comparing the gas phase positions of the (001) and (111) diamonds when oxidised also shows that the (111) has a lower electron affinity, which is to also be expected[10].

5.2.2 Oxidation states of (111) diamond

There is a lot of disagreement on which components of the O 1s are the corresponding surface species, with variations of C=O, C-OH and C-O-C all being labelled in numerous references as being the highest, lowest and central binding energy positions each[10].

The benefit of oxidising both the (001) and (111) diamond in-situ under pure oxygen allows for exact determination of these species as due to the difference in hybridization. What can be deduced from the oxidation of the (111) is that due to the single electron only being available for bonding that only C-O and C-OH bonds can form on the surface if it's (1x1). However there are several papers which suggest that depending on the level of oxidation and the method of preparation, the (111):O termination can actually be a reconstructed (2x1) surface where Pandey chains form. This can allow for formation of C=O bonds[11-13]. This is potentially validated in the XPS, and the temperature step between 300 and 400°C shown in figures 5.1.9/11 proving a critical step. C=O bonds which are present at 300°C started to desorb or break down when taken to 400°C and fully removed after 2 hours. Several papers also suggest that at 400°C the (2x1) reconstruction will break apart, which would also match the experimental data gathered. Although it can be known that the (111) diamond surface would be more stable with a C-OH bond, there is a lack of H in this oxidation process for OH to occur. We see an increase in the C-O:C-OH ratio as where C-C bonds are being broken, it's being replace with C-O*. Comparisons between the various oxidation states of (111) and (001) diamond are helped by the high resolution NEXAFS. The pre-edge features for the H/O:(001) and O:(001) diamond show an overlapping of features, where the predominate peak in the O:(001) from the C-O-C at around 286.5eV, and the peak from the H:(001) being residual OH species merging together for the O:(111) around 287eV. The feature at 285 photon energy is usually assigned to π bonding in sp^2 carbon[14-15]. However due to orientation of the sample and the polarisation of the beam the π*orbitals of C=O bonds are detected along with key differences which represent the different ratios of C-H, and C-O-O-C are considerably different from each other.

These methods can be used to determine the definitive positions of the O-components in the C 1s, however there are large variations in the positioning of C-OH/=O/-O-C binding energies as these are also dependant on the local environment of carbon atoms. An electron from a carbon in a large ether chain will show a difference in binding energy when compared to a

carbon forming a singular ether bond with its neighbour. This along with a much weaker sensitivity makes determination of these groups possible from the C 1s useful but not clear. High resolution scans at low kinetic energy such as in 5.1.11 allow for greater surface sensitivity to be achieved. The area percentages of those components match what was shown in the O 1s. For future experiments the ability to use Low-energy electron diffraction to measure the unit cell would be ideal for determining surface structures. The potential to measure UPS in-situ during the oxidation process to measure differences in workfunction would also be Important, but unfortunately there wasn't a He(I) or (II) source at Manchester and the lowest photon energy available at B07 is 200eV.

5.2.3 Water dosing of (001) diamond surfaces

There is a shift of 0.15eV in the C 1s between the UHV and 1mbar dosed spectra and the 5 and 10mbar spectra, this is believed to be due to a charge transfer between the water ions and the diamond surface. DFT studies have shown this is possible where calculations have suggested this shift to be 0.16eV[16]. In the case of water, it is believed the H_2O ionises and interacts with the diamond surface and weakly binds itself, forming H_3O^+[17,18,21]. Other groups have reported that when moving from NAP to ambient conditions in the case of oxygen actually then reverts any ionisation at the surface, for water dosing however it's reasonable to assume that under regular ambient conditions dependant on the humidity water vapour in atmosphere can vary from 1 to 4%, which would only constitute effectively 10-40mbar of pressure. Unfortunately, due to the limitations of NAP and electron scattering the capability of being able to measure XPS whilst under 40mbar of water is currently impossible at B07 or Manchester. This is available at other facilities however the time taken for measuring an acceptable core level intensity of a substrate under NAP conditions changes from 40 minutes in UHV to 8hours at 10mbar of water for good resolution. Measuring 40 mbar would require several days for resolvable data.

5.2.4 Oxygen dosing (001) diamond

Much like with water, there is a charge transfer between the diamond between the O_2 gas and the diamond surface. The shift from the regular O 1s position occurs at 3-5mbar, however unlike with water, at pressures of 7 and 10mbar the O 1s returns to its original position, this is believed to be due to the effect of multiple layers of oxygen causing this oxygen association to break down, such that rather than the oxygen gas interacting with the surface oxygen and ionising, at larger pressures or multiple layers of oxygen the gas interacts with itself rather than the substrate[19-21]. The question which is 'At what point of thickness do you go from surface adsorbates to two materials interacting' possibly may be answered in this question for oxygen. This has been reported on in literature however it's been typically reported this occurs at 10mbar rather than 7. This may have been due to the inabilities for precise control of gas flow of oxygen into the chambers, or due to recent works focus on even higher pressure's (>30mbar).

5.3 Conclusion

The difference in oxidation state of (111) and (001) diamond surfaces using photoelectron spectroscopy techniques has been demonstrated. It has been shown that acid etching a diamond forms a much lower ether to ketone ratio than oxygen annealing which reduces the positive electron affinity of the oxygen termination. This large amount of ketone has been proven to be irremovable using different oxidation techniques, where potentially high temperature UHV annealments or H* plasmas may be the best method of removing this surface to then obtain a more desirable surface. The differences in electron affinity between these methods can also be calculated using the gas phase peak position, which produced a value of 1.27eV. Band diagrams showing these differences are displayed below in Figure 5.3.1. A higher percentage of hydroxyl bonding can also be achieved by dosing with water vapour rather than using acid or oxygen gas. The importance of the terminations being more desirable via a gas/water dosing is essential for device fabrication. For large scale fabrication

acid etching large quantities of samples would be considerably more difficult then annealing a large amount of samples in an industrial furnace at relatively low temperatures.

DFT calculations have shown that large amounts of ketone on the surface are also unstable and may form due to incomplete oxidation procedures, causing surface defects, (2x1) reconstructions and formation of peroxide species. These species are then shown to occur experimentally in NAP-XPS, only occurring in the acid-etched diamond which has large amounts of ketone. This chapter has demonstrated that the avoidance of acid-etches for oxygen terminated diamonds should be a standard operating procedure for all oxidation processes. As annealing in 400°C oxygen is demonstrably more efficient at removing surface adsorbates and sp^2 back bonded carbon.

Through comparisons of high-resolution NAP-XPS and NEXAFS, the correct assignment of the chemical species in the O 1s can be definitively assigned to either ketone, hydroxyl or ether bonding to the diamond surface.

Charge transfer between H_3O^+ ions and oxygen terminated diamond can also be shown via a shifting of the C 1s peak, where the shift matches reported values in DFT calculations.

Figure 5.3.1 shows the band diagrams for both the acid etched, and hydrogen plasma treated diamonds after both had been annealed in oxygen.

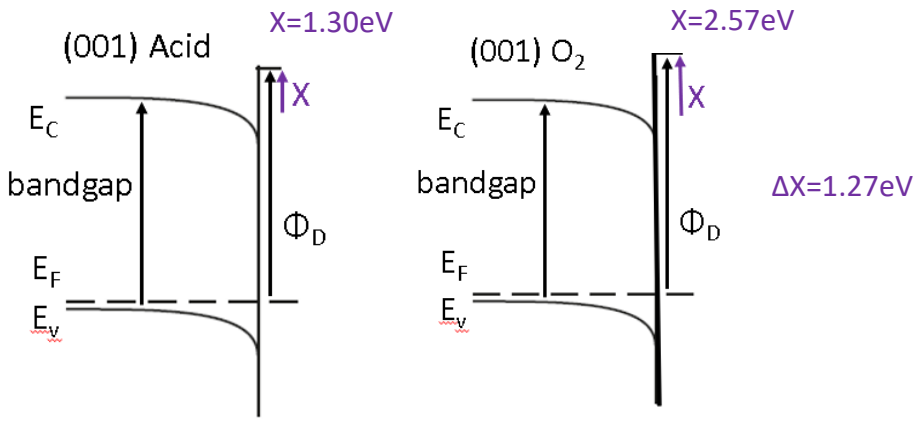

Figure 5.3.1 – Diagram showing the change in the band-diagrams for the acid treated (001) after being annealed in oxygen compared to the (001) diamond which had been terminated purely in oxygen. The workfunction and therefore electronic affinity greatly change. For devices where a large workfunction is essential then the acid is significantly worse then annealing a clean, hydrogen terminated diamond in oxygen.

References:

[1] - Karin Larsson. Simulation of Diamond Surface Chemistry: Reactivity and Properties. June 2019. DOI: 10.5772/intechopen.86865

[2] - D. Petrini* and and K. Larsson. A Theoretical Study of the Energetic Stability and Geometry of Hydrogen- and Oxygen-Terminated Diamond (100) Surfaces. The Journal of Physical Chemistry C. Vol111. P795-801. 2007. DOI: 10.1021/jp063383h

[3] - Peter K. Baumann, T. P. Humphreys, Robert Nemanich. Comparison of surface cleaning processes for diamond C(001). Materials Research Society Symposium – Proceedings.1994.

[4] - Nianjun Yang, Siyu Yu, Julie V. Macpherson, Yasuaki Einaga, Hongying Zhao,D Guohua Zhao, Greg M. Swain and Xin Jiang. Conductive diamond: synthesis, properties, and electrochemical applications. Chem. Soc. Rev. Vol48. P157-204. 2019.

[5] - Maier, F., Ristein, J., & Ley, L. (n.d.). Electron affinity of plasma-hydrogenated and chemically oxidized diamond (100) surfaces. Phys Rev B. Vol 65. 2001. https://doi.org/10.1103/PhysRevB.64.165411

[6] – S. Sangtaewesin ET Al. Origins of Diamond Surface Noise Probed By Correlating Single-Spin Measurements With Surface Spectroscopy. Phys Review X. Vol 9. September 2019.

[7] - T. T. Pham M. Gutiérrez, C. Masante, N. Rouger, D. Eon, E. Gheeraert, D. Araùjo, and J. Pernot: High quality Al2O3/(100) oxygen-terminated diamond interface for MOSFETs fabrication Applied Physics Letters 112:10.

[8] - Di Hu. Surface Modification And Electronic Structure Characterisation Of Carbon Based and Iron Based Materials. PhD Thesis. 2017. http://hdl.handle.net/2160/04016083-f5c2-4542-a75a-74ee93b36100.

[9] - Stephanus Axnanda ,Marcus Scheele, Ethan Crumlin, Baohua Mao, Rui Chang, Sana Ran,I Mohamed Faiz, Suidong Wang . Paul Alivisatos. Direct Work Function Measurement By Gas Phase Photoelectron Spectroscopy and Its Application on PBS Nanoparticles. Nano Letters. Vol13 (12). P6176-6182. 2013.

[10] - Baumann, P. ., & Nemanich, R. Surface cleaning, electronic states and electron affinity of diamond (100), (111) and (110) surfaces. Surface Science, Vol409(2). P320–335. 1998. https://doi.org/10.1016/S0039-6028(98)00259-3.

[11] - Kian Ping Loh,*, X. N. Xie,S. W. Yang, and, and J. C. Zheng. Oxygen Adsorption on (111)-Oriented Diamond: A Study with Ultraviolet Photoelectron Spectroscopy, Temperature-Programmed Desorption, and Periodic Density Functional Theory.The Journal of Physical Chemistry B Vol106 (20), P5230-5240. 2002. DOI: 10.1021/jp0139437

[12] - Pandey, K. C. New dimerized-chain model for the reconstruction of the diamond (111)-(2 × 1) surface. Physical Review B, Vol25(6), P4338–4341. 1982. https://doi.org/10.1103/PhysRevB.25.4338

[13] - Frauenheim, T., Stephan, U., Blaudeck, P., Porezag, D., Busmann, H.-G., Zimmermann-Edling, W., & Lauer, S. Stability, reconstruction, and electronic properties of diamond (100) and (111) surfaces. Physical Review B, Vol48(24). P18189–18202. 1993. https://doi.org/10.1103/PhysRevB.48.18189

[14] - H. H. Hsieh, Y. K. Chang, and W. F. Pong. X-ray-absorption studies of boron-doped diamond films. Applied Physics Letters Vol75:15. P2229-2231. 1999.

[15] - Stöhr, J. Introduction. In NEXAFS Spectroscopy (First edit, pp. 1–7). Springer-Verlag. 1992. https://doi.org/10.1007/978-3-662-02853-7_1.

[16] - D. Petrini* and and K. Larsson. Electron Transfer from a Diamond (100) Surface to an Atmospheric Water Adlayer: A Quantum Mechanical StudyD. Petrini* and and K. LarssonThe Journal of Physical Chemistry C Vol 111 (37). P13804-13812. 2007. DOI: 10.1021/jp070565i.

[17] - O. Manelli, S. Corni, and M. C. Righi Water Adsorption on Native and Hydrogenated Diamond (001) Surfaces. The Journal of Physical Chemistry C. Vol114 (15). P7045-7053. 2010.

[18] - Xingyu Gao,*, Lei Liu,Dongchen Qi,Shi Chen, and, A. T. S. Wee, Ti Ouyang and, Kian Ping Loh, Xiaojiang Yu and, and Herbert O. Moser The Journal of Physical Chemistry C. Vol112 (7). P2487-2491. 2008.

[19] - Flammini, R., Satta, M., Bellucci, A., Girolami, M., Wiame, F., & Trucchi, D. M. Water desorption effects on the surface electrical resistance of air-exposed hydrogenated diamond. Applied Surface Science, Vol 512. May 2020. https://doi.org/10.1016/j.apsusc.2020.145491
[20] - Bob L. Mackey, John N. Russell, Jr, John E. Crowell, Pehr E. Pehrsson,, Brian D. Thoms, and, and James E. Butler. Oxygen Adsorption on the (110)-Oriented Diamond Surface The Journal of Physical Chemistry B Vol105 (18). P3803-3812. 2001. DOI: 10.1021/jp003586k
[21] - Mir M. Hassan and Karin Larsson. Effect of Surface Termination on Diamond (100) Surface Electrochemistry. The Journal of Physical Chemistry C. Vol118 (40). P22995-23002. 2014. DOI: 10.1021/jp500685q

Chapter 6 – Oxidation of detonation nanodiamonds

The motivation behind this work was the desire to better understand the oxidation process of nanodiamonds. Currently the standard procedure for nanodiamond oxidation is either an acid treatment or annealing in air at 400+ Celsius. However, little is understood about how the temperature dependence effects the surface functionalisation of the nanodiamond[1-3] .

This chapter will discuss the various preparation methods of detonation nanodiamonds for the removal of sp^2 and for the oxygen termination of the nanodiamond surface. Initial samples were obtained from the raw-powder after the detonation process in South Korea, and the diamonds were treated in an acid-etch procedure of a 3:1 ratio of H_2SO_4:HNO_3 for 72 hours at 80°C or alternatively air annealed up to 450°C. Comparisons of the sp^3 to sp^2 ratio can be calculated from the Raman spectroscopy.

H-terminated detonation nanodiamonds (91% hydrogen, 9% oxygen) were obtained from Element 6, which were treated through a series of solvent and milling processes and exposed to a hydrogen plasma. TEM was conducted to characterise crystallinity. The NAP-XPS system in the University of Manchester was used for In-situ oxidation XPS measurements. H-terminated nanodiamonds were annealed in 1mbar of oxygen over the course of 48 hours. The nanodiamonds were heated up in 20°C steps from 200°C to 420°C where the O 1s and C 1s core level spectra were taken in real-time. The temperature was only increased in 20°C when oxygen uptake plateaued. The gas phase was also measured so that changes in the gas phase binding energy can be used to calculate changes in workfunction such as in Chapter 5. Relaxation calculations were conducted to determine the stability of the oxygen surface. All nanodiamonds measured using PES in this chapter were deposited on a platinum (Pt) substrate and thin uniform films were created by in-vacuo evaporation of the DND suspensions to minimise any coffee-stain ring effects.

For all XPS data analysed shown in this chapter, psuedo-Voigts have been used with a GL ratio of 0.35, with linked widths between all components, with a width of 1.63 for the O 1s, and 0.9 for the C 1s with +/-0.05 freedom either side. All DFT calculations we conducted using quantum espresso and used a PBE pseudo-potential. All MD calculations were set with time-steps of 1ps.

6.1 Results

6.1.1 Preparation of DND-Soot

Figure 6.1.1 shows the Raman spectroscopy for the DND-soot from as received which hasn't received any treatments post detonation process in red, the soot after receiving the acid-etch procedure in blue, and the 450°C air anneal in black. Some features in the acid-etch spectra are caused by the periodicity of the laser and gratings.

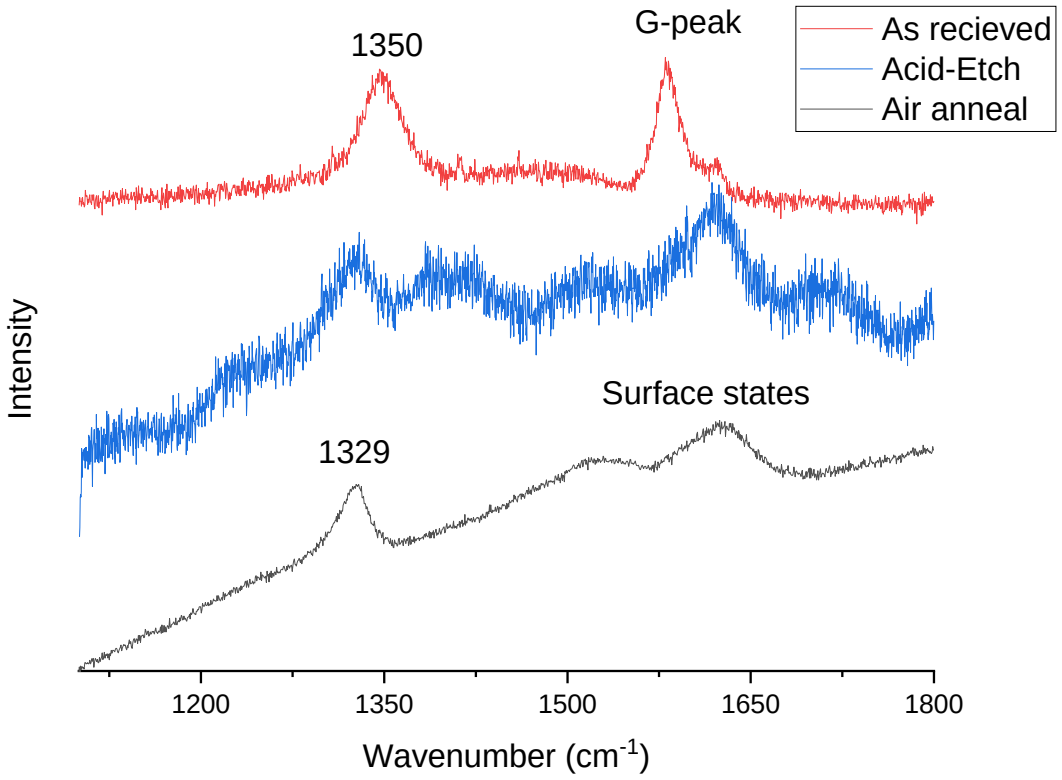

Figure 6.1.1: Raman spectroscopy of the raw DND-soot and after two different treatments. The as received powder has a strong D peak centred near 1350cm^{-1} suggesting sp^2 carbon. Whereas the D band for both the acid etch and air anneal both demonstrate a peak centred around 1329cm^{-1} which is associated as the nanodiamond Raman peak. the quality and suspension of DNDs after the air anneal is visibly better based on the signal to noise, suggesting potential contaminants on the acid-etched DND's. The G peak is representative of sp^2 hybridisation, which is why it is appearing for the graphitic covered DND's, but not the air annealed as any sp^2 carbon should have been removed.

Figure 6.1.2 shows the DND's illuminated with a 325nm UV source to induce photoluminescence in DND suspensions of the as received and both oxidation treatments, where the air annealed DND's can be visually seen to fluoresce. The resultant PL is also shown in Figure 6.1.3 when the air annealed DND's are deposited on a silicon wafer.

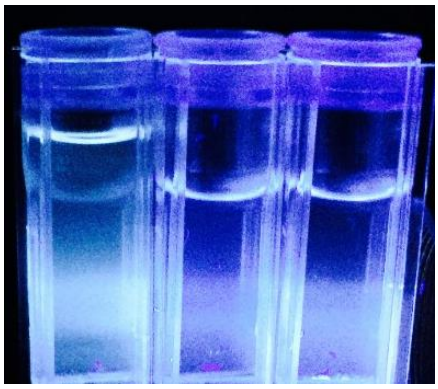

Figure 6.1.2: From left to right; air annealed, acid etched and as-received DND powders were suspended in water and then exposed to a 325nm UV source for induced photoluminescence. The air annealed underwent photoluminescence suggesting that the band has shifted, and a complete oxidation has been achieved and that there is little surface contaminants. Neither the acid etched and as received DND suspensions undergo PL.

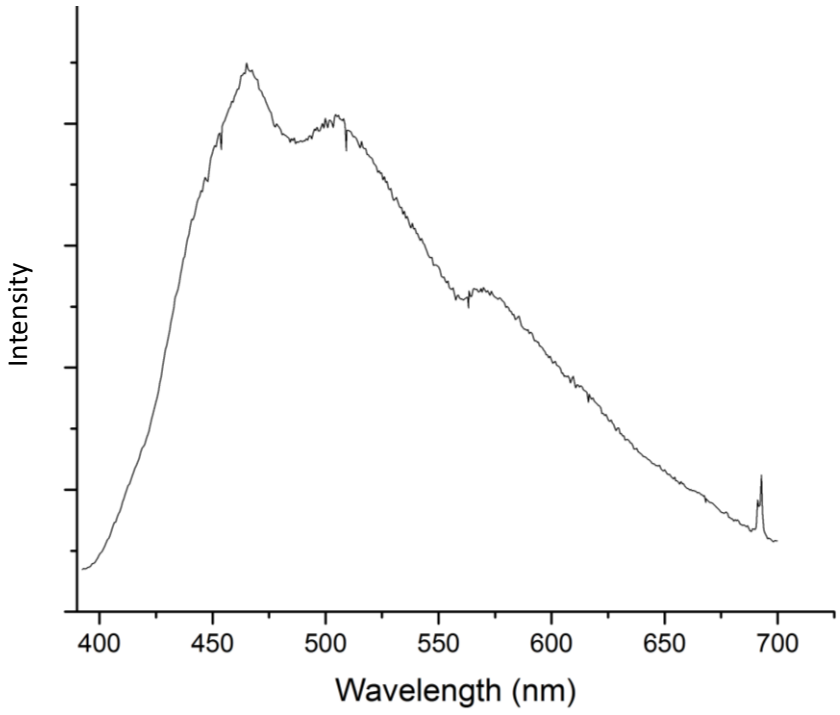

Figure 6.1.3: PL spectra of the treated O:DNDs centred around 470nm which is shifted to a lower wavenumber then reported elsewhere. Research has shown the effect of the electron transfer between substrate and DND's having an effect on the PL spectra which can alter the energy required for PL to occur. Measurements we're also taken at -259°C and 20°C but showed little to no changes. The peaks at 470, 510 and 570nm represent oxygen surface species, sp^2 carbon and NV^0 respectively.

6.1.2 Oxidation of H-DND's.

Figure 6.1.4 shows the TEM of H-terminated DND's deposited as a thin film using a micropippete.

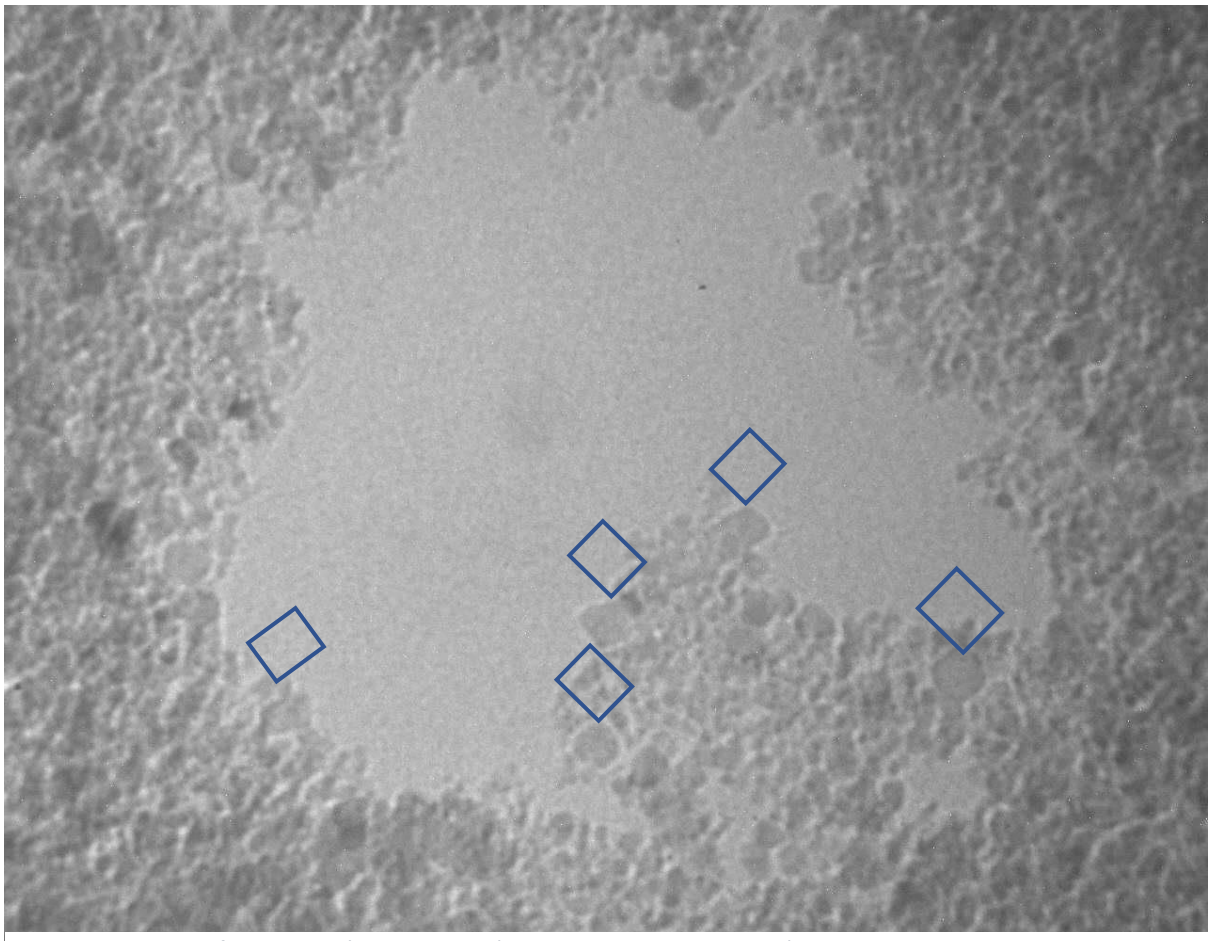

Figure 6.1.4: TEM of the H:DND's which show's very distinct crystal edge's shown in the blue squares in comparison to DND's seen in literature, this allows for comparisons to single crystal diamonds when discussing surface stoichiometry.

Figure 6.1.5 shows a DFT relaxed crystal structure of a DND which has an O-termination for the (001) and H-termination for the (111) orientations. The core (60 atoms) of the model was constrained such that the surface and sub-surface carbon atoms had some freedom of movement.

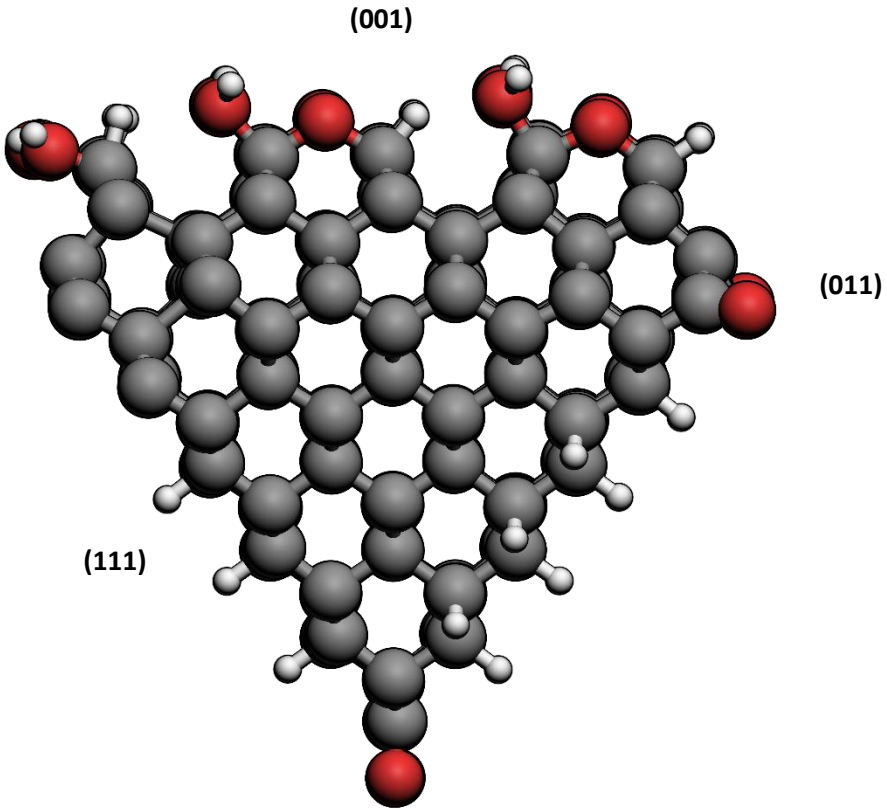

Figure 6.1.5: Model showing a 2.8nm DND which shows the preferred surface bonding for the various terminations, due to nature of the hybridisation and the small number of atoms. Although some advantages can be obtained from single crystals it is important to note for example that the (001)ND Surface is unstable for a full ether coverage.

Figure 6.1.6 shows the evolution of the O 1s in-situ whilst the H-terminated diamonds are annealed in 1mbar of oxygen at increasing temperature steps. Not all the temperature steps there were measured are displayed on this graph. However, the important steps at which visible changes to the surface chemistry were observed have been shown. They were in-vacuo evaporated onto a Au substrate. The measurements were taken, and several survey scans were conducted to find an area with no platinum signal such that we could be confident the measured oxidation in the XPS was purely from the DND's. whilst the TEM does show holes in the film, it should be noted that an area with a hole was intentionally found and was difficult to do so. When conducting the TEM to determine the sizes of the nanodiamonds would have been impossible without finding an area with holes, as there was no way of telling individual DND's apart from one another in what was mostly a black uniform film.

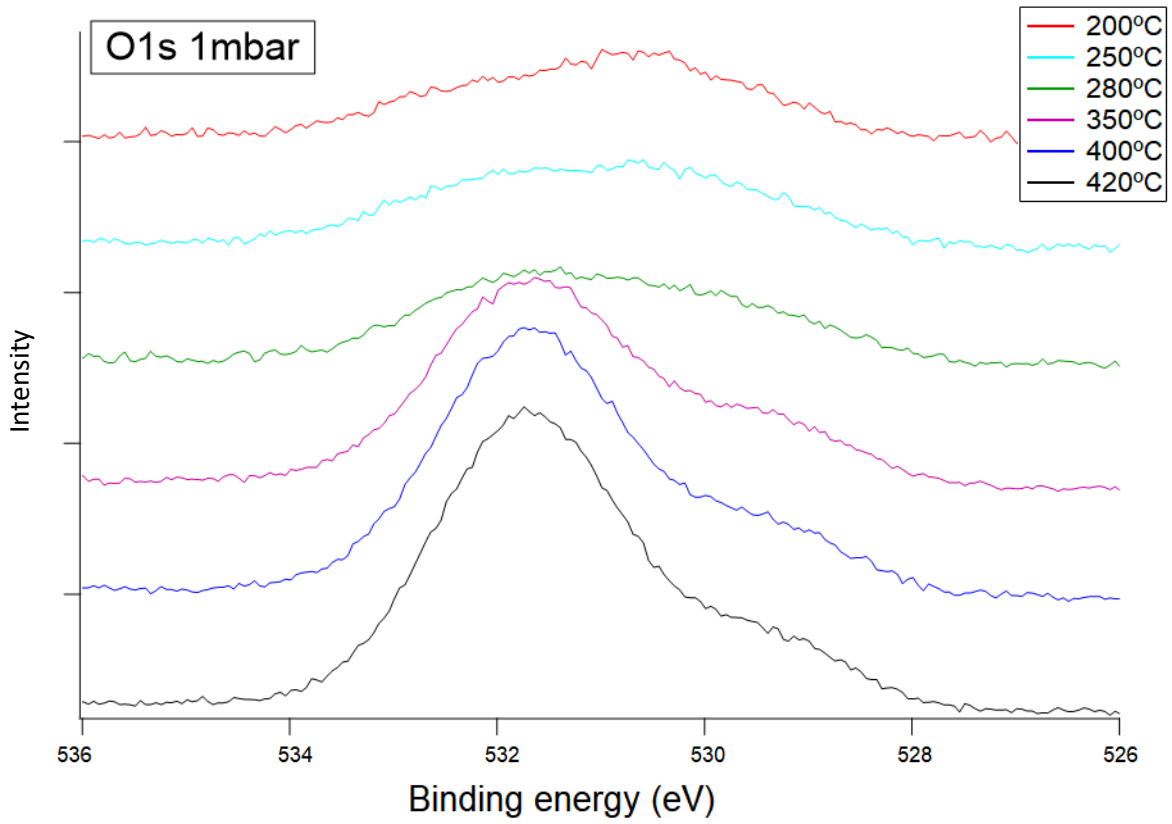

Figure 6.1.6: Growth of the O 1s during the oxidation of H-terminated nanodiamonds measured using NAP-XPS at temperature. There are minimal changes initially however the uptake of oxygen didn't start till 350°C where large amounts of oxygen chemically bonded to the surface. Minimal oxygen gains are then gained from 350-420°C

Figure 6.1.7 show the O 1s for various key temperatures of the oxidation process which are points at which oxidation either stopped for more than 40°C or there was visible changes to the O 1s structure. There is real-time data for analysis at each individual temperature step however it was evident during the course of the experiment that rather than a continuous process whilst increasing temperature, that there was set temperatures at which oxygen species formed on the surface and large ranges up to 80°C where there was no change in the O 1s.

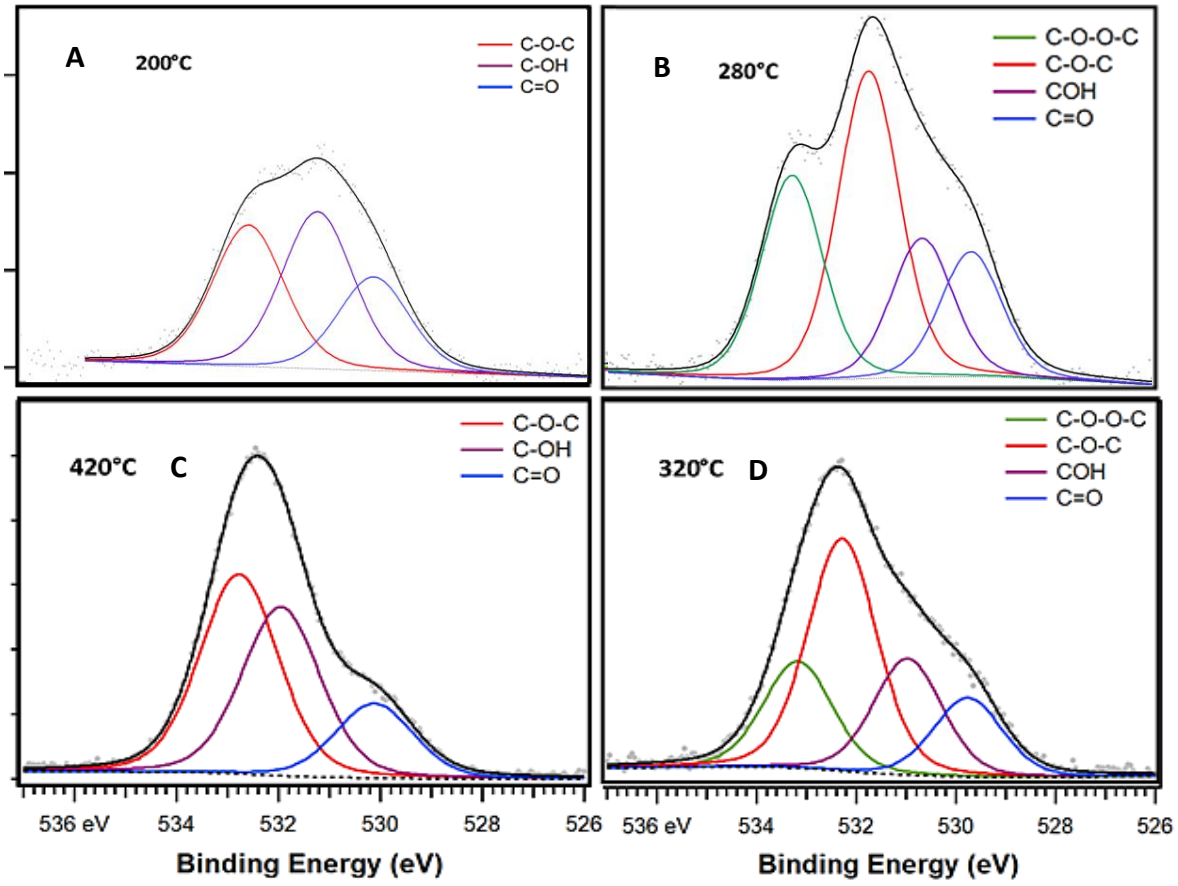

Figure 6.1.7A-D shows the O 1s spectra of the H:DNDs at various points of the oxidation at 200, 280,320 and 420°C respectively. Each step shows a different species growth. Between 200°C and 280°C there is an uptake in ether species, and at 280°C the formation of peroxide occurs. Between 280°C and 320°C the peroxide is stable and there is a further increase in ether bonding. Between 320°C and 420°C there is a slight increase in ether however a large amount of hydroxyl forms, throughout this entire oxidation process the amount of ketone groups on the surface remains relatively consistent.

Figure 6.1.8 shows the gas phase peak positioning for all of the oxidation temperatures shown in Figure 6.1.6.

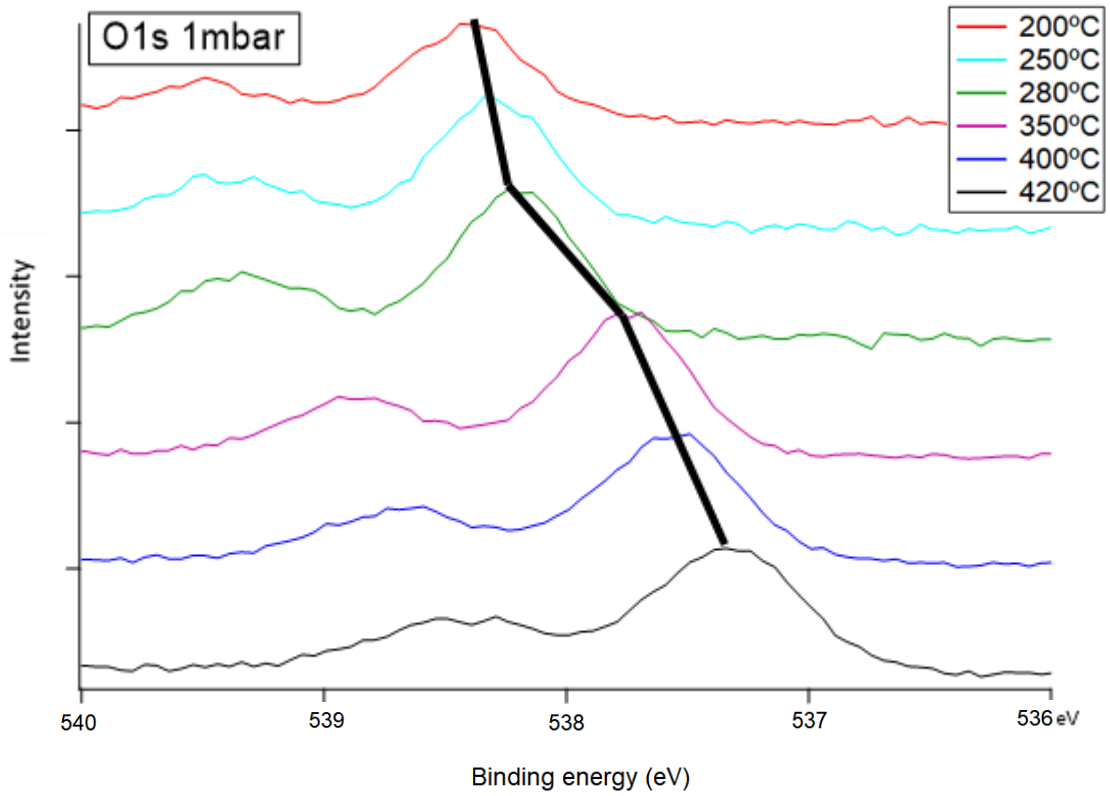

Figure 6.1.8: O 1s of the gas phase O_2 as a function of temperature, where the shift of the gas phase is related to a changing workfunction of the nanodiamonds. Small shifts are visible between 200°C -280°C and 350°C - 420°C, however there is a large peak shift between 280°C and 350°C which coincides with the increase in ether formation on the DND's surface during this temperature range.

Figure 6.1.9 shows the UPS data for the nanodiamonds before and after oxidation. This oxidation was not conducted in-situ however and was produced by ex-situ air annealing up to 420°C of H-terminated nanodiamonds and measuring it in the REES system in Aberystwyth.

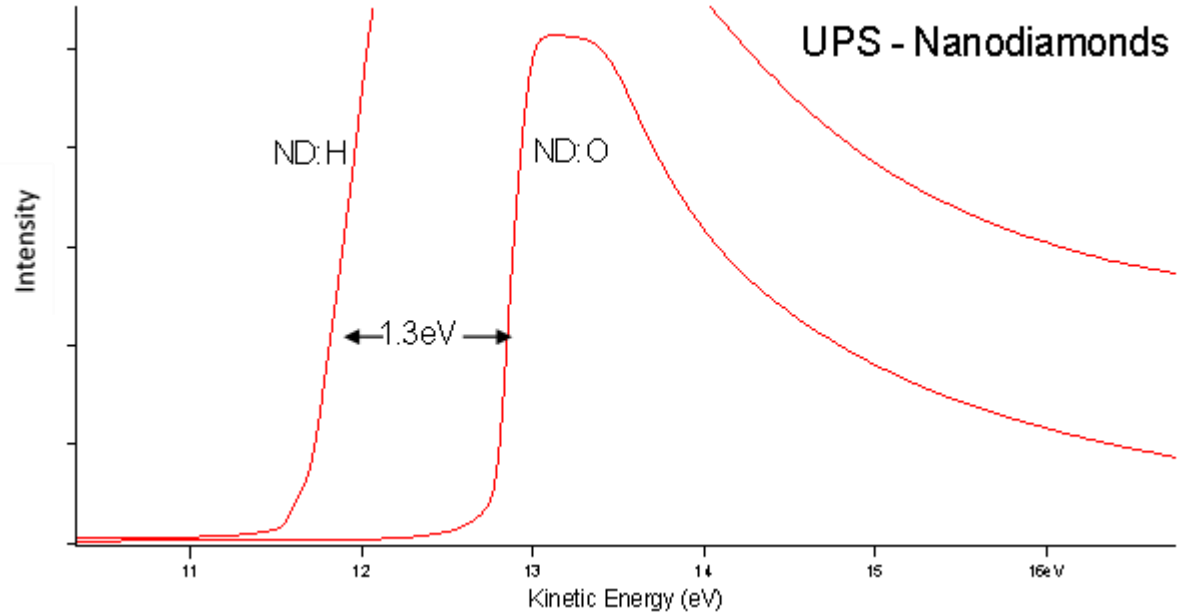

Figure 6.1.9: UPS spectra for both O and H terminated nanodiamonds showing a difference in their work functions of 1.3eV. This shift matches well with what is reported in literature for the difference in DND's between the two terminations.

Figure 6.1.10 shows the widescan of the H:DNDs pre and post oxidation at Manchester after annealing the sample to 420°C in oxygen, where there Is a visible increase in the O 1s:C 1s ratio

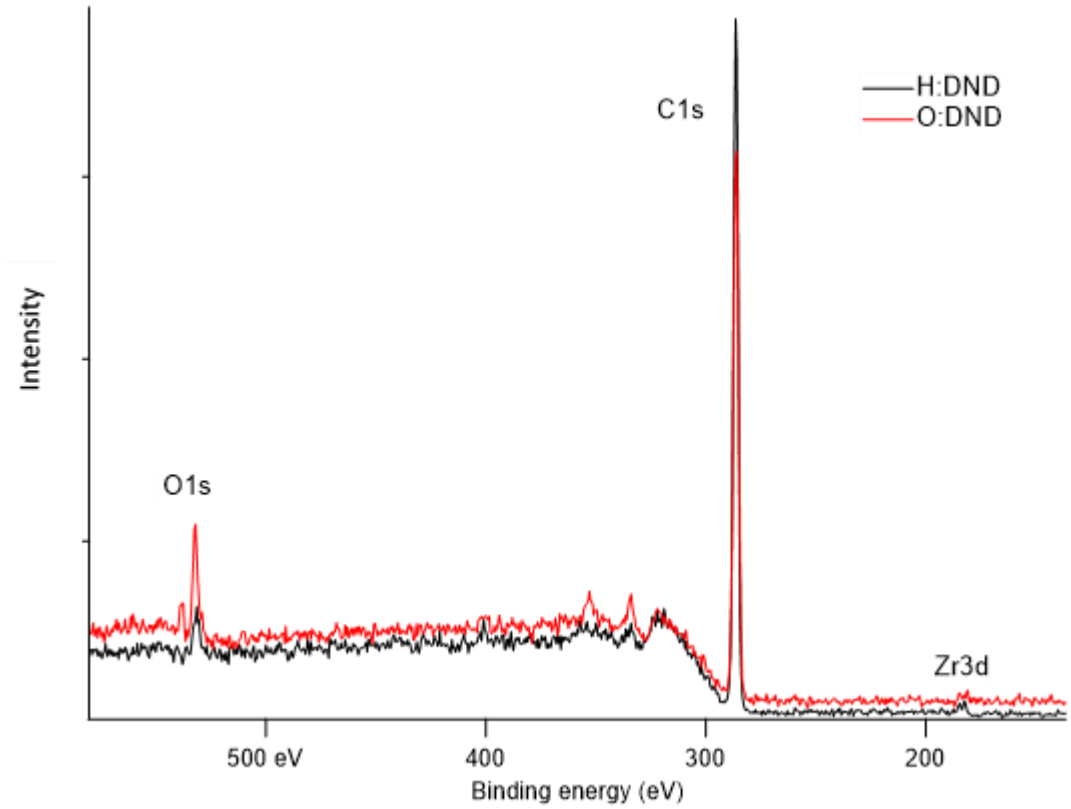

Figure 6.1.10: Widescan of the H and O terminated DND's such that the ratio of the C 1s:O 1s can be visualised. The percentage of Oxygen increases from 3% pre-oxidation which is most likely from surface contaminants, to 17% post oxidation which equates to having almost a 0.7ML of oxygenated surface of an DND assuming it is 5nm. Zirconium can be seen which is believed to be from Cubic Zirconia used in the milling process, however the atomic % is so small (<0.5%) that the relative oxygen contribution from it to the O 1s is minimal.

Figure 6.1.11 shows the C 1s spectra of the nanodiamonds after the O_2 gas anneal up to 420°C at Manchester University, and when the sample had been cooled down in an O_2 environment to allow room temperature to be achieved quickly.

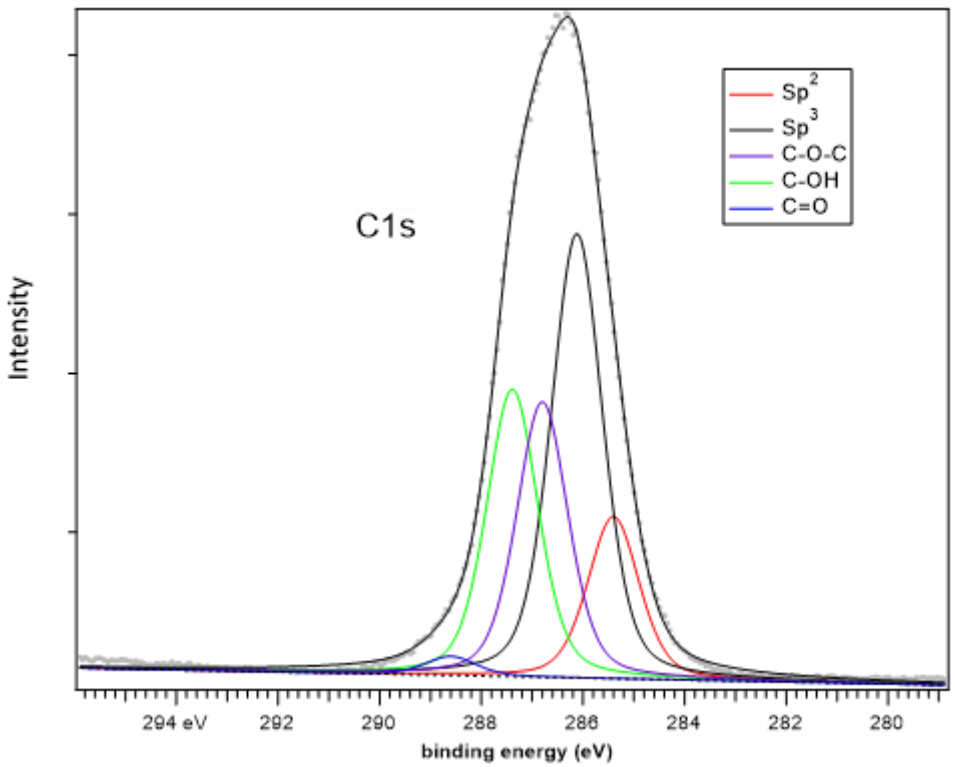

Figure 6.1.10: C 1s of the DND's post oxidation in-situ at Manchester. The percentage of OH on the surface has increased and overtaken the C-O-C bonds on the surface. this may be due to OH being a preferred formation at lower temperatures or residual hydrogen being free to bond onto oxygen sites upon the removal of the oxygen gas. To ensure an honest peak assignment constraints were kept consistent and peak widths set to match those of literature. High-resolution surface sensitive measurements of the C 1s were taken by Kerry Hazeldine at Aarhus synchrotron where photon energy was altered to determine the peak positions of the surface components. These components matched the positions of the components for the single crystal diamond work, but had an increased width of 0.4FWHM. For this spectra all the peak relative positions are being constrained too the positions for the single crystal consistently.

6.2 Discussion

6.2.1 Acid etch vs air anneal.

Looking at the Raman spectroscopy between the as received detonation soot, acid-etched and air-annealed samples we can see that both oxidation treatments remove the majority of sp^2 carbon, changing from D peak from 1350cm^{-1} to 1329cm^{-1} which is the difference between graphitic and diamond crystallographic structures. Due to diamond being a crystal lattice, in comparison to a sheet, they produce different vibrational modes upon excitation where diamond is 1332cm^{-1}, nanodiamonds are 1329cm^{-1} and graphite is 1350cm^{-1}. The signal to noise was considerably better for the air-annealed samples compared to acid-etched, where there are several potential reasons for this[4-6];

1. Contaminants although broken down in the acid end up adsorbing back onto the surface.
2. The acid has deformed some of the structure of the ND's.
3. Due to impurities in specifically nitric acid (such as metals) there's potential that the surface has been damaged.

It's worth noting that when suspending the DND's in water the acid-etched samples were severely unstable, this could be that the acid etches didn't work correctly creating either an incomplete termination or there's still some sp_2 dangling bonds on the surface. However, both the air anneal and acid etch have been repeated several times and the results has always been identical to what's been shown in Figure 6.1.1.

The oxidation having an effect on the PL and its relevance will be discussed more in Chapter 8, however it is important to note that although the emission spectra matches literature well, the exact centre is shifted slightly by about 20nm. As mentioned in Figure 6.1.3 the substrate has an effect on the emission of PL for nanodiamond[7]. Repeat experiments were tested with the annealed samples deposited onto platinum and gold but no PL was observed, this is theorised to be due to their workfunctions being large enough that holes are trapped into the substrate pulling away electrons from the DND's such that the de-excitation and emission via the fluorescence process never occurs[7-9].

The emission at around 680nm is rather unusual, although its centre aligns with the centre for the NV^- fluorescence the shape is unrepresentative of this where instead of a broad peak it looks sharp. The likely cause for this emission is most likely a surface defect, with the main suspect potentially a metal contaminant imbedded into the DND's[8].

6.2.2 Oxidation of H-terminated DND's.

The TEM show's that DND's are of an extremely high quality. Focusing in on individual DND's reveals sharp edges which suggest a very crystalline nanodiamond structure with potentially very little sp^2 or graphitic rings surrounding them. Although the samples for TEM were prepped with a very dilute solution, the visible clumping of them together suggests there is some agglomeration in the suspension[6].

The relaxation calculations showed that despite the previous slab calculations showing a preference of ether bonding, due to the small number of surface atoms and the flexibility of the diamond surface, the C-O-C bridge sites for stability are less essential for stabilisation of the surface structure. It also showed that the crystal orientations have different preferred terminations much like a bulk diamond. This may indicate that when oxidising the nanodiamond, a preferential oxygen species may be easier obtained for DNDs than bulk diamonds. It also shows that the quality of the DNDs is important; the higher crystallinity and larger sizes might display a more stable and higher electron affinity than DND's such as the ones used in 6.1.1.[10].

Tables 6.1 shows peak position versus temperature during the in-situ oxygen annealing cycle.

	Chemical Species positions (eV)			
Temperature (°C)	C=O	C-OH	C-O-C	C-O-O-C
200	530.4	532.1	529.9	N\A
280	530.5	532.1	533.0	534.6
320	530.5	532.2	533.0	534.2
420	530.5	532.2	533.1	N\A

Table 6.1: Positions of the chemical species and how they changed throughout the experiment. The biggest point of interest is actually the shift of the peroxide peak between 280-320 Celsius as it started to break down.

Table 6.2 shows the change in the area intensities of the chemical species on the diamond surface at different temperatures.

	Chemical Species normalised intensities			
Temperature (°C)	C=O	C-OH	C-O-C	C-O-O-C
200	0.27	0.45	0.40	N\A
280	0.27	0.3	0.66	0.44
320	0.28	0.37	0.69	0.35
420	0.28	0.80	0.84	N\A

Table 6.2: Area intensities of all the different O 1s spectra components observed during the annealing of nanodiamonds in oxygen.

Table 6.3 shows the overall oxygen percentage in the wide scans at different temperatures.

Temperature(°C)	200	280	320	420
O 1s %	3%	6%	7%	17%

Table 6.3: Table to show how the O 1s intensity as a percentage of the survey widescan increased at the important temperature steps.

From looking at the raw intensity and the oxygen species evolution in the O 1s core level in the Tables 6.1/2 and Figures 6.16/7, there are a few key oxidation steps which might have high importance for future applications of O:DNDs. Based on the O 1s to C 1s intensity up until 350°C there was less than a 25% surface coverage of oxygen on the DNDs. At certain temperature stages specific oxygen groups grow or modify in steps, which can have further applications for a controlled method of obtaining specific groups of oxygen species on nanodiamonds relatively simply. However, this may have the downfall that the overall surface oxygen percentage may be low. Ketone groups seem to attach almost instantly to the DNDs, most likely on step edges or on defect sites where the replacement of sp^2 carbon may leave singular carbon atoms bare. After that initial ketone species growth at 200°C increased incrementally throughout the anneal. This could also indicate that as the annealing procedure burns away any sp^2 on the surface, it attaches on the bare sp^3 atom. Hydroxyl at 200°C is also at its maximum of its contribution to the surface oxygen, therefore if OH groups are required

for a specific chemistry need, but other groups are undesirable, annealing up to 200°C may be an easier method then current methods of obtaining hydroxyl terminations as mentioned in Chapter 2. At 280°C we can observe that the amount of ether that has grown on the surface has increased. OH surface bonding had remained consistent, ketone had also slightly increased and peroxide has started to form also. Between 280°C and 320°C ether growth continues until it is by far the most notable surface species as shown in Figure 6.1.7 and Table 6.2, which may be a key step if C-O-C is the most desirable bond as at 320°C ether is by percentage of all oxygen surface species at its maximum. After annealing above 320°C, peroxide is no longer stable on the DND's and is completely gone by 350°C, indicating that the process of which peroxide forms such as reconstructions or large ketone ratio's as seen in Chapter 5 for (001) diamonds fix themselves. Interestingly, as the peroxide becomes unstable at above 320°C and disappears by 350°C it's between 320 and 420°C that hydroxyl growth then increases where it's growth overall and in comparison to ether, where OH had stagnated beforehand. As the total intensity and the O 1s:C 1s ratio between 320°C and 420°C increases dramatically as shown in Table 6.3, this suggests that wherever the peroxide bonding is breaking down OH and some C-O-C groups are forming instead[11-14].

Much like in Chapter 5 with calculating workfunction changes using the peak position of O_2, the effect of the workfunction of a material on the measured binding energy of a gas is much more evident in this step-by-step oxidation process[14]. Table 6.4 shows the oxygen gas phase peak position at various temperatures.

Temperature (°C)	Oxygen gas peak position (eV)
200	539.0
250	538.9
280	538.9
350	538.2
400	538.1
420	537.9

Table 6.3. The position of the oxygen gas phase peak at different temperatures. It can be seen that in the first 80°C, the peak only shifts by 0.1eV, however between 280° and 350°C, that 70°C step causes a change of 0.7eV,this is when we see the oxidation start to significantly increase, thus we expect the electron affinity to change the most during this temperature step.

The biggest shift in peak position is observed when the predominate oxygen growth is through the creation ether species. This matches with what is observed for bulk single crystal diamond that ether bonding is the most important factor for the positive electron affinity in oxygen terminations. The total workfunction shift between the H-termination and O-termination is 1.44eV by using the same equation given in 5.1, the change of workfunction can be calculated from -1.316E_B as was shown in Chapter 5.2. where 0.9eV of that occurs in the 280 to 350°C alone. This value is in good agreement with the value obtained from the UPS from the air annealed, and what's been seen in literature by others of 1.2-1.3eV as a difference between the two terminations. The overall electron affinity for each surface can't be determined, as the correction factor, C[15].

Looking at the widescans it is evident that based on the O 1s:C 1s ratio that an oxygen termination has been achieved. Before the anneal, the H-termination DND's had an oxygen coverage of 2.4%, but this is most likely due to surface contaminants or leftover oxygen which wasn't removed during the H-termination process. Post anneal the oxygen percentage is 16.8%, assumptions on whether this equates to a total surface coverage of oxygen due to fact that the size of the DNDs varies massively as can be seen in the TEM, and the larger sizes would have a much smaller surface:bulk ratio than smaller crystals. We can also see in the widescan a very small amount of ZrO_2, this is believed to be used in the milling process of the raw DND powders.

6.3 Conclusion

DND soot was procured and treated with both acid-etch and air-anneal treatments to remove graphitic carbon shells from the DNDs. This was successfully achieved, however concerns over our final product purity can be answered in both the PL and Raman spectroscopy which shows that the air anneal produces a purer final product. With a greater diamond signal and a lower sp^2 signal.

H-terminated DND's were annealed from 200°C to 420°C in 20°C steps to analyse the oxidation steps at various temperatures. The oxidation state of DND's annealed in pure oxygen is dependent on the temperature of the DND, where at certain temperature growth

of specific oxygen species can be observed. This has relevance in situations where a desired oxygen species is required but the use of acid's or reagents is unavailable or undesirable due to contamination chances.

The change in workfunction between the H and O terminated nanodiamonds was shown through the measuring of the gas-phase O_2 peak position and validated using UPS where the values for both data sets matches literature. The major driving force for the change in workfunction is the growth of ether groups on the DND's between 280 and 350°C, contributing 0.92eV of the total 1.44eV measured by itself.

DFT and TEM suggest that high-quality DND's can be thought of as small particles of diamond where each face is almost equivalent to its bulk counterpart; however due to a reduction in surface size the stability advantages of long chains of ether bonds isn't as effective, meaning that the nanodiamond surface has a more flexibility resulting in different surface species compared to the single crystal diamond surface. Although there is potential they are agglomerated and have to be broken down before used in various applications [13]

Figure 6.3.1 show's the difference in the band profiles before and after the oxygenation of the DND surface.

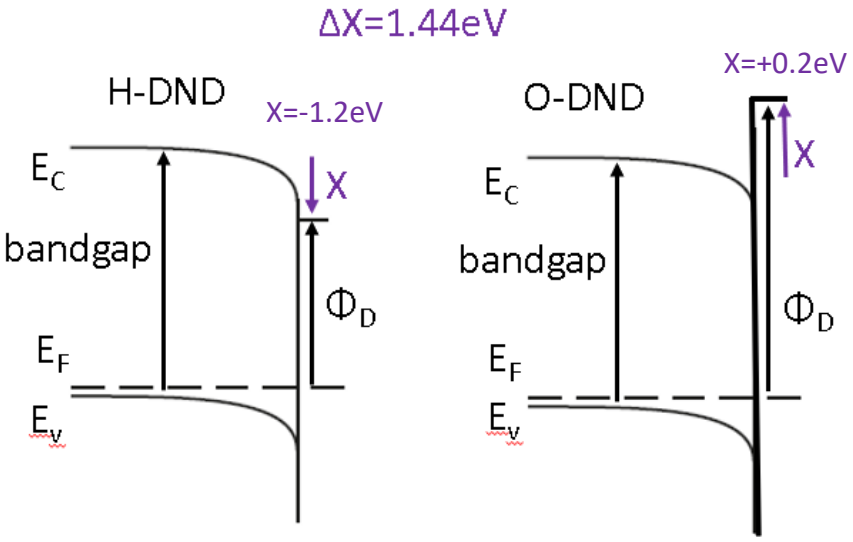

Figure 6.3.1: Band profiles for the oxygen and hydrogen terminated nanodiamonds where the both exhibit altering electron affinities as discussed in chapter 2. The affinities were calculated using the full Equation 5.1

References:

[1] – Lai, L.; Bardnard, A. A. Nanoscale. Vol 3. P2566-2575. 2011.

[2] -Bogatyreva, G. P.; Marinich, M. A.; Oleinik, G. S.; Bazalii, G. A.; Bilochenko, V. A.; Panova, A. N. J. Superhard Mater. Vol33. P208–216.2011.

[3]- Osswald, S.; Yushin, G.; Mochalin, V.; Kucheyev, S. O.; Gogotsi, Y. J. Am. Chem. Soc. Vol128. P11635–11642. 2006.

[4] - Mona, J., Tu, J.-S., Kang, T.-Y., Tsai, C.-Y., Perevedentseva, E., & Cheng, C.-L.. Surface modification of nanodiamond: Photoluminescence and Raman Studies. Diamond and Related Materials, Vol24. P134–138. 2012. https://doi.org/10.1016/J.DIAMOND.2011.12.027.

[5] - Mochalin, V., Osswald, S., & Gogotsi, Y. Contribution of Functional Groups to the Raman Spectrum of Nanodiamond Powders. Chemistry of Materials, 21(2), 273–279. 2009. https://doi.org/10.1021/cm802057q

[6] - Mermoux, M., Chang, S., Girard, H. A., & Arnault, J.-C. Raman spectroscopy study of detonation nanodiamond. Diamond and Related Materials, Vol87, P248–260. 2018. https://doi.org/10.1016/J.DIAMOND.2018.06.001

[7] - Smith, B. R., Gruber, D., & Plakhotnik, T. The effects of surface oxidation on luminescence of nano diamonds. Diamond and Related Materials, Vol19(4). P314–318. 2010. https://doi.org/10.1016/J.DIAMOND.2009.12.009

[8] - Stehlik, S., Ondic, L., Berhane, A. M., Aharonovich, I., Girard, H. A., Arnault, J.-C., & Rezek, B. Photoluminescence of nanodiamonds influenced by charge transfer from silicon and metal substrates. Diamond and Related Materials, Vol63. P91–96. 2016. https://doi.org/10.1016/j.diamond.2015.08.009

[9] Chung, P.-H., Perevedentseva, E., & Cheng, C.-L. The particle size-dependent photoluminescence of nanodiamonds. Surface Science, Vol601(18). P3866–3870. 2007. https://doi.org/10.1016/J.SUSC.2007.04.150
[10] – Karin Larsson. Simulation Of Diamond Surface Chemsitry: Reactivity And Properties. June 2019. KARIN LARSSON. SIMULATION OF DIAMOND SURFACE CHEMISTRY: REACTIVITY AND PROPERTIES. DOI: 10.5772/INTECHOPEN.86865
[11] - Sebastian Osswald, Gleb Yushin, Vadym Mochalin, Sergei O. Kucheyev, Yury Gogotsi Control of sp2/sp3 Carbon Ratio and Surface Chemistry of Nanodiamond Powders by Selective Oxidation in Air. Vol 128. P11635-11642. 2006. https://doi.org/10.1021/JA063303N
[12] - Krüger, A., Kataoka, F., Ozawa, M., Fujino, T., Suzuki, Y., Aleksenskii, A. E., Vul', A. Y., & Ōsawa, E. Unusually tight aggregation in detonation nanodiamond: Identification and disintegration. Carbon, Vol43(8) P1722–1730. 2005. https://doi.org/10.1016/J.CARBON.2005.02.020
[13] - Krueger, A. Current issues and challenges in surface chemistry of nanodiamonds. Nanodiamonds, P183–242. 2017. https://doi.org/10.1016/B978-0-32-343029-6.00008-8
[14] - Stephanus Axnanda ,Marcus Scheele, Ethan Crumlin, Baohua Mao, Rui Chang, Sana Ran,I Mohamed Faiz, Suidong Wang . Paul Alivisatos. Direct Work Function Measurement By Gas Phase Photoelectron Spectroscopy and Its Application on PBS Nanoparticles. Nano Letters. Vol13 (12). P6176-6182. 2013.
[15] -O . Williams Arnault, Kruger et al. Nanodiamond (RSC Nanoscience & Nanotechnology). Royal society of Chemistry. May 2014.
[16] - Osawa, E., Sasaki, S., & Yamanoi, R. Deagglomeration of Detonation Nanodiamond. In Ultananocrystalline Diamond. Elsevier. P165-179. 2012. https://doi.org/10.1016/B978-1-4377-3465-2.00006-2

Chapter 7 – Adsorption of Fluorouracil (5FU) onto diamond surfaces.

This chapter will discuss experiments in controlling the amount of 5FU on diamond surfaces for applications in drug delivery and a continuation on work initially started by Dr Di Hu[1] at Aberystwyth University. Our group previously had deposited 5FU on H/O:(001) terminated diamond and measured film thickness and molecule orientation through the use of XPS and NEXAFS respectively[1].

DFT calculations using Quantum-Espresso have been conducted on H/O terminated diamond as well as the bare surface to determine the stability of the molecule in different environments. Raman spectroscopy has been conducted on 5FU in super-critical antisolvents deposited on a (001) diamond surface, in addition to measurements taken using Ag nanoflowers which are capable of surface enhanced Raman spectroscopy (SERS) to determine if the stability of diamond would inhibit the degradation of 5FU on the nanoparticles where measurements were taken hours apart from each other. Vibrational modes of 5FU were calculated using Gaussian09 software[2] to determine what the peaks in the Raman spectra represent.

5FU as shown in Chapter 2 was attached to 5nm DND nanodiamonds with hydrogen and oxygen terminations and PES measurements were taken after 1mbar of water dosing to analyse stability, film thickness and orientation of the molecule. Dynamic light scattering measurements were taken as a complimentary method and to analyse the suspension of 5FU:DND systems in water where 5FU is typically insoluble. Spectral imaging was then conducted for 5FU:O-DND's to demonstrate if the photoluminescence can be used for bio-imaging. Measurements were taken at both Manchester University and at the B07 branchline at Diamond Light Source.

In subsequent measurements 40nm NV^- ND's were then coated with 5FU and the 633nm emission was investigated to evaluate if it would be strong enough for bio-imaging applications.

Oxygen terminated single crystal diamond was achieved using boiling sulphuric acid and potassium nitrate. Oxygen DNDs were achieved through a 450°C air anneal of raw DND soot. SERS active Silver Nanoflowers (AgNfl) were purchased from sciventions, and the

H:terminated DNDs and 40nm Fluorescent nanodiamonds (FNDs) were obtained from Element Six.

For XPS measurements C 1s peak fits were constrained with a 0.65GL ratio with an initial width of 0.9 with flexibility of +/-0.05 either side with all components constrained to each other.

7.1 Results

7.1.1 – DFT calculations of 5FU on diamond surfaces.

Figure 7.1.1 shows the the molecular dynamics calculation of 5FU on a clean diamond surface, showing a degradation of the molecule where an H breaks off from the molecule.

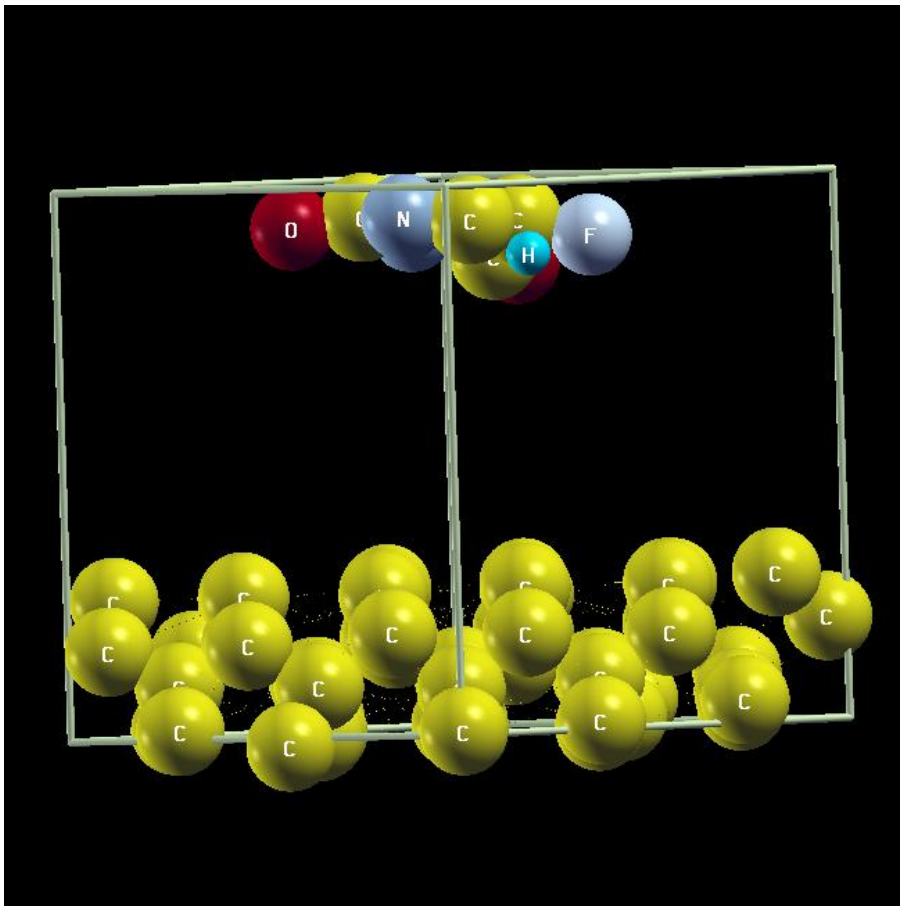

Figure 7.1.1: Breakdown of 5FU on clean diamond (001) and the removal of H from a nitrogen atom from the 5FU. This H atom can either; A) form a HF molecule as in[4], or attach to the diamond surface.

Figures 7.1.2 and 7.1.3 shows the orientation comparison between the 5FU molecule when sat on a OH:(111) terminated diamond in comparison to the O:(001) terminated diamond from Chapter 5, where there is a subtle change in orientation but 5FU remains stable on both.

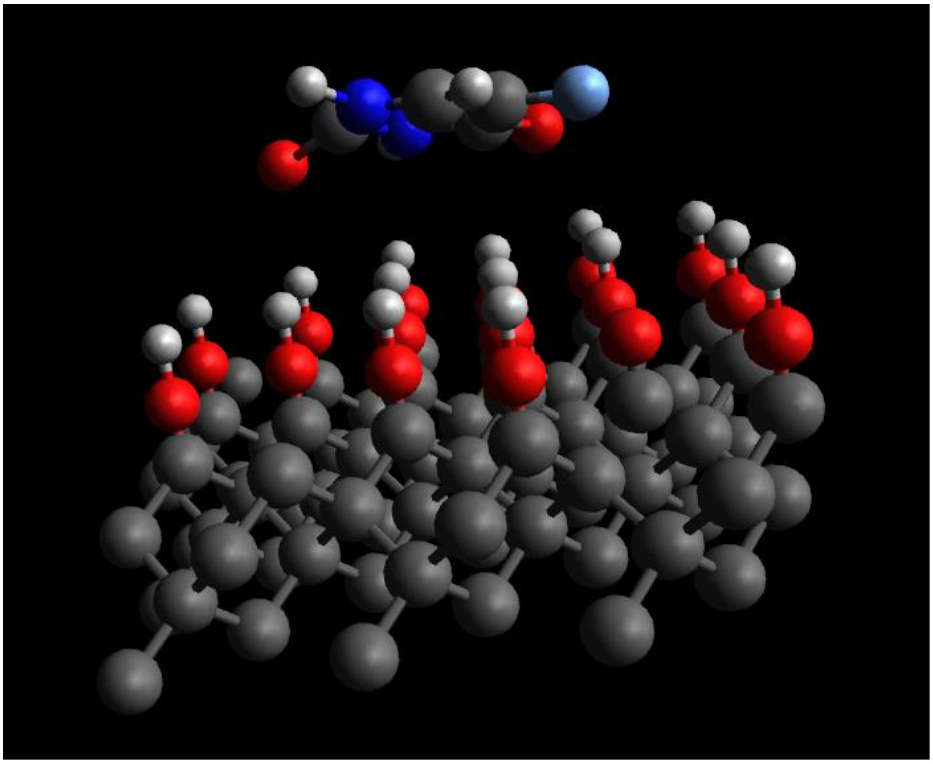

Figure 7.1.2: 5FU's preferred orientation on OH terminated (111) diamond. The molecule is stable and exhibits a generally flat structure.

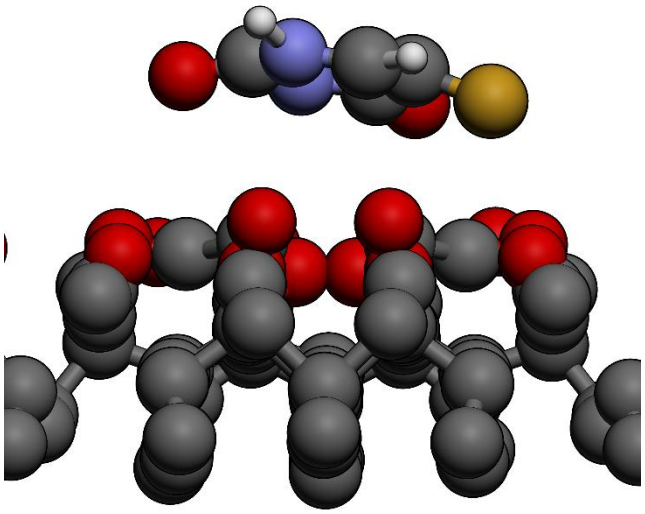

Figure 7.1.3: 5FU on a (001) oxygen terminated diamond with a mixture of C-O-C, C=O and C-O-O-C bonding on the surface, unlike with the OH surface the 5FU bow's more away from the substrate.

7.1.2 – Raman analysis of degradation of 5FU on Ag:Diamond interfaces.

Figure 7.1.4 shows a diagram of how the SERS interaction appears to work for these silver nanoflowers (AgNfl)[3-4]and the resulting afm image from the AgNfl deposited on an O:(001) single crystal diamond.

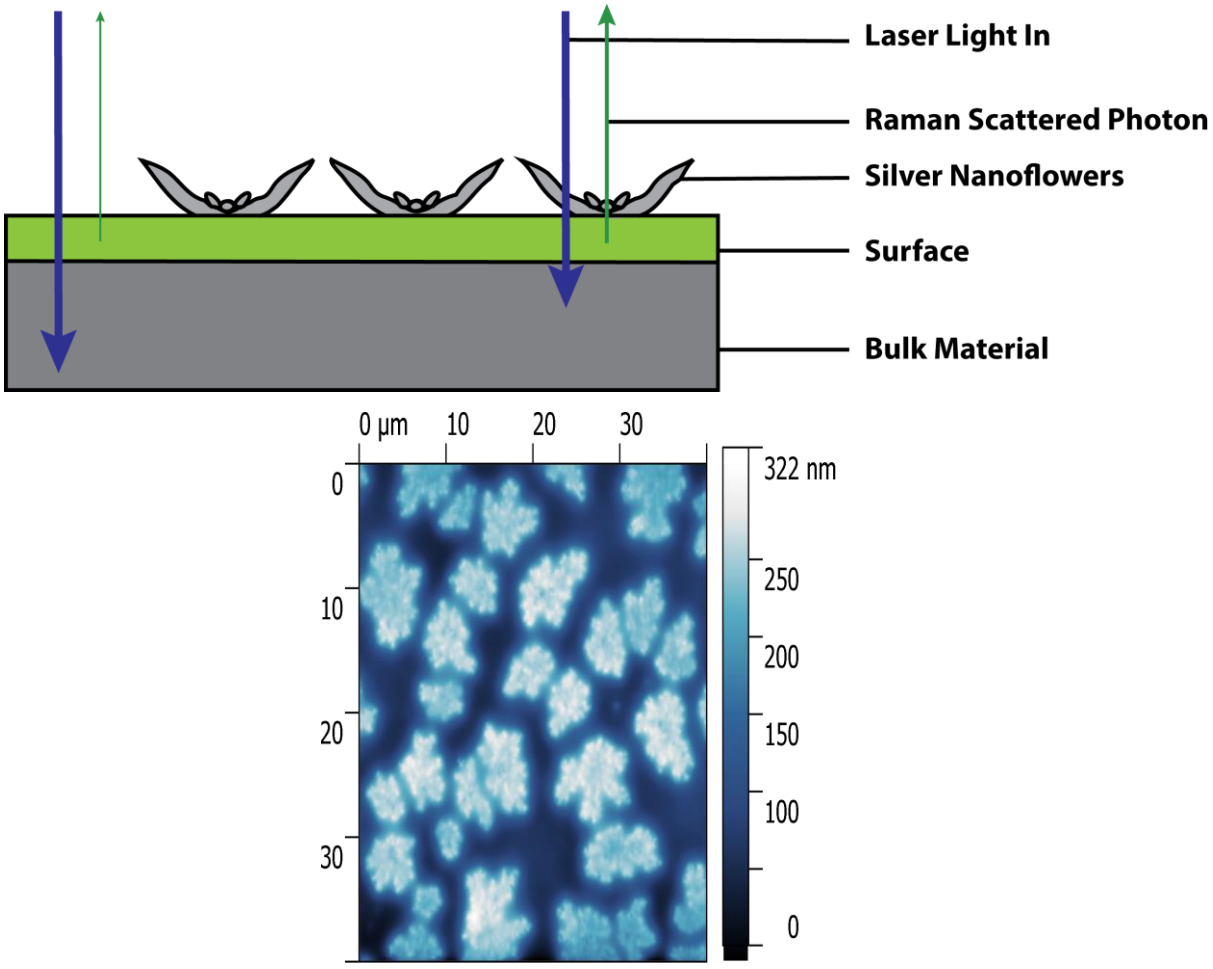

Figure 7.1.4 – Diagram of the SERS setup for monitoring 5FU degradation on AgNfl, and AFM showing the nanoflowers structure and size.

Figure 7.1.5 shows the Raman spectra of the 5FU nanoparticles on a O:(001) diamond, and Figure 7.1.6 shows the SERS using the AgNfl with the 5FU at different time intervals. Figure 7.1.7 represents the calculated vibrational modes of 5FU and the corresponding wavenumber for each peak.

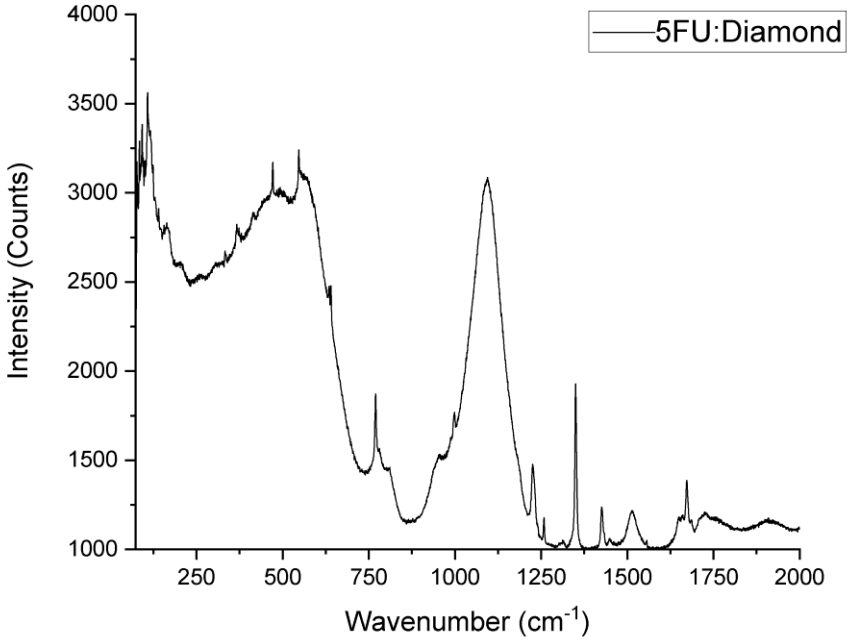

Figure 7.1.5: Raman spectroscopy of the 5FU molecule particles on an oxygen terminated diamond. Due to the lack of symmetry in the 5FU molecule the only vibrational modes which are detectable are ring stretches or breathing modes.

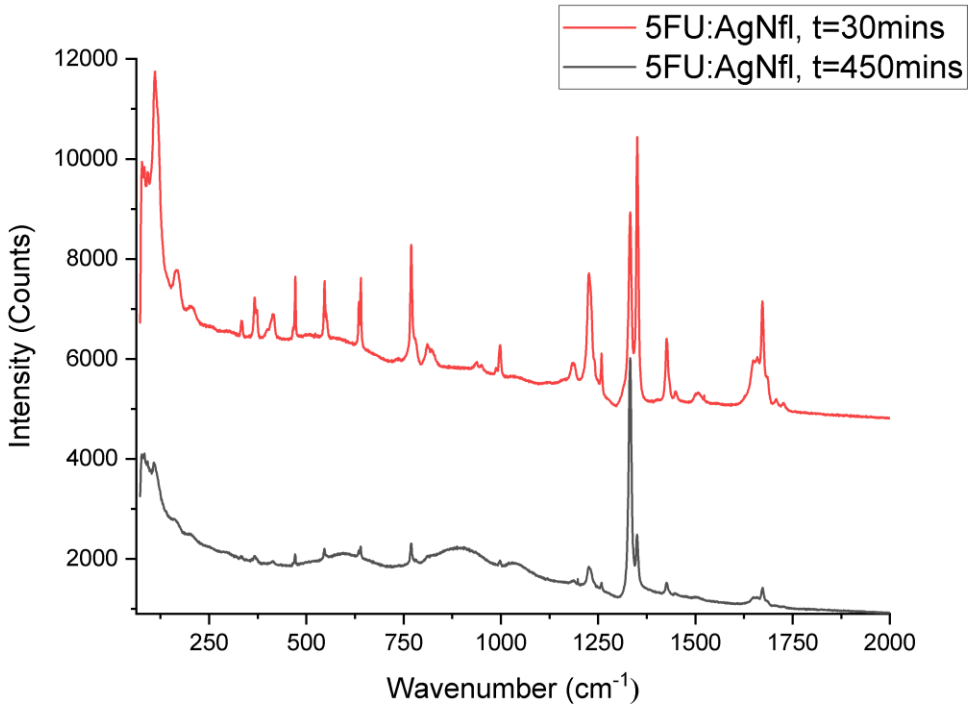

Figure 7.1.6: SERS of the 5FU nanoparticles deposited on the AgNfl:Diamond surface. After 8 hours the molecule is showing a dramatically decreased Raman signal, suggesting that the molecule is degrading over time on the silver nanoflowers which agrees with previous experiments of 5FU:Ag interactions.[5]

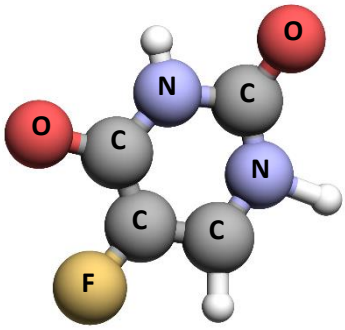

Vibration (cm^{-1})	Vibrational mode
108.6	pyrimidine ring stretch
550.2	In-plane – ring bend
1094.3	Out of plane –pyrimidine ring bend
1225.4	C-F + ring bend
1350.0	Ring Wag + C-H
1425.7	Ring Wag + N-H
1514.9	In-plane N-H in bend
1672.7	Symmetric C=O

Figure 7.1.7: Calculated Raman active vibrational modes and the corresponding wavenumber such that individual peaks can be compared to the respective bond. A diagram of 5FU is given for better association of these modes. Calculated using the G09 software package.

7.1.3 - 5FU on H:DNDs.

1ml of 2w.t% H:DNDs were mixed with 0.01g of 5FU and left to settle for 30 minutes for sedimentation fractionation due to the insolubility of 5FU in water such that any coagulants sunk to the bottom of the solution. The top of the solution was then drop-cast onto a gold foil and in-vacuo evaporated. Figure 7.1.8 shows the XPS widescan for the 5FU:H-DND's after dosing the chamber with 1mbar of water at Manchester university. The atomic percentages are in relation to just the 5FU:DNDs calculated in casaXPS[6]. From these percentages the ratio of 5FU:DND can be calculated using the NIST effective attenuation length database and software.

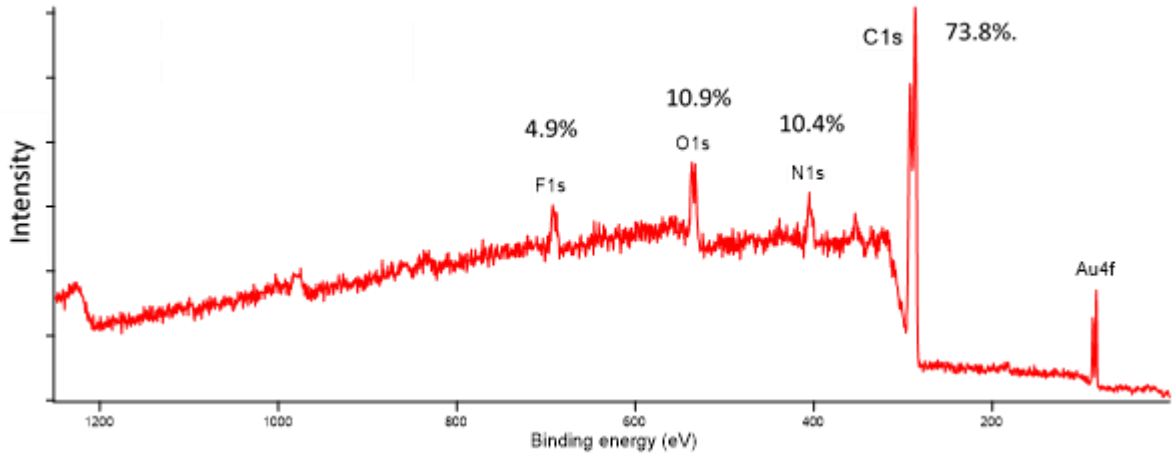

Figure 7.1.8: Widescan of 5FU:H-DND solution, which is roughly 23% 5FU-DND. The Au 4f peak coming through suggests that an incomplete coverage. All atomic percentages are purely for the 5FU/ND.

Figure 7.1.9 shows the DLS measurements of the H:DNDs, 5FU and the solution containing them both.

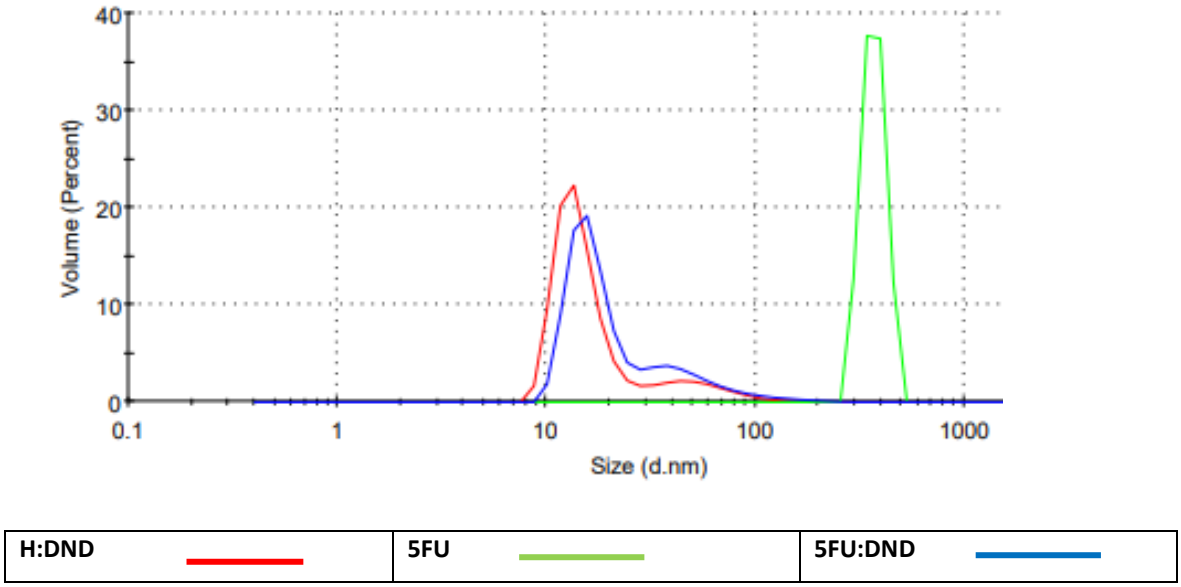

Figure 7.1.9: DLS measurements of H:DND, 5FU and 5FU:DND solutions respectively in terms of the percentage of the solution by size.

7.1.4 - 5FU on O:DNDs.

1ml of 1w.t% O:DNDs was mixed with 0.005g of 5FU and left to settle for 30 minutes such that any coagulants sunk to the bottom of the solution for sedimentation fractionation. The top of the solution was then drop-cast onto a gold foil and in-vacuo evaporated and measured at the B07 branchline at Diamond Light Source.

Figure 7.1.10 shows the variation of intensity ratio between the 5FU:DND dependant on whether 870 or 490eV photon energy was used. Figure 7.1.11 shows the fitted C 1s core level at 490eV. The C 1s was used as comparisons between the layers of 5FU to DND can be made, when an attempt to obtain an F 1s was made before a suitable number of scans could be obtained for good resolution the molecule had broken down.

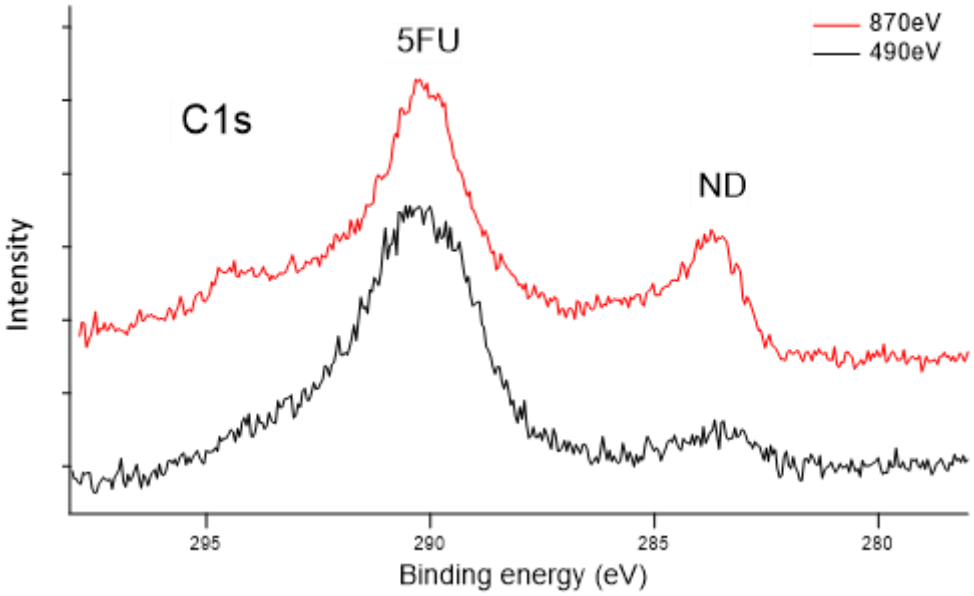

Figure 7.1.10: C 1s of the 5FU:O-DND at two photon energies, showing that as the photon energy and the probing depth are increased, the ratio of DND:5FU increases. The spectral features look more defined and show different shapes at certain energies suggesting potential damage at the surface this is indicated by the loss of the features on the higher binding energy side (C-F) where the fluorine also disappeared from the survey spectra.

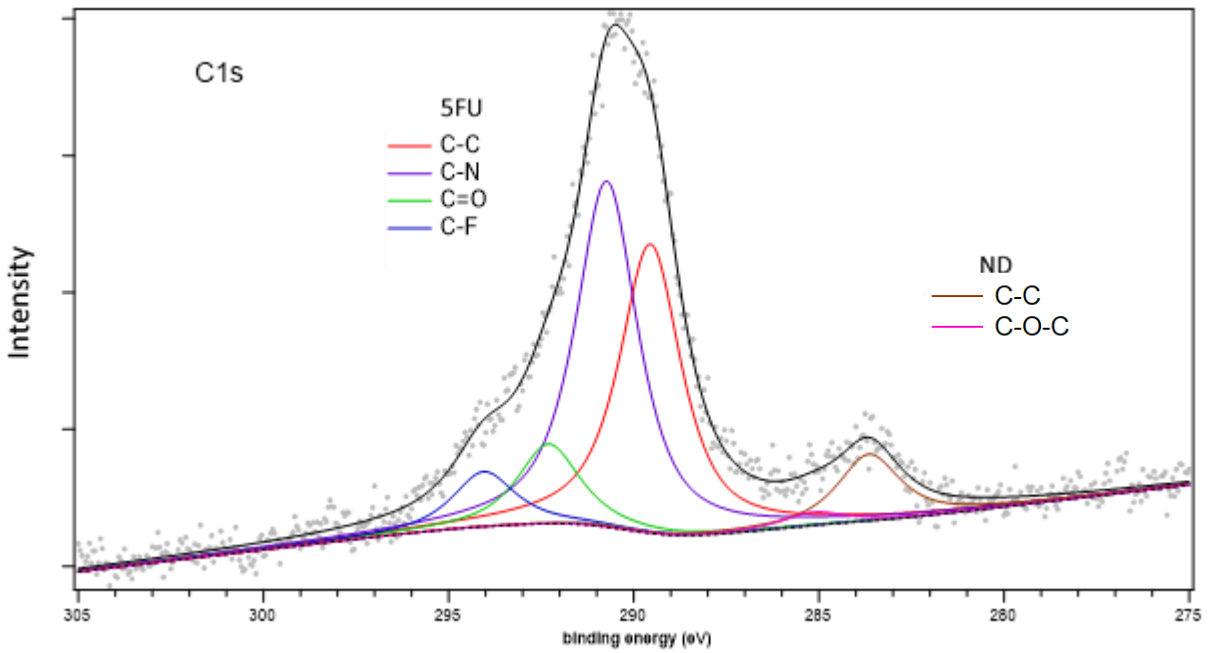

Figure 7.1.11: C 1s core level Spectra with peaks fit for 5FU and the O-DND at 490eV photon energy.

Figures 7.1.12 and 7.1.13 show the N-K edge and O-K edge for the 5FU:DND film respectively which were collected at B07.

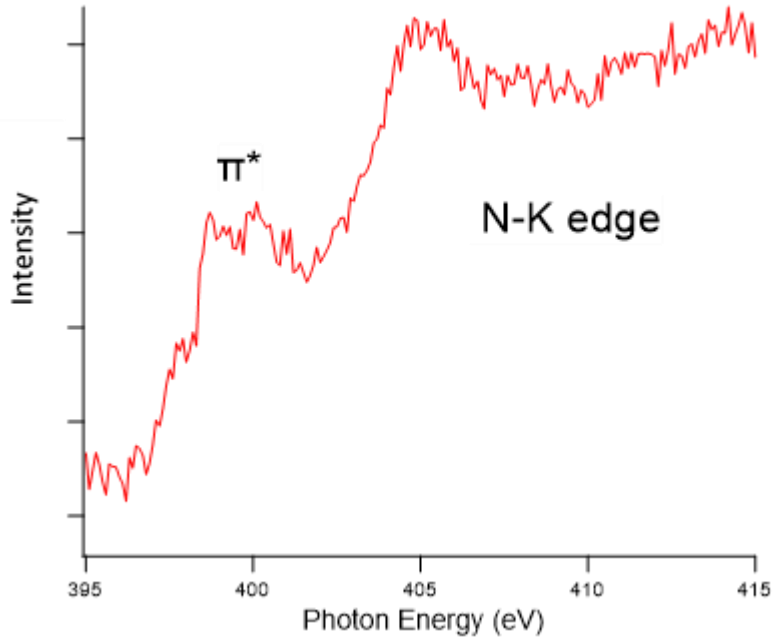

Figure 7.1.12 – Auger N-K edge of the 5FU molecule which from information in the π we can determine if any degradation has taken place and the orientation of the molecule, which the observation of a π* suggests a flat orientation with an incidence angle of 54°. The π*is broad due to the different environments the nitrogen in the ring exist in and some differences in the orientation of the molecule..*

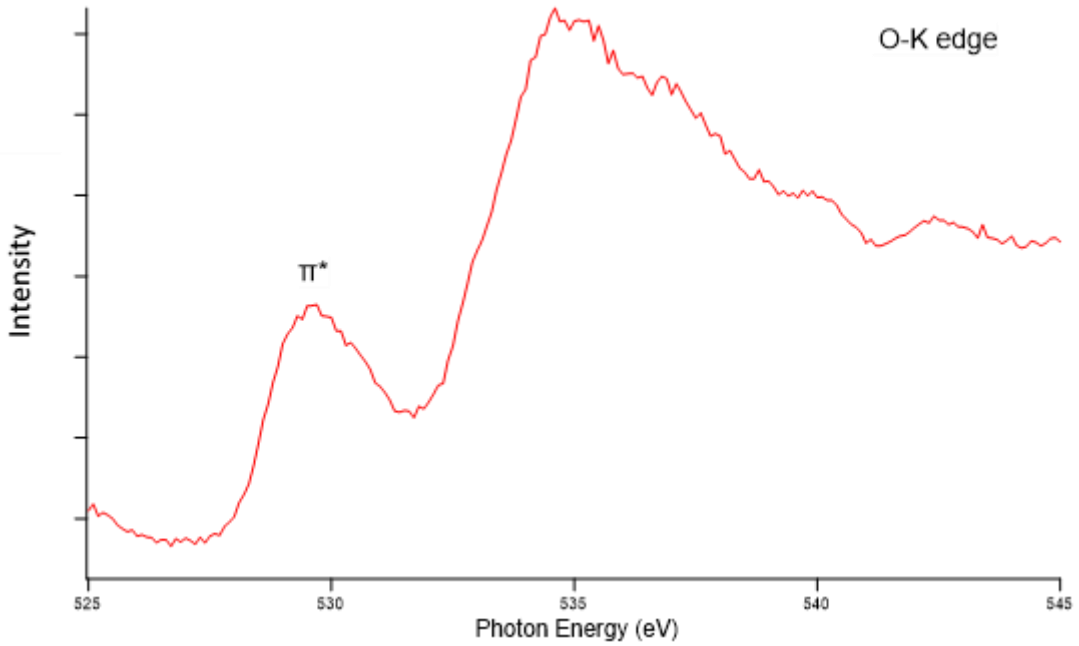

Figure 7.1.13: Auger O-K edge where the Pi orbital, from this we can attempt to determine the orientation of the C=O bond and gain information on the orientation of the 5FU molecule on the surface. The broadness will be due to some scattering effects and the difference types of C-O environments will be present on the DND surface as well as differences in orientation of the molecule. As the nanodiamonds are spheres, not all detectable 5FU will be laying flat on the top surface.*

Figure 7.1.14 shows a hyperspectral image taken of the 5FU:O-DND and the corresponding photoluminescence spectra indicating that coagulation is occurring. 5FU has a strong absorption in the blue band of the spectra and has a fluorescence spectra centred around 570nm[13-14].

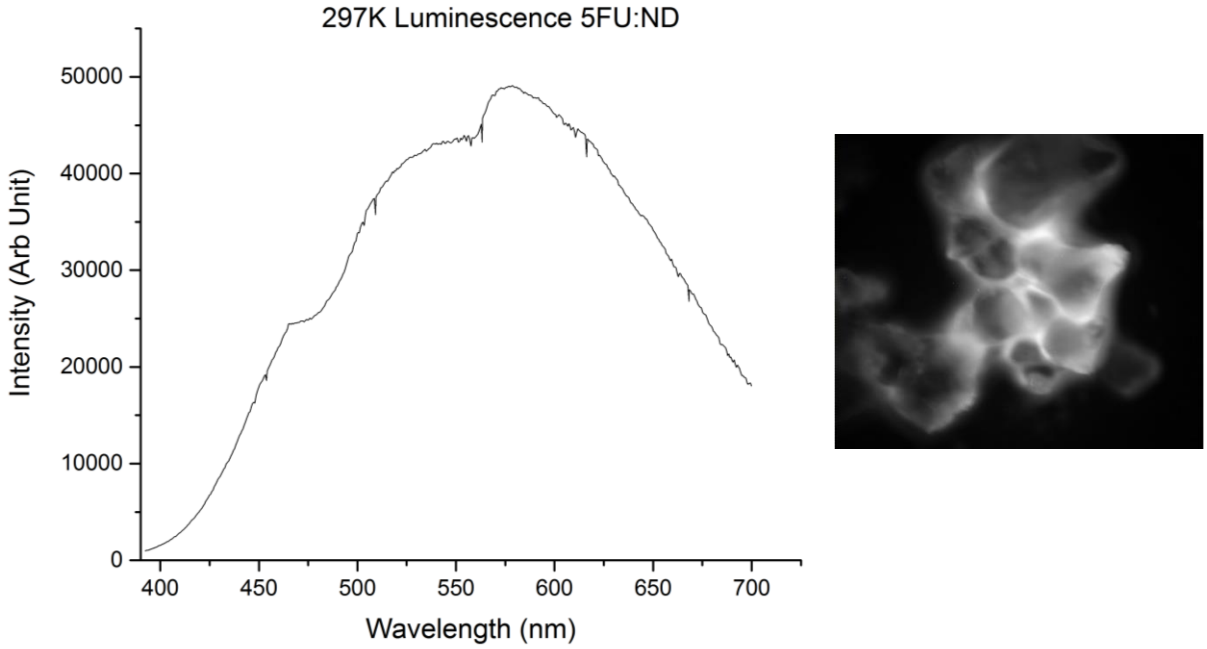

Figure 7.1.14: Luminescence spectra and the resultant spectral image from 430-500nm from exciting the 5Fu coated O:DNDs with a 325nm UV source. Bright patches in the image which are representative of the DND fluorescence are occurring where due to large coagulations in the suspension inhibit a full 5FU surface coverage of the DND surface.

7.1.5 - Use of 40nm NV^- DND's for drug delivery applications.

Figure 7.1.15 shows TEM of the 40nm NV^- NDs. These are shown to display high crystal quality which, as mentioned in Chapter 6, is important for the understanding of surface termination species.

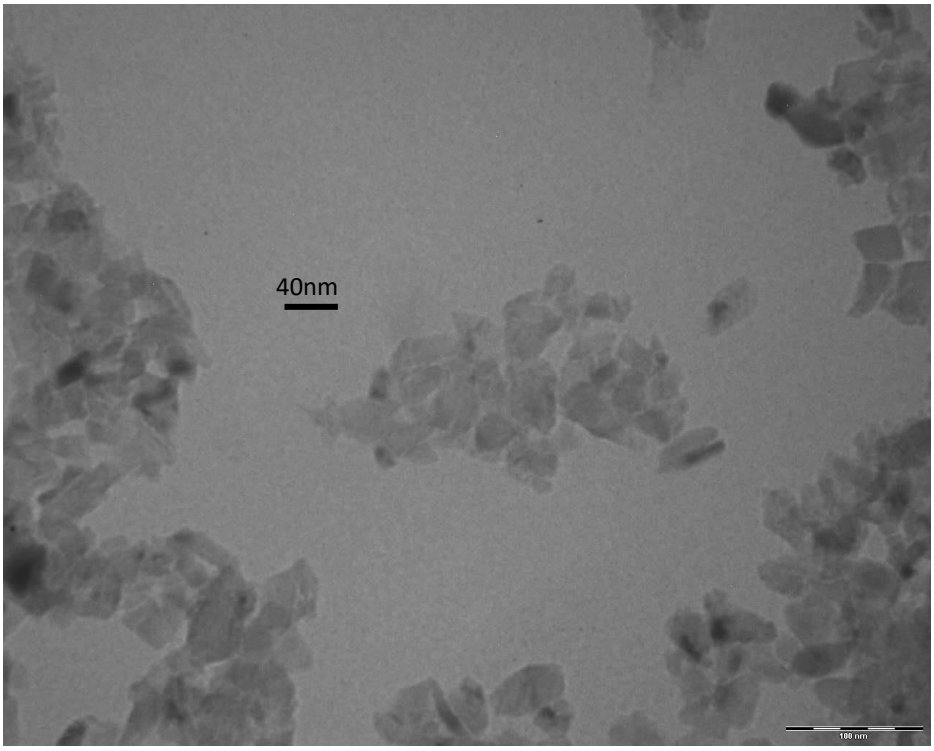

Figure 7.1.15 – TEM of 40nm ND's which display strong crystal edges indicating a lack of graphitic rings, this allows for a simpler understanding of the terminations of the surfaces. It is assumed that each face exhibits structure similar to the bulk crystal.

Figure 7.1.16 shows the confocal microscopy of the 40nm NV- Fluorescent NDs (FND), which were probed with a 596nm laser. From comparing the PL of the DND's to the 5FU:DNDs, we know that 5FU does not absorb in this wavelength.

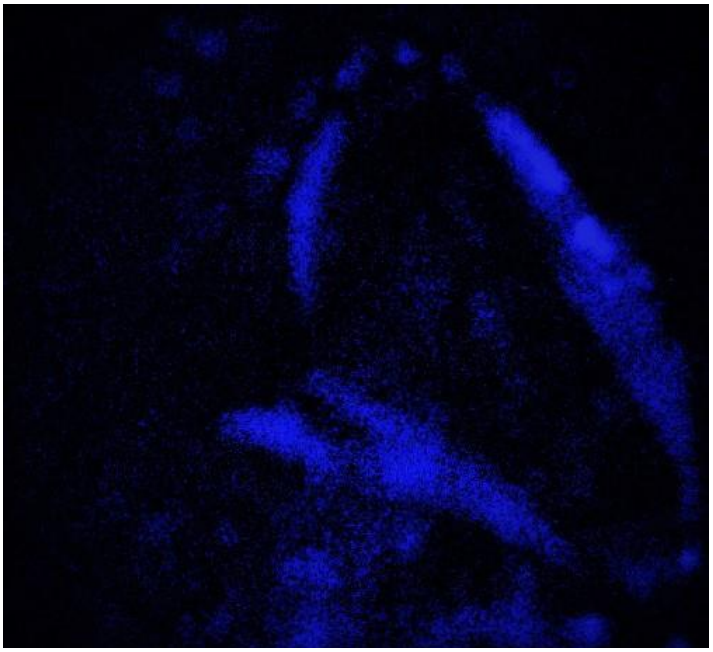

Figure 7.1.16: Confocal microscopy of the NV^-ND's which were pumped with a 596 laser to simulate the probing of the NV^- vacancy in 5FU:ND scenarios. Each pixel has a 80x80nm resolution.

7.2 Discussion

7.2.1 - DFT of 5FU on (001) diamond surfaces.

When considering the clean surface, hydrogen is stripped away from the 5FU, with the assumption that the diamond surface is trying to terminate itself. It would then follow suit, such as the previous studies indicated, that being as F would rather be in an H-F state in comparison to C-F that it might strip the individually bonded hydrogen from the surface.[5] However this was not observed during the calculation and is merely a hypothesis. This means that any free diamond bonds will damage the 5FU molecule, and the loss of a single hydrogen can drastically effect the chemical in its role as an anti-cancer drug as the N-H site is replaced to form fluorouridine triphosphate (FUTP) or fluorodeoxyuridine monophosphate (FdUMP) which is a requirement for break down of RNA and DNA and inhibition of thymidylate synthase[6-7].

5FU appears to be stable on O terminated surfaces, and the DFT calculation of the flat laying 5FU molecule agrees with the NEXAFs data obtained by Di Hu[1]. The orientation of the molecule is important as stacking defects occur in organic molecules which stack perpendicular to the surface[5] which would limit the number of total molecules which will be electrostatically attracted. This has implications for bulk diamond use as catheters or stents in the future as the termination will play an essential role in obtaining the desired effect whether it be to reduce clumping on the surface or act as a slow release mechanism.

7.2.2 –Measuring degradation of 5FU using SERS.

Measuring the bulk powder on its own, whether it be on a conventional silver film or diamond is unproductive, being as the molecule has low symmetry and generally likes to form polar balls in solutions where 200nm is a best case scenario for particle size using DMSO, observing a uniform thin film is impractical[9]. Attempts were made make a film but produced poor results. From Raman spectroscopy we can see the ring vibrational modes however they hold little information about the molecule or the stability of individual bonds, and as discussed in Section 7.2.1 each one is essential for the molecule to exhibit its benefits to patients.

The measurements using the SERS active AgNfl provided surprising results. Where Figure 7.1.6 show that it isn't just that the silver mediates the breakdown of the molecules from $C3H_2FN2O2$ into $C_3HN_2O_2$ and HF[5-10], but over a long enough period of time the entire

molecule breaks as a reduction in all individual bond's and the ring vibrational modes all decrease. This could be the difference between previous experiments being done in UHV, or that the HF starts to attack the molecule itself over a period. Scans were repeated 3 times in separate areas of the surface to ensure no localised heating from the laser was causing the breakdown of the molecule. The spectra shown are the average of those three areas. No measurable decrease over time for the ring bend or wagging for the 5FU on the single crystal diamond in the Raman spectroscopy was observed.

This raises the question that currently in medical delivery of 5FU, is the flow rate of the drug quick enough that the percentage of 5FU molecules that sit on the Ag sites and breakdown unobservable? Future experiments involving the use of NAP to flow in vapours of 5FU on silver and various other surfaces would be interesting to see if there is a required amount of time that 5FU has to interact with silver before total breakdown is measurable at different pressures[5,10].

7.2.3 – H/O DND interactions with 5FU.

From the PES, calculating the film thickness of 5FU on the nanodiamond surface gave values of 2nm for the oxygen termination, and 0.9nm for the hydrogen. This was conducted using the NIST effective attenuation length data base software. Where the equation is as follows:

$$Eq\ 7.1 \qquad \frac{I_A}{I_B} = K\frac{1-\exp\left(-\frac{d}{\lambda_A cos\theta}\right)}{\exp\left(-\frac{d}{\lambda_B cos\theta}\right)}$$

Where I_A is the intensity of the top layer of a material in XPS of which the thickness is desired, and I_B is the intensity of the underlayer. The thickness of layer a is defined by d, where θ is the angle of measurement and $\lambda_{A/b}$ are the effective materials attenuation lengths. The relative intensity ratios between the two was calculated from the percentage of 5FU from the F 1s percentage, as due to charging determining the differences between 5FU and DND in the C 1s would be difficult. The ratio's for the H/O:DND was determined from the spectra from Figures 7.1.8/11 respectively. For the H terminated samples at Manchester, 23% of the scan was contributed to from 5FU (λ=1486.6eV), whereas comparing the C 1s at B07 (λ=490eV) 89.7% of the spectra was 5FU.

The thickness measurements follows suit from the XPS data D. Hu obtained for the bulk crystal terminations, although the oxygen:DND had less 5FU than the single crystal, and the hydrogen had more. Unfortunately when looking at the C 1s for different probing depths by varying the photon energy, it could be seen that the fluorine was almost completely removed. Looking at the higher photon energies showed that the 5FU just below the surface was still stable, but after 30 minutes there was no evidence of any C-F bonds. Unfortunately, when an F 1s spectra was attempted there was not any visible signal by the 2nd scan. One explanation can be thought of is that the molecule itself degraded from the beam due to the large flux present at synchrotrons. The N-K edge matches what was observed for 5FU on the single crystal, suggesting that the molecule lays parallel to the surface.

The dynamic light scattering also shows some coagulation in the H-terminated DNDs, and that even coating them with 5FU all that happens is this 1nm coating is applied to the smaller of the particles. It does appear to bind a lot more to these larger clumps forming what would appear to be layers of 4-5nm, this may due to several 5FU molecules being trapped between different DNDs and causing even further coagulation[11]. However as can be seen from the solution containing just 5FU, the particle size has been brought down drastically, such that the average particle containing 5FU is 10% of the size. This can have improved benefits in drug delivery where 5FU is theorised to be less efficient than expected due to the fact it forms these polar 5FU agglomerations in solution that have difficultly penetrating cell walls. Through the control of the oxidation of the DNDs the layer of 5FU can be varied by a nm, although this may not seem significant it is a >50% increase in the transported amount of 5FU. If the situation arises that the amount of DNDs introduced into the patient must be kept to a minimum to avoid concerns of large DND deposits in the body, O:DNDs may be the best alternative. This is without taking into consideration however the research going into what types of functionalised nanodiamonds end up in specific sites in a patient's body. In this work both terminations also survived the initial water dosing of 1mbar to prove the stability of the drugs on the nanodiamond in the NAP cell at manchester. This is important as it shows that whilst 5FU is insoluble in water, it can be suspended in water via the physical adsorption onto DND surfaces and remains adsorbed even out of solution during dosing allowing for easier drug delivery and potential to avoid using more toxic solutions to suspend them.

From the luminescence data we can also observe that in comparison with the ND data from Chapter 6.1.2, the 5FU exhibits its absorption around 480nm and quenches the diamond fluorescence, this is important as for applications in bio-imaging any quenching from the 5FU will reduce the expected signal[12]. We observed no loss in any emission past 550nmm however, Which is ideal for biosensing using NV^- diamonds as shown in Figure 7.1.16. This is if the NV^- peak is isolated from the rest of the spectra, the intensity will be strong enough such that potentially individual nanodiamonds can be imaged.

The TEM and microscopy showed promising signs for future applications of terminating FND's with a specific chemical species, designated to control the amount of 5FU adsorbed for drug delivery applications with the benefits of reducing particle size and increasing chance of cell uptake, whilst allowing for bio-sensing in-situ. Further work would be to terminate these 40nm NDs with oxygen, hydrogen and amine terminations and mix them with 5FU to obtain XPS and DLS measurements as well as repeated confocal microscopy measurements. Ideally for future experiments an ultrasonic probe would be beneficial to help breakdown any coagulation in solution.

7.3 Conclusions

The amount of 5FU that is adsorbed onto a nanodiamond surface can be controlled by modifying the nanodiamond surface. H-terminated DNDs adsorb 1nm of 5FU, whilst O-terminated adsorbed 2nm, whereas the bare diamond surface stripped away hydrogen from the 5FU. The molecule also suffered beam-damage during synchrotron investigations due to the high flux with the C-F bond breaking. Information in the N-K edge and O-K edge provided orientation information about the molecule on the surface where it lays in a flat orientation on the nanodiamond surface.

DNDs and FNDs can be used as biomarkers whilst also delivering 5FU, with 5FU quenching any UV photoluminescence emission the probing of an nitrogen vacancy will remain unaffected if pumped with a 532nm+ source. 5FU coated nanodiamonds decrease the particle size of 5FU in solutions by over 1000%, this may allow for better cell uptake and therefore larger efficiency in the chemotherapy treatment.

References:

[1] –Di Hu. Surface Modification And Electronic Structure Characterisation Of Carbon-Based And Iron Based Materials. PhD Thesis. Awarded 2017. HTTP://HDL.HANDLE.NET/2160/04016083-F5C2-4542-A75A-74EE93B36100.

[2] – M. J Frisch et al. Gaussian 09. Gaussian, Inc., Wallingford CT, 2016.

[3] – N. Cathcart, V. Kitaev, Multifaceted Prismatic Silver Nanoparticles: Synthesis By Chloride-Directed Selective Growth From Thiolate-Protected Clusters And SERS properties. Nanoscale. Issue 22. 2012. https://doi.org/10.1039/C2NR32031B.

[4] – S. Roy, C. M. Ajmal. S. Baik. J. Kim, Silver Nanoflowers For Single-Particle SERS With 10 pM Sensitivity. Nanotechnology. Vol 28. P46-57. 2017.

[5] - Mazzola, F., Trinh, T., Cooil, S., Østli, E. R., Torbjørn, E., Skjønsfjell, B., Kjelstrup, S., Preobrajenski, A., Cafolla, A. A., Evans, D. A., Breiby, D. W., & Wells, J. W. Silver catalyzed Fluorouracil degradation; a promising new role for graphene. November, 2014.
[6] - Walton, J, Wincott, P, Fairley, N & Carrick, A 2010, Peak Fitting with CasaXPS: A Casa Pocket Book. Accolyte Science, Knutsford, UK.

[7] – Miura. K, Kinouchi. M, Ishida. K, ET AL. 5-FU Metabolism In Cancer And Orally Administrable 5-FU Drugs. Cancers. Basel. Volume 2. P1717-1730. 2017.

[8] – P. Banerjee, D. Mukherjee, T. K. Maiti, N. Sarkar. Unveiling the Self-Assembling Behavior of 5-Fluorouracil and its N,N'-Dimethyl Derivative: A Spectroscopic and Microscopic Approach. Langmuir. Vol 31. P10978-10988. 2017.

[9] – P. Kalantarian, A.R. Najafabadi, I. Haririan ET AL. Preparation of 5-Fluorouracil Nanoparticles By Supercritical Antisolvents For Pulmonary Delivery. Int J Medcine. Volume 5. P763-770. 2010. DOI:10.2147/IJN.S12415

[10] - RISINGGÅRD, H. K., Et AL. Degradation Of The Chemotherapy Drug 5-Fluorouracil On Medical-Grade Silver Surface. Applied Surface Science. Vol435. P1213-1219. https://doi.org/10.1016/J.APSUSC.2017.11.221

[11] - A. Krüger, F. Kataoka, M. Ozawa, T. Fujino, Y. Suzuki, A.E. Aleksenskii, A. Ya. Vul, E. Ōsawa. Unusually Tight Aggregation In Detonation Nanodiamond:Identification and Disintegration. Carbon. Vol 43. P1722-1730. 2005. https://doi.org/10.1016/J.CARBON.2005.02.020.

[12] – Michael C. Milone ET AL. Therapeutic Drug Monitoring Of Selected Anticancer Drugs.

[12] - MICHAEL C. MILONE ET AL. THERAPEUTIC DRUG MONITORING OF SELECTED ANTICANCER DRUGS THERAPEUTIC DRUG MONITORING. Amitava Dasgupta. Elsevier. P291-321. 2012.

[13] - Pascu. M. L. et al. 5-Fluorouracil as a photosensitiser. In vivo. Issue 19. 215-220. 2006.

[14] – Ying. Y et al. A Nobel 5-FU/rGO/BOE Hybrid Hydrogen Shell On A Tumor Cell:One-Step Photosynthesis And Synergisitic Chemo/Photo-thermal/Photodynamic Effect. RSC adv. P2415-2425. 2017. DOI: 10.1039/C6RA25834D.

Chapter 8 – Surface treatments of gallium oxide and their effect on the oxidation state.

Aberystwyth surface science group has previously conducted research to show that there is a downward band-bending on ZnO surfaces and that the desorption of the OH termination can alter the properties of the surface from an accumulation to a depletion layer. The thermal stability of a surface termination in this instances are essential as oxygen vacancies form easily on Ga_2O_3 surfaces[1]. Electronic devices which may suffer from poor thermal conductivity and therefore studies into the desorption of surface terminations on similar TCO's is essential.

This chapter presents measurements taken from a $(\bar{2}01)$ single crystal of β-Ga_2O_3 with N-type Sn dopant of $3x10^{18}cm^{-3}$ donor concentration and Au/Ti ohmic contacts using real-time XPS measurements to characterise surface changes during a temperature cycle. Changes in peak area, binding energy reveal temperature dependence which may be due to changes in surface stoichiometry. These shifts depend on the preparation of the crystal so a variety of different treatments to oxidise the surface have been used. The peak shift and recovery whilst cooling the sample was potentially dependant on the surface treatment used to oxidise the surface.

Changes are interpreted in terms of the surface OH species which start to desorb at high temperature are dependent on the surface treatment. It is also shown that at even higher temperatures that the Ga_2O_3 decomposes to a Ga metal state.

These experiments were conducted using the REES system at Aberystwyth University as described in Chapter 4. All core level data has been fitted using a pseudo-Voigt profile with a 0.65G/L ratio with constrained widths. The width for the Ga $2p_{3/2}$ component was set to 1.7eV whilst for the Ga $2p_{3/2}$ and 1.45eV for the O 1s, with the initial guess being allowed +/-0.05 freedom.

Work in this chapter contributed to R.M Gazoni's publication discussing surface treatment effects on the band bending[2].

8.1 Results

8.1.1 – As received β-Ga_2O_3 Core level photoemission

Figure 8.1.1 shows the Ga $2p_{3/2}$ and O 1s core level emission spectra for the as loaded sample labelled A and B, whereas C-D demonstrates the loss of surface species after a 600°C anneal. It is believed the hydroxylation of the surface occurs naturally via H_2O interactions with the surface.[3]

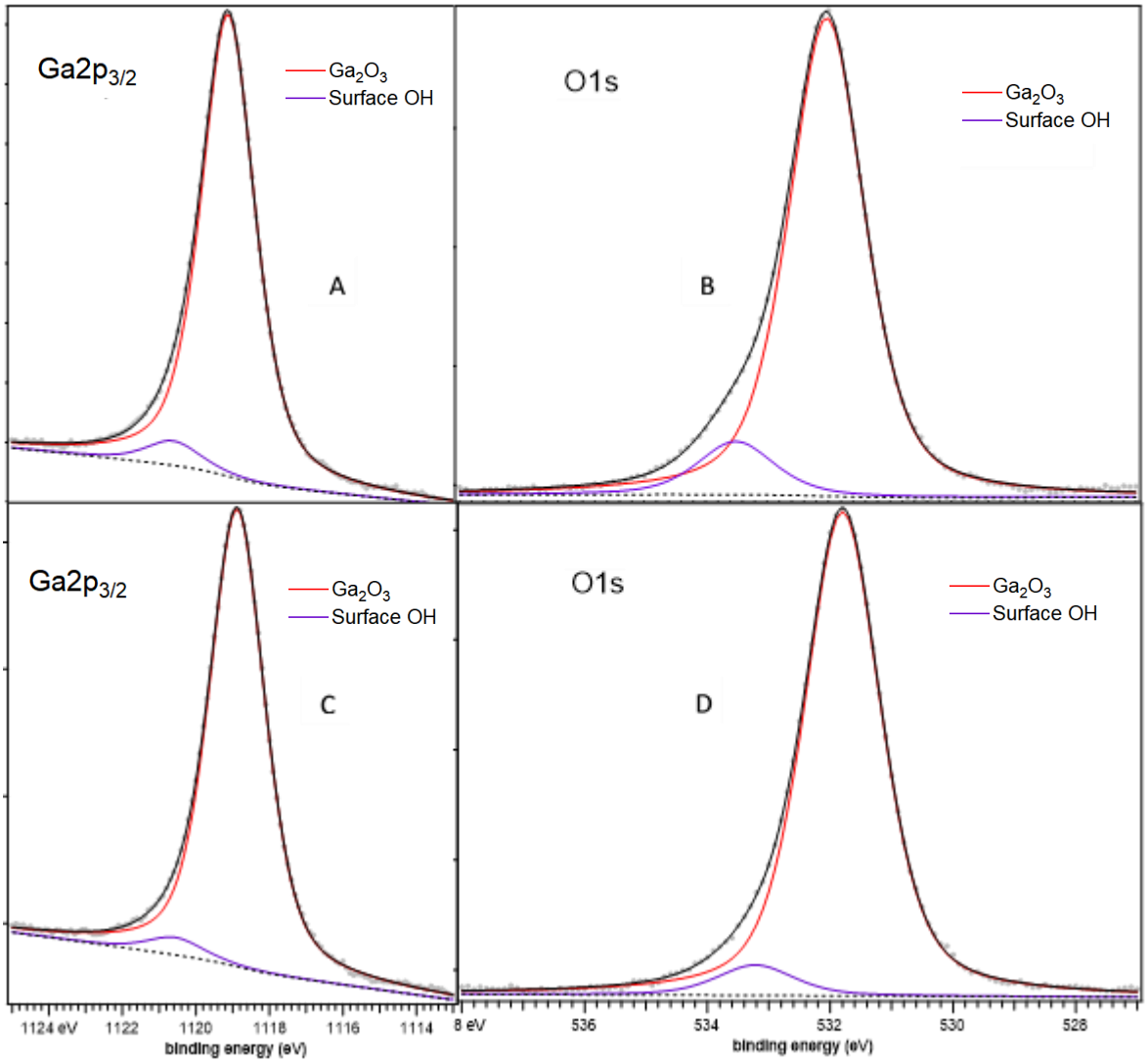

Figure 8.1.1A-D: Ga $2p_{3/2}$ and O 1s core levels of the as received Ga_2O_3 sample before and after a 600°C anneal. There is a reduction in the surface OH after the anneal. A and B show before temperature cycle, and C and D show after the temperature cycle.

8.1.2 Real-time XPS measurements of as received Ga_2O_3.

Figure 8.1.2 shows a 2D image of the real-time measurements of the Ga $2p_{3/2}$ and O 1s snapshot core level spectra during a heating-cooling cycle from 30-600-50°C over 400 minutes. Figure 8.1.3 shows the peak position of the Ga $2p_{3/2}$ during the same cycle which shows the shift in kinetic energy of the Ga $2p_{3/2}$ core level peak.

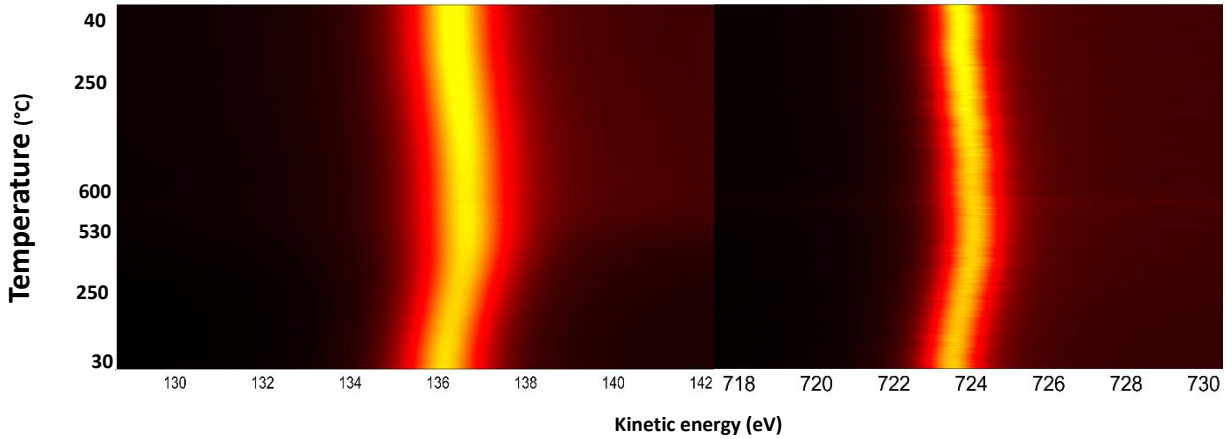

Figure 8.1.2: 2D image plots Ga 2p and O 1s core-level spectra during a heating cycle of 30-600-50°C. It can be seen there is a broadening of the Ga $2p_{3/2}$ that remains constant above 400°C and that the shift in peak position recovers on the cooldown.

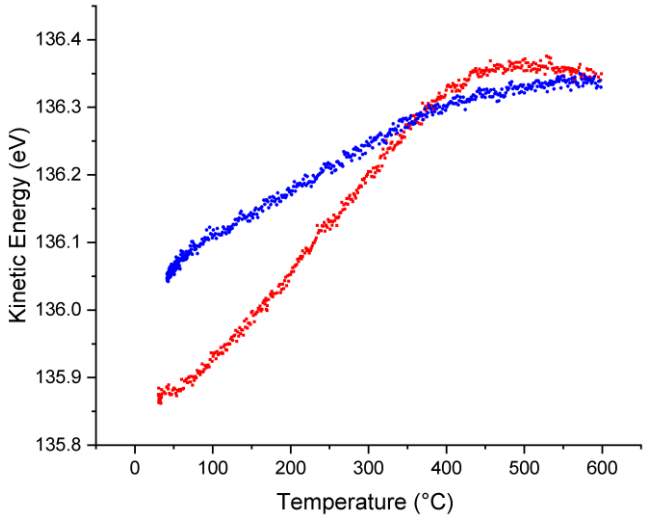

Figure 8.1.3: Peak position vs temperature for the Ga $2p_{3/2}$ core level spectra during the heating cycle, where the red line indicates the heating stage and blue points indicate the cooling stage for the same temperature cycle as indicated in Figure 8.1.2.

The Ga $2p_{3/2}$ and O 1s real-time measurements show the same features, and the plot for the O 1s position vs temperature is similar to the Ga 2p in Figure 8.1.2C, the shape of the graph indicates a change occurs around 460°C at which the peak position plateaus and refuses to shift any higher.

The sample was checked for charging[4] by altering the flux on the sample from the X-ray source on the sample by altering the distance between the two, however no changes in core level position were observed for this experiment and all the experiments from this point onward. The real-time fits work via setting a pseudo-Voigt peak for the very first scan, and with allowing it some flexibility (variations in width was over 0.2eV due to the heating of the sample causing a broadening of the peak). The peak centre was taken as the measured shift in kinetic energy.

8.1.3 Core level measurements and REES of NaOH treated β-Ga_2O_3

The β-Ga_2O_3 sample after annealing to 600°C in UHV was treated in 1M of NaOH at 60°C for 30 minutes. The sample was then rinsed in de-ionised water and then dried using N_2 gas. This treatment is predicted to produce a stronger type of bonding on the surface, the sample was then loaded into the REES system, and heated then cooled from 30-600-30°C during 400 minutes and real-time measurements of the core levels were taken.

Figure 8.1.4 shows the Ga $2p_{3/2}$ and O 1s core levels before heating.

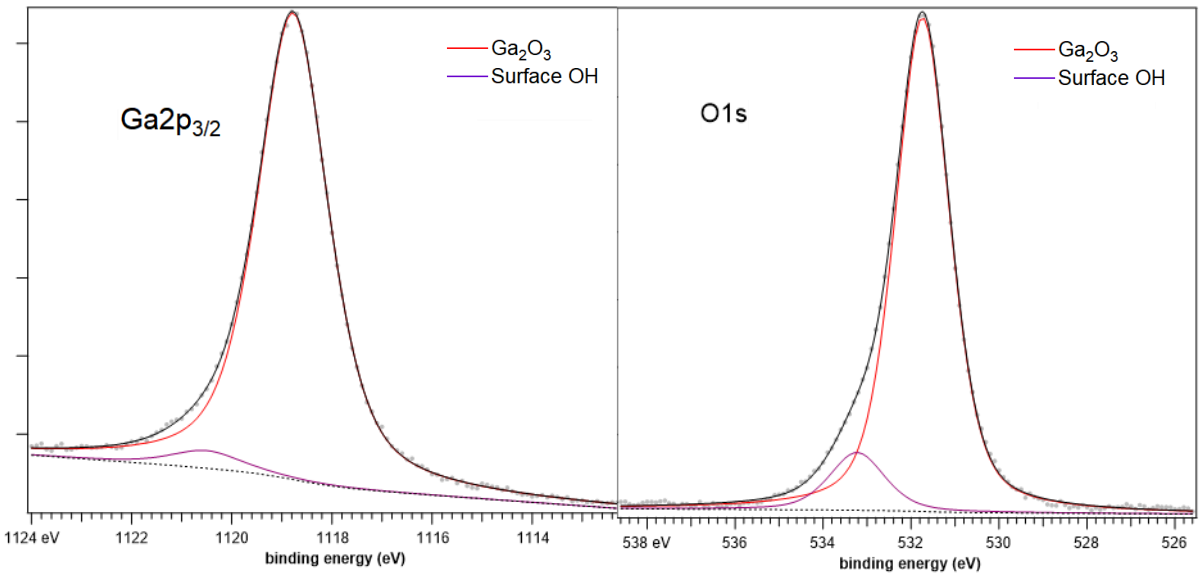

Figure 8.1.4: Ga $2p_{3/2}$ and O 1s spectra before the heating cycle after treating the β-Ga_2O_3 in NaOH. Showing a re-oxidation of the surface after annealing it off in section 7.1. There is more OH on this surface then the as received.

Figure 8.1.5 shows the real-time spectra for the Ga $2p_{3/2}$ and the O 1s core level spectra. Figure 8.1.6 shows the peak position vs temperature during the same heating cycle showing a different shift profile when compared to the as received.

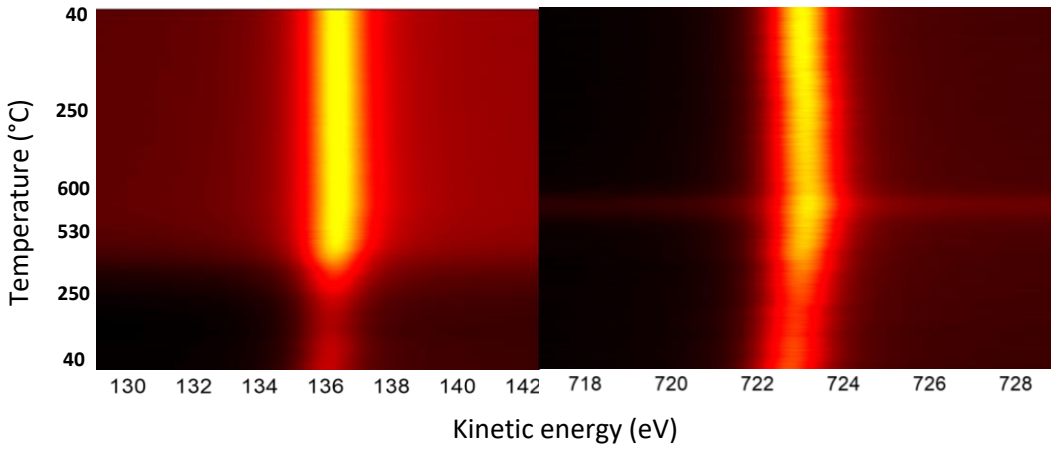

Figure 7.1.5: REES 3D images of the Ga $2p_{3/2}$ and O 1s core levels, the initial low intensity is due to the large amount of surface carbon contaminants on the β-Ga_2O_3 after NaOH treatment.

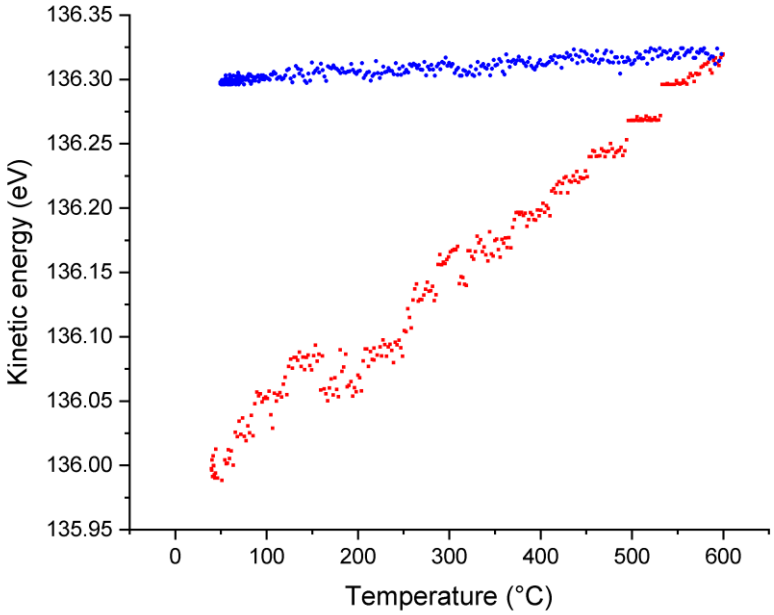

Figure 8.1.6: Ga $2p_{3/2}$ core level spectra showing the difference in peak position vs temperature for the NaOH measured in real time during the heating cycle, which exhibits a different profile in comparison to the as received.

There is a difference in the change in the peak position when cooling down between the as received and the NaOH treated surfaces, the peak maintained its shift throughout the cycle

and remained constant during cooling. The band bending may be fixed in this case for higher temperatures.

8.1.4 Core level measurements and REES of H_2SO_4 treated β-Ga_2O_3

The NaOH treated β-Ga_2O_3 sample after being annealed to 600°C in UHV was treated in 40% concentration of H_2SO_4 in DI water at 100°C for 30 minutes. The sample was then rinsed in DI water and then dried using N_2 gas. The oxidation of the surface whilst in the presence of H_2SO_4 is believed to produce an OH termination which is free standing.[4] The sample was then loaded into the REES system and heated then cooled from 30-600-30°C for 400 minutes and real-time measurements of the core level snapshots were recorded.

Fig 8.3.7A-B shows the Ga $2p_{3/2}$ and O 1s core levels before the heating cycle whereas C-D show the resulting core levels after the heating cycle and being left in UHV for 18 hours.

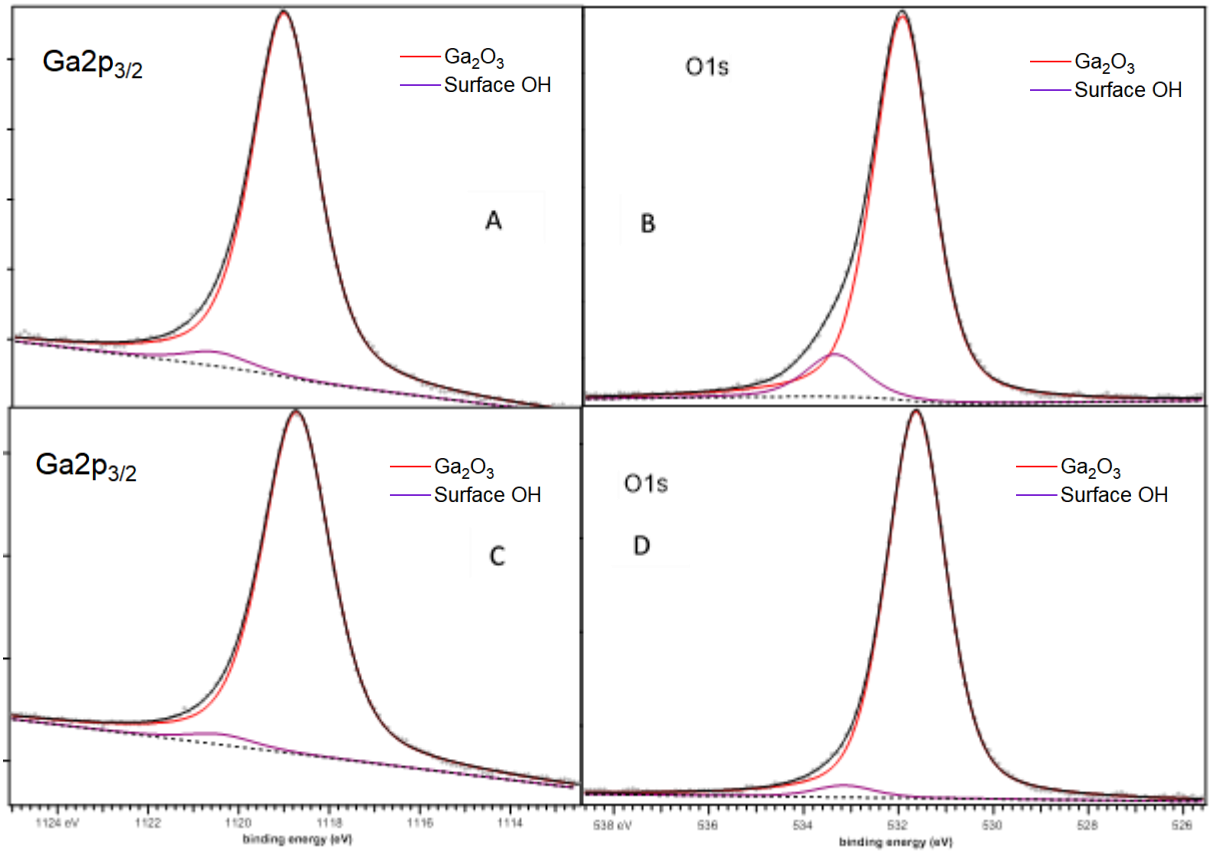

Figure 8.1.7 A-D shows the core levels for the β-Ga_2O_3 before and after the heating cycle, which as can be seen there is a notable reduction in the OH surface groups post anneal.

8.1.9 shows the peak position vs temperature during the same heating cycle showing a different shift profile when compared to the as received.

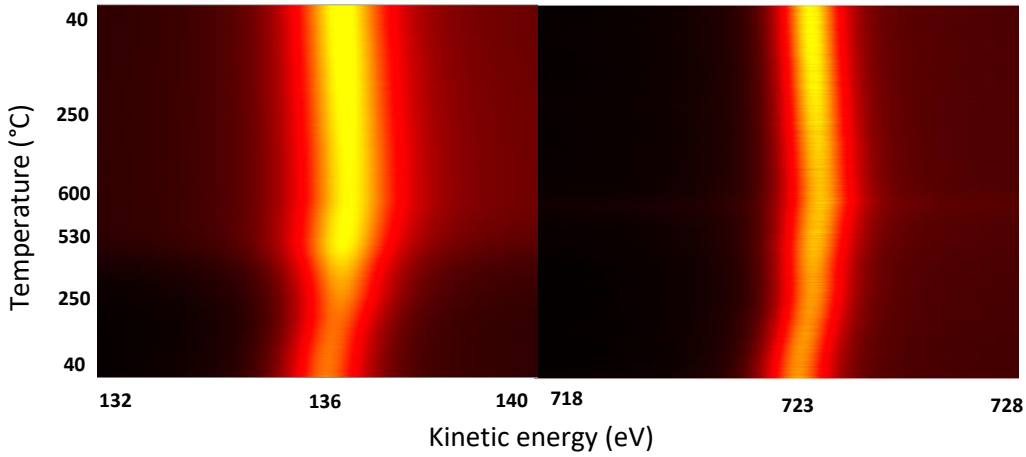

Figure 8.1.8: 2D image of the peak position and width of the Ga $2p_{3/2}$ and O 1s core level spectra during the annealing cycle measured in real time. Initial low intensity in the Ga $2p_{3/2}$ is due to surface adsorbates.

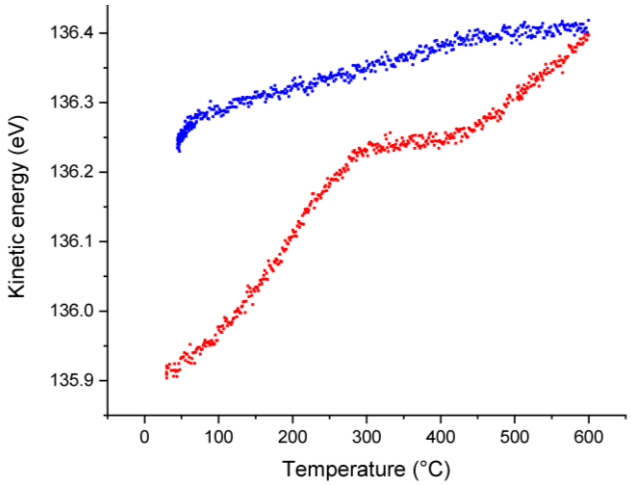

Figure 8.1.9: Peak position vs temperature for the Ga $2p_{3/2}$ during the annealing cycle of the β-Ga_2O_3 measured in real time, showing a different profile to the previous two surfaces.

From Figure 8.1.9 we can see that there is a plateau between 280-400°C which may indicate a range at which there is change in the process occurring at the surface. The peak shift whilst heating is different from the other two treatments, but the cooling down is similar to the as received sample.

8.1.5 Decomposition and metallisation of NaOH treated β-Ga_2O_3

An NaOH treated β-Ga_2O_3 was annealed up to 860°C during a cycle to determine the temperature at which the surface OH is completely desorbed from the surface. Figures 7.1.10 shows the Ga $2p_{3/2}$ and O 1s core levels after the sample has been annealed to 860°C. Figure 8.1.11 shows a plot of the real-time data of the core level of the Ga 2p during the same cycle as 8.1.10

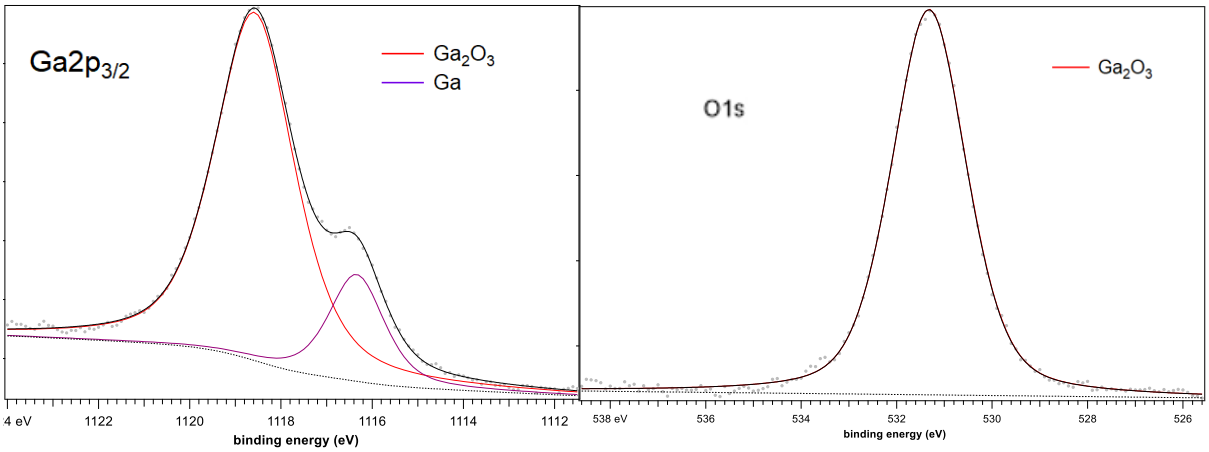

Figure 8.1.10: Ga $2p_{3/2}$ and O 1s core levels of β-Ga_2O_3 after annealing the NaOH treated sample up to 860°C, the position of the metallic gallium peak matches the literature value.[5]

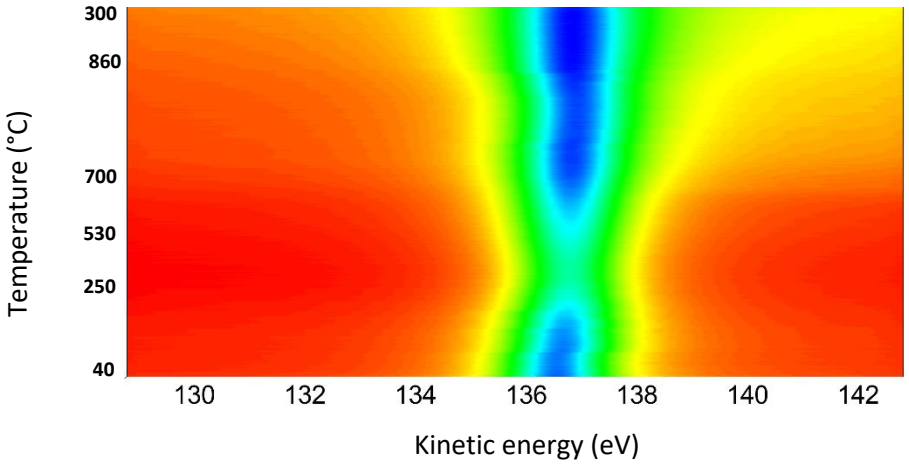

Figure 8.1.11: 2D image of the Ga 2p core level collecting in real time during the annealing cycle, the increase in peak width towards the higher temperature is due to the formation of metallic gallium on the surface.

The oxygen did not start desorbing until 740°C, however upon reaching 860°C the sample degraded to having a monolayer of gallium on the surface.

8.2 Discussion.

The OH termination of β-Ga_2O_3 causes an upward band-bending of the conduction and valence bands near the surface, however the type of chemical treatments which were used to achieve the termination varies the nature of the OH bonding and coverage. Knowledge of the stability and variations in the band-bending is crucial for optimisation of β-Ga_2O_3 for device applications[7].

The area of the core levels from all the real-time measurements were calculated to deduce the stability of each surface's OH group. Table 8.1 shows the data for the ratio between the Ga $2p_{3/2}$ and O 1s spectra for before each cycle compared to at 600°C which is obtained from the area of the real-time spectra.

Table 8.1: the ratios of the Ga $2p_{3/2}$ and O 1s core level spectra before and after the temperature cycles obtained from the real-time measurements.

Surface treatment	**Ga 2p:O 1s as loaded**	**Ga 2p:O 1s at 600°C**	**Ga 2p:O 1s Difference.**
Natural formation	*4.96*	*5.98*	*1.02*
NaOH	*4.82*	*4.96*	*0.14*
H_2SO_4	*5.03*	*6.39*	*1.36*

There is also information in the ratio of the GaOH- Ga_2O_3 which is provided in Table 8.2 and calculated from the core-level spectra which was measured 16 hours after the sample had cooled down to 50°C and the real-time data. For the NaOH treatment the ratio was measured using the real-time data.

Table 8.2: Ratio of the OH:Ga_2O_3 in the core-level O 1s spectra.

Surface treatment	**OH: Ga_2O_3 as loaded**	**OH: Ga_2O_3 post anneal**	**OH: Ga_2O_3 percentage Difference.**
Natural formation	*11.2%*	*6.3%*	*4.9%*
NaOH	*11.7%*	*11.3%*	*0.4%*
H_2SO_4	*11.0%*	*3.01%*	*7.99%*

The naturally formed OH termination desorption only occurred after 250°C and maintained relatively stable up until 550°C at which point desorption ceased. This indicates a temperature region at which the little remaining OH on the surface is stable. Desorption of the OH species on the NaOH treatment was minimal, only occurring during small intervals at 150, 260 and 510°C. Acid treatment (H_2SO_4) created the least stable termination, where OH groups started to desorb from the surface at 160°C where it steadily continued until reaching a maximum at 420°C when comparing the O 1s:Ga 2p area ratios in Table 8.1. An Ga 2p:O 1s ratio of around 5.0 equivalates to 1ML of OH on the surface, whereas Figure 8.1.7 indicates a almost complete desorption. It is important to note the high-resolution core levels taken and shown are 15-18 hours after the final REES measurements, as cooling down to RT takes over 10 hours. Due to the nature of the BN ceramic heater in the REES system storing hydrogen we believe it does re-hydroxylate the surface over time, however even as seen in the core levels the final values are much lower. The theory behind this increase in stability for the NaOH treated surface is that the H is also bonded to surface O atoms, increasing the amount of energy required to break the surface OH away from the β-Ga_2O_3[11].

The electronic band-bending can be explained by the peak-shifts in the core levels in the XPS. The shift in kinetic energy can be directly compared to the shift in the band bending. With any measurements of wide-bandgap semiconductors evidence of photovoltage or charging have to be investigated to ensure the peak-shift is related to band bending. The X-ray source was taken back to reduce the flux on the samples to ensure any measured shift was not due to photovoltage and measurements at two different fluxes produced the same peak positions in core level spectra. The sample also had Au/Ti contacts annealed into the back and front faces to ensure no charging occurred also. The unique shape of the peak shift versus temperature for each treatment whilst undergoing the same heating cycles validates the proposal that peak shifts are from surface band bending. The image plots as well as the scatter plots demonstrate that each different surface treatment affects not only the total band bending of the surface, but also the rate of bending and rate of recovery that occurs also. Table 8.3 summarises the shifts in terms of the max shift and final shift during the realtime measurements, and the shift between the core levels before the heating cycle and 18 hours after the heating cycle., where the shifts also match those reported in literature[7-8].

Table 8.3: The Ga $2p_{3/2}$ core level shifts measured in kinetic energy, where the maximum shift is the max it peak shifted whilst heating, the final shift which indicates the core-level shift at 50°C, and the shift measured when core levels were taken 15 hours afterwards.

Surface treatment	Maximum shift (eV)	Final shift (eV)	Post 15 hour shift (eV)
Natural formation	*0.48*	*0.17*	*0.15*
NaOH	*0.3*	*0.3*	*0.3**
H_2SO_4	*0.49*	*0.31*	*0.29*

Where NaOH maintains its shift from REES core levels, suggesting that any changes induced are stable at RT and might be potentially due to a change in nature of the OH bonding on the surface whilst still maintaining a ML of OH termination. Whereas for the naturally formed and H_2SO_4 treated surfaces, the recovering of the shift can be thought as a re-hydroxylation of the clean surface, an experiment involving take each sample post anneal out to the load lock of the UHV system, vent to air for 30 minutes, and then remeasure the sample was thought as a good way to prove this theory, however due to time constraints this was not possible but leaves further work for conclusive proof. This work is similar and the concepts behind what causes the surface downward band bending to researched previously conducted in the group on ZnO[10] and follows on from the work demonstrated in this thesis on diamond/nanodiamond, that for wide band-gap semiconductors the method of preparation and the produced oxygen species on the surface are important for device fabrication in various aspects.

The temperature required for the removal of the OH species from the NaOH is very close to the temperature of degradation for β-Ga_2O_3. Since there were only small amounts of metallic gallium visible in the XPS, it can be assumed that the surface becomes irreversibly damaged, with potentially the Ga-O bonds breaking and releasing the oxygen, leaving metallic gallium on the surface. In this instance, it may be safer to use other techniques (such as the acid treatment) first when attempting to remove the OH groups rather than just annealing to high temperature. The β-Ga_2O_3 still showed a slight shifting of the band-bending even after metallisation which would be expected for a semiconductor with a metal film on the surface, this would form a schottky junction causing the gallium oxide to undergo band bending to match the gallium fermi level. When the crystal was removed from UHV the crystal was

treated in 1M of H_2SO_4 and we found that in XPS there was no metallic gallium on the surface, this might suggest any gallium on the surface is free-standing rather than chemically bonded.

8.3 Conclusion

The data shown above shows that the method of oxidation for β-Ga_2O_3 is important for producing a thermally stable OH termination, and that the termination itself causes a surface band-bending which can be modified by annealing in high-temperature in UHV.

It's shown that NaOH treated surfaces are thermally stable up to 700°C and that H_2SO_4 treated surfaces are the least stable. The band bending has been shown to increased more drastically after annealing the H_2SO_4 treated sample, however the peak-shift is more stable for the NaOH surface. This show's there may be a difference in the way the OH bonds to the surface which is shown in DFT calculations[9-10]. Manipulation of the band-bending via carful surface treatments will have great benefits for potential metal-semiconductor contacts and heterojunctions. [12-13]

Figure 8.3.1 shows a band profile for the Ga: β-Ga_2O_3 interface.

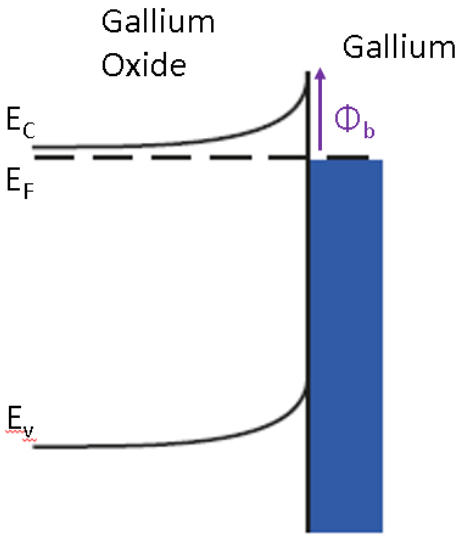

Figure 8.3.1. Band diagram showing the Schottky junction that occurs when metallic gallium is on the surface of the gallium oxide. The bands bend to meet the Fermi-edge of the gallium, creating a barrier height, Φ_b

References:

[1] - Li, Z., Liu, Y., Zhang, A. et al. Quasi-two-dimensional b-Ga2O3 field effect transistors with large drain current density and low contact resistance via controlled formation of interfacial oxygen vacancies. Nano Res. Vol12. P143–148. 2019.

[2] – R. M Gazoni, L. Carroll, J. I. Scott, S. Astley, D. A. Evans, A. J. Downard, R. J, Reeves, M. W. Allen. Relationship Between The Hydroxyl Termination And Band Bending at (201) ¯ b-Ga2O3 surfaces. Physical Review B. July 2020. DOI: 10.1103/PhysRevB.102.035304

[3] - Roozbeh Anvari Dr. Dino Spagnoli Prof. Dr. Giacinta Parish Prof. Dr. Brett Nener. Density Functional Theory Simulations of Water Adsorption and Activation on the (−201) b-Ga2O3 Surface. Chemistry, a European Journal. Vol24. P7445-7455. May 2018.

[4] - Juan A Colón Santana, Charging effects in x-ray photoelectron spectroscopy. Quantitative Core Level Photoelectron Spectroscopy. Pages 4-1. March 2015.

[5] C.D. Wagner, A.V. Naumkin, A. Kraut-Vass, J.W. Allison, C.J. Powell, J.R.Jr. Rumble, NIST Standard Reference Database 20, Version 3.4 (web version) (http:/srdata.nist.gov/xps/) 2003.

[6] - Jiancheng Yang, Zachary Sparks, Fan Ren, Stephen J. Pearton and Marko Tadjer. Effect of surface treatments on electrical properties of b-Ga2O3. Journal of Vacuum Science & Technology Vol36. 2018.

[7] - J. E. N. Swallow, J. B. Varley, L. A. H. Jones, J. T. Gibbon, L. F. J. Piper, V. R. Dhanak, and T. D. Veal. Transition from electron accumulation to depletion at b-Ga2O3 surfaces: The Role Of Hydrogen And The Charge Neutrality Level. APL Materials. Vol7. 2019.

[8] - A. Navarro-Quezada, Z. Galazka, S. Alamé, D. Skuridina, P. Vogt, and N. Esser. Surface Properties Of Annealed Semiconducting B-Ga2O3 (100) Single Crystals For Epitaxy Appl. Surf. Sci. Vol349. P368-373. 2015.

[7] – S. Kohei. MBE Grown Ga2O3 And Its Power Device Applications. Journal Of Crystal Growth. Vol 378. P591-595. 2013.

[8] -R. Heinhold. Influence Of Polarity and Hydroxyl Termination On The Band Bending at ZnO Surfaces. Physical Review B. Vol88. P235. 2013..

[9] X. Zhou, E. J. M. Hensen, R. A. Van Santen, and C. Li. DFT Simulations of Water Adsorption and Activation on Low-Index a-Ga2O3. SurfacesChemEurope. Vol 20. P6915-6926. 2014.
[10] Y. Ma, X. Zhao, M. Niu, W. Li, X. Wang, C. Zhai, T. Wang, Y.Tang, and X. Dai. Monoclinic Ga2O3 (100) Surface As A Robust Photocatalyst For Water-Splitting RSC Adv. 7. January 2017.
[11] – R. Anvari, D. Spagnoli, G. Parish, B. Nener, Density Functional Theory Simulations of Water Adsorption and Activation on the (−201) b-Ga2O3 Surface. ChemEur. Vol24. P7445-7455. 2018.
[12] – Y. Yao, R. Gangireddy, J. Kim, K. K. Das, R. F. Davis, L. M. Porter. Electrical behavior of b-Ga2O3 Schottky Diodes With Different Schottky Metals. J. Vac. Sci. Tech. Vol 35. 2017.
[13] – C. Hou, r. M. Gazoni. R. J. Reeves, M. W. Allen. High-Temperature (350 °C) Oxidized Iridium Schottky Contacts On b-Ga2O3. Appl, Phys. Lett. Vol 114. 2019.

Chapter 9 – Further Work and Conclusions

9.1 Further work

9.1.1 – Oxidation of diamond/nanodiamonds under NAP

The oxidation of both the single crystal and nanodiamonds has only been measured using photoelectron spectroscopy using O_2 and H_2O. However, there are various other gases which would be interesting, such as the use of carbon monoxide to see if the molecule is broken down for use as a catalytic convertor. There is also the potential of using an oxidised surface with CO to see if the carbon monoxide will form CO_2 and remove oxygen species at a high enough temperature. The use of nitrous oxide would have also been interesting in having the capability of measuring with any N is left on the diamond surface and being able to measure if then forms N_2. Ozone would also be interesting to use as it is a more unstable molecule which may allow for a lower-temperature oxidation to occur on a hydrogen terminated (001) diamond.

Other acid etches for comparison to the one used in this thesis would also be beneficial, where other groups use a piranha etch (H_2SO_4 and H_2O_2) which is believed to produce a difference in the surface species also.

Annealing and measurements at higher temperatures are also preferable, where it's been reported that 450°C is the optimal oxidation temperature of DNDs but unfortunately the NAP cell in Manchester is limited by the seals between the NAP-cell and UHV chamber. Approaching 420°C led to an increase in pressure of UHV chamber from $8x10^{-10}$ mbar up to $4x10^{-8}$mbar where concerns about oxidation of the X-ray source had to be considered. Higher temperatures based on the rate of pressure increase would have also taken the X-ray source above its recommended operating pressure.

Measurements of the single crystals crystallographic structure using LEED measurements would be extremely advantageous, as any (2x1) surface reconstructions could have been measured however unfortunately there was not the capabilities to do this at both Manchester University and Diamond Light Source at the time.

UPS measurements during the oxidation, such that the workfunction for each termination or at set temperatures can be calculated and directly compared to the gas-phase shifts. B07 is limited to 200eV photon energy which is too high for UPS and the NAP cell at Manchester is unable to fit a He(I/II) source due to the limitations of instrumentation. Valence Band spectra however can be obtained at B07.

More complex calculations involving finding minimum energy structures for a variety of different bonds (such as max ether length before a C=O/C-OH occurs) would be ideal, and FTIR measurements to confirm the surface chemistry on DNDs during oxidation would provide a complimentary method to the PES.

9.1.2 - Fluorouracil on diamond

DLS measurements for the nanodiamond/5FU:ND suspensions after ultra-sonication would provide a much better particle size due to the agglomeration of particles. Synchrotron measurements of the 5FU on the O:DND without the breakdown of the C-F bond would also provide a complete story. The testing of the efficiency of the 5FU:ND mixture in HeLa cancer cells is also the next step for the research. Trialling 5FU:ND solutions have been discussed with several potential partners however experiments have yet to start.

9.1.3 - Other terminations of nanodiamonds

Measuring nanodiamonds in a variety of gases at temperature at NAP has many potential future pathways. Future experiments by Aberystwyth University materials group in the upcoming year are trialling a variety of different gases to determine if the process of achieving different terminations which aren't currently discussed are possible.

9.1.4 - Oxidation of gallium oxide.

DFT calculations to demonstrate the type of OH bonding that forms on the surface dependant on the environment the Ga_2O_3 is introduced too would provide a better understanding of the stoichiometry between them. It would also help to determine the reasons why the NaOH is more thermally stable than the others. Other oxidation methods such as NAP-PES measurements exposing the crystal to H_2O or O_2 would also be interesting to see if the upward band-bending could be increased even further. Measuring how the shift and OH ratio changes

and recovers for lower temperature cycles would also provide information and further validation the change in binding energy is a real effect.

UPS measurements or other methods of measuring the work function of the sample and LEED/PEEM to measure the structure of the metallic gallium on the surface.

9.2 Conclusions

This thesis demonstrates the work conducted on the effect of the oxidation method on the oxygen species of wideband-gap semiconductors. Dependant on the preparation used, the band-bending, electron affinity and thermal stability can alter drastically. There is a difference in the ratios of chemical species on oxygen terminated (001) diamond when comparing an acid etch and oxygen anneal from a hydrogenated surface. Annealing the acid etched surface anneal in oxygen modifies the surface but going from the acid etched surface to the oxygen annealed surface is impossible. This shows there is limit that the maximum electron affinity of an oxygen terminated diamond etched in acid has, which is much lower than the air annealed. This is believed to be due to C=O bonds on the surface. Annealing the acid etched diamond in oxygen coverts ketone into peroxide bonding on the surface, which is validated by DFT calculations.

The PES shows that the oxidation of nanodiamonds has specific growth temperatures where one type of oxygen species grows. Peroxide bonds form on the nanodiamond are stable for only a temperature range of 280° to 320°C where it's theorised that it's the conversion of ketone groups into either a C-OH bond or reconstructing the crystal surface. The oxygen terminated diamond showed an increase of 1.4/1.3eV in workfunction from measurements of the O_2 gas and UPS measurements taken ex-situ in the Aberystwyth system respectively.

The electrostatic attraction of 5FU onto diamond and nanodiamond surfaces has been studied using a mix of DFT studies and PES techniques. The effect of the oxidation state, and therefore the electron affinity affects the amount of 5FU that adsorbs onto diamond surface where a clean diamond surface will strip an H off the molecule. NEXAFS confirms that on O:surface that the molecule has a flat laying orientation even for nanodiamonds. Mixtures of ND:5FU can bring down the particle size of 5FU by over 10 times. This has implications for drug delivery applications and may increase the chance of cell adsorption.

The type of oxidation treatment of Ga_2O_3 affects the amount of surface OH species, the thermal stability and the upward band-bending of the bandgap. Whilst NaOH treatments produce a thermally stable OH termination the acid etches produced a stoichiometry which decreased by over 70% between room temperature and 600°C. The break down temperature of the NaOH surface species was found to be above 800°C, where at 860°C the Ga_2O_3 surface decomposed down into metallic gallium. This is important for device fabrication where the H_2SO_4 treated surface started to decompose from 120°C.

The work conducted in this thesis between the treatment of DND's, single crystal diamond and Ga_2O_3 the data suggests that the use of acid treatments is highly unrecommended. Acid treatments have been shown to roughen crystal surfaces where there is residual polishing lines, produces an un-optimal termination which is both thermally unstable and can be considered inferior to other methods of oxidation, and can introduce further contamination to substrates and is more difficult to process. For device applications, crystals will need to be fabricated and modified in bulk. This may prove difficult for the use of acids, whereas treating a tray of crystals to a 400°C anneal in a suitable environment such as O_2 would be considerably easier to use post treatment.